



AFRL-RX-WP-TR-2010-4244

METALLIC AND CERAMIC MATERIAL DEVELOPMENT RESEARCH

**Emmanuel E. Boakye, Michael V. Braginsky, Carmen M. Carney, Yoon Suk Choi,
George J. Jefferson, Kristin A. Keller, Young-Won Kim, HeeDong Lee, Tai-II Mah,
Sarath K. Menon, Pavel Mogilevsky, Triplicane A. Parthasarthy, M. Dennis Petry,
Satish L. Rao, Oleg N. Senkov, Michael J. Scott, Vikas Sinha, and You Hai Wen**

UES Inc.

**MAY 2010
Final Report**

Approved for public release; distribution unlimited.

See additional restrictions described on inside pages

STINFO COPY

**AIR FORCE RESEARCH LABORATORY
MATERIALS AND MANUFACTURING DIRECTORATE
WRIGHT-PATTERSON AIR FORCE BASE, OH 45433-7750
AIR FORCE MATERIEL COMMAND
UNITED STATES AIR FORCE**

NOTICE AND SIGNATURE PAGE

Using Government drawings, specifications, or other data included in this document for any purpose other than Government procurement does not in any way obligate the U.S. Government. The fact that the Government formulated or supplied the drawings, specifications, or other data does not license the holder or any other person or corporation; or convey any rights or permission to manufacture, use, or sell any patented invention that may relate to them.

This report was cleared for public release by the Wright-Patterson Public Affairs Office and is available to the general public, including foreign nationals. Copies may be obtained from the Defense Technical Information Center (DTIC) (<http://www.dtic.mil>).

AFRL-RX-WP-TR-2010-4244 HAS BEEN REVIEWED AND IS APPROVED FOR PUBLICATION IN ACCORDANCE WITH ASSIGNED DISTRIBUTION STATEMENT.

*/signature//

JOHN H. BARNES, Project Engineer
Metals, Ceramics, & NDE Division
Materials & Manufacturing Directorate

*/signature//

PAUL L. RET, Chief
Metals Branch
Metals, Ceramics, & NDE Division
Materials & Manufacturing Directorate

*/signature//

MICHAEL J. KINSELLA, Chief
Ceramics Branch
Metals, Ceramics & NDE Division
Materials & Manufacturing Directorate

*/signature//

ROBERT T. MARSHALL, Deputy Chief
Metals, Ceramics & NDE Division
Materials & Manufacturing Directorate

This report is published in the interest of scientific and technical information exchange, and its publication does not constitute the Government's approval or disapproval of its ideas or findings.

Disseminated copies will show “/signature//” stamped or typed above the signature blocks.

REPORT DOCUMENTATION PAGE					<i>Form Approved</i> <i>OMB No. 0704-0188</i>	
The public reporting burden for this collection of information is estimated to average 1 hour per response, including the time for reviewing instructions, existing data sources, gathering and maintaining the data needed, and completing and reviewing the collection of information. Send comments regarding this burden estimate or any other aspect of this collection of information, including suggestions for reducing this burden, to Department of Defense, Washington Headquarters Services, Directorate for Information Operations and Reports (0704-0188), 1215 Jefferson Davis Highway, Suite 1204, Arlington, VA 22202-4302. Respondents should be aware that notwithstanding any other provision of law, no person shall be subject to any penalty for failing to comply with a collection of information if it does not display a currently valid OMB control number. PLEASE DO NOT RETURN YOUR FORM TO THE ABOVE ADDRESS.						
1. REPORT DATE (DD-MM-YY) May 2010			2. REPORT TYPE Final		3. DATES COVERED (From - To) 30 November 2004 – 30 April 2010	
4. TITLE AND SUBTITLE METALLIC AND CERAMIC MATERIAL DEVELOPMENT RESEARCH					5a. CONTRACT NUMBER FA8650-04-D-5233	
					5b. GRANT NUMBER	
					5c. PROGRAM ELEMENT NUMBER 62102F	
6. AUTHOR(S) Emmanuel E. Boakye, Michael V. Braginsky, Carmen M. Carney, Yoon Suk Choi, George J. Jefferson, Kristin A. Keller, Young-Won Kim, HeeDong Lee, Tai-II Mah, Sarath K. Menon, Pavel Mogilevsky, Triplicane A. Parthasarthy, M. Dennis Petry, Satish L. Rao, Oleg N. Senkov, Michael J. Scott, Vikas Sinha, and You Hai Wen					5d. PROJECT NUMBER 2311	
					5e. TASK NUMBER 00	
					5f. WORK UNIT NUMBER 23110002	
7. PERFORMING ORGANIZATION NAME(S) AND ADDRESS(ES) UES Inc. 4401 Dayton-Xenia Road Dayton OH 45432-1894					8. PERFORMING ORGANIZATION REPORT NUMBER	
9. SPONSORING/MONITORING AGENCY NAME(S) AND ADDRESS(ES) Air Force Research Laboratory Materials and Manufacturing Directorate Wright-Patterson Air Force Base, OH 45433-7750 Air Force Materiel Command United States Air Force					10. SPONSORING/MONITORING AGENCY ACRONYM(S) AFRL/RXL	
					11. SPONSORING/MONITORING AGENCY REPORT NUMBER(S) AFRL-RX-WP-TR-2010-4244	
12. DISTRIBUTION/AVAILABILITY STATEMENT Approved for public release; distribution unlimited.						
13. SUPPLEMENTARY NOTES PAO case number 88ABW-2010-3434, cleared 21 June 2010. Report contains color.						
14. ABSTRACT This final report details progress made on various topics related to advanced metallic, advanced metallic composites and ceramic materials. The development and sustainment of Air Force systems depends on both the optimal performance of traditional materials and the continued exploration of materials technologies. Major requirements driving the research into these new technologies include: 1) reducing the weight of engineering components of aircraft, 2) increasing the operating temperatures of engines, 3) providing advanced materials for thermal protection systems, and 4) producing geopolymer-based material for space mirror applications. Research was carried out three different classes of materials, advanced metallics, advanced metallic composites, and ceramics. In the latter case, both monolithic and fiber-reinforced materials were evaluated, along with geopolymers. The process-microstructure-property relationships were extensively and critically assessed for these material classes. Much of this research has been published elsewhere in the open literature as journal articles and papers.						
15. SUBJECT TERMS beta gamma alloys, plasticity, metallic glasses, ceramic composites, TPS, UHTCs, geopolymers						
16. SECURITY CLASSIFICATION OF:			17. LIMITATION OF ABSTRACT: SAR	18. NUMBER OF PAGES 154	19a. NAME OF RESPONSIBLE PERSON (Monitor) John H. Barnes	
a. REPORT Unclassified	b. ABSTRACT Unclassified	c. THIS PAGE Unclassified			19b. TELEPHONE NUMBER (Include Area Code) N/A	

Table of Contents

Section	Page
List of Figures	vii
List of Tables	xi
Forward	xii
1.0 Executive Summary	1
2.0 TASK ORDER 0001 – ADVANCED METALS RESEARCH	2
2.1 CP-FEM Based Materials Modeling.....	2
2.1.1 Unit-Cell Based Plasticity Modeling of Ni-Base Single Crystals	2
2.1.2 Modeling Plasticity of Ni ₃ Al-Based Intermetallic Single Crystals	3
2.1.3 Modeling of Micro-Compression Tests of Anisotropic Single Crystals	3
2.2 Modeling and Predictions of Materials Properties.....	4
2.2.1 Microtest on Nickel Pillars	4
2.2.2 Modeling Size Effect on Yield Strength (YS) of Faced Centered Cubic (FCC) Metals.....	4
2.2.3 Review of Size Effect and Implications	4
2.3 Modeling of Dislocation Behaviors	4
2.3.1 DDS of Precipitation Hardening in Inverse Superalloys	4
2.3.2 Criticality and Stochastic Flow in Microcrystal Plasticity	5
2.3.3 Estimating the Strength of Single-Ended Dislocation Sources in Micrometer-Sized Single Crystals	5
2.4 Modeling of Microstructures and Phase Evolution	6
2.4.1 A Phase-Field Model for Heat Treatment Applications in Ni-base Alloys.....	6
2.4.2 Phase-Field Modeling of Microstructural Evolution During Solidification in Al-Sc Alloy	6
2.5 Science for Sustainment.....	6
2.6 Publications.....	7
2.7 Presentations	8
2.8 References.....	8
3.0 TASK ORDER 0002 – RESEARCH FOR METALLIC MATERIALS WITH HIGH STRUCTURAL EFFICIENCY	10
3.1 Amorphous and Nanocrystalline Metals.....	10
3.1.1 Development and Characterization of a Nanocrystalline Aluminum Alloy From Amorphous Powder	10
3.1.2 Development of Thermodynamic and Topological Criteria for Amorphization and Glass Forming Ability.....	10
3.1.3 Development of New Bulk Metallic Glasses and Analysis of their Glass Forming Ability, Thermal Stability and Thermodynamic Properties	11
3.1.4 Oxidation and Corrosion Resistance of Ca-Based Bulk Metallic Glasses	12
3.1.5 Elastic and Thermal Properties of Ca-Based Bulk Metallic Glasses	13
3.1.6 Thermodynamic and Kinetic Behavior of Supercooled Glass-Forming Liquids.....	14
3.2 Super-High Strength Cast-and-Wrought Aluminum Alloys.....	14
3.2.1 Thermo-Mechanical Processing of a Cast 7xxx Al Alloy Modified with Sc	14

Table of Contents (Continued)

Section	Page
3.2.2 Optimization of Microstructure Heat, and Tensile Properties of a High Strength Direct Chill Cast Al-Zn-Mg-Cu Alloy Modified with Sc and Zr	15
3.2.3 Cryogenic and Elevated Temperature Strengths of a Wrought Al-Zn-Mg-Cu Alloy Modified with Sc and Zr	15
3.2.4 Effect of Sc on Aging Kinetics in a High-Strength Direct Chill Cast Al-Zn-Mg-Cu Alloy	16
3.3 Boron-Modified Titanium Alloys	16
3.4 Nickel-Based Superalloys	17
3.5 Publications	17
4.6 Invited Presentations	19
3.7 Presentations	20
3.8 Invention Disclosures/Patients	22
3.9 Conference Proceedings Edited	22
3.10 Awards/Service	22
3.11 References	22
4.0 TASK ORDER 0003 – RESEARCH FOR CERAMIC COMPOSITES	25
4.1 Ceramic Composite Research - Introduction	25
4.2 Technical Results and Discussion	25
4.2.1 Fiber Coating Development	25
4.2.1.1 Coatings on Oxide Fibers	26
4.2.1.2 Coatings on SiC Fibers	27
4.2.2 Analysis of Rare Earth Monazite/Xenotime	28
4.2.3 ZnO Nanowires	29
4.2.4 Oxide-Oxide Composites	29
4.2.5 Camphene Processing of Oxide-Oxide Composites	29
4.2.6 AFIT Collaboration - Creep Behavior of Porous Matrix Oxide-Oxide Composites	29
4.2.7 Dense Matrix Oxide Composites	31
4.3 Summary of Unpublished Work	31
4.3.1 Mechanism of Oxidation Inhibition of SiC by Monazite and Phosphorus	32
4.3.2 Oxide Composites	31
4.3.2.1 Nextel 610, 720/LaPO ₄ /Al ₂ O ₃ composites from ATK COI – Tow Coatings	31
4.3.2.2 Long Term Heat Treatment of Nextel 610/LaPO ₄ /Al ₂ O ₃ Composites	34
4.3.2.3 Nextel 610/LaPO ₄ /Alumina-YAG Composites – Cloth Coating	36
4.3.2.4 Camphene Processing with 3D Fiber Preforms	37
4.3.2.5 The Effect of Precursor Morphology on Densification of Monazite Fiber Coatings for Ceramic Composites	38
4.4 Collaborative Interactions with Outside Agencies	39
4.4.1 NRL	39
4.4.2 AFRL/RXQL (Tyndall AFB)	40
4.4.3 ATK/COI	41
4.5 Publications	41

Table of Contents (Continued)

Section	Page
4.6 Presentations	42
4.6.1 Invited Presentations	42
4.6.2 Presentations	43
4.7 Invention Disclosures/Patents	44
4.8 Book Chapters	44
4.9 Awards	45
4.10 References	45
5.0 TASK ORDER 0004 – ADVANCED COMPOSITE RESEARCH	47
5.1 Introduction	47
5.2 Technical Results and Discussion	48
5.2.1 Evaluation of Oxide Composites in Combustor Rig	48
5.2.2 Effect of Salt Water Exposure on Fiber Strengths	48
5.2.3 Physics of Failure	48
5.2.4 Analytical Evaluation of Hybrid Ceramic Design Concepts	49
5.2.5 Analysis of Ceramics Toughened by Non-Conventional Fiber Reinforcement	49
5.2.6 Thermal History Sensor Based on Glass-Ceramics	50
5.2.7 Tailorable Thermal Expansion Hybrid Structures	50
5.2.8 Deformation of Oxide Systems	51
5.2.9 SiC-Ti ₃ Si ₂ Composites	51
5.2.10 3D Weave Architecture Modeling	52
6.3 Summary of Unpublished Work	52
5.3.1 Modeling of Ceramic Matrix Composites With Complex 3D Fiber Architecture	52
5.3.1.1 Direct Meshing	52
5.3.1.2 Embedded Element (Domain Superposition)	52
5.3.1.3 Embedded Boundary	53
5.3.2 Ceramic Matrix Creep and Shrinkage Modeling	53
5.3.3 Modeling of a Ceramic Combustor Liner	54
5.3.4 YAG Laser Materials	56
5.3.4.1 Single Crystal YAG Fiber Production	56
5.3.4.2 Polycrystalline YAG Fiber/Thin Disk/Slab Production	60
5.3.4.3 Polycrystalline YAG Laser Host Material Modeling	61
5.3.5 Catalyst/Bedplate	64
5.3.5.1 Catalyst Materials Evaluation/Production	64
5.3.5.2 Thruster Bedplate Fabrication	67
5.3.5.3 HAN Thruster Modeling	68
5.3.6 Ternary Eutectic in the B ₄ C-SiC-TiB ₂ System	68
5.3.7 High Temperature Resistive Heating Element	70
5.3.8 Deformation of Oxide Systems	73
5.3.9 Al ₂ O ₃ – GdAlO ₃ Eutectic Characterization	74
5.3.10 AION	74
5.4 Facilities	75
5.4.1 UCI	75

Table of Contents (Continued)

Section	Page
5.4.2 Safety	76
5.4.3 Equipment	77
5.5 Publications	78
5.6 Presentations	78
5.7 Book Chapters	79
5.8 Patents/Invention Disclosures	79
5.9 References	79
6.0 TASK ORDER 0005 – SPACE MIRROR PROGRAM	82
6.1 Introduction	82
6.2 Overview	84
6.2.1 Subtask 1 - Production of Negative CTE Nano-Powders for CTE Tailorability of Inorganic Geo-Polymer Adhesives	84
6.2.1.1 Experimental Procedures and Results	85
6.2.1.2 Scale-Ups for Powder Production	90
6.2.1.3 Subtask 1 Summary	90
6.2.2 Subtask 2 – Modify the CTE Tailored Adhesives to Achieve the Objective of Zero Shrinkage Upon Curing	91
6.2.2.1 Tailoring Thermal Expansion of Geopolymer with Negative CTE Oxide Powders	91
6.2.2.2 Experimental Procedure and Results	92
6.2.2.3 CTE Tailored Cr ₂ O ₃ -ZrW ₂ O ₈ Composite	94
6.2.2.4 CTE Characterization of Organic Resin (EPON 828) Composites with Silane-coated ZrW ₂ O ₈ Powder	95
6.2.2.5 ZWO (ZrW ₂ O ₃) Coating on Glass Balloons	104
6.2.3 Geopolymers with a Zero Curing Shrinkage	106
6.2.3.1 Geopolymers	106
6.2.3.2 In-house research for Geopolymers	106
6.2.3.3 Exploration of Commercial Geopolymers	114
6.2.4 Subtask 3: Hybrid Mirror Replication	118
6.3 Publications	118
6.4 References	118
7.0 TASK ORDER 0006– METALLIC TPS	120
7.1 Beta Gamma Alloy Development	120
7.1.1 Conventional Gamma Alloys	120
7.1.2 Alloy Design Concept and Experiments	120
7.1.3 Results and Discussion	121
7.1.3.1 Determination of Composition Range and Transformation Pathways	121
7.1.3.2 Select Beta Gamma Alloys	123
7.1.3.3 Evaluation of Alloys 7A, 7B, 7C, 7D	124
7.1.4 High Beta Containing Beta Gamma Alloys	127
7.2 Summary	128

Table of Contents (Concluded)

Section	Page
7.3 Publications.....	128
7.4 References.....	129
8.0 TASK ORDER 0007 – UHTC TPS.....	130
8.1 Introduction.....	130
8.2 Oxidation Resistance of UHTC Materials	130
8.3 A Model for the Oxidation of ZrB_2 , HfB_2 and TiB_2	131
8.4 A Model for Transitions in Oxidation Regimes of ZrB_2	131
8.5 Evaluation of SPS Phenomena.....	131
8.6 UHTC Exposure in the Direct-Connect Scramjet Combustor Test Facility	132
8.7 Summary of Unpublished Work	132
8.7.1 Effect of Additives on Oxidation Resistance of UHTC Materials	132
8.7.2 Mechanical Testing of UHTC Materials	133
8.7.3 Fiber-Reinforced UHTC Materials	134
8.7.3.1 Subcontract with SRI International	134
8.7.3.2 In-House UHTC CMC Fabrication Trials.....	136
8.7.4 Stability of Monazite-coated SiC Fiber with SMP10.....	136
8.7.5 Resistance Heater	136
8.7.6 UHTC Samples for MISSE	136
8.8 Publications.....	137
8.9 Presentations	137
List of Acronyms, Abbreviations, and Symbols.....	138

List of Figures

Figure	Page
1. Tensile Test Results for Nextel/LaPO ₄ /Alumina Composites	32
2. SEM Micrograph of 8HS Coated Woven Nextel 720 Fiber	33
3. COI-Fabricated Nextel 720/Alumina Composites (Control and Monazite-Coated) After Exposure at Various Temperatures for 100 hours in Air	34
4. Strength Values for Nextel 610/LaPO ₄ /Alumina Composites as a Function of Heat Treatment Time at 1200 °C	35
5. SEM Micrographs of Nextel 610/LaPO ₄ /Alumina Composite after 5000 h HT	36
6. Microstructures of Freeze-Dried (Camphene Process) 3-D Composites (Nextel 440/Mullite-Alumina)	38
7. Microstructures of Thin (<200 nm, TEM) and Thick (~1500 nm, SEM) Monazite Coatings Derived from Mixed 80% spherical – 20% Rod-Shaped Precursor on Sapphire	39
8. 2D Simulation of Fiber-Constrained Matrix Shrinkage Stress in a Cylindrical CMC Part.....	53
9. (a) ‘Split’ Ceramic Liner on Metallic Support, (b) Comparison of Stressing in Split and Continuous Liners	54
10. Axisymmetric Ceramic Liner on Metallic Support	54
11. Axisymmetric Temperature and Stress Distributions in Both Inner and Outer Liners.....	55
12. Examples of Different End Geometries	55
13. Axisymmetric Temperature and Stress Distributions in Both Full and Sub-scale Inner Liners	56
14. Micrographs of Single Crystal YAG Fiber.....	60
15. Charts Showing Locus of Maximum Power Output from Fiber Lasers, along with Factors that Limit the Maximum Power in Fiber Lasers	62
16. Contributions of Various Factors that Influence the Maximum Power in a Fiber Laser.....	63
17. Vapor Pressures of Monoxides of Y, Al and Nd and the Calculated Evaporation Rates of the Elements in a Vacuum of 10 ⁻⁶ atm	63
18. Experimental Results after an Anneal for 100 h at 1800 °C of a Nd-doped YAG	64
19. X-ray Diffraction of IrCl ₃ Coated Single Crystal YAG-Reduced in H ₂ -5.5g/L 6 Coats	65
20. IrCl ₃ Coating on YAG, 6 coats, 54.6 g/L Ir Solution	66
21. IrCl ₃ Coating on YAG, 2-6 coats, 5.46g/L Ir Solution	66
22. HAN Thruster Powder Containment UHTC Bedplate	68
23. Transient Thermal Analysis of the Two Baseplate Designs.....	68
24. Ternary Phase Diagram of B ₄ C-SiC-TiB ₂ System.....	69
25. HfB ₂ – 20% SiC Piece Exposed in the RBSV Test Rig	72
26. Model Predictions of Sample Temperatures Compared with Data Obtained During a Run of the Strip Heater using 20SiC-HfB ₂ Sample	73
27. Hot-Pressed MgO Doped AlON	75
28. Refluxed Particle Morphologies after Hydrothermal Processing for 7 hours at Different Temperatures	86
29. Particle Morphologies without Refluxing after Hydrothermal Processing at 175 °C for Different Time periods	86
30. Acicular Crystalline Cubic ZrW ₂ O ₈ After Calcination at 600 °C.....	87

List of Figures (Continued)

Figure	Page
31. Crystalline Cubic ZrW_2O_8 After Calcination Followed by Ball Milling the Crystalline Hydrates.....	88
32. X-ray Powder Diffraction Patterns	88
33. X-ray Diffraction Patterns of Cubic Zirconium Tungstate	89
34. SEM micrographs of Zirconium Tungstate Powder	89
35. Molecular Diagram of Aluminosilicate Geopolymer	91
36. Thermal Expansion Behavior of Geopolymer-Based Materials	93
37. XRD Results of (1) Geo-Composite, (2) Pure Geopolymer, and (3) Meta-Kaolin	94
38. Thermal Expansion Properties of the Cr_2O_3 - ZrW_2O_8 Composite.....	95
39. FT-IR Results of the As-silane Coated ZrW_2O_8	96
40. Dark Field Images of Silane-Modified ZrW_2O_8 Powders	97
41. CTE-Tailored EPON 828 Resin Composites for CTE and Thermal Fatigue Characterization	98
42. CTE Variations of Three Thermally Fatigued Specimens Versus the Number of CTE Measurements	99
43. CTE Variations of the EPON 828 Resin Composites with ZWO Filler.....	99
44. Variation of the Average CTE Measurements em.....	103-104
45. SEM Micrographs Showing (a) Control and (b) As-Coated Glass Balloons	105
46. The as-coated balloons: (a) SEI mode and (b) BSI mode.....	106
47. 3-D Structure of a Geopolymer.....	107
48. Thermal Shock Experiment Matrix	112
49. Various Geopolymers and Geopolymer Composites Developed in AFRL	113
50. X-ray Diffraction Analysis of Davy 20 Commercial Geopolymer Before and After Curing Process	114
51. CTE Measurements of Commercial Geopolymer (Davy 20) by TMA	114
52. Surface of the As-Released Davy 20 Commercial Geopolymer with (1) Curved Surface and (2) Flat Surface	116
53. Weight Change of Davy 20 on Heating and Cooling	117
54. (a) Isothermal Section (900 °C) Around the Three-Phase ($\gamma+\alpha_2+\beta$) Field of a Ti-Al- M_{eq} ($M_{eq} = \text{Nb}_{eq}$ of All Alloying Elements) Phase Diagram Showing the Areas of Conventional Gamma Alloys (G) and Three Types of Beta Gamma Alloys (A, B, C) (b) Schematic of a Predicted Isopleth, Ti-44Al-x M_{eq} , that Cuts Through Beta Gamma Alloy Regions along PQ and Shows Their Three Estimated Transformation Pathways	122
55. BEI of Cast Microstructures of (a) a Conventional Gamma Alloy K5 and (b) a Typical Group B Beta Gamma Alloy.....	123
56. Equilibrium Distributions of Constituent Phases Against Temperature Shown for Alloy Ingot Material (a) 7A, (b) 7B, (c) 7C and (d) 7D the beta-phase distribution contains a local maximum peak centered around ~1200 °C.....	125
57. Strength and Strain-to-Failure Variation against Temperature in Alloy 7A (triplex), 7B (triplex) and 7D (NFL or Nearly Fully Lamellar) Materials.....	126

List of Figures (Concluded)

Figure	Page
58. (a) Tensile YS and FS Values Plotted Against the Maximum (or Starting) Heat Treatment Temperature for both 7A and 7B Specimens and (b) Yield Strength and Fracture Strain in Alloy 7A Extrusion against Gamma Volume Fraction in Heat-Treated Conditions	127
59. (a) BEI of Alloy 8G ISM Ingot Microstructure After HIP (1150 °C under 173 MPa for 3 h) and (b) Phase Distribution as a Function of Temperature	128
60. Weight Gain per Surface Area for UHTCs (a) HfB ₂ -SiC and (b) ZrB ₂ -SiC with Various additives.....	133
61. SRI-produced SiC/UHTC Minicomposites	135
62. Higher Magnification SEM Image of UF43 Sample (Figure 61b)	135

List of Tables

Table	Page
1. Tensile Strength of Coated Nextel 720 Fiber	33
2. Results for SPS Processing of NRL-Supplied SiC Powder	40
3. CTE Measurements of As-Cured Specimens	98
4. CTE Measurements After Thermal Cycling	101
5. Averaged CTE with the Degree of Variance	101
6. Averaged CTE Values and Variances of Nine Samples	102
7. Trigger Compositions	108
8. Sample Compositions with Reduced Water Triggers	109
9. Trigger Compositions	110
10. Chemical Composition of Fly Ash and Slag.....	111
11. CTE of Davy 20 Commercial Geopolymer	115
12. Beta Forming Chemical Effectiveness (CE) and Their Normalized Values to Nb, Nb _{eq} , in Ti Alloys and Beta Gamma Alloys	121
13. Desired Phase Distributions in Beta Gamma Alloys at T<1000°C	122
14. Aim and Analyzed Compositions of Beta Gamma Alloys	124

Forward

This report was prepared by the Materials and Processes Division of UES, Inc., Dayton, Ohio under Air Force Contract No. FA8650-04-D-5233. Mr. John H. Barnes of the Metals, Ceramics and Non-Destructive Evaluation Division of the Air Force Research Laboratory was the Government Project Engineer. The research reported herein covers the period 30 November 2004 to 30 April 2010.

2.0 Executive Summary

The development and sustainment of Air Force systems depends on both the optimal performance of traditional materials and the continued exploration of materials technologies. Major requirements driving the research into these new technologies include: 1) reducing the weight of engineering components of aircraft, 2) increasing the operating temperatures of engines, 3) providing advanced materials for thermal protection systems, and 4) producing geopolymer-based material for space mirror applications. Success in meeting these requirements will lead to improved performance efficiency, fuel cost savings, enabling technologies for ultra high temperature applications, and the production of lightweight mirrors. Materials systems based on intermetallics, advanced metallic composites and ceramics show great promise in fulfilling these requirements.

Over the contract period, UES carried out research on three primary classes of materials: advanced metallics, advanced metallic composites and ceramics. In the latter case, the research was focused initially on fiber-reinforced materials, but the scope of the work was expanded to include monolithic materials, including UHTCs, geopolymers and polycrystalline YAG for laser applications. The process-microstructure-property relationships were extensively and critically assessed for these material classes.

This final report details progress made on various topics related to advanced metallic, advanced metallic composites and ceramic materials. For each topic area, the report summarizes the major findings, provides a description of current work not previously reported, and a list of publications/presentations/book chapters and invention disclosures/patents.

2.0 TASK ORDER 0001 – ADVANCED METALS RESEARCH

2.1 CP-FEM Based Materials Modeling

2.1.1 Unit-Cell Based Plasticity Modeling of Ni-Base Single Crystals

The [001] tensile flow of a single-crystal superalloy (CMSX-4) having a high volume fraction of regularly-arrayed cuboidal γ' precipitates was simulated using a non-local gradient-dependent plasticity model, proposed by Acharya and Beaudoin, for the constitutive description of the γ -phase matrix. The γ' precipitate was assumed to be elastic throughout the deformation, and unit-cell meshes were adopted for representation of the γ/γ' microstructure. Numerical studies focused on clarification of the effects of the γ/γ' geometry, the deformation constraint induced by such a geometry, the applied boundary conditions (BC) and the flow properties of the γ and γ' phases on the macroscopic flow behavior. The simulated flow curves showed flow softening in the early stage of straining. The flow softening was accompanied by the organized catastrophic plastic flow of the γ -phase matrix, which resulted from the breakdown of the geometric (or kinematic) constraints imposed by the γ/γ' microstructure. The flow-softening behavior was influenced by the thickness of γ -phase channels (a volume fraction of the γ' precipitate), the flow property of the γ -phase matrix and the geometry of the γ' -precipitate edge. In particular, a change of the radius of the γ' -precipitate edge resulted in a dramatic variation of the flow curve. The present unit cell simulations exhibited good predictions for the γ' -precipitate size dependence of the flow stress at the moderate strains. However, an underestimation of the flow stresses in the elastic-plastic transition regime is still unsolved for the present unit cell simulations, and indicates that more careful constitutive treatments are required for the γ and γ' phases in the elastic-plastic transition regime [1].

The unique microstructure of two-phase single-crystal superalloys, particularly for those having a high volume fraction of γ' precipitates such as CMSX-4 and SRR99, can be described as a roughly periodic array of large (0.5 - 1 μm), cuboidal γ' precipitates surrounded by narrow channels ($< 0.1 \mu\text{m}$) of the γ matrix. Upon loading at high temperatures, one may expect that the soft γ -phase matrix will deform much more readily than the γ' -phase precipitates, but the γ' phase induces geometrical constraints that result in complex stress states that affect the deformation of the matrix and hence the flow properties. We investigated how the geometries of the γ and γ' phases influence the tensile and compressive flow responses of a [001]-oriented CMSX-4 single-crystal superalloy by modeling the elasto-viscoplastic behaviors of the γ and γ' phases using a unit cell for the representation of the γ/γ' microstructure. The T-C asymmetry in the elastic-plastic transition regime was opposite to the one in the plastic regime, and the magnitude of the T-C asymmetry in the elastic-plastic transition regime depended upon the elastic properties of the γ matrix. The numerical results suggest that the deformation constraint effect induced by the γ/γ' geometry gives rise to different flow responses between tension and compression both in the elastic-plastic transition regime and in the plastic regime, hence resulting in asymmetric tension-compression flow stresses [2, 3].

2.1.2 Modeling Plasticity of Ni₃Al-Based Intermetallic Single Crystals

Our first version of a constitutive model was developed in order to capture the unique thermo-mechanical flow behavior of L1₂-structured Ni₃(Al,X) alloys. This model utilized a framework for flow-stress partitioning, which was previously proposed by Ezz and Hirsch, and also incorporated a model for exhaustion hardening proposed by Caillard. The simulation results well represent the major aspects of the thermo-mechanical flow behavior of Ni₃(Al,X) alloys, such as a flow-stress anomaly, its strain dependence and a work-hardening-rate anomaly. However, the first version of the model still has selected limitations [4].

In subsequent work, the first version of the model was significantly modified. A comprehensive mechanism-based crystallographic constitutive model has been developed for L1₂-structured Ni₃Al-based intermetallic single crystals. The new model represents the unusual thermo-mechanical behaviors of Ni₃Al, such as the anomalous temperature dependence of both the flow stress and strain-hardening rate (SHR), the strain dependence of these anomalous behaviors, and an orientation-dependent tension-compression asymmetry. The model framework was based on two major contributions to plastic flow, namely the repeated cross-slip exhaustion and athermal defeat of screw-character dislocations, and the motion of macro-kinks (MKs). The contribution of irreversible obstacle storage was incorporated into the constitutive formulations as a resistance against the glide of MKs. The model was implemented in a finite element method numerical framework, and the simulation results showed qualitative agreement with experimental observations [5].

The two-step (T₁ & T₂) deformation behavior of Ni₃Al-based single crystals was modeled under the framework of a new constitutive model proposed in [5]. A new set of formulations and criteria that identify thermally reversible and irreversible components of the constitutive variables and define the relative significance of those components was developed and implemented within the new constitutive framework. The simulation results well captured the general qualitative trends of the flow behavior upon re-straining at T₂ after pre-straining at T₁ for both T₁ > T₂ and T₁ < T₂. Modeling results suggested that the dislocation substructures generated at T₁ need to be treated as partially or fully transferable to plastic flow at T₂, at least through the early stage of re-straining, in order to capture all major pre-strain effects. In particular, the large strengthening effect at T₂ for even a few percent of pre-strain at T₁ was obtainable only by controlling the availability of mobile dislocations and sources at T₂ [6].

2.1.3 Modeling of Micro-Compression Tests of Anisotropic Single Crystals

Using a crystallographic elastic-viscoplastic finite element method the present study investigated two primary factors influencing the measured properties from micro-compression tests for anisotropic single crystals: the effect of the sample geometry on the measured elastic response, and the effect of misalignment between the compression platen and the sample on the measured elastic and plastic response [7].

2.2 Modeling and Prediction of Materials Properties

2.2.1 Microtests on Nickel Pillars

Spatial scales in crystal plasticity are understood to influence flow stresses and work-hardening rates. A direct assessment of the crystal-size dependence of the critical resolved shear stress has been made for single-slip oriented crystals of pure Ni having sample diameters that range from 40 to 1.0 μm . The sample dimensions directly limit the length scales available for plasticity, but without significant external or kinematical constraint. The results show strength increases of up to 15 times over pure Ni and size-affected hardening rates. Stresses are lower, but strengthening persists to larger sizes than for the prior work on face-centered cubic metal whiskers. The results emphasize that at the micron-size scale and below both external geometry and internal structure affect the micromechanisms of deformation and strength [8].

2.2.2 Modeling Size Effect on Yield Strength (YS) of Face Centered Cubic (FCC) Metals

Recent works show that the YS of metals increases steeply with decreasing sample size. In this work, it is shown that this sample size effect can be rationalized almost completely by considering the stochastic of dislocation source lengths in samples of finite size. The statistical first and second moments of the effective source length are derived as a function of sample size. The sample strength predicted from this effective length compares well with data [9].

2.2.3 Review of Size Effect and Implications

An important frontier in both metallurgy and mechanics is the development of a modelling framework that accurately represents length-scale effects and dislocation structure. Emerging mechanics formulations incorporate a length scale tied to distortion gradients aimed at modelling the effects from geometrically necessary dislocations (GND). However, recent experimental studies show important intrinsic size effects exist separately from an evolving GND structure at a mesoscopic scale. The present studies probed for intrinsic size effects at this scale using experimental methods that more closely approach the size scales accessible via discrete dislocation simulation (DDS) in 3D. Uniaxial compression tests of single crystals of pure Ni, Ni_3Al alloys, Ni superalloys and fine grained polycrystalline Ni showed material-unique size dependent responses. Notable among these are a range of strengths and clear intermittency of flow that reveals self-organization. Mechanistically self consistent simulation of such results, by either discrete dislocation or continuum methods, stands as an unsolved challenge for emerging materials modeling approaches [10].

2.3 Modeling of Dislocation Behaviors

2.3.1 DDS of Precipitation Hardening in Inverse Superalloys

The low temperature yield stress of a γ' (Ni_3Al) matrix - γ (Ni) precipitate ‘inverse’ superalloy, containing 40% Ni precipitates (γ'), is calculated by discrete-dislocation simulations. Two different precipitate sizes and two anti-phase boundary energies are considered. The results of these simulations are compared with corresponding results from γ - γ' superalloys. In general, the

results show that precipitation hardening in inverse superalloys is weaker than for regular superalloys. Similar to studies of superalloys, many of these results can be rationalized from the results of simulations on simple homogenized precipitate structures. The Hirsch, Kelly and Ardell precipitation strengthening model, developed for low stacking-fault energy spherical precipitates in a high stacking fault-energy matrix, adapted for inverse superalloys, shows qualitative agreement with the simulation results for spherical γ' precipitates [11].

2.3.2 Criticality and Stochastic Flow in Microcrystal Plasticity

The microcrystal plasticity studies presented here have focused on the measurement, analysis and simulation of the physical phenomena occurring in deforming single crystals having dimensions at the micron size-scale. Single-slip oriented Ni microcrystals having diameters ranging from 1.0-40 μm were tested at several strain rates, through Stage I and into Stage II glide. The stress-strain response of this material varied with specimen diameter, loading rate and degree of strain, but always exhibited an intermittent nature. Subsequent analysis of that intermittency clearly demonstrated that the deformation response of the Ni microcrystals exhibited the characteristic attributes of self-organized criticality (SOC). The statistics of SOC change as the crystal moves from Stage I to Stage II and III [12].

2.3.3 Estimating the Strength of Single-Ended Dislocation Sources in Micrometer-Sized Single Crystals

A recent study indicated that the behavior of single-ended dislocation sources contributes to the flow strength of micrometer-scale crystals. In this study 3D discrete dislocation dynamics simulations are used to calculate the effects of anisotropy of dislocation line tension (increasing Poisson's ratio) on the strength of single-ended dislocation sources in micrometer-sized volumes with free surfaces, and to compare them with the strength of double-ended sources of equal length. This is done by directly modeling their plastic response within a 1 micron³ volume composed of a single crystal, face centered cubic (FCC) metal. In general, double-ended sources are stronger than single-ended sources of an equal length and exhibit no significant effects from truncating the long-range elastic fields at this scale. The double-ended source strength increases with Poisson ratio (ν), exhibiting an increase of about 50% at $\nu = 0.38$ (value for Ni) as compared to the value at $\nu = 0$. Independent of dislocation line direction, for ν greater than 0.20, the strengths of single-ended sources depend upon the sense of the stress applied. The value for α , in the expression for strength, $\tau(L) = \alpha(L)\mu b/L$ is shown to vary from 0.4 to 0.84 depending upon the character of the dislocation and the direction of operation of the source at $\nu = 0.38$ and $L = 933b$. By varying the lengths of the sources from 933 to 233***b***, it was shown that the scaling of the strength of single-ended and double-ended sources with their length both follow a $\ln(L/b)/(L/b)$ dependence. Surface image stresses are shown to have little effect on the critical stress of single-ended sources at a length of $\sim 250b$ or greater. This suggests that for 3D discrete dislocation dynamics simulations of the plastic deformation of micrometer sized crystals in the size range, 0.5 – 20 μm , image stresses making the surface traction-free can be neglected. The relationship between these findings and a recent statistical model for the hardening of small volumes is also discussed [13].

2.4 Modeling of Microstructures and Phase Evolution

2.4.1 A Phase-Field Model for Heat Treatment Applications in Ni-base Alloys

This work details our attempts towards developing a phase-field model into an engineering tool that can be used to simulate microstructural evolution under a prescribed heat treatment procedure. Most previous work is limited to isothermal conditions. We have performed isothermal simulations for a few Ni-Al alloys at various temperatures. Growth kinetics and particle number density evolution with time are documented and compared with experimental observations. Temperature dependence of phase-field input parameters are described for modeling realistic heat treatment. In the selection of gradient coefficient constants, we found it difficult to fit the interfacial energy and anti-phase domain boundary energy simultaneously without causing microstructure instability in the simulations. In comparison with experimentally observed kinetics, we found that the gamma/gamma prime interfacial energy has to be around 70 mJ/m² at 550 °C to achieve reasonable agreement in mean particle size evolution although a wide spread of this energy was reported by fitting to experimentally measured coarsening kinetics. We proposed a fast calibration procedure of the phase field model by two isothermal experiments and this concept will be further tested in more complex alloys [14].

2.4.2 Phase-Field Modeling of Microstructural Evolution During Solidification in Al-Sc Alloys

The addition of relatively small quantities of Sc to Al alloys is known to dramatically reduce grain size in Al castings. Two possible mechanisms for this grain size refinement have been proposed: the heterogeneous nucleation of the FCC-Al solid solution phase on Al₃Sc particles that form first during solidification or a strong chemically-dependent anisotropy of solid-liquid interfacial energy on the nucleation and growth of the FCC phase. Here the relative roles of heterogeneous nucleation and anisotropic solid-liquid interfacial energy on dendritic growth are studied using a 2-dimensional phase-field model. The role of crystallographic orientation of the nucleating phase is incorporated in the model and preliminary results on the solidification behavior of a binary Al-0.375at%Sc alloy are discussed. Simulations show that the nature of distribution of the Al₃Sc particles has a very strong effect on the evolving microstructure while significant variation (10%) in solid-liquid anisotropic interfacial free energy does not appear to have any noticeable effect on the solidification microstructure [15].

2.5 Science for Sustainment

The various metallurgical sources that influence electrical conductivity were identified and analyzed using literature data. Systematic experiments were conducted to understand the effects of manufacturing heat treatment on the metallurgical variables and the attendant effects on conductivity measured using eddy current technique. The data was used to generate a calibrated model that captures the effects of metallurgical changes on electrical conductivity [16].

2.6 Publications

1. Y.S. Choi, T.A. Parthasarathy, D.M. Dimiduk and M.D. Uchic, "Numerical study of the flow responses and the geometric constraint effects in Ni-base two-phase single crystals using strain gradient plasticity," *Mater. Sci. and Eng.*, **A397** 69-83 (2005).
2. Y.S. Choi, T.A. Parthasarathy, D.M. Dimiduk and M.D. Uchic, "Tension-Compression Asymmetry in Plasticity Modeling of a Single Crystal Superalloy Using a "Unit Cell" Approach," *Mater. Sci. Forum*, **475-479** 3295-3298 (2005).
3. Y.S. Choi, T.A. Parthasarathy, D.M. Dimiduk and M.D. Uchic, "Microstructural Effects in Modeling the Flow Behavior of Single-Crystal Superalloys," *Metall. and Mater. Trans.*, **A37** 545-550 (2006).
4. Y.S. Choi, D.M. Dimiduk, M.D. Uchic and T.A. Parthasarathy, "A crystallographic constitutive model for Ni₃Al(L1₂) intermetallics," *Mater. Sci. and Eng.*, **A400-401** 256-259 (2005).
5. Y.S. Choi, D.M. Dimiduk, M.D. Uchic and T.A. Parthasarathy, "Modeling Plasticity of Ni₃Al-Based L1₂ Intermetallic Single Crystals. I. Anomalous Temperature Dependence of the Flow Behavior," *Phil. Mag.*, **87** 1939-1965 (2007).
6. Y.S. Choi, D.M. Dimiduk, M.D. Uchic and T.A. Parthasarathy, "Modeling plasticity of Ni₃Al-based L1₂ intermetallic single crystals. II. Two-step (T₁ & T₂) deformation behaviour," *Phil. Mag.*, **87** 4759-4775 (2007).
7. Y.S. Choi, M.D. Uchic, T.A. Parthasarathy and D.M. Dimiduk, "Numerical study on microcompression tests of anisotropic single crystals," *Scripta Mater.*, **57** 849-852 (2007).
8. D. M. Dimiduk, M. D. Uchic, and T. A. Parthasarathy, "Size-Affected Single-Slip Behavior of Pure Nickel Microcrystals," *Acta Mater.*, 4065-4077 (2005).
9. T. A. Parthasarathy, S. I. Rao, D. M. Dimiduk, M. D. Uchic, and D. R. Trinkle, "Contribution to size effect of yield strength from the stochastics of dislocation source lengths in finite samples," *Scripta Mater.*, **56** 313-316 (2007).
10. D. M. Dimiduk, M. D. Uchic, S. I. Rao, C. Woodward, and T. A. Parthasarathy, "Overview of experiments on microcrystal plasticity in FCC-derivative materials: selected challenges for modeling and simulation of plasticity," *Modell. Simul. Mater. Sci. Eng.*, **15** 135-147 (2007).
11. S. Rao, T.A. Parthasarathy, D. Dimiduk and P. Hazzledine, "Discrete dislocation simulations of precipitation hardening in inverse superalloys," *Phil. Mag.*, **86** 215-225 (2006).
12. D.M. Dimiduk, M.D. Uchic, S.I. Rao, C. Woodward and T.A. Parthasarathy, "Experiments and Three-Dimensional Dislocation Simulations of Microplasticity in Selected Materials," *IUTAM Conference Proceedings*, 2006.
13. S.Rao, D.M. Dimiduk, M.Tang, T.A. Parthasarathy, M.D.Uchic and C. Woodward, "Estimating the strength of single-ended sources in micrometer-sized single crystals," *Phil. Mag.*, **87** 4777-4794 (2007).
14. Y.H. Wen, B. Wang, J.P. Simmons, and Y. Wang, "A Phase-field model for heat treatment applications in Ni-base alloys," *Acta Mater.*, **54** 2087 (2006).
15. Y.H. Wen, E. S. K. Menon, and C. Woodward, "Phase-Field Modeling of Microstructural Evolution during Solidification in Al-Sc Alloys," pp. 223-231 in Proc. Materials Science and Technology 2006: Materials and Systems -Volume 2. Edited by D. Evans, A. Eckel, T. Parthasarathy, and R. E. Dutton, (2006).

16. T. A. Parthasarathy, S. Boone, S. I. Rao, P. Wang, P. Nagy, and M. Blodgett, "Investigation of Microstructural Effects on Electrical Resistivity and their Implications for Eddy Current Methods in Measuring Residual Stresses in IN718," *ENDE Proceedings*, **in press** (2009).

2.7 Presentations

1. Y.S. Choi, T.A. Parthasarathy, D.M. Dimiduk and M.D. Uchic, "Tension-Compression Asymmetry in Plasticity Modeling of a Single Crystal Superalloy Using a "Unit Cell" Approach," presented at the 5th Pacific Rim International Conference on Advanced Materials and Processing (PRICM-5), Nov. 2-5, 2004, Beijing, China.
2. Y.S. Choi, D.M. Dimiduk, M.D. Uchic and T.A. Parthasarathy, "Modeling the Anomalous Flow Behaviors of Ni₃(Al,X) Single Crystals," presented at the 7th World Congress on Computational Mechanics (WCCM-VII), July 16-22, 2006, Los Angeles, CA.
3. Y.S. Choi, D.M. Dimiduk, M.D. Uchic and T.A. Parthasarathy, "Mechanism-Based Constitutive Modeling for Ni₃Al-Based L1₂ Intermetallic Single Crystals: Anomalous Temperature Dependence of the Flow Behavior," presented at the TMS Annual Meeting, Feb. 25-Mar. 1, 2007, Orlando, FL.
4. Y.S. Choi, D.M. Dimiduk, M.D. Uchic and T.A. Parthasarathy, "Microstructure-Sensitive, Mechanism-Based Plasticity Modeling of Materials," presented at the TMS Annual Meeting, Mar. 9-13, 2008, New Orleans, LA.

2.8 References

1. Y.S. Choi, T.A. Parthasarathy, D.M. Dimiduk and M.D. Uchic, "Numerical study of the flow responses and the geometric constraint effects in Ni-base two-phase single crystals using strain gradient plasticity," *Mater. Sci. and Eng.*, **A397** 69-83 (2005).
2. Y.S. Choi, T.A. Parthasarathy, D.M. Dimiduk and M.D. Uchic, "Tension-Compression Asymmetry in Plasticity Modeling of a Single Crystal Superalloy Using a "Unit Cell" Approach," *Mater. Sci. Forum*, **475-479** 3295-3298 (2005).
3. Y.S. Choi, T.A. Parthasarathy, D.M. Dimiduk and M.D. Uchic, "Microstructural Effects in Modeling the Flow Behavior of Single-Crystal Superalloys," *Metall. and Mater. Trans.*, **A37** 545-550 (2006).
4. Y.S. Choi, D.M. Dimiduk, M.D. Uchic and T.A. Parthasarathy, "A crystallographic constitutive model for Ni₃Al(L12) intermetallics," *Mater. Sci. and Eng.*, **A400-401** 256-259 (2005).
5. Y.S. Choi, D.M. Dimiduk, M.D. Uchic and T.A. Parthasarathy, "Modeling Plasticity of Ni₃Al-Based L1₂ Intermetallic Single Crystals. I. Anomalous Temperature Dependence of the Flow Behavior," *Phil. Mag.*, **87** 1939-1965 (2007).
6. Y.S. Choi, D.M. Dimiduk, M.D. Uchic and T.A. Parthasarathy, "Modeling plasticity of Ni₃Al-based L1₂ intermetallic single crystals. II. Two-step (T₁ & T₂) deformation behaviour," *Phil. Mag.*, **87** 4759-4775 (2007).
7. Y.S. Choi, M.D. Uchic, T.A. Parthasarathy and D.M. Dimiduk, "Numerical study on microcompression tests of anisotropic single crystals," *Scripta Mater.*, **57** 849-852 (2007).

8. D. M. Dimiduk, M. D. Uchic, and T. A. Parthasarathy, "Size-Affected Single-Slip Behavior of Pure Nickel Microcrystals," *Acta Mater.*, 4065-4077 (2005).
9. T. A. Parthasarathy, S. I. Rao, D. M. Dimiduk, M. D. Uchic, and D. R. Trinkle, "Contribution to size effect of yield strength from the stochastics of dislocation source lengths in finite samples," *Scripta Mater.*, **56** 313-316 (2007).
10. D. M. Dimiduk, M. D. Uchic, S. I. Rao, C. Woodward, and T. A. Parthasarathy, "Overview of experiments on microcrystal plasticity in FCC-derivative materials: selected challenges for modeling and simulation of plasticity," *Modell. Simul. Mater. Sci. Eng.*, **15** 135-147 (2007).
11. S. Rao, T.A. Parthasarathy, D. Dimiduk and P. Hazzledine, "Discrete dislocation simulations of precipitation hardening in inverse superalloys," *Phil. Mag*, **86** 215-225 (2006).
12. D.M. Dimiduk, M.D. Uchic, S.I. Rao, C. Woodward and T.A. Parthasarathy, "Experiments and Three-Dimensional Dislocation Simulations of Microplasticity in Selected Materials," *IUTAM Conference Proceedings*, 2006.
13. S. Rao, D.M. Dimiduk, M. Tang, T.A. Parthasarathy, M.D. Uchic and C. Woodward, "Estimating the strength of single-ended sources in micrometer-sized single crystals," *Phil. Mag.*, **87** 4777-4794 (2007).
14. Y.H. Wen, B. Wang, J.P. Simmons, and Y. Wang, "A Phase-field model for heat treatment applications in Ni-base alloys," *Acta Mater.*, **54** 2087 (2006).
15. Y.H. Wen, E. S. K. Menon, and C. Woodward, "Phase-Field Modeling of Microstructural Evolution during Solidification in Al-Sc Alloys," pp. 223-231 in Proc. Materials Science and Technology 2006: Materials and Systems -Volume 2. Edited by D. Evans, A. Eckel, T. Parthasarathy, and R. E. Dutton, (2006).
16. T. A. Parthasarathy, S. Boone, S. I. Rao, P. Wang, P. Nagy, and M. Blodgett, "Investigation of Microstructural Effects on Electrical Resistivity and their Implications for Eddy Current Methods in Measuring Residual Stresses in IN718," *ENDE Proceedings*, **in press** (2009).

3.0 TASK ORDER 0002 – RESEARCH FOR METALLIC MATERIALS WITH HIGH STRUCTURAL EFFICIENCY

3.1 Amorphous and Nanocrystalline Metals

3.1.1 Development and Characterization of a Nanocrystalline Aluminum Alloy From Amorphous Powder

Amorphous aluminum alloy powders produced by gas atomization were consolidated using equal channel angular pressing (ECAP) and direct extrusion. The powder particle size was below 30 μm and the as-received powder was $\sim 70\text{--}80\%$ amorphous. ECAP compaction of loose powder was conducted in the temperature range of 200–300 $^{\circ}\text{C}$. The microstructure of the compacted material was studied after different levels of ECAP deformation, which allowed analysis of the mechanism of particle interactions, deformation and bonding during different stages of consolidation. Very non-homogeneous deformation of the compacted material was detected. At the temperatures of compaction, amorphous powder particles were much softer than fully crystalline powder particles, and they were severely deformed while the crystalline particles remained nearly spherical. Almost full consolidation occurred in regions predominantly consisting of amorphous and semi-amorphous powder particles at true strains of ~ 2 . However, further excessive deformation led to strain localization and shear crack formation in the consolidated regions. Regions dominated by fully crystalline spherical particles with brittle intermetallic phases showed poor consolidation due to particle rotations and particle fracture; leading to weak particle bonding. The results show that ECAP consolidation is impeded by the presence of fully crystalline particles in the powder. Direct extrusion compaction was conducted at 210, 250, 400, and 450 $^{\circ}\text{C}$. After compaction at 210 $^{\circ}\text{C}$, the material was about 70% amorphous and it had 98–99% of the theoretical density. A fully dense alloy with a nanocrystalline structure (grain size $\sim 700\text{ nm}$) was produced after extrusion at 450 $^{\circ}\text{C}$. Extrusion at 250 and 400 $^{\circ}\text{C}$ led to poor consolidation of the powder due to formation of brittle intermetallic phases with volume fraction of about 40%. The room temperature micro-hardness of the semiamorphous and fully crystalline material consolidated by direct extrusion was about 3.4 and 2.1 GPa, respectively, which can be translated to compression yield strengths of 1030 and 638 MPa, respectively. The consolidated material had some tensile ductility only at test temperatures of 300 $^{\circ}\text{C}$ and higher. The tensile yield strength was $\sim 220\text{ MPa}$ at 300 $^{\circ}\text{C}$ and 100 MPa at 400 $^{\circ}\text{C}$ [1].

3.1.2 Development of Thermodynamic and Topological Criteria for Amorphization and Glass Forming Ability

The effects of composition, atomic radii, atomic size ratios, and elastic constants of the constitutive elements on the glass-forming ability of metallic glasses have been identified using a thermodynamic model. This model is based on the comparison of the Gibbs free energy and entropy between a nonequilibrium crystalline solid solution and the undercooled liquid. According to this model, the glass-forming ability (reduced glass transition temperature, T_g/T_m) of an alloy should increase with (a) an increase in the atom size and/or shear modulus of the solvent; (b) an increase in the bulk modulus of a solute; and (c) a decrease in the melting temperature of the alloy. At constant values for other parameters, the glass-forming ability is

maximum at a certain concentration and relative atomic size of a solute. These topological criteria have been successfully used to produce a number of Ca-based bulk metallic glasses [2, 3, 4].

A thermodynamic analysis of the driving force for the onset of crystallization of different phases from the undercooled liquid in the Ca-Mg-Zn system was conducted. A strong dependence of the driving force on the alloy composition was found and the alloys corresponding to the local minima of the onset driving force were identified. These alloys were found to have good glass forming ability, having a maximum critical thickness at which they remained fully amorphous during copper mold casting of up to 10 mm. Although glass forming ability has a general tendency to increase with a decrease in the onset driving force, it is also enhanced with an increase in the liquid/solid interface energy of a crystalline phase and an increase of the fragility index D , so that undercooled liquids with equivalent onset driving forces can have different glass forming abilities. The combination of low onset driving forces, high solid/liquid interfacial energy, and “strong” liquid behavior (high liquid fragility index D) results in a better glass forming ability of alloys in the CaMg_2 precipitation phase field and with compositions near $\text{Ca}_{60}\text{Mg}_{20}\text{Zn}_{20}$. This provides the first general analytic approach for identifying the best glass forming compositions across broad compositional regimes spanning more than one primary crystalline phase in metallic glasses [5].

Analysis of the relaxation time of the glass forming liquids at near liquidus temperatures was conducted, correlation between the critical cooling rate for glass formation, fragility of the glass forming liquid, and reduced glass transition temperature was identified, and a glass forming ability (GFA) parameter ($F1 = 2[(m/m_{\min})(1/T_{rg}-1)+2]^{-1}$) was proposed. This GFA parameter, which increases with a decrease in the critical cooling rate, is a function of the reduced glass transition temperature T_{rg} and a fragility index m , and it varies from ~ 0 in the case of extremely fragile liquid to $2T_{rg}/(1+T_{rg})$ in the case of extremely strong liquid. An exponential relationship between the critical cooling rate for glass formation and the parameter $F1$ was identified and verified using available experimental data for metallic and nonmetallic glasses [6].

3.1.3 Development of New Bulk Metallic Glasses and Analysis of Their Glass Forming Ability, Thermal Stability and Thermodynamic Properties

Compositions of over one hundred ternary Ca-Mg-Zn and Ca-Mg-Cu and quaternary Ca-Mg-Zn-Cu bulk metallic glasses were identified and produced using specific criteria for glass formation developed by Senkov and Miracle. These bulk glassy alloys were prepared by a copper mold casting method as plates of different thicknesses varying from 0.5 mm to 10 mm. The maximum thickness, at which an alloy remains fully amorphous, glass transition temperature, crystallization temperature, temperature interval of the super-cooled liquid region, solidus and liquidus temperatures, as well as heats of crystallization and melting, were reported for these alloys. Their glass forming ability was correlated to the alloy chemistry, melting temperature, and driving force for crystallization of super-cooled liquid. A structural assessment using the efficient cluster packing model was also applied and showed a good ability to represent these glasses. Compression tests were conducted on quaternary amorphous alloys at room temperature and in the temperature range of super-cooled liquid. The as-cast Ca-Mg-Zn-Cu amorphous alloys were found to be brittle at room temperature and ductile the temperature range

of super-cooled liquid. After preliminary compression straining at a temperature slightly above the glass transition temperature T_g , the alloys showed some ductility at room temperature [7, 8, 9, 10].

A number of low density bulk metallic glasses were identified and produced in Ca-Mg-Al, Ca-Mg-Al-Zn, Ca-Mg-Al-Cu and Ca-Mg-Al-Zn-Cu alloy systems using specific criteria for glass formation developed by Senkov and Miracle. The maximum fully amorphous thickness $t_{\max} = 9$ mm was achieved in a $\text{Ca}_{55}\text{Mg}_{18}\text{Al}_{15}\text{Zn}_{11}\text{Cu}_{11}$ alloy. Two alloys, $\text{Ca}_{60}\text{Mg}_{20}\text{Al}_{10}\text{Zn}_{10}$ and $\text{Ca}_{55}\text{Mg}_{18}\text{Al}_{15}\text{Zn}_{11}\text{Cu}_{11}$ had t_{\max} from 5 to 6 mm, eleven alloys had t_{\max} from 2 to 4 mm, and 5 alloys had t_{\max} of 1.0 to 1.5 mm. An addition of Al usually reduced the glass forming ability, but it improved the glass stability by increasing T_g and T_x . The glassy alloys developed in this work have a wide temperature interval for solidification, which indicates that their compositions are rather far from eutectic points. It is therefore expected that even better glass former can be found in these alloy systems by modifying the compositions in order to reduce the solidification temperature range. The compositions of these alloys provide efficiently packed cluster structures. Application of the efficient cluster packing model suggests that these glasses are formed by efficiently-packed Mg-centered clusters, while Al and Zn are preferred at cluster-octahedral β sites, and Cu is native to cluster-tetrahedral γ sites. A significant amount of interchangeability between Al, Zn and Cu solutes seems to be supported in this family of glasses. Ca-Mg-Al and Ca-Mg-(Al,Zn) are represented as <10, 9> topological ternary glasses, while Ca-Mg-Al-Cu and Ca-Mg-(Al,Zn)-Cu are <10, 9, 8> topological quaternary glasses [10, 11, 12].

Several cerium-based Ce-Al-Cu-Ni amorphous alloys were discovered and produced using specific topological and thermodynamic criteria developed in earlier work by Senkov and Miracle. Differential scanning calorimetry (DSC) and X-ray diffraction techniques were used to investigate the thermal properties, thermal stability and crystallization kinetics of the amorphous samples. The glass transition temperature, crystallization temperature, solidus and liquidus temperatures, as well as the enthalpies of crystallization and melting were reported for these alloys. GFA and glass stability were estimated as the functions of the alloy composition and reduced glass transition temperature [13].

3.1.4 Oxidation and Corrosion Resistance of Ca-Based Bulk Metallic Glasses

The electrochemical behavior of three Ca-based Bulk Metallic Glasses (BMGs) was examined and compared to a crystalline, Mg-based alloy, as well as other amorphous and crystalline materials reported in the literature. Based upon cyclic-anodic polarization studies in a 0.05 M Na_2SO_4 electrolyte and these comparisons, the following conclusions were drawn. (1) The $\text{Ca}_{65}\text{Mg}_{15}\text{Zn}_{20}$ alloy was active at the open-circuit potentials, with the highest mean corrosion penetration rate (CPR) of 5691 $\mu\text{m}/\text{year}$. (2) Both the $\text{Ca}_{50}\text{Mg}_{20}\text{Cu}_{30}$ and $\text{Ca}_{55}\text{Mg}_{18}\text{Zn}_{11}\text{Cu}_{16}$ BMG alloys showed slight passivity at the open-circuit potentials, with lower mean CPRs of 1503 and 311 $\mu\text{m}/\text{year}$, respectively. These CPRs were found to be statistically equivalent to that of the Mg-based, crystalline alloy (ZK60) at the tested levels. (3) In addition, the $\text{Ca}_{65}\text{Mg}_{15}\text{Zn}_{20}$ and $\text{Ca}_{55}\text{Mg}_{18}\text{Zn}_{11}\text{Cu}_{16}$ alloys were found to be susceptible to localized corrosion in the form of pitting. (4) Post-test SEM analyses seemed to indicate that pitting was associated with small particles within the amorphous matrix. (5) Based upon comparisons with studies from the literature, it seems that the $\text{Ca}_{55}\text{Mg}_{18}\text{Zn}_{11}\text{Cu}_{16}$ and $\text{Ca}_{50}\text{Mg}_{20}\text{Cu}_{30}$ alloys are comparable to some

Fe-based BMGs and Mg-based crystalline alloys, while all three of these Ca-based BMGs are not as corrosion resistant as the Zr-based BMG alloys [14].

The room-temperature oxidation behaviors of three Ca-based bulk amorphous alloys, $\text{Ca}_{65}\text{Mg}_{15}\text{Zn}_{20}$, $\text{Ca}_{50}\text{Mg}_{20}\text{Cu}_{30}$, and $\text{Ca}_{55}\text{Mg}_{18}\text{Zn}_{11}\text{Cu}_{16}$, were examined under normal flowing laboratory air and compared with the oxidation behaviors of these alloys in the crystalline form under identical conditions. The degree of oxidation for alloys in the amorphous and crystalline conditions was investigated by periodically measuring the mass change over the oxidation time. From the results of the oxidation mass change, and oxide thickness measurements obtained from scanning-electron-microscopy (SEM) studies, it was determined that the $\text{Ca}_{55}\text{Mg}_{18}\text{Zn}_{11}\text{Cu}_{16}$ BMG possessed the most favorable oxidation resistance, followed closely by the $\text{Ca}_{50}\text{Mg}_{20}\text{Cu}_{30}$ BMG, with the $\text{Ca}_{65}\text{Mg}_{15}\text{Zn}_{20}$ BMG having the least favorable oxidation resistance. The trend in glass-forming abilities of the three compositions follows the same trend as the oxidation resistance in the three alloys. In all cases, the oxidation resistance of the amorphous alloys was superior to the oxidation resistance of the same alloys in the crystalline state, due to formation of different, more protective oxides [15].

The corrosion properties of ternary, ($\text{Ca}_{65}\text{Mg}_{15}\text{Zn}_{20}$ and $\text{Ca}_{50}\text{Mg}_{20}\text{Cu}_{30}$), quaternary, ($\text{Ca}_{55}\text{Mg}_{18}\text{Zn}_{11}\text{Cu}_{16}$), and quinary, ($\text{Ca}_{55}\text{Mg}_{15}\text{Al}_{10}\text{Zn}_{15}\text{Cu}_5$), amorphous alloys were evaluated using static aqueous submersion at room temperature. Ca-Mg-Zn and Ca-Mg-Cu alloy systems experienced destructive corrosion reactions by decomposing in multiple oxide and hydro-oxide phases. The Ca-Mg-Zn-Cu and Ca-Mg-Zn-Cu-Al based amorphous alloys demonstrated positive corrosion properties, forming corrosion films up to 23 μm thick in the quaternary alloy and 11 μm thick in the quinary composition. Corrosion products were evaluated using X-ray diffraction (XRD), X-ray Fluorescence (XRF), SEM, and Energy Dispersive Spectroscopy (EDS) [16].

3.1.5. Elastic and Thermal Properties of Ca-Based Bulk Metallic Glasses

Low-temperature specific heat and elastic moduli measurements were conducted for Ca-Mg-Zn-Cu bulk metallic glasses. The deviations from the Debye behavior observed in both specific heat capacity and elastic moduli were modeled with a simple Einstein oscillator with characteristic temperature $\Theta_E = 80$ K and the density of states increased with an increase in the Ca and Zn contents. The presence of this local mode can also account for the deviation from normal ‘Varshni behavior’ observed in the temperature dependence of the elastic moduli [17].

The elastic properties and internal friction of Ca-based BMGs, $\text{Ca}_{50}\text{Mg}_{20}\text{Cu}_{30}$, $\text{Ca}_{55}\text{Mg}_{18}\text{Zn}_{11}\text{Cu}_{16}$ and $\text{Ca}_{65}\text{Mg}_{15}\text{Zn}_{20}$ (numbers indicate at.%) were measured as a function of temperature between 5 and 400 $^{\circ}\text{C}$. Below the glass transition temperature, both Young’s modulus and shear modulus decrease and the Poisson ratio increases with an increase in temperature. Above the glass transition temperature, these trends reverse due to crystallization. At temperatures close to the glass transition temperature, the onset of a peak in the internal friction Q^{-1} , attributed to crystallization, was observed. The elastic constants were sensitive to the composition of BMGs, so that higher moduli were measured for glasses with higher Cu and lower Ca concentrations. This trend is in agreement with calculations based on the volume fraction of the elemental constituents [10, 18].

3.1.6 Thermodynamic and Kinetic Behavior of Supercooled Glass-Forming Liquids

A phenomenological relationship between reduced excess heat capacity of super-cooled liquid

$\frac{\Delta C_p^{exc}(T_g)}{\Delta S_m}$ at the glass transition temperature T_g , fragility index m and reduced glass transition

temperature $T_{rg} = T_g/T_m$, where T_m is the melting (liquidus) temperature, was derived for fragile non-polymeric glass-forming liquids under the assumptions that the fragile behavior of these liquids is described by the Vogel-Fulcher-Tammann (VFT) equation, the excess heat capacity of liquid is a hyperbolic function of the absolute temperature, and the VFT temperature T_0 is equal

to the Kauzmann temperature T_K . It was found that $\frac{\Delta C_p^{exc}(T_g)}{\Delta S_m}$ is a composite function of m and

T_{rg} , which indicates that the empirical correlation $\frac{\Delta C_p^{exc}(T_g)}{\Delta S_m} = 0.025m$ recently identified by

Wang et al. [L.M. Wang, C.A. Angell, and R. Richert, J. Chem Phys. 125, 074505 (2006)] is probably valid only for liquids which have nearly the same values of T_{rg} . [19]

Correlations between three characteristic temperatures: glass transition, T_g , Kauzmann, T_K , and Vogel-Fulcher-Tammann, T_0 , were identified from the analysis of more than 60 metallic and non-metallic glass-forming materials. It was found that $T_g \geq T_K \geq T_0$ and T_K is the geometric mean of T_g and T_0 ($T_K^2 = T_g \times T_0$). The relation $T_K \geq T_0$ indicates that the excess total entropy of a super-cooled liquid ΔS approaches zero at a higher temperature than the configurational entropy ΔS_{conf} , and such behavior was explained by the stronger temperature dependence of the excess vibrational entropy of the liquid, ΔS_{vib} , than that of the corresponding glass, ΔS_{vib}^g . A relationship between the fragility index m , reduced excess heat capacity $\Delta C_p(T_g)/S_m$, and reduced glass transition temperature, T_{rg} , was identified using the found correlation between the characteristic temperatures [20].

3.2 Super-High Strength Cast-and-Wrought Aluminum Alloys

3.2.1 Thermo-Mechanical Processing of a Cast 7xxx Al Alloy Modified with Sc

Aluminum alloys modified with Sc offer significant enhancements in mechanical properties and are attracting attention for aerospace applications. Thermo-mechanical processing (TMP) is an important step in the shape-forming of these alloys to obtain desired shape, microstructure, and mechanical property combinations. The Sc addition is expected to affect the TMP response of Al alloys and thorough understanding of this response would help in the design and optimization of the process sequences. In this work, simulation of the TMP simulation of an advanced Sc-modified Al-Zn-Mg-Cu alloy produced via direct chill continuous casting was performed with the use of hot compression tests. These tests were conducted in the temperature range of 250 – 500 °C and strain rate range of 3×10^{-4} – 10 s^{-1} . A processing map for hot working was generated based on the analyses of temperature and strain rate sensitivity of the flow stress over the above ranges. Hot deformation mechanisms were identified and correlated with the microstructure and hot tensile behavior. The influence of Sc on the hot workability of the alloy was established, and

the optimum parameters for TMP were identified. The dynamic recrystallization domain in the strain rate range of $1 \times 10^{-3} \text{ s}^{-1}$ to $1 \times 10^{-2} \text{ s}^{-1}$ having a peak efficiency at 450 °C was found to be the domain having the best intrinsic workability for this alloy. Beyond this strain rate range, as well as at temperatures above 500 °C and below 350 °C, the regions of instability and unsafe domains for processing were identified [21].

3.2.2 Optimization of Microstructure, Heat Treatment, and Tensile Properties of a High-Strength Direct Chill Cast Al-Zn-Mg-Cu Alloy Modified with Sc and Zr

The effect of combined addition of Sc and Zr on the microstructure and tensile properties of the direct chill (DC) cast ingots of developmental Al-Zn-Mg-Cu alloys was evaluated. The properties in both the longitudinal and transverse directions of the cast ingots were determined in as-cast and heat-treated conditions, at room and cryogenic temperatures. Homogenization, solution treatment and aging schedules were optimized to obtain superior mechanical properties. In particular, after the optimized heat treatment the Sc-containing developmental cast alloys showed the tensile properties, which were much better than the properties of any commercial cast Al alloys and similar to the properties of a forged 7075-T6 alloy. The following conclusions were drawn from this study. (1) The alloy without Sc addition had coarse twinned columnar grains grown from the surface to the center of the cast ingot and shrinkage-induced pre-solidification cracks in the central part of the ingot. The alloy showed rather good tensile ductility (~15%) in the longitudinal (axial) direction and nil ductility in the transverse direction of the ingot. The ductility did not improve after solution treatment and aging. The orientation of the weak twinned grain boundaries with respect to the specimen testing direction was suggested to control the brittle behavior. (2) Additions of Sc from 0.18 to 0.48 wt.% provided considerable grain refinement and inhibited formation of twinned columnar grains and cracks in the cast ingots. The dendrite growth directions changed from $\langle 110 \rangle$ in the alloy without Sc to $\langle 100 \rangle$ in the Sc-containing alloys. (3) The Sc-containing alloy ingots showed isotropic properties, in both as-cast and cast plus heat treated conditions. Typical YS of 490 MPa, UTS of 590 MPa and plastic strain of 15% at room temperature and YS of 610 MPa, UTS of 720 MPa and plastic strain of 10% at the liquid nitrogen temperature were achieved in the cast alloy modified with 0.38% Sc after heat treatment. These values exceed the properties of 7075-T6 alloy forgings [22, 23].

3.2.3 Cryogenic and Elevated Temperature Strengths of a Wrought Al-Zn-Mg-Cu Alloy Modified with Sc and Zr

The effect of minor additions of Sc and Zr on tensile properties of two developmental wrought Al-Zn-Mg-Cu alloys was studied in a temperature range from -196 °C to 300 °C. Due to presence of Sc and Zr in a fine dispersoid form, both low temperature and elevated temperature strengths of these alloys are much higher than those of similar 7000 series alloys that do not contain these elements. After short holding times (up to 10 hours) at 205 °C, the strength of these alloys is higher than those of high-temperature Al alloys 2219-T6 and 2618-T6; however, the latter alloys show better strength after longer holding times. It is suggested that additional alloying of the Sc-containing Al-Zn-Mg-Cu alloys with other dispersoid-forming elements, such as Ni, Fe, Mn, and Si, with a respective decrease in the amounts of Zn and Mg, may further

improve the elevated temperature strength and decrease the loss of strength with extended elevated temperature exposure [24, 25].

3.2.4 Effect of Sc on Aging Kinetics in a High-Strength Direct Chill Cast Al-Zn-Mg-Cu Alloy

The effect of Sc additions on the kinetics of precipitation of GP zones and η' particles during natural and artificial aging, as well as resulting precipitation strengthening, was studied in a direct chill cast high-strength Al-Zn-Mg-Cu alloy. Microhardness, room temperature tensile properties, and phase composition of the alloys were determined after different steps of aging. The strengthening mechanisms were discussed. It was shown that minor additions of Sc increased the strength of the Al-Zn-Mg-Cu alloy after casting and solution heat treatment due to precipitation of fine coherent $\text{Al}_3(\text{Sc,Zr})$ particles. Analysis of the aging kinetics revealed that Sc had no effect on the natural aging, which was controlled by formation and growth of GP I zones. On the other hand, the Sc additions accelerated the aging process at 120 °C and 150 °C within a period of time of formation and growth of GP II zones and η' particles. It was concluded that the presence of Sc accelerated formation and growth of GP II zones in the Al-Zn-Mg-Cu alloys which led to the earlier precipitation of the η' phase. However, at longer aging times at 120 °C and 150 °C, the aging response of the Sc-containing alloys slowed down due to faster coarsening of the η' particles and their transformation into η particles. A model of formation of vacancy-rich clusters (VRCs), precursors to GP zones, in the Al-Zn-Mg- based alloys was proposed. According to this model, the observed effects of Sc on aging are results of the Sc-induced increase in the number density of the GP II clusters and the concentration of quenched-in solute bound excess vacancies [26, 27].

3.3 Boron-Modified Titanium Alloys

Ingot breakdown, an essential step in titanium processing, is aimed primarily at reducing the cast grain size in an ingot from several millimeters to about 200 μm . Prior work at the Air Force Research Laboratory has shown that a minor perturbation of titanium alloy compositions – the addition of 0.05 to 0.1 wt% boron – results in as-cast grain sizes that are equivalent to those obtained after ingot breakdown in conventionally processed titanium blooms. This opens the possibility of eliminating expensive and time-consuming thermo-mechanical processing (TMP) steps necessary for obtaining fine-grained microstructures. In a concurrent work funded by Edison Material Technology Center (EMTEC), the production of plates and sheets by directly rolling as-cast Ti-6Al-4V-0.1B was explored. Ingots of boron-modified Ti-6Al-4V were produced by two single melt processing techniques – plasma arc melting (PAM) and ISM. Samples of 25 mm thickness were subjected to rolling in the alpha-beta regime to produce plates (~6 mm thick) and sheets (~2 mm thick). Mechanical property evaluation at room temperature indicated that the Ti-6Al-4V-0.1B plates and sheets, produced with significantly fewer processing steps, possess properties that are comparable to conventional Ti-6Al-4V mill product [28].

The superplastic formability of titanium alloys, such as Ti-6Al-4V, is an important consideration for many applications of these alloys. The superplastic forming (SPF) of Ti-6Al-4V is typically carried out at temperatures around 900 °C. However, other researchers have reported that the

SPF of Ti-6Al-4V can be done at lower temperatures ($\sim 775^\circ\text{C}$) if a fine-grain alloy is used. There are many advantages of reducing the SPF temperature of Ti-6Al-4V, including processing cost reduction and also a reduction in the thickness of alpha case formed. Micro-alloying of titanium alloys with boron produces significant grain refinement in these alloys, and so may provide an approach for SPF at low temperatures. In an earlier work, the superplastic behavior of boron-modified Ti-6Al-4V was investigated at temperatures in the beta phase field. In the current work, the superplastic behavior of boron modified Ti-6Al-4V was examined at a range of temperatures in the $(\alpha+\beta)$ phase field. The results of the current research indicate that the sheets produced by direct rolling of as-cast Ti-6Al-4V-0.1B (as described above) exhibit good superplastic behavior (tensile elongations $> 200\%$) in the superplastic forming temperature range of standard Ti-6Al-4V [29].

3.4 Nickel-Based Superalloys [30]

Low Solvus High Refractory (LSHR) is a high strength Ni-base superalloy, which has been developed primarily for turbine disk applications. LSHR may also be attractive for other applications in the sheet product form. In the current work, the microstructure evolution of LSHR at different times and temperatures (in the vicinity of the γ' - solvus) has been examined. The microstructures have been characterized via Scanning Electron Microscopy (SEM) and Electron BackScattered Diffraction-Orientation Imaging Microscopy (EBSD-OIM) techniques. The compressive flow behavior at temperatures in both the sub-solvus and super-solvus regimes has been determined. The microstructural modifications resulting from the compression tests have also been examined. The results of the current work are discussed in the context of hot working of LSHR [30].

3.5 Publications

1. O.N. Senkov, S.V. Senkova, and D.B. Miracle, "Compaction of Amorphous Aluminum Alloy Powder by Direct Extrusion and Equal Channel Angular Extrusion," *Mater. Sci. & Eng.*, **A393** 12-21 (2005).
2. O.N. Senkov, D.B. Miracle, and H.M. Mullens, "Topological Criteria for Amorphization Based on Thermodynamic Approach," *J. Applied Physics*, **97** 103502/1-7 (2005).
3. D.B. Miracle, W.S. Sanders, O.N. Senkov, and P.S. Meltzer, "Predicting the Composition of Metallic Glasses," *Technology Horizons*, **6** [5] 40-41 (2005).
4. O.N. Senkov and D.B. Miracle, "Recent Advances in Development of Bulk Metallic Glasses," pp. 249-266 in *Processing and Fabrication of Advanced Materials XIV*. Edited by T.S. Srivatsan, R.A. Varin, R. Abbaschian, and S. Viswanathan, ASM International, Pittsburgh, PA, (2005).
5. S. Gorsse, G. Orveillon, O.N. Senkov, and D.B. Miracle, "Thermodynamic Analysis of Glass Forming Ability in a Ca-Mg-Zn Ternary System," *Phys. Rev. B*, **73** 224202/1-9 (2006).
6. O.N. Senkov, "Correlation Between Fragility and Glass Forming Ability of Metallic Alloys," *Phys. Rev. B*, **76** 104202/1-6 (2007).
7. O.N. Senkov and J.M. Scott, "Glass Forming Ability and Thermal Stability of Ternary Ca-Mg-Zn Bulk Metallic Glasses," *J. Non-Cryst. Solids*, **351** 3087-3094 (2005).

8. O.N. Senkov, J.M. Scott, and D.B. Miracle, "Composition Range and Glass Forming Ability of Ternary Ca-Mg-Cu Bulk Metallic Glasses," *J. Alloys & Comp.*, **424** 394-399 (2006).
9. O.N. Senkov, D.B. Miracle, and J.M. Scott, "Development and Characterization of Ca-Mg-Zn-Cu Bulk Metallic Glasses," *Intermetallics*, **14** 1055-1060 (2006).
10. O.N. Senkov, D.B. Miracle, V. Keppens, and P.K. Liaw, "Development and Characterization of Low-Density Ca-Based Bulk Metallic Glasses: An Overview," *Metall. Mater. Trans.*, **A39** 1888-1900 (2008).
11. O.N. Senkov, J.M. Scott, and D.B. Miracle, "Development and Characterization of Ca-Mg-Al-Based Bulk Metallic Glasses," *Mater. Trans.*, **48** 1610-1616 (2007).
12. O.N. Senkov, J.M. Scott and D.B. Miracle, "Effect of Al addition on glass forming ability and glass stability of Ca-Mg-Zn-Cu based bulk metallic glasses," *Metall. Mater. Trans.*, **A39** 1901-1907 (2008).
13. G. Orveillon, O.N. Senkov, J.-L. Soubeyroux, B. Chevalier, and S. Gorsse, "Composition Selection and Glass Forming Ability of Ce-Based Amorphous Alloys," *Adv. Eng. Mater.*, **9** 483-486 (2007).
14. M.L. Morrison, R.A. Buchanan, O.N. Senkov, D.B. Miracle, and P.K. Liaw, "Electrochemical Behavior of Ca-based Bulk Metallic Glasses," *Metall. Mater. Trans.*, **A37** 1239-1245 (2006).
15. B.R. Barnard, P.K. Liaw, R.A. Buchanan, O. N. Senkov, and D. B. Miracle, "Oxidation of Ca-based Bulk Amorphous Materials," *Mater. Trans.*, **48** 1870-1878 (2007).
16. J. E. Dahlman, O. N. Senkov, J. M. Scott, and D. B. Miracle, "Corrosion Properties of Ca-Based Bulk Metallic Glasses," *Mater. Trans.*, **48** 1850-1854 (2007).
17. V. Keppens, Z. Zhang, O.N. Senkov, and D.B. Miracle, "Localized Einstein Modes in Ca-based Bulk Metallic Glasses," *Phil. Mag.*, **87** 503-508 (2007).
18. Z. Zhang, V. Keppens, O.N. Senkov, and D.B. Miracle, "Elastic Properties of Ca-Based Bulk Metallic Glasses Studied by Resonant Ultrasound Spectroscopy," *Mater. Sci. Eng.*, **A471** 151-154 (2007).
19. O.N. Senkov and D.B. Miracle, "Correlation Between Thermodynamic and Kinetic Fragilities in Non-Polymeric Glass-Forming Liquids," *J. Chem. Physics*, **128** 124508/1-3 (2008)
20. O.N. Senkov and D.B. Miracle, "Correlation Between Thermodynamic and Kinetic Properties of Glass-Forming Liquids," pp. 7-15 in Bulk Metallic Glasses—2007. Edited by J. Schroers, R. Busch, N. Nishiyama, and M. Li, Mater. Res. Soc. Symp. Proc. Vol. 1048, Warrendale, PA, (2007).
21. R. Bhat, S. Tamirisa, and O. Senkov, "Thermo-mechanical Processing of a Cast 7XXX Al Alloy Modified with Sc," pp. 239-244 in Trends in Materials and Manufacturing Technologies for Transportation Industries. Edited by T.R. Bieler, J.E.Carsley, H.L. Fraser, J.W. Sears, and J.E. Smugeresky, TMS, Warrendale, PA, (2005).
22. S.V. Senkova, R.B. Bhat, O.N. Senkov, Microstructure and Tensile Properties of Developmental Al-Zn-Mg-Cu Cast Alloys Modified with Sc And Zr," pp. 245-250 in Trends in Materials and Manufacturing Technologies for Transportation Industries. Edited by T.R. Bieler, J.E.Carsley, H.L. Fraser, J.W. Sears, and J.E. Smugeresky, TMS, Warrendale, PA, (2005).

23. O.N. Senkov, R.B. Bhat, S.V. Senkova, and J.D. Schloz, "Microstructure and Properties of Cast Ingots of Al-Zn-Mg-Cu Alloys Modified with Sc and Zr," *Metall. Mater. Trans. A*, **36** 2115-2126 (2005).
24. O.N. Senkov, D.B. Miracle, and T.R. Anderl, "Super-High Strength Aluminum Alloy," *Technology Horizons*, **7** [3] 40-41 (2006).
25. S.V. Senkova, O.N. Senkov, and D.B. Miracle, "Cryogenic and Elevated Temperature Strengths of an Al-Zn-Mg-Cu Alloy modified with Sc and Zr," *Metall. Mater. Trans.*, **A37** 3569-3575 (2006).
26. M.R. Shaghiev, S.V. Senkova, and O.N. Senkov, "Precipitation in Al-Zn-Mg-Cu Alloys Modified with Sc and Zr During Aging," pp. 213-222 in Materials Science and Technology (MS&T) 2006: Materials and Systems, Vol. 2. TMS, Materials Park, OH, (2006).
27. O.N. Senkov, S.V. Senkova, and M.R. Shaghiev, "Effect of Sc on Aging Kinetics in a Direct Chill Cast Al-Zn-Mg-Cu Alloy," *Metall. Mater. Trans.*, **A39** 1034-1053 (2008).
28. R. Srinivasan, S. Tamirisakandala, D. Miracle, K.O. Yu, V. Sinha, F. Sun, M. Bennett, and J. M. Scott, "Production of Plates and Sheets from As-Cast Ti-6Al-4V via Boron Modification," *Ti-2007 Science and Technology: Proceedings of the 11th World Conference on Titanium*, 977-980 (2007).

3.6 Invited Presentations

1. O.N. Senkov and D.B. Miracle, "Recent Advances in Development of Bulk Metallic Glasses," presented at the 14th Symposium on Processing and Fabrication of Advanced Materials (PFAM XIV), Materials Science & Technology 2005 (MS&T '05), Pittsburgh, PA, September 26-28, 2005.
2. O.N. Senkov, J.M. Scott, and S. Gorsse, "Development and Characterization of Ca-Mg-Zn-Cu Bulk Metallic Glasses," presented at the Symposium on Bulk Metallic Glasses (BMG-2), TMS-2005 Annual Meeting, San Francisco, CA, February 2005.
3. O.N. Senkov, J.M. Scott, and D.B. Miracle, "Composition Dependence of the Glass Forming Ability in Ternary Ca-Mg-Zn and Ca-Mg-Cu Systems," presented at the 3rd Symposium on Bulk Metallic Glasses (BMG-3), TMS-2006 Annual Meeting, San Antonio, CA, March 2006.
4. D.B. Miracle and O.N. Senkov, "Recent Advances in Development of Bulk Metallic Glasses," presented at the 3rd Symposium on Bulk Metallic Glasses (BMG-3), TMS-2006 Annual Meeting, San Antonio, CA, March 2006.
5. O.N. Senkov, "A Super-High Strength Aluminum Alloy for Liquid Hydrogen Turbopump Applications," presented at the 14th International Conference on Composite Engineering (ICCE-14), Boulder, CO, July, 2006.
6. O.N. Senkov, "Development and Characterization of Low Density Ca-Based Bulk Metallic Glasses: An Overview," presented at the 4th Symposium on Bulk Metallic Glasses (BMG-4), TMS-2007 Annual Meeting, Orlando, FL, 25 February – 1 March, 2007.
7. O.N. Senkov, "Effect of Liquid Fragility on Glass Forming Ability of Metallic Alloys," presented at the 5th Symposium on Bulk Metallic Glasses (BMG-V), TMS-2008 Annual Meeting & Exhibition, New Orleans, LA, 9-13 March, 2008.

3.7 Presentations

1. S.V. Senkova, M.R. Shagiev, and O.N. Senkov, "Effect of Sc on Microstructure and Properties of Cast Ingots of Al-Zn-Mg-Cu alloys," presented at the Accelerated Insertion of Materials Workshop, Dayton, OH, November, 2005.
2. O.N. Senkov, "Cryogenic Mechanical Properties of a Sc-modified 7XXX Alloy Forging," presented at Aeromat-2005, Orlando, FL, June, 2005.
3. R. Bhat, S. Senkova and O. Senkov, "Scale up Efforts in the Development of a 7xxx Al Alloy Modified with Scandium," presented at Aeromat-2005, Orlando, FL, June, 2005.
4. M. J. Caton, S.V. Senkova and O. N. Senkov, "Fatigue Properties of a Super-High Strength Developmental Al-Zn-Mg-Sc Alloy for Use in Cryogenic Applications," presented at Aeromat-2005, Orlando, FL, June, 2005.
5. O.N. Senkov and J.M. Scott, "Development and Characterization of Ca-Mg-Zn-Cu Bulk Metallic Glasses," presented at the 4th International Conference on Bulk Metallic Glasses (BMG-4), Gatlinburg, TN, May, 2005.
6. O.N. Senkov, D.B. Miracle and H.M. Mullens, "A Combined Thermodynamic and Topological Model for the Stability of Metallic Glasses," presented at the 12th International Symposium on Metastable and Nano Materials (ISMANAM05), Paris, France, July, 2005.
7. O.N. Senkov, "Cryogenic Mechanical Properties of a Sc-modified 7xxx Alloy Forging," presented at the Materials Science & Technology 2005 (MS&T '05), Pittsburgh, PA, September 26-28, 2005.
8. O.N. Senkov and R.E. Perez, "Properties of Liquid Hydrogen Turbopump Impeller Preforms Made of a Super-High Strength Aluminum Alloy," presented at the Symposium on Application of Materials Science for Military Systems, Materials Science & Technology 2005 (MS&T '05), Pittsburgh, PA, September 26-28, 2005.
9. R. Bhat, S. Tamirisa and O.N. Senkov, "Thermo-mechanical Processing of a Cast 7XXX Al Alloy Modified with Sc," presented at the Sixth Global Innovations Proceedings Trends in Materials and Manufacturing Technologies for Transportation Industries, TMS-2005 Annual Meeting, San Francisco, February, 2005.
10. S.V. Senkova, R.B. Bhat, and O.N. Senkov, "Microstructure and Tensile Properties of Developmental Al-Zn-Mg-Cu Cast Alloys Modified with Sc and Zr," presented at the Sixth Global Innovations Proceedings Trends in Materials and Manufacturing Technologies for Transportation Industries, TMS-2005 Annual Meeting, San Francisco, February, 2005.
11. O.N. Senkov, S.V. Senkova, and R.B. Bhat, "Effect of Crystallographic Texture on Tensile Properties of a 7XXX Alloy with Sc Addition," presented at the Sixth Global Innovations Proceedings Trends in Materials and Manufacturing Technologies for Transportation Industries, TMS-2005 Annual Meeting, San Francisco, February, 2005.
12. J.M. Scott, J.E. Dahlman, O.N. Senkov, and D.B. Miracle, "Corrosion Resistance of Ca-Based Bulk Metallic Glasses," presented at the 5th International Conference on Bulk Metallic Glasses (BMG-V), Awaji, Japan, October 1-6, 2006.
13. O.N. Senkov, J.M. Scott, and D.B. Miracle, "Effect of Al Addition on Glass Forming Ability and Glass Stability of Ca-Mg-Zn-Cu Bulk Metal Glasses," presented at the 5th International Conference on Bulk Metallic Glasses (BMG-V), Awaji, Japan, October 1-6, 2006.

14. M.R. Shagiev, S.V. Senkova, and O.N. Senkov, "Precipitation in Al-Zn-Mg-Cu Alloys Modified with Sc and Zr During Aging," presented at the Symposium on Materials for Responsive Space Access, Materials Science & Technology 2006 (MS&T'06), Cincinnati, OH, October 15-19, 2006.
15. O.N. Senkov, S.V. Senkova, and M.R. Shagiev, "Microstructure and Properties of Cast Ingots of Al-Zn-Mg-Cu Alloys Modified with Sc and Zr," presented at the Symposium on Materials for Responsive Space Access, Materials Science & Technology 2006 (MS&T'06), Cincinnati, OH, October 15-19, 2006.
16. O.N. Senkov, "A Super-High Strength Aluminum Alloy for use at Ambient and Cryogenic Temperatures," presented at the Symposium on Materials for Responsive Space Access, Materials Science & Technology 2006 (MS&T'06), Cincinnati, OH, October 15-19, 2006.
17. O. N. Senkov, J. M. Scott, and D. B. Miracle, "Low Density Ca-Mg-Al-Based Bulk Metallic Glasses," presented at the 4th Symposium on Bulk Metallic Glasses (BMG-4), TMS-2007 Annual Meeting, Orlando, FL, February 25 – March 1, 2007.
18. O.N. Senkov, S.V. Senkova, M.R. Shagiev, and D.B. Miracle, "Elevated Temperature Strength of Al-Zn-Mg-Cu Alloys modified with Sc and Zr," presented at the TMS-2007 Annual Meeting, Orlando, FL, February 25 – March 1, 2007.
19. M.R. Shagiev, S.V. Senkova, and O.N. Senkov, "Precipitation of $Al_3(Sc,Zr)$ Particles in an Al-Zn-Mg-Cu-Sc-Zr Alloy During Heat Treatment," presented at the TMS-2007 Annual Meeting, Orlando, FL, February 25 – March 1, 2007.
20. S.T. Reis, N.Ross, R.K. Brown, D.B. Miracle, O.N. Senkov, and R. Lederich, "TTT Diagram for Magnesium and Zirconium-Based Bulk Amorphous Alloys," presented at the 4th Symposium on Bulk Metallic Glasses (BMG-4), TMS-2007 Annual Meeting, Orlando, FL, February 25 – March 1, 2007.
21. S.M. Gorantla, Y. Wang, F.S. Miller, R.S. Mishra, D.B. Miracle, and O. N. Senkov, "Multi-functional Optimization Approach for Predicting Bulk Metallic Glass Systems," presented at the 4th Symposium on Bulk Metallic Glasses (BMG-4), TMS-2007 Annual Meeting, Orlando, FL, February 25 – March 1, 2007.
22. N. Ross, Y. Wang, R.S. Mishra, D.B. Miracle, O.N. Senkov and R. J. Lederich, "Formability of an Mg-Cu-Ag-Y Metallic Glass," presented at the 4th Symposium on Bulk Metallic Glasses (BMG-4), TMS-2007 Annual Meeting, Orlando, FL, February 25 – March 1, 2007.
23. B. R. Barnard, P. K. Liaw, R. A. Buchanan, O. N. Senkov, and D. B. Miracle, "Room-Temperature Oxidation of Ca-based Bulk Amorphous Materials," presented at the 4th Symposium on Bulk Metallic Glasses (BMG-4), TMS-2007 Annual Meeting, Orlando, FL, February 25 – March 1, 2007.
24. O. N. Senkov, "Correlation Between Fragility and Glass Forming Ability of Metallic Alloys," presented at the Symposium on Amorphous Materials, MRS Fall Meeting, Boston, MA, November 25-30, 2007.
25. O.N. Senkov and D.B. Miracle, "Correlation between Thermodynamic and Kinetic Properties of Glass-Forming Liquids, Symposium on Amorphous Materials," presented at MRS Fall Meeting, Boston, MA, November 25-30, 2007.

26. V. Sinha, S. Tamirisakandala, M. Scott, R. Srinivasan and D. B. Miracle, "Texture and Superplasticity in Boron Modified Ti-6Al-4V Alloy," presented at the Symposium on Advanced Metallic Composites and Alloys for High Performance Applications, TMS Annual Meeting, Orlando, FL, February 25 - March 1, 2007.
27. O.N. Senkov, M.R. Shagiev, S.V. Senkova, and D.B. Miracle, "Aging of Al-Zn-Mg-Cu Alloys with Minor Sc Additions," presented at the Symposium on Aluminum Alloys: Fabrication, Characterization and Applications, TMS-2008 Annual Meeting & Exhibition, New Orleans, LA, 9-13 March, 2008.

3.8 Invention Disclosures/Patents

1. O.N. Senkov, S.V. Senkova, M.G. Mendiratta, D.B. Miracle, Y.V. Milman, D.V. Lotsko and A.I. Sirko, High Strength Aluminum Alloy Composition, US Patent #7060139, June 13, 2006.
2. O.N. Senkov, S.V. Senkova, M.G. Mendiratta, D.B. Miracle, Method of Making a High Strength Aluminum Alloy Composition, US Patent #7048815, May 23, 2006.

3.9 Conference Proceedings Edited

1. O.N. Senkov, D.B. Miracle, and S.A. Firstov (Eds.) *Metallic Materials with High Structural Efficiency*, NATO Science Series, Kluwer Acad. Publishers, Dordrecht, 2004.

3.10 Awards/Service

1. Dr. Oleg Senkov elected Leading Scientist of the World by International Biographical Centre, Cambridge, England (2005).
2. Dr. Oleg Senkov is a Key Reader for Metallurgical and Materials Transactions A.
3. Dr. Oleg Senkov is a Reviewer for *Acta Materialia*, *Materials Science and Engineering*, *Journal of Alloys and Compounds*, *Scripta Materialia*, *Journal of Applied Physics*, *Journal of Chemical Physics*, and *Journal of Non-Crystalline Solids*.

3.11 References

-
1. O.N. Senkov, S.V. Senkova, and D.B. Miracle, "Compaction of Amorphous Aluminum Alloy Powder by Direct Extrusion and Equal Channel Angular Extrusion," *Mater. Sci. & Eng.*, **A393** 12-21 (2005).
 2. O.N. Senkov, D.B. Miracle, and H.M. Mullens, "Topological Criteria for Amorphization Based on Thermodynamic Approach," *J. Appl. Phys.*, **97** 103502/1-7 (2005).
 3. D.B. Miracle, W.S. Sanders, O.N. Senkov, and P.S. Meltzer, "Predicting the Composition of Metallic Glasses," *Technology Horizons*, **6** [5] 40-41 (2005).
 4. O.N. Senkov and D.B. Miracle, Recent Advances in Development of Bulk Metallic Glasses, pp. 249-266 in *Processing and Fabrication of Advanced Materials XIV*. Edited by T.S. Srivatsan, R.A. Varin, R. Abbaschian, and S. Viswanathan, ASM International, Pittsburgh, PA, 2005.

-
5. S. Gorsse, G. Orveillon, O.N. Senkov, and D.B. Miracle, "Thermodynamic Analysis of Glass Forming Ability in a Ca-Mg-Zn Ternary System," *Phys. Rev. B*, **73** 224202/1-9 (2006).
 6. O.N. Senkov, "Correlation Between Fragility and Glass Forming Ability of Metallic Alloys," *Phys. Rev. B*, **76** 104202/1-6 (2007).
 7. O.N. Senkov and J.M. Scott, "Glass Forming Ability and Thermal Stability of Ternary Ca-Mg-Zn Bulk Metallic Glasses," *J. Non-Cryst. Solids*, **351** 3087-3094 (2005).
 8. O.N. Senkov, J.M. Scott, and D.B. Miracle, "Composition Range and Glass Forming Ability of Ternary Ca-Mg-Cu Bulk Metallic Glasses," *J. Alloys & Comp.*, **424** 394-399 (2006).
 9. O.N. Senkov, D.B. Miracle, and J.M. Scott, "Development and Characterization of Ca-Mg-Zn-Cu Bulk Metallic Glasses," *Intermetallics*, **14** 1055-1060 (2006).
 10. O.N. Senkov, D.B. Miracle, V. Keppens, and P.K. Liaw, "Development and Characterization of Low-Density Ca-Based Bulk Metallic Glasses: An Overview," *Metall. Mater. Trans.*, **A39** 1888-1900 (2008).
 11. O.N. Senkov, J.M. Scott, and D.B. Miracle, "Development and Characterization of Ca-Mg-Al-Based Bulk Metallic Glasses," *Mater. Trans.*, **48** 1610-1616 (2007).
 12. O.N. Senkov, J.M. Scott and D.B. Miracle, "Effect of Al addition on glass forming ability and glass stability of Ca-Mg-Zn-Cu based bulk metallic glasses," *Metall. Mater. Trans.*, **A39** 1901-1907 (2008).
 13. G. Orveillon, O.N. Senkov, J.-L. Soubeyroux, B. Chevalier, and S. Gorsse, "Composition Selection and Glass Forming Ability of Ce-Based Amorphous Alloys," *Adv. Eng. Mater.*, **9** 483-486 (2007).
 14. M.L. Morrison, R.A. Buchanan, O.N. Senkov, D.B. Miracle, and P.K. Liaw, "Electrochemical Behavior of Ca-based Bulk Metallic Glasses," *Metall. Mater. Trans.*, **A37** 1239-1245 (2006).
 15. B.R. Barnard, P.K. Liaw, R.A. Buchanan, O.N. Senkov, and D.B. Miracle, "Oxidation of Ca-based Bulk Amorphous Materials," *Mater. Trans.*, **48** 1870-1878 (2007).
 16. J.E. Dahlman, O.N. Senkov, J.M. Scott, and D.B. Miracle, "Corrosion Properties of Ca-Based Bulk Metallic Glasses," *Mater. Trans.*, **48** 1850-1854 (2007).
 17. V. Keppens, Z. Zhang, O. N. Senkov, and D. B. Miracle, "Localized Einstein Modes in Ca-based Bulk Metallic Glasses," *Phil. Mag.*, **87** 503-508 (2007).
 18. Z. Zhang, V. Keppens, O.N. Senkov, and D.B. Miracle, "Elastic Properties of Ca-Based Bulk Metallic Glasses Studied by Resonant Ultrasound Spectroscopy," *Mater. Sci. Eng.*, **A471** 151-154 (2007).
 19. O.N. Senkov and D.B. Miracle, "Correlation Between Thermodynamic and Kinetic Fragilities in Non-Polymeric Glass-Forming Liquids," *J. Chem. Phys.*, **128** 124508/1-3 (2008).
 20. O.N. Senkov and D.B. Miracle, "Correlation Between Thermodynamic and Kinetic Properties of Glass-Forming Liquids," pp. 7-15 in *Bulk Metallic Glasses—2007*. Edited by J. Schroers, R. Busch, N. Nishiyama, and M. Li, Mater. Res. Soc. Symp. Proc. Vol. 1048, Warrendale, PA, 2007.

-
21. R. Bhat, S. Tamirisa, and O. Senkov, Thermo-mechanical Processing of a Cast 7XXX Al Alloy Modified with Sc, pp. 239-244 in Trends in Materials and Manufacturing Technologies for Transportation Industries. Edited by T.R. Bieler, J.E.Carsley, H.L. Fraser, J.W. Sears, and J.E. Smugeresky, TMS, Warrendale, PA, 2005.
 22. S.V. Senkova, R.B. Bhat, and O.N. Senkov, "Microstructure and Tensile Properties of Developmental Al-Zn-Mg-Cu Cast Alloys Modified with Sc And Zr," pp. 245-250 in Trends in Materials and Manufacturing Technologies for Transportation Industries. Edited by T.R. Bieler, J.E.Carsley, H.L. Fraser, J.W. Sears, and J.E. Smugeresky, TMS, Warrendale, PA, 2005.
 23. O.N. Senkov, R.B. Bhat, S.V. Senkova, and J.D. Schloz, "Microstructure and Properties of Cast Ingots of Al-Zn-Mg-Cu Alloys Modified with Sc and Zr," *Metall. Mater. Trans.*, **A36** 2115-2126 (2005).
 24. O.N. Senkov, D.B. Miracle, and T.R. Anderl, "Super-High Strength Aluminum Alloy," *Technology Horizons*, **7** [3] (2006) 40-41 (2006).
 25. S.V. Senkova, O.N. Senkov, and D.B. Miracle, "Cryogenic and Elevated Temperature Strengths of an Al-Zn-Mg-Cu Alloy modified with Sc and Zr," *Metall. Mater. Trans.*, **A37** 3569-3575 (2006).
 26. M.R. Shaghiev, S.V. Senkova, O.N. Senkov, Precipitation in Al-Zn-Mg-Cu Alloys Modified with Sc and Zr During Aging, pp. 213-222 in Materials Science and Technology (MS&T) 2006: Materials and Systems, Vol. 2, TMS, Materials Park, OH, 2006.
 27. O.N. Senkov, S.V. Senkova, M.R. Shaghiev, Effect of Sc on Aging Kinetics in a Direct Chill Cast Al-Zn-Mg-Cu Alloy, *Metall. Mater. Trans.*, **A39** 1034-1053 (2008).
 28. V. Sinha, S. Tamirisakandala, M. Scott, R. Srinivasan and D. B. Miracle, Texture and Superplasticity in Boron Modified Ti-6Al-4V Alloy, presented at the Symposium on Advanced Metallic Composites and Alloys for High Performance Applications, TMS Annual Meeting, Orlando, FL, February 25 - March 1, 2007.
 29. R. Srinivasan, S. Tamirisakandala, D. Miracle, K.O. Yu, V. Sinha, F. Sun, M. Bennett, and J. M. Scott, "Production of Plates and Sheets from As-Cast Ti-6Al-4V via Boron Modification," *Ti-2007 Science and Technology: Proceedings of the 11th World Conference on Titanium*, 977-980 (2007).
 30. V. Sinha, J.M. Scott, D. Ballard and P. Martin, "Microstructure Evolution and Deformation in Low Solvus High Refractory (LSHR) Ni-base Superalloy," presented at the Symposium on Characterization of Minerals, Metals, and Materials: Emerging Characterization Techniques, TMS Annual Meeting, New Orleans, LA, March 9-13, 2008.

3.0 TASK ORDER 0003 – RESEARCH FOR CERAMIC COMPOSITES

3.1 Ceramic Composite Research - Introduction

Ceramic composites offer the most potential for meeting the increasing demand for high temperature structural materials in aircraft engines, hypersonic engines and space propulsion. Increased fuel efficiency and thus decreased operating costs, reduced aircraft size and signature, decreased lifetime costs, and enabling technologies are some of the advantages of inserting ceramic components in air and space craft. In particular, hypersonic technology relies almost entirely on un-cooled ceramic components to become a reality beyond demonstrators and unmanned small missiles. Ceramics also offer significant weight reductions due to their lower densities, and have excellent optical and electrical properties of interest in some applications such as low-observables, IR windows, and laser-gain materials for advanced weapons.

Through this contract period, UES's work has resulted in considerable advances in the area of ceramic composites. Under guidance from, and in collaboration with, personnel in the AFRL/RXLN Ceramics group, UES scientists continued to develop high temperature, oxidation resistant fiber coatings (LaPO_4 , CaWO_4 , $(\text{Y,Lu})\text{PO}_4$) for both oxide and non-oxide based composites. Oxide matrix composites containing AFRL/RXLN monazite (LaPO_4) coatings have been produced both in-house and by ATK-COI, the primary oxide-oxide supplier in the U.S. The goal of this work has been to generate sufficient data to enable the transition of these materials to actual applications. Alternative processing techniques for ceramic composite production were also developed during this time period.

The research and development under the current task order was conducted using interdisciplinary approaches, including interaction with groups involved in behavior and life prediction, process modeling, and research on new non-destructive evaluation methods. The research was also conducted in a collaborative manner, working with government engineers (AFRL/RXLN), visiting scientists and other on-site contractors as applicable. Collaborations with organizations outside of AFRL/RXLN were also encouraged during this time period.

3.2 Technical Results and Discussion

3.2.1 Fiber Coating Development

Spherical 10 nm rhabdophane ($\text{LaPO}_4 \cdot \text{H}_2\text{O}$) particles were made by controlled precipitation in water using lanthanum citrate chelate and phosphoric acid ($\text{La-Cit1}/\text{H}_3\text{PO}_4$) at a temperature of 30 °C. Rod-shaped 10 nm-100 nm rhabdophane particles were made by direct precipitation from lanthanum nitrate and phosphoric acid ($\text{La}(\text{NO}_3)_3/\text{H}_3\text{PO}_4$). The lanthanum nitrate to phosphoric acid molar ratios (La:P) were fixed at 1:1 and 1:5 for both methods to study their effect on particle size and shape. The particles were characterized with DTA/TGA, XRD, TEM, SEM, Fourier Transform infrared spectroscopy, and z potential measurements. The spherical particle surfaces had adsorbed citric acid. The point of zero charge of the rod-shaped and spherical particles was pH 5.4 and 4.3, respectively. Formation mechanisms for the spherical particles are discussed in reference [1].

The particle morphology, weight loss, and rheology of rhabdophane ($\text{LaPO}_4 \cdot \text{H}_2\text{O}$) sols with either spherical or rod-shaped particles were characterized and compared. Some spherical particle sols were doped with aluminum. Particle size was characterized by light scattering and transmission electron microscopy (TEM). The additives that promote spherical particle formation also cause greater high temperature weight loss than similar rod-shaped particle sols. As expected, the shear-rate dependence of sol viscosity was much weaker for spherical particle sols. The viscosity of sols with both types of particles was modeled using particle aspect ratios and bound water layer thicknesses as variables. A bound water layer thickness of 3–5 nm was suggested by modeling, except in aluminum-doped sols, where a much larger thickness was suggested. Modeled aspect ratios were larger than those observed by TEM. Weakly bound agglomerates may be present in both types of sols [2].

Rare earth phosphates with rare earths of Gd, Tb, and Dy can form either monazite or xenotime. Hydrated lanthanide phosphate precursors for monazite and xenotime were made in aqueous solution. The particles were formed by adding dilute phosphoric acid (H_3PO_4) to either; (a) lanthanide citrate (Ln-Cit) or (b) lanthanide nitrate (LnNO_3) [Ln=La, Gd, Tb, Dy, and Y] solutions followed by altering the pH from B1 to B10 with ammonium hydroxide. Precursor particle size and morphology was characterized by scanning electron microscopy (SEM) and weight loss was characterized by thermogravimetric analysis (TGA). The phase presence at temperature was determined by differential thermal analysis (DTA) and X-ray diffraction. The influence of precursor preparation method on the presence of either monazite or xenotime after heat treatment was presented in reference [3].

3.2.1.1 Coatings on Oxide Fibers

A rhabdophane ($\text{LaPO}_4 \cdot \text{H}_2\text{O}$) sol with fine spherical particles was used to coat Nextel™ 720 fiber tows continuously with monazite (LaPO_4). The coatings are compared with those made previously from rod-shaped particles. The coated fibers were heat-treated at 1000 °C–1300 °C for 1, 10, and 100 h. The effect of heat treatment temperature and time on coating microstructure was characterized by scanning electron microscopy and transmission electron microscopy, and the strengths of the coated fibers were measured after coating and heat treatment. Grain shapes and grain growth rates were measured. Coating thickness uniformity was quantified by a fit to a truncated extreme-value distribution. Coating hermeticity was evaluated by analysis of grain growth rates. The spherical particles promote more rapid coating densification and local hermeticity, but introduce problems with sintering shrinkage cracking that are not present in coatings derived from rod-shaped particles [4].

Woven cloths of Nextel 610 and 720 fibers were coated with monazite by precipitation. The cloths were first saturated with concentrated precursor solutions, and then submerged in warm water to initiate precipitation onto the fiber surfaces. Coatings were characterized by SEM and TEM; thermogravimetric analysis was performed on LaPO_4 powders precipitated in solution under the same conditions as the coatings were deposited. Coating thickness distributions were measured and analyzed. Coated fiber strength was measured following heat treatment for 2 h at 1200 °C. Processing conditions which retain a substantial fraction of the uncoated fiber strength were identified and discussed in the context of the current understanding of strength degradation in coated fibers. Strength retention of coated Nextel 610 fibers following heat treatment was

broadly insensitive to precursor solution chemistry and was more strongly affected by intercoat firings, which govern the final coating microstructure. For fixed processing conditions, more strength degradation was observed in the Nextel 720 fiber, due to higher residual stresses in the fiber [5].

Equiaxed yttrium–lanthanum phosphate nanoparticles ($\text{Y}_{0.7}\text{La}_{0.3}\text{PO}_4 \cdot 0.7\text{H}_2\text{O}$) were made and used to continuously coat Nextel 720 fiber tows. The particles were precipitated from a mixture of yttrium and lanthanum citrate chelate and phosphoric acid (H_3PO_4), and characterized with differential thermal analysis and thermogravimetric analysis, X-ray diffraction, SEM and TEM. The coated fibers were heat treated at 1000 °C– 1300 °C for 1, 10, and 100 h. Coating grain growth kinetics and coated fiber strengths were determined and compared with equiaxed La-monazite coatings. The relationships between coating porosity, coating hermeticity, and coated fiber strength were discussed in reference [6].

Monazite coatings were deposited on woven cloths and tows of Nextel 610 fibers by heterogeneous nucleation and growth using solution precursors. Initial experiments revealed two coating regimes in which monazite was either precipitated both in solution and onto the fiber surfaces or only onto the fiber surfaces depending on the precursor solution concentration and fiber surface area. In both cases, regions of tightly packed fibers within the cloth were uncoated. Image analysis of coated fiber cross sections revealed a strong correlation between fiber separation and coating thickness, suggesting that the coating of tightly packed fibers was limited by transport of the reactants in solution to these areas. By adopting a coating procedure in which the tightly packed regions are saturated with reactants before precipitation, more uniform coatings of monazite were obtained throughout the cloth; however, the strength of as-coated and heat-treated fibers was degraded [7]. Subsequent work has focused on minimizing this strength degradation through control of coating/heat treatment parameters.

Monazite (La , Ce , Nd , and GdPO_4) and xenotime (Tb , Dy , and YPO_4) coatings were deposited on woven Nextel 610 and 720 fibers by heterogeneous precipitation from a rare-earth citrate/ phosphoric acid precursor. Coating phases and microstructure were characterized by SEM and TEM, and coated fiber strength was measured after heat treatment at 1200 °C for 2 h. Coated fiber strength increased with decreasing ionic radius of the rare earth cation in the monazite and xenotime coatings, and correlated with the high-temperature weight loss and the densification rate of the coatings. Dense coatings with trapped porosity and high weight loss at a high temperature degrade fiber strength the most. The degradation is consistent with stress corrosion driven by thermal residual stress from coating precursor decomposition products trapped in the coating at a high temperature [8].

3.2.1.2 Coatings on SiC Fibers

Commercially available SiC fibers were coated with monazite (LaPO_4) using a continuous vertical coater at 1100 °C. Coated fibers were heat treated in dry air, argon, and laboratory air at 1200 °C for 1–20 h. The tensile strengths of uncoated and coated fibers were measured and evaluated before and after heat treatment. Fiber coating did not degrade SiC fiber strength, but heat treatment afterwards caused significant degradation that correlated with the silica scale thickness. Coating morphology, microstructure, and SiC oxidation were observed with scanning

electron microscopy and transmission electron microscopy. Monazite reacted with SiC to form lanthanum silicate ($\text{La}_2\text{Si}_2\text{O}_7$) in argon, but was stable with SiC in air. Despite the large coefficient of thermal expansion difference between monazite and SiC, micron thick monazite coatings did not debond from most types of SiC fibers. Possible explanations for the thermomechanical stability of the monazite fiber coatings were discussed in reference [9].

The effect of monazite on the oxidation of SiC was studied in laboratory and dry air. Monazite inhibited the oxidation of Tyranno-SATM, Tyranno-ZXTM, SylramicTM, and Hi-NicalonTM SiC fibers. Oxidation of pure chemical vapor deposition SiC and undoped SiC single crystals was not inhibited by monazite. Dry oxidation of both uncoated and monazite-coated Tyranno-SA fibers initially displayed parabolic kinetics with an activation energy of 180–190 kJ/mol. Subsequently, the oxidation rate of monazite-coated fibers increased and the oxide-scale growth rate approached that of the uncoated fibers. No differences in the composition or structure of the silica oxidation product could be detected between uncoated and coated fibers using transmission electron microscopy and energy-dispersive spectroscopy. Possible mechanisms of the inhibition of SiC oxidation by monazite were discussed in reference [10].

3.2.2 Analysis of Rare Earth Monazite/Xenotime

The composition and lattice parameters of co-precipitated ($\text{La}_{0.3}\text{Y}_{0.7}$) orthophosphate were studied using X-ray diffraction (XRD), TEM, and energy dispersive X-ray spectroscopy (EDX). The results indicate that the as-precipitated powder consists of single-phase $(\text{Y}_{0.7}, \text{La}_{0.3})\text{PO}_4 \cdot 0.7\text{H}_2\text{O}$ rhabdophane nanoparticles. Heat treatment at 950 °C caused the decomposition of rhabdophane into a $(\text{La}_{1-x}\text{Y}_x)\text{PO}_4$ monazite solid solution and YPO_4 xenotime. The solid solubility of Y in LaPO_4 monazite from 1000 °C to 1600 °C was studied using XRD, TEM, and EDX. The implications of the findings for controlling the coefficient of thermal expansion of the prospective two-phase monazite–xenotime fiber coatings for ceramic composites applications were discussed in reference [11].

The composition, lattice parameters, and elastic constants of natural single crystal YPO_4 xenotime from Novo Horizonte (Brazil) were determined using EPMA, XRD, and the pulse-echo technique. The composition indicates a 24% substitution of Y sites with other rare-earth elements. The lattice parameters of the studied crystal deviated only slightly from those reported for synthetic YPO_4 and were in a good agreement with trends obeyed by other orthophosphates with the xenotime structure. The measured elastic constants C11, C33, C44, and C66 were consistent with synthetic crystals when accounting for porosity. C12 and C13 constants were evaluated based on the comparison with other materials with the xenotime structure. The elastic constants could be rationalized using interionic force constants and bond energies [12].

The regular solid solution model has been applied to solid solubility in the monazite–xenotime systems and is verified against the available experimental data for LaPO_4 – YPO_4 and CePO_4 – YPO_4 systems. The model was then used to predict the miscibility gaps in a number of other monazite–xenotime systems. The implications for prospective two-phase monazite–xenotime fiber coatings for applications in ceramic matrix composites (CMCs) were discussed in reference [13].

3.2.3 ZnO Nanowires

Growth habits and defects in epitaxial ZnO nanowires grown from Au catalyst on (00.1) GaN/sapphire substrate using the vapor-liquid-solid (VLS) technique were studied using electron microscopy and x-ray diffraction. The results revealed the presence of both horizontal (crawling-like) and vertical nanowires having similar orientation relationship to the substrate $(00.1)_{\text{ZnO}} \parallel (00.1)_{\text{GaN}}$, $[11.0]_{\text{ZnO}} \parallel [11.0]_{\text{GaN}}$. The crawling-like growth precedes the vertical growth, and the coalescence and overgrowth of the crawling nanowires produce a highly defective layer which separates the substrate and vertical nanorods. Transmission electron microscopy revealed a high density of planar defects in this interfacial layer. A significant density of stacking faults residing on the (0001) planes was also observed in the shorter vertical nanorods. The crawling nanowires are under residual compressive strain, whereas the vertical nanorods grow strain-free [14].

3.2.4 Oxide-Oxide Composites

The desire for increased temperatures and durability in myriad power and processing systems has driven research on oxide-oxide composites. As with all ceramic composites, these materials require a crack deflecting mechanism to prevent brittle failure. Both porous matrices and fiber coating have been shown to perform this function. Composites containing interface coatings are still in the research stage, while porous-matrix materials are production items and are being evaluated in a variety of applications. Although current technology composites offer very attractive properties, significant improvement can be expected in future systems. A review paper was published that reviewed the status of the technology for high-temperature ($>1000^\circ\text{C}$) oxide-oxide composites and prospects for future developments [15].

3.2.5 Camphene Processing of Oxide-Oxide Composites

The potential for producing crack-free oxide matrix composites was demonstrated using a unique combination of freeze drying and a non-shrinking matrix. Freeze-drying eliminated cracks associated with drying shrinkage and cracks induced by sintering shrinkage were minimized by adjusting the matrix composition. These crack-free oxide matrix composites, initially porous, were reinfiltated to improve the composite density and ultimately the composite properties [16].

3.2.6 AFIT Collaboration - Creep Behavior of Porous Matrix Oxide-Oxide Composites

AFRL/RXLN collaborated with AFIT (Dr. Ruggles-Wrenn) to examine the mechanical behavior of porous oxide matrix composites containing coated fibers. In most cases, composite panels were fabricated in-house using conventional aqueous-based processing methods, while the testing was completed by AFIT students. In reference 19, mercury porosimetry measurements were made in-house on a commercial oxide-oxide composite (ATK-COI).

The creep behavior of a $\text{N610/LaPO}_4/\text{Al}_2\text{O}_3$ composite was evaluated in this work. The composite consists of a porous alumina matrix reinforced with Nextel 610 fibers coated with monazite in a symmetric cross-ply $(0^\circ/90^\circ/0^\circ/90^\circ)_s$ orientation. The tensile stress-strain behavior was investigated and the tensile properties measured at room temperature and in the 900–1200

°C range. The addition of monazite coating resulted in ~50% improvement in ultimate tensile strength (UTS) at temperatures ≤ 1100 °C, and in 37% improvement in UTS at 1200 °C. Tensile creep behavior was examined at temperatures in the 900–1100 °C range for creep stresses ranging from 40 to 150 MPa. Primary and secondary creep regimes were observed in creep tests at 900 °C. At temperatures above 900 °C, the composite exhibited primary, secondary and tertiary creep. Minimum creep rate was reached in all tests. Creep rates accelerated with increasing temperature and creep stress. At 900 °C, creep run-out, defined as 100 h at creep stress, was achieved for stress levels ≤ 120 MPa. The residual strength and modulus of all specimens that achieved run-out were characterized. Comparison with results obtained for N610/Al₂O₃ (control) specimens revealed that the use of the monazite coating resulted in improved creep resistance at 900 °C. Creep performance deteriorated rapidly as temperatures increased above 900 °C. Composite microstructure, as well as damage and failure mechanisms were investigated [17].

The compressive creep behavior of a N610/LaPO₄/Al₂O₃ composite was investigated at 900 °C and 1100 °C. The composite consists of a porous alumina matrix reinforced with Nextel 610 fibers coated with monazite in a symmetric cross-ply (0°/90°/0°/90° orientation). The compressive stress–strain behavior was investigated and the compressive properties were measured. Compressive creep behavior was examined for creep stresses in the –50 to –95 MPa range. Minimum creep rate was reached in all tests. At 900 °C, both monazite-containing and control (N610/Al₂O₃) specimens produced creep strains $\leq -0.05\%$. At 1100 °C, compressive creep strains approached –9%, and compressive creep strain rates, -10^{-7} s^{-1} . Creep run-out, defined as 100 h at creep stress, was achieved in all tests. Composite microstructure, damage and failure mechanisms, as well as effects of variation in microstructure on mechanical response were examined. Differences in processing and consequently in the composite microstructure had a significant effect on compressive response of the ceramic–matrix composite (CMC) [18].

The influence of loading rate on monotonic tensile behavior and tensile properties of an oxide–oxide ceramic composite was evaluated in laboratory air at 1200 °C. The composite consists of a porous alumina matrix reinforced with woven mullite/alumina (Nextel 720) fibers, has no interface between the fiber and matrix, and relies on the porous matrix for flaw tolerance. Tensile tests conducted at loading rates of 0.0025 and 25 MPa/s revealed a strong effect of rate on the stress–strain behavior as well as on the ultimate tensile strength (UTS), elastic modulus and failure strain. At 0.0025 MPa/s, increase in stress results in non-monotonic change in strain, with the rate of change of strain reversing its sign at stresses 25 MPa/s. Several samples were subjected to additional heat treatments prior to testing in order to determine whether this unusual stress–strain behavior was an artifact of incomplete processing of fibers in the as-received material. The unusual material response in the 0–30 MPa stress range was further investigated in creep tests conducted with the applied stresses ≤ 26 MPa. Negative creep (i.e. decrease in strain under constant stress) was observed. Porosity measurements indicate that a decrease in matrix porosity and matrix densification may be taking place in the N720/A composite exposed to 1200 °C at stresses < 30 MPa for prolonged periods of time [19].

3.2.7 Dense Matrix Oxide Composites

A quantitative model describing the densification of porous compacts using liquid solutions that take into account the gradual sealing-off of the porosity was proposed. The model was applied to experimental data on densification of alumina compacts and alumina fiber-reinforced ceramic composites infiltrated by an aqueous CrO_3 solution. The results obtained with the present model were in good agreement with those expected based on the statistical models and computer simulations of the packing of spheres. Recommendations to improve the efficiency of the densification of porous materials using precursor solutions were suggested based on the results of the present work and presented in reference [20].

Densification of porous alumina by CrO_3 infiltration was investigated on model composites containing a sapphire interface. Gas–solid deposition of Cr_2O_3 from a CrO_3 source on sapphire and glass at 600 °C was also investigated. The deposited Cr_2O_3 layers were characterized using X-ray diffraction and transmission electron microscopy. It was found that, similar to gas-phase deposition on sapphire, in CrO_3 -infiltrated porous alumina, Cr_2O_3 grows epitaxially on adjacent alumina surfaces, suggesting a gas–solid condensation mechanism. The deposition rate and morphology of the Cr_2O_3 film deposited on alumina depends strongly on the crystallographic orientation [21].

3.3 Summary of Unpublished Work

3.3.1 Mechanism of Oxidation Inhibition of SiC by Monazite and Phosphorus

The goal of this study was to verify the role of Al dopant in SiC on the oxidation inhibition of SiC by monazite and phosphorus. Samples of Al-implanted SiC coated with monazite, treated in phosphoric acid, as well as control samples were oxidized at 1200 °C/2 h in dry air. Cross-section TEM foils were prepared and analyzed. No clear inhibition effect similar to Al-doped SA fibers was observed. However, phosphorus distribution in the oxide scale on Al-implanted SiC was clearly different from that in SA fibers. It appears therefore, that Al-ion implanted SiC may not reproduce the oxidation behavior of the Al-doped SA fibers.

3.3.2 Oxide Composites

3.3.2.1 Nextel 610, 720/ $\text{LaPO}_4/\text{Al}_2\text{O}_3$ composites from ATK COI – Tow Coatings

Nextel 610 and 720 fiber tow, coated with monazite by AFRL and UES, were sent to ATK COI Corporation in early 2005. Filament-wound composites produced with this coated fiber were received in the summer of 2005 and sent for machining (Bomas) into tensile test specimens. During this contract period, the composites were tensile tested by AFRL/RXLN – UDRI. The composites were tested in the as-received condition and after heat treatment at 1200 °C for 10, 100 and 1000 hours (Figure 1). The tensile tests revealed that the Nextel 720-based composites showed no strength degradation after exposure at 1200 °C for up to 100 hours, with only a slight (~5%) strength loss after 1000 hours, along with an ~11% increase in the modulus. The Nextel 610 composites showed ~38% strength decrease after the 1200 °C/1000 h HT, with the majority (~26%) of this decrease occurring within 100 h. This correlates well with previous data obtained

for AFRL-produced composites. Virtually no change in the modulus was observed (less than 2% increase) after the long-term heat treatment. Fiber pull-out was seen in all cases, although the Nextel 720-based composites showed longer pull-out lengths. Deformation of the monazite coating was apparent in both the Nextel 610 and Nextel 720-reinforced composites.

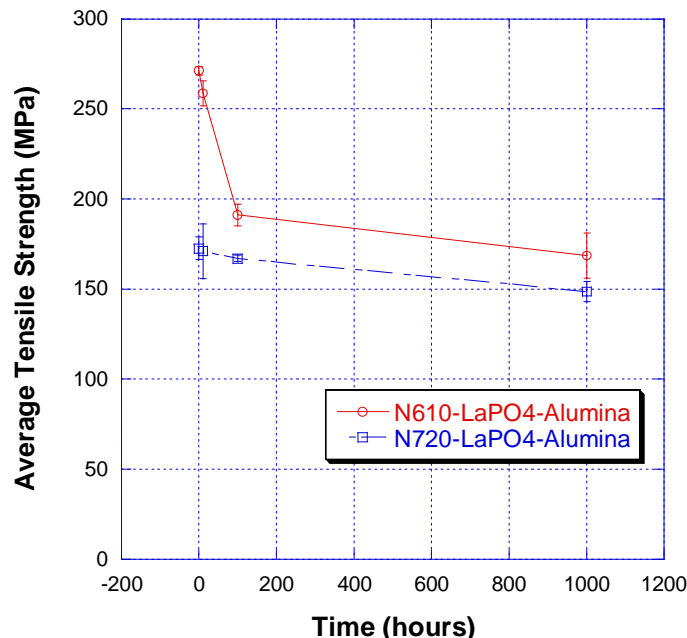


Figure 1. Tensile Test Results for Nextel/LaPO₄/Alumina Composites

Based on the positive mechanical test results (as-received, after exposure at 1200 °C for 10, 100, and 1000 h) further collaborative research was planned with ATK-COIC. Since ATK-COIC's standard CMC processing is based on woven cloth lay-ups, monazite-coated Nextel 720 fibers, coated by UES, were sent to T.E.A.M. Textile Engineering and Manufacturing, Rhode Island to be woven into a 1 ft x 27.5 ft 2D 8HS coated Nextel 720 cloth. The strengths of the as-coated tow, sized tow and tows extracted from the woven cloth were measured and compared to previous measured tow strengths of Nextel 720 (Table 1). The results showed no strength degradation after either sizing or weaving the coated tow. An SEM cross section analysis of the coated cloth showed that the coatings survived the sizing and the weaving process (Figure 2).

The Nextel 720 fiber was coated using the high output fiber coater built at UES, which allows for a more rapid turn-around time for the coatings. Further, monazite-coated fiber is now commercially available through UES, Inc.

Table 1. Tensile Strength of Coated Nextel 720 Fiber

	Tow Strength (MPa)	Filament Strength (GPa)
Uncoated*	804	1.99
Monazite, Coated	838	2.05†
Monazite, Coated and Sized	906	1.97†
Monazite, Coated Sized and Woven	930	1.98†

† Tows were desized at 900 °C for 5 minutes.

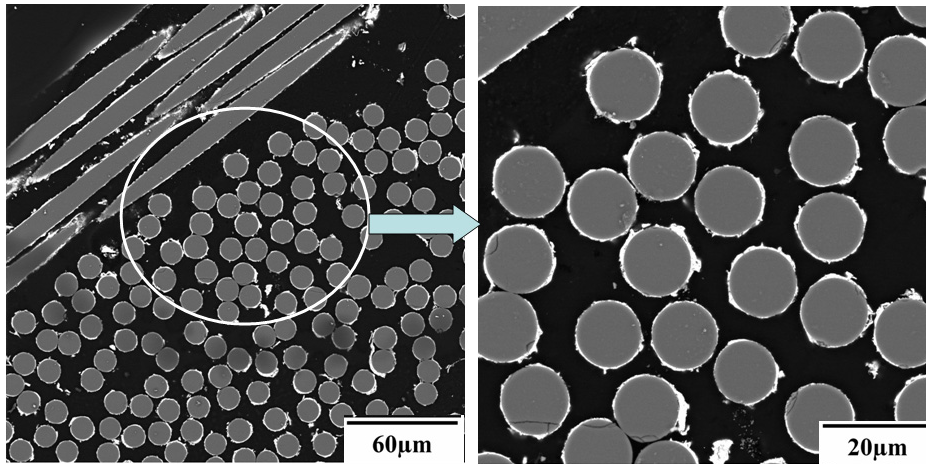


Figure 2. SEM Micrograph of 8HS Coated Woven Nextel 720 Fiber

Control samples containing uncoated fiber were also fabricated for comparison purposes. The first sets of panels were machined by ATK-COI according to their standard test matrix; however, these did not match the specimen dimensions required for the AFRL/RXLN testing. A second series of panels were then fabricated and these panels were received in late 2007. The panels were sent to Bomas Machining for machining into test coupons, including straight-sided tensile bars (100 mm x 10 mm) and 1" diameter ILT (interlaminar tensile) samples.

The samples were tensile tested in the as-received condition and after heat treatment at 1200 °C and 1300 °C for up to 1000 hours in air. The tests were conducted under the direction of Mr. L. P. Zawada of AFRL/RXLN and the results are shown in Figure 3a. The results have been normalized in terms of fiber volume fraction. Both the control samples and the monazite-coated fiber samples showed similar behavior trends, with virtually no change after 100 hours at 1200 °C and a significant change after 100 hours at 1300 °C. An approximate 15% loss was seen after 1000 hours at 1200 °C.

The monazite-containing samples showed a lower initial strength. One possible cause of the lower strength is fiber loss during both the coating and weaving process. To assess this possibility, the coated fabric was mounted, polished and the number of fibers in each tow was

counted manually. A minimum of ten tows were counted using this procedure. The tow should contain 400-420 fibers (manufacturer's data) and the manual counts showed an average value close to 400. This minor loss of fiber would not explain the difference in the composite strength.

Both sample types showed increasing interlaminar strength after heat treatment (Figure 3b) due to matrix strengthening through sintering. The monazite-containing samples showed lower overall interlaminar strengths, presumably due to the weak fiber/matrix interface. A denser matrix would provide improved strengths for these materials; the reinfiltrated composites showed a higher interlaminar strength in the as-received condition.

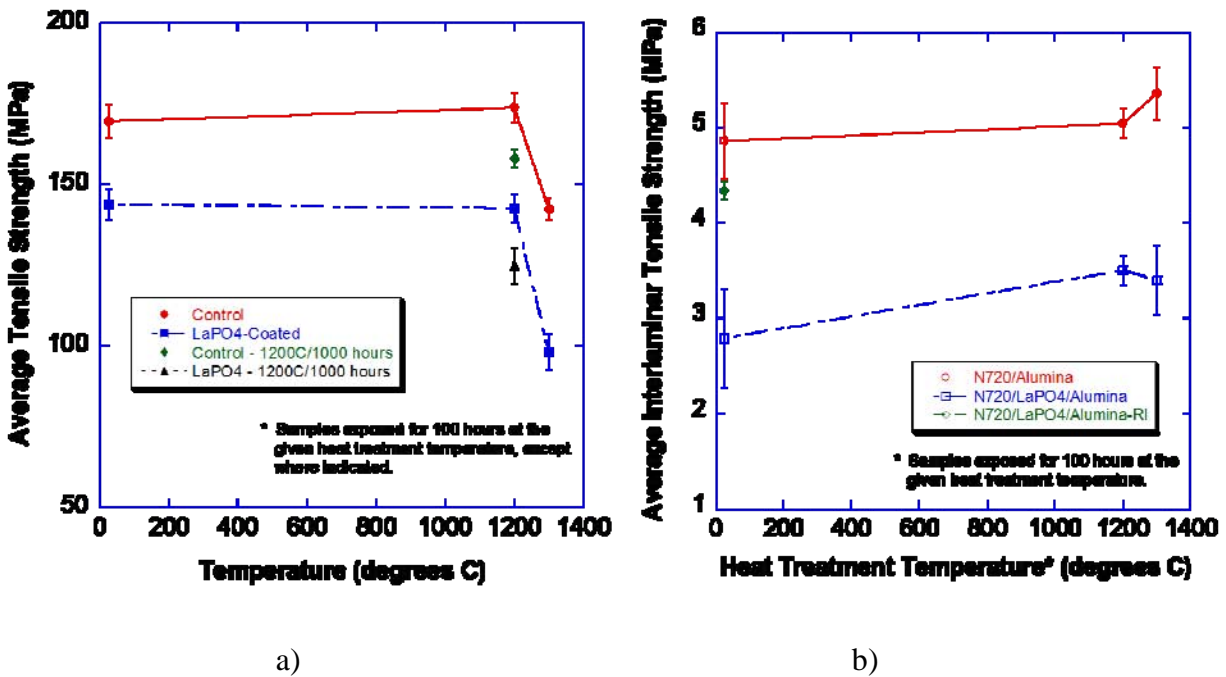


Figure 3. COI-Fabricated Nextel 720/Alumina Composites (Control and Monazite-Coated)
After Exposure at Various Temperatures for 100 hours in Air
a) Average Tensile Strengths
b) Average Interlaminar Tensile Strengths

3.3.2.2 Long Term Heat Treatment of Nextel 610/LaPO₄/Al₂O₃ Composites

Nextel 610/LaPO₄/Al₂O₃ composites were fabricated in-house during the winter of 2005 for long-term exposure at 1200 °C in air. These samples were [0°/90°]_s in orientation, with fiber volume fractions between 30-34%. The composites were water-jet machined into dog-bone specimens prior to heat treatment. Heat treatment times were 50, 100, 250, 500, 1000, 2500, 5000 and 10,000 hours. Control samples, with no fiber coatings, were also produced, but only exposed through 250 hours. Tensile tests have been completed for the samples exposed up to 5000 hours (Figure 4). There was some scatter in the results due in part to misalignment during machining, which resulted in some samples being slightly off-axis ($\pm 5^\circ$). The general trend

showed a strength reduction of ~50% for the monazite-containing samples after 5000 hours at 1200 °C; however, control samples were degraded after exposure for only 5 hours at 1200 °C.

SEM analysis of the Nextel 610/LaPO₄/Al₂O₃ composite heat treated for 5000 hours revealed extensive grain growth in the fiber (Figure 5b), which subsequently led to fiber strength loss. The monazite coating did remain intact on the fiber and crack deflection was observed in the composite (Figure 5a). Although the 10,000 hour heat treatment was completed, these samples were not tested, due to the low strength and grain growth in the fiber observed for the 5000 h samples.

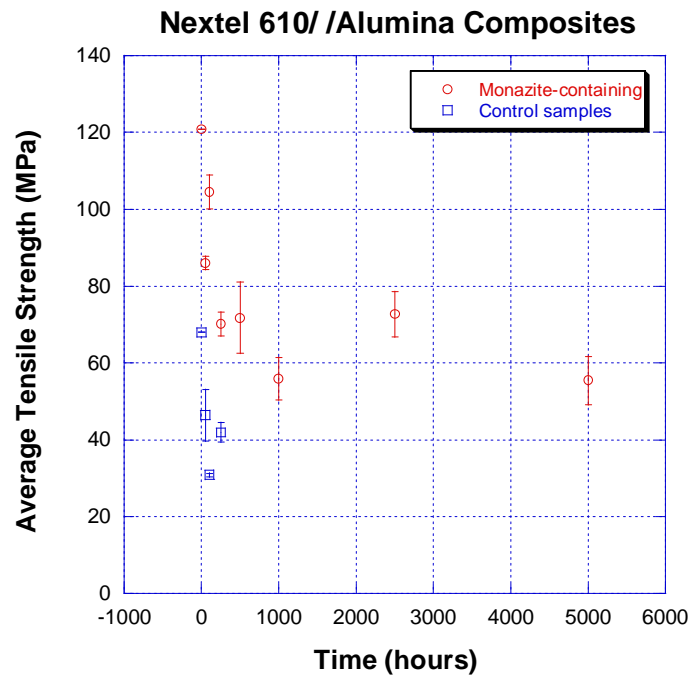


Figure 4. Strength Values for Nextel 610/LaPO₄/Alumina Composites as a Function of Heat Treatment Time at 1200 °C

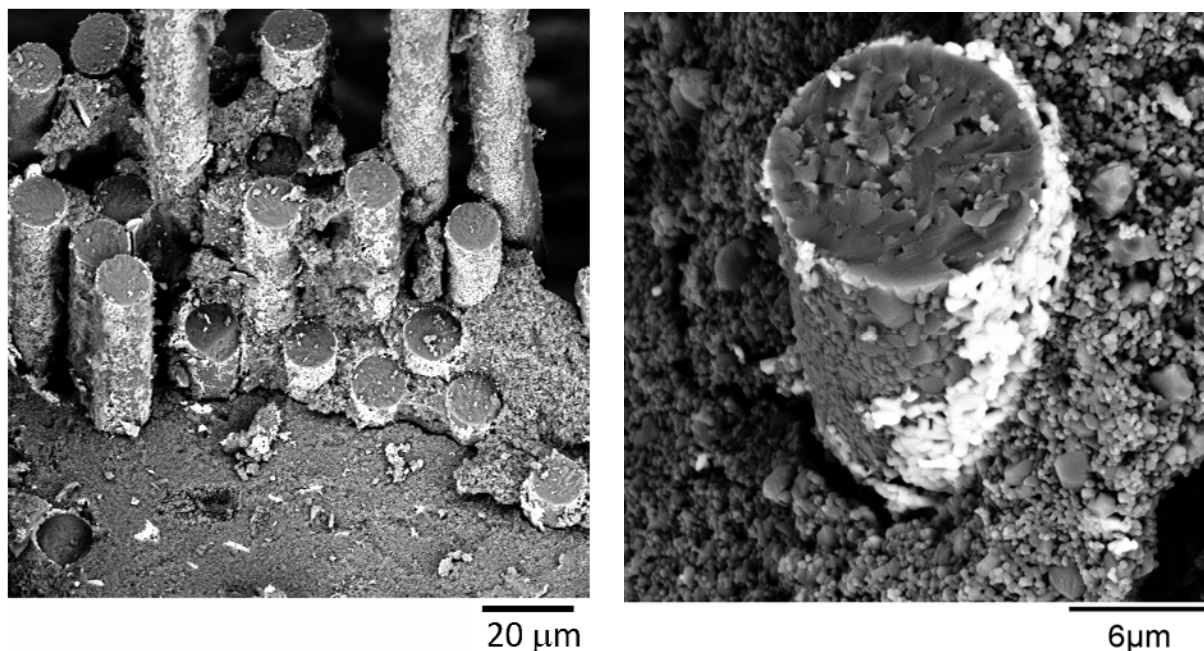
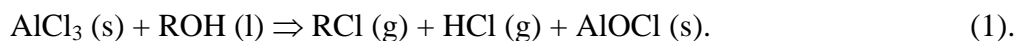


Figure 5. SEM Micrographs of Nextel 610/LaPO₄/Alumina Composite after 5000 h HT
 (a) Lower Magnification View Showing Crack Deflection
 (b) High Magnification View of Fiber Surface/Monazite Coating (Bright Phase)

3.3.2.3 Nextel 610/LaPO₄/Alumina-YAG Composites – Cloth Coating

The camphene processing method was used to fabricate Nextel 610/Alumina-YAG (25:75) composites containing Nextel 610 fabrics monazite-coated using varying processing steps. Dr. G. Fair of AFRL/RXLN coated large sections of Nextel fabric for use in these composites. Four (7" x 4") composites were fabricated; each composite contained a different fiber coating: 1) uncoated, 2) LaPO₄ (5 x SNDS), 3) LaPO₄ (5 x phytic acid) and 4) LaPO₄ (3 x phytic acid, 2 x SNDS). The LaPO₄ coatings were fabricated using the "saturate and dunk (SNDS)" method, which provides a porous coating, with the "phytic acid" method, which provides a more hermetic coating or with a combination of the two. A more hermetic coating is likely needed to protect the fiber during composite processing.

The as-processed composites were porous (~58-66% theoretical density) and were reinfiltrated with an AlOCl/acetonitrile solution. Aluminum oxychloride (AlOCl) was fabricated by mixing anhydrous AlCl₃ and anhydrous methanol (both Alfa-Aesar, Ward Hill, MA) as the starting materials, utilizing the following equation:



The mixture was heated slowly until the reaction went to completion, yielding AlOCl. After reaction, the solid AlOCl was dissolved into acetonitrile (anhydrous, Alfa-Aesar, Ward Hill, MA) to form a 35 wt.% AlOCl solution.

The four composite panels were reinfiltrated twelve times with the AlOCl/acetonitrile solution. DTA/TGA analysis of the dried AlOCl material was run for guidance on the heat treatment of the infiltrated panels. The panels soaked in the solution for 2-3 h with each infiltration cycle. The panels were dried in air for 30 minutes and then in an oven (~100 °C) for 30 minutes prior to HT at 1 °C/min to 600 °C/1 h, then 5 °C/min to 1100 °C/1 h. After the 12th infiltration, the sample was heated to 1200 °C/1 h. The composite densities increased over 12% overall, with the final densities ranging from ~71-79% of theoretical.

The composites were machined into 10 mm x 100 mm straight-sided tensile samples and 1" diameter ILT (interlaminar tension) samples by Bomas Machine Specialties Inc. (Somerville, MA). Testing of the composites was conducted by Mr. L. P. Zawada (AFRL/RXLN). Tensile testing revealed extremely low tensile strengths for all four sample types. Two ILT tests (1 control sample and 1 phytic acid sample) were also conducted and they showed similarly low strengths. It is presumed that the strength loss is due to stress corrosion of the fiber from the corrosive chlorine-containing species; however, this has yet to be confirmed.

Causes for the extreme strength loss were investigated; however, no conclusions were drawn. One obvious difference shown in the fracture surfaces is the etching of the fiber surface. Dr. G. Fair of AFRL/RXLN continued the SEM microstructural evaluation of these composites.

3.3.2.4 Camphene Processing with 3D Fiber Preforms

The camphene process was expanded to use with 3-D fiber preforms (Nextel 440 fiber) that were fabricated in the early 1990's. The goal of this work was to produce a denser, crack-free matrix in a 3-D fiber architecture and it builds on our previous experience in using freeze-drying (aqueous-based) to produce a 3-D composite [22]. In the earlier work, the results were not sufficiently promising to continue the effort, due in part to the use of an aqueous system.

An 80-20 (by volume) mullite-alumina system was chosen as the matrix and a solids loading of 25 vol.% was used initially. The powder was dispersed in camphene and Hypermer (dispersant) using warm ball-milling overnight. The fiber sample was placed in a pressure infiltration unit, using an exterior band heater and heat lamps to warm the unit to ~50-55 °C. After reasonable stabilization of the temperature, the warm slurry was poured into the unit and pressure was applied (maximum pressure ~60 psi). No vacuum was used to avoid premature sublimation of the camphene. The matrix slurry filtered through the sample and the filtration was stopped after approximately 20 minutes. After sublimation in air for several days, the sample was heat treated at 1150 °C/2 h. A lower temperature was chosen, due to the temperature limitations of the N440 fiber.

This first sample showed multiple matrix cracking (Figure 6a), as typically seen in oxide matrix composites. A second trial was initiated using a slurry with a lower solids loading (~20 vol.%). In this case, the composite exhibited pores that were remnant of the camphene solidification (Figure 6b). In both cases, however, infiltration within the tow was not optimal. Further work in this area will focus on improving the tow infiltration and correlating the amount of camphene removal with the microstructural features.

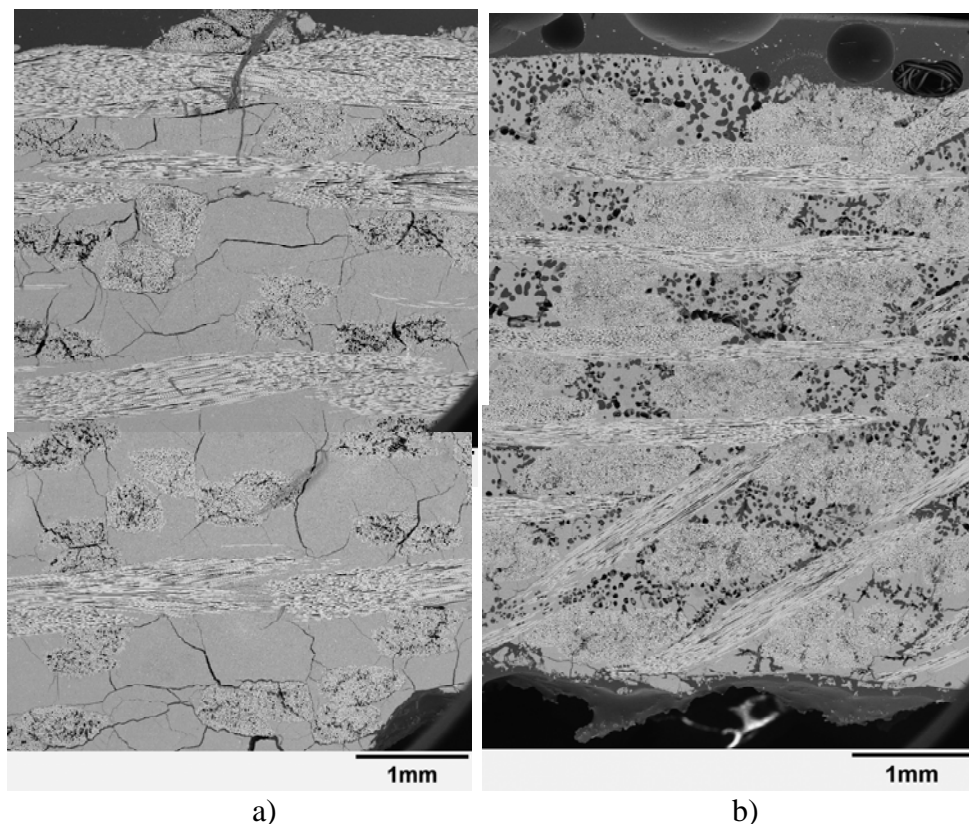


Figure 6. Microstructures of Freeze-Dried (Camphene Process) 3-D Composites (Nextel 440/Mullite-Alumina)
a) Trial #1, 25 vol.% Solids Loading
b) Trial #2, 20 vol.% Solids Loading

3.3.2.5 The Effect of Precursor Morphology on Densification of Monazite Fiber Coatings for Ceramic Composites

Hermetic monazite coatings are desirable to prevent fiber degradation in oxide-oxide composites. Rhabdophane precursor sols that produce two distinctively different monazite particle morphologies, one rod-shape and one with spherical particles, were developed. Our research has shown that coatings produced with the rod-shaped precursor suffer from spheroidization, while spherical coatings based on the spherical precursor suffer from shrink cracking. Thus, coatings based on the rod-shaped precursor require a minimum thickness of 500-600 nm, below which spheroidization occurs. In contrast, coatings based on the spherical precursor do not spheroidize above a thickness of 100 nm, but suffer from shrink cracking above ~400 nm thickness. A composite coating precursor consisting of 80% spherical precursor and 20% rod-shape precursor was determined to have a processing window of 200-1500 nm coating thickness, which can be sintered to hermeticity without spheroidization or cracking (Figure 7). Appropriate coating technology has been developed in model experiments and transitioned to continuous fiber coating.

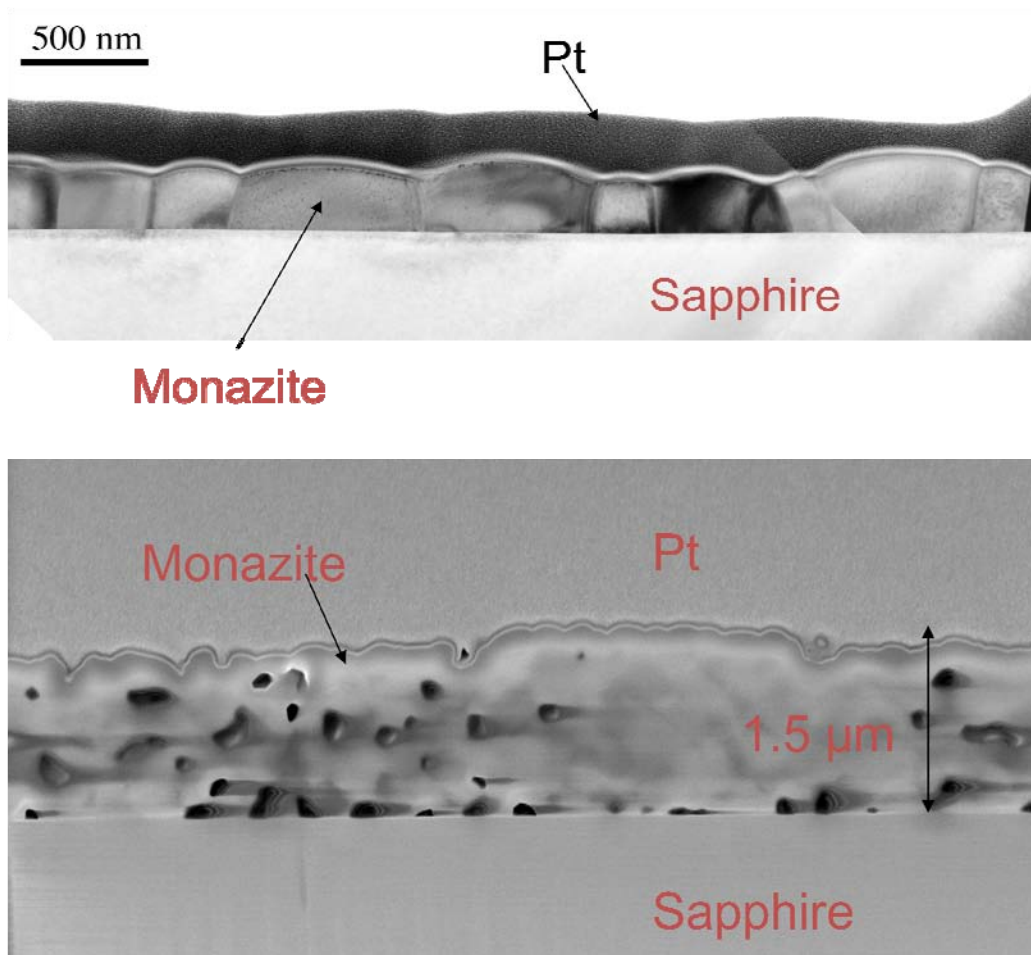


Figure 7. Microstructure of Thin (<200 nm, TEM) and Thick (~1500 nm, SEM) Monazite Coatings Derived from Mixed 80% spherical – 20% Rod-Shaped Precursor on Sapphire

3.4 Collaborative Interactions with Outside Agencies

Most of the interactions with other DoD agencies were based on the SPS unit that was purchased and installed during this contract period. At the time of installation, this unit was one of only two known units in the country. Researchers from NASA-Ames, NRL, Oregon State and Missouri Science and Technology University came to AFRL/RXLN to utilize the equipment. Highlights of selected interactions are given in the following sections.

3.4.1 NRL

Researchers from the Navy Research Laboratory (NRL), Dr. G. Villalobos and Dr. J. Sanghera, traveled to AFRL/RXLN to use the SPS unit in September 2007. Their goal was to produce transparent oxide material using the SPS unit. Three trials of ytterbium-doped yttria powder

were run using a small (20 mm diameter) graphite die, which was chosen based upon the amount of material available. The three samples were not completely successful in that transparent materials were not attained; however, the ease and efficiency of the unit was impressive to the visitors. One major issue for NRL was the minimum load of 5 kN that is needed in the unit, which translates to a significant pressure for the small die (~2500 psi for a 20 mm diameter die). NRL sent more powder to AFRL/RXLN for trial using the larger, 40 mm diameter die where the 5 kN minimum load translates to only 500 psi. This powder was pressed using the SPS; however, the sample did crack into three pieces upon removal from the die.

Dr. G. Villalobos also supplied fine SiC powder, produced at NRL, for SPS consolidation. The powder was anticipated to yield a translucent/transparent SiC material through the SPS process. Several differing powder batches were received and densified using literature-inspired processing cycles. The first round of SiC samples were not especially dense (between 80-90% dense) and these were sent back to NRL for analysis. NRL subsequently sent these samples for hot isostatic pressing (HIPping) in hopes of attaining 100% density. The samples did not achieve transparency; however, the results were promising enough to continue the program.

Another batch of SiC powder was sent from NRL and consolidated using SPS technology. Table 2 shows both the processing program used and the density of the samples obtained after SPS processing. Program A had a maximum temperature of 2000 °C, with a 27 minute hold time and a force of 20 kN, while Program B utilized a lower maximum temperature of 1850 °C and a slightly higher maximum force (23.6 kN). Overall, the samples were still somewhat porous. These samples were sent to NRL for analysis. It is anticipated that the collaboration between AFRL/RXLN and NRL will continue on this topic.

Table 2. Results for SPS Processing of NRL-Supplied SiC Powder

Powder	Program	Density*
SiC45A	A	Very porous
SiC45B	A	2.97 g/cm ³
SiC45B1700	A	1.29 g/cm ³ **
SiC45A	B	2.97 g/cm ³
SiC45B	B	2.51 g/cm ³
SiC45B1700	B	2.92 g/cm ³

3.4.2 AFRL/RXQL (Tyndall AFB)

Researchers at AFRL/RXQL sent a reasonably large number of geopolymer-based samples for XRD analysis (>40). The initial samples were analyzed and the results sent to RXQL. Previous discussions between RXLN and RXQL have indicated that there is the potential for a more

formal collaboration between the groups, based upon RXLN's current effort in geopolymers (Task 0005).

3.4.3 ATK/COI

A series of SiC-based composites (6 types) displaying varying mechanical properties were subjected to mercury porosimetry analysis to examine possible microstructural variations between samples. The results were compiled and transferred to Dr. P. Jero (AFRL/RXLN), who then sent them to ATK/COI for comparison with previous work. Although the results showed some slight variations between the samples, there was no dramatic difference that could be immediately connected with the mechanical property variation.

3.5 Publications

1. E. E. Boakye, and P. Mogilevsky and R. S. Hay, "Synthesis of Nanosized Spherical Rhabdophane Particles," *J. Am. Ceram. Soc.*, **88** [10] 2740–2746 (2005).
2. R. S. Hay, E. E. Boakye and P. Mogilevsky, "Spherical Rhabdophane Sols. I: Rheology and Particle Morphology," *J. Am. Ceram. Soc.*, **90** [5] 1574–1579 (2007).
3. E. E. Boakye, P. Mogilevsky, R. S. Hay and G. E. Fair, "Synthesis and Phase Composition of Lanthanide Phosphate Nanoparticles LnPO_4 ($\text{Ln}=\text{La, Gd, Tb, Dy, Y}$) and Solid Solutions for Fiber Coatings," *J. Am. Ceram. Soc.*, **91** [12] 3841–3849 (2008).
4. E. E. Boakye, R. S. Hay and P. Mogilevsky, "Spherical Rhabdophane Sols. II: Fiber Coating," *J. Am. Ceram. Soc.*, **90** [5] 1580–1588 (2007).
5. G. E. Fair, R. S. Hay and E. E. Boakye, "Precipitation Coating of Monazite on Woven Ceramic Fibers: II. Effect of Processing Conditions on Coating Morphology and Strength Retention of NextelTM 610 and 720 Fibers," *J. Am. Ceram. Soc.*, **91** [5] 1508–1516 (2008).
6. E. E. Boakye, R. S. Hay, P. Mogilevsky, and M. K. Cinibulk, "Two Phase Monazite/Xenotime $30\text{LaPO}_4\text{--}70\text{YPO}_4$ Coating of Ceramic Fiber Tows," *J. Am. Ceram. Soc.*, **91** [1] 17–25 (2008).
7. G. E. Fair, R. S. Hay and E. E. Boakye, "Precipitation Coating of Monazite on Woven Ceramic Fibers: I. Feasibility," *J. Am. Ceram. Soc.*, **90** [2] 448–455 (2007).
8. G. E. Fair, R. S. Hay and E. E. Boakye, "Precipitation Coating of Rare-Earth Orthophosphates on Woven Ceramic Fibers—Effect of Rare-Earth Cation on Coating Morphology and Coated Fiber Strength," *J. Am. Ceram. Soc.*, **91** [7] 2117–2123 (2008).
9. E. E. Boakye, P. Mogilevsky, T. A. Parthasarathy, R. S. Hay, J. Welter, and R. J. Kerans, "Monazite Coatings on SiC Fibers I: Fiber Strength and Thermal Stability," *J. Am. Ceram. Soc.*, **89** [11] 3475–3480 (2006).
10. P. Mogilevsky, E. E. Boakye, R. S. Hay, J. Welter, and R. J. Kerans, "Monazite Coatings on SiC Fibers II: Oxidation Protection," *J. Am. Ceram. Soc.*, **89** [11] 3481–3490 (2006).
11. P. Mogilevsky and E. E. Boakye, "Solid Solubility and Thermal Expansion in a $\text{LaPO}_4\text{--YPO}_4$ System," *J. Am. Ceram. Soc.*, **90** [6] 1899–1907 (2007).
12. P. Mogilevsky, E. B. Zaretsky, T. A. Parthasarathy and F. Meisenkothen, "Composition, lattice parameters, and room temperature elastic constants of natural single crystal xenotime from Novo Horizonte," *Phys. Chem. Minerals*, **33**:691–698 (2006).

13. P. Mogilevsky, "On the miscibility gap in monazite–xenotime systems," *Phys. Chem. Minerals*, **34**:201–214 (2007).
14. Levin, A. Davydov, B. Nikoobakht, N. Sanford and P. Mogilevsky, "Growth habits and defects in ZnO nanowires grown on GaN/sapphire substrates," *Appl. Phys. Lett.*, **87** 103110 (2005).
15. K. A. Keller, G. Jefferson and R. J. Kerans, "Progress in Oxide Composites," *Ann. Chim. Sci. Mat.*, **30** [6] 547-563 (2005).
16. T. Mah, K. A. Keller, M. K. Cinibulk and R. J. Kerans, "Towards Crack-Free Oxide-Oxide CMC Development," in Proc. of Sixth International Conference on High Temperature Ceramic Matrix Composites (HTCMC-6), New Dehli, India, 2007.
17. M. B. Ruggles-Wrenn, S. S. Musil, S. Mall, and K. A. Keller, "Creep Behavior of Nextel™610/Monazite/Alumina Composite at Elevated Temperatures," *Comp. Sci. and Tech.*, **66** 2089–2099 (2006).
18. M. B. Ruggles-Wrenn, A. T. Radzicki, S. S. Baek, and K. A. Keller, "Effect of loading rate on the monotonic tensile behavior and tensile strength of an oxide–oxide ceramic composite at 1200 °C," *Mater. Sci. & Eng.*, **A492** 88–94 (2008).
19. P. R. Jackson, M. B. Ruggles-Wrenn, S. S. Baek, and K. A. Keller, "Compressive creep behavior of an oxide–oxide ceramic composite with monazite fiber coating at elevated temperatures," *Mater. Sci. & Eng.*, **A454–455** 590–601 (2007).
20. P. Mogilevsky, R. J. Kerans, H. D. Lee, K. A. Keller, and T. A. Parthasarathy, "On Densification of Porous Materials Using Precursor Solutions," *J. Am. Ceram. Soc.*, **90** [10] 3073–3084 (2007).
21. P. Mogilevsky and H. D. Lee, "On the Mechanism of Densification of Porous Alumina by Infiltration with an Aqueous Solution of Chromium Oxide," *J. Am. Ceram. Soc.*, **91** [2] 675–678 (2008).
22. E. H. Moore, T. Mah and K. A. Keller, "3D Composite Fabrication Through Matrix Slurry Pressure Infiltration," *Ceram. Eng. Sci. Proc.*, **15** (4) 113-120 (1994).

3.6 Presentations

3.6.1 Invited Presentations

1. E. E. Boakye, P. Mogilevsky, R. S. Hay and M. K. Cinibulk "Monazite Fiber Coatings for Oxide Composites," presented at the 6th Pacific Rim Conference on Ceramic and Glass Technology, Maui, HI (2005).
2. T. Mah, et al., "Towards Crack-Free Oxide-Oxide CMC Development," presented at the Sixth International Conference on High Temperature Ceramic Matrix Composites (HTCMC-6), New Dehli, India (2007).
3. Hay, R. S., P. Mogilevsky, et al., "Deformation Twinning and Transformation Plasticity in Rare Earth Orthophosphates," presented at TMS 2008, 137th Annual Meeting and Exposition, New Orleans, LA (2008).

3.6.2 Presentations

1. E. E. Boakye and P. Mogilevsky, "Yttrium-Lanthanum Phosphate Fiber Coatings," presented at the 29th Annual Conference on Composites, Materials and Structures (US. Only/ITAR-Restricted Sessions), Cape Canaveral/Cocoa Beach, FL, January 24-27, 2005.
2. P. Mogilevsky and E. E. Boakye, "Phase Equilibrium and CTE in the Monazite-Xenotime System", presented at the 29th Annual Conference on Composites, Materials and Structures (US. Only/ITAR-Restricted Sessions), Cape Canaveral/Cocoa Beach, FL, January 24-27, 2005.
3. P. Mogilevsky and E. E. Boakye, "The Effect of the Precursor Morphology on Densification of Monazite Fiber Coatings for Ceramic Composites," presented at the 29th Annual Conference on Composites, Materials and Structures (US. Only/ITAR-Restricted Sessions), Cape Canaveral/Cocoa Beach, FL, January 24-27, 2005.
4. G. Fair and E. E. Boakye, "Precipitation of Coating of Monazite on Ceramic Fiber Cloths and Tows", presented at the 29th Annual Conference on Composites, Materials and Structures (US. Only/ITAR-Restricted Sessions), Cape Canaveral/Cocoa Beach, FL, January 24-27, 2005.
5. H. Lee, E. E. Boakye, P. Mogilevsky and T. Mah, "La-Monazite Coating of Nextel 610 Cloth Via Hydrothermal Process," presented at the 29th Annual Conference on Composites, Materials and Structures (US. Only/ITAR-Restricted Sessions), Cape Canaveral/Cocoa Beach, FL, January 24-27, 2005.
6. K. Keller, T. Mah, E. E. Boakye, T. Parthasarathy, P. Mogilevsky and G. Fair, "Development of Oxide-Oxide Composites Containing Controlled Interfaces," presented at the 29th Annual Conference on Composites, Materials and Structures (US. Only/ITAR-Restricted Sessions), Cape Canaveral/Cocoa Beach, FL, January 24-27, 2005.
7. E. E. Boakye and P. Mogilevsky, R. S. Hay, M. Cinibulk, "Yttrium Lanthanum Phosphate Fiber Coatings on Nextel 720," presented at the 31th Annual Conference on Composites, Materials and Structures (US. Only/ITAR-Restricted Sessions), Cape Canaveral/Cocoa Beach, FL, January 2007.
8. E.E. Boakye, P. Mogilevsky, M.K. Cinibulk and R.S. Hay, "Oxide Fiber Coatings for SiC/SiC Composites," presented at the 34th International Cocoa Beach Conference & Exposition on Advanced Ceramics & Composites, Daytona Beach, FL, January 24-29, (2010).
9. T. Mah, K. Keller, et al., "Crack-free Oxide-Oxide CMC Development. Presented at the 30th Annual Conference on Composites, Materials and Structures (US. Only/ITAR-Restricted Sessions) Cape Canaveral/Cocoa Beach, FL, January 2006.
10. R. S. Hay, E. E. Boakye, et al., "Progress in Fiber Coating Characterization," presented at the 30th Annual Meeting on Advanced Ceramics and Composites, Cape Canaveral/Cocoa Beach, FL, January 2006.
11. M. K. Cinibulk, G. E. Fair, et al., "Viability of Monazite Fiber Coatings for SiC-Based Composites," presented at the 30th Annual Conference on Composites, Materials and Structures (US. Only/ITAR-Restricted Sessions), Cape Canaveral/Cocoa Beach, FL, January 2006.
12. E. B. Zaretsky and P. Mogilevsky "Mechanisms of plastic deformation and shock-induced phase transformation in natural and synthetic single crystal scheelite," presented

at the 44th European High Pressure Research Group International Conference, Prague, 2006.

13. E. Boakye P. Mogilevsky, R. S. Hay and M. Cinibulk, "Grain Growth Kinetics of Monazite/Xenotime Mixtures on Nextel 720," presented at 31st International Cocoa Beach Conference & Exposition on Advanced Ceramics and Composites, Daytona Beach, FL, January 22-26, 2007.
14. T. Mah, K. Keller, M. Cinibulk, and R. J. Kerans, "Crack-Free Oxide-Oxide CMC Development," presented at the 31st Annual International Cocoa Beach Conference on Advanced Ceramics and Composites, Daytona Beach, FL, January 22-26, 2007.
15. E.B. Zaretsky and P. Mogilevsky, "Dynamic response of natural and synthetic scheelite single crystals," presented at the TMS-2007 Annual Meeting, Orlando, FL, February 25 – March 1, 2007.
16. E. Boakye, R. S. Hay, P. Mogilevsky, and G. E. Fair "Synthesis and Phase Composition of Lanthanide Orthophosphate Particles and Solid Solutions," presented at 32nd International Cocoa Beach Conference & Exposition on Advanced Ceramics and Composites, Daytona Beach, FL, January 27-February 1, 2008.
17. G. Fair, R. S. Hay, T.A. Parthasarathy, E. Boakye and K. Keller, "Effect of rare-Earth Cation on Sliding Stress of RePO_4 – Coated Sapphire Fibers in Dense Matrix Composites," presented at 32nd International Cocoa Beach Conference & Exposition on Advanced Ceramics and Composites, Daytona Beach, FL, January 27-February 1, 2008.
18. G. Fair R. S. Hay and E. Boakye, "Precipitation Coating of Monazite on Woven Ceramic Fibers: Effect of Processing Conditions on Strength Retention in Oxide Fibers," presented at 32nd International Cocoa Beach Conference & Exposition on Advanced Ceramics and Composites, Daytona Beach, FL, January 27-February 1, 2008.
19. E. Boakye P. Mogilevsky, R. S. Hay and G. E. Fair "Precipitation of $(\text{Gd,Dy})\text{PO}_4$ Solid Solutions and Coatings on Sapphire Fibers," presented at 33rd International Cocoa Beach Conference & Exposition on Advanced Ceramics and Composites, Daytona Beach, FL, January 18-23, 2009.
20. R. S. Hay, G. E. Fair, E. E. Boakye P. Mogilevsky and T. A. Parthasarathy, "Softening of Rare Earth Orthophosphates by Transformation Plasticity: Possible Applications to Fiber-Matrix Interphases in Ceramic Composites, presented at 33rd International Cocoa Beach Conference & Exposition on Advanced Ceramics and Composites, Daytona Beach, FL, January 18-23, 2009.

3.7 Invention Disclosures/Patents

1. E. E. Boakye, P. Mogilevsky, and R. S. Hay, "A Process of Densifying Monazite Film on Sapphire Plate and NextelTM 720 Fiber," U.S. Disclosure and Record of Invention (2004).
2. T. A. Parthasarathy, K. Keller, T. Mah, and G. Fair, "Oxide Composites for Brake Friction Materials," U.S. Disclosure and Record of Invention (Jan, 2005).
3. T. Mah, K. Keller, and M.K. Cinibulk, "Method of Making Crack-Free Oxide Ceramic Matrix Composites," U.S. Disclosure and Record of Invention (August, 2009).

3.8 Book Chapters

1. G. Jefferson, K. Keller, R. S. Hay and R. J. Kerans, "Oxide-Oxide Composites with Fiber

Coatings,” pp. 187-204 in Ceramic Matrix Composites. Edited by Prof. Dr.-Ing. Walter Krenkel, Wiley-VCH Verlag GmbH & Co. KGaA, 2008.

3.9 Awards

1. Dr. T. A. Parthasarathy was elected as a Fellow of the American Ceramic Society, 2009.
2. Dr. T. A. Parthasarathy is an Associate Editor for the Journal of the American Ceramic Society.
3. Dr. T. A. Parthasarathy is listed in the Essential Science Indicator, which lists the top 1% of scientists in material science, based on citations of published work over a 10 year period.

3.10 References

1. E. E. Boakye, and P. Mogilevsky and R. S. Hay, “Synthesis of Nanosized Spherical Rhabdophane Particles,” *J. Am. Ceram. Soc.*, **88** [10] 2740–2746 (2005).
2. R. S. Hay, E. E. Boakye and P. Mogilevsky, “Spherical Rhabdophane Sols. I: Rheology and Particle Morphology,” *J. Am. Ceram. Soc.*, **90** [5] 1574–1579 (2007).
3. E. E. Boakye, P. Mogilevsky, R. S. Hay and G. E. Fair, “Synthesis and Phase Composition of Lanthanide Phosphate Nanoparticles LnPO_4 ($\text{Ln}=\text{La, Gd, Tb, Dy, Y}$) and Solid Solutions for Fiber Coatings,” *J. Am. Ceram. Soc.*, **91** [12] 3841–3849 (2008).
4. E. E. Boakye, R. S. Hay and P. Mogilevsky, “Spherical Rhabdophane Sols. II: Fiber Coating,” *J. Am. Ceram. Soc.*, **90** [5] 1580–1588 (2007).
5. G. E. Fair, R. S. Hay and E. E. Boakye, “Precipitation Coating of Monazite on Woven Ceramic Fibers: II. Effect of Processing Conditions on Coating Morphology and Strength Retention of Nextel 610 and 720 Fibers,” *J. Am. Ceram. Soc.*, **91** [5] 1508–1516 (2008).
6. E. E. Boakye, R. S. Hay, P. Mogilevsky, and M. K. Cinibulk, “Two Phase Monazite/Xenotime $30\text{LaPO}_4\text{--}70\text{YPO}_4$ Coating of Ceramic Fiber Tows,” *J. Am. Ceram. Soc.*, **91** [1] 17–25 (2008).
7. G. E. Fair, R. S. Hay and E. E. Boakye, “Precipitation Coating of Monazite on Woven Ceramic Fibers: I. Feasibility,” *J. Am. Ceram. Soc.*, **90** [2] 448–455 (2007).
8. G. E. Fair, R. S. Hay and E. E. Boakye, “Precipitation Coating of Rare-Earth Orthophosphates on Woven Ceramic Fibers—Effect of Rare-Earth Cation on Coating Morphology and Coated Fiber Strength,” *J. Am. Ceram. Soc.*, **91** [7] 2117–2123 (2008).
9. E. E. Boakye, P. Mogilevsky, T. A. Parthasarathy, R. S. Hay, J. Welter, and R. J. Kerans, “Monazite Coatings on SiC Fibers I: Fiber Strength and Thermal Stability,” *J. Am. Ceram. Soc.*, **89** [11] 3475–3480 (2006).
10. P. Mogilevsky, E. E. Boakye, R. S. Hay, J. Welter, and R. J. Kerans, “Monazite Coatings on SiC Fibers II: Oxidation Protection,” *J. Am. Ceram. Soc.*, **89** [11] 3481–3490 (2006).
11. P. Mogilevsky and E. E. Boakye, “Solid Solubility and Thermal Expansion in a $\text{LaPO}_4\text{--YPO}_4$ System,” *J. Am. Ceram. Soc.*, **90** [6] 1899–1907 (2007).
12. P. Mogilevsky, E. B. Zaretsky, T. A. Parthasarathy and F. Meisenkothen, “Composition, lattice parameters, and room temperature elastic constants of natural single crystal xenotime from Novo Horizonte,” *Phys. Chem. Minerals*, **33**:691–698 (2006).
13. P. Mogilevsky, “On the miscibility gap in monazite–xenotime systems,” *Phys. Chem. Minerals*, **34**:201–214 (2007).

14. Levin, A. Davydov, B. Nikoobakht, N. Sanford and P. Mogilevsky, "Growth habits and defects in ZnO nanowires grown on GaN/sapphire substrates," *Appl. Phys. Lett.*, **87** 103110 (2005).
15. K. A. Keller, G. Jefferson and R. J. Kerans, "Progress in Oxide Composites," *Ann. Chim. Sci. Mat.*, **30** [6] 547-563 (2005).
16. T. Mah, K. A. Keller, M. K. Cinibulk and R. J. Kerans, "Towards Crack-Free Oxide-Oxide CMC Development," in Proc. of Sixth International Conference on High Temperature Ceramic Matrix Composites (HTCMC-6), New Dehli, India, 2007.
17. M. B. Ruggles-Wrenn, S. S. Musil, S. Mall, and K. A. Keller, "Creep Behavior of NextelTM610/Monazite/Alumina Composite at Elevated Temperatures," *Comp. Sci. and Tech.*, **66** 2089–2099 (2006).
18. M. B. Ruggles-Wrenn, A. T. Radzicki, S. S. Baek, and K. A. Keller, "Effect of loading rate on the monotonic tensile behavior and tensile strength of an oxide–oxide ceramic composite at 1200°C," *Mater. Sci. and Eng.*, **A492** 88–94 (2008).
19. P. R. Jackson, M. B. Ruggles-Wrenn, S. S. Baek, and K. A. Keller, "Compressive creep behavior of an oxide–oxide ceramic composite with monazite fiber coating at elevated temperatures," *Mater. Sci. and Eng.*, **A454–455** 590–601 (2007).
20. P. Mogilevsky, R. J. Kerans, H. D. Lee, K. A. Keller, and T. A. Parthasarathy, "On Densification of Porous Materials Using Precursor Solutions," *J. Am. Ceram. Soc.*, **90** [10] 3073–3084 (2007).
21. P. Mogilevsky and H. D. Lee, "On the Mechanism of Densification of Porous Alumina by Infiltration with an Aqueous Solution of Chromium Oxide," *J. Am. Ceram. Soc.*, **91** [2] 675–678 (2008).
22. E. H. Moore, T. Mah and K. A. Keller, "3D Composite Fabrication Through Matrix Slurry Pressure Infiltration," *Ceram. Eng. Sci. Proc.*, **15** (4) 113-120 (1994).

6.0 TASK ORDER 0004 – ADVANCED COMPOSITE RESEARCH

6.1 Introduction

The work conducted under Task 4 primarily focused on supporting research related to organizations outside of the Materials and Manufacturing Directorate. A significant amount of modeling work was completed on ceramic matrix composites, covering topics ranging from the application of oxide composites in combustor liners to modeling of 3D weave architectures. The production of these models has increased the understanding of the material behavior in specific applications and has led to improvements in components currently being manufactured and tested. Continued modeling will allow for greater understanding and control over component properties and will ultimately increase the transition rate of ceramic composites into actual applications.

Other topics examined during this contract period include the production of single crystal YAG fibers and polycrystalline Yttrium Alumina Garnet (YAG) fibers/slabs, along with the modeling of the operation maps for YAG that show the locus of power and the parameters that limit the maximum power of operation. Single crystal YAG fiber was produced and initial trials on polycrystalline YAG fibers were conducted. Laser quality, nanosized YAG powder was produced at UES for use in fabricating polycrystalline YAG fiber/slabs and a large batch (~1 kg) of powder will be supplied to AFRL/RXLN in FY10.

Work conducted in collaboration with AFRL/RZ focused on the evaluation and production of catalyst and thruster bedplate material for spacecraft propulsion. AFRL/RXLN and UES personnel analyzed catalyst material obtained from AFRL/RZ, while also producing iridium-coated catalyst material for evaluation. Alternative bedplate materials were identified (YAG, HfB_2 -20% SiC) and several bedplates were produced for evaluation. Both the catalyst and YAG bedplate materials were delivered to AFRL/RZ for analysis.

Work conducted in collaboration with AFRL/RB revealed that ultra high temperature ceramic materials (UHTC, HfB_2 -20 % SiC) can potentially be used for heating elements for a ground thermo-structural test that mimics the thermal loads and atmosphere encountered in reentry from space. This work is very promising and a continued collaboration between AFRL/RXLN and AFRL/RB is expected.

Although initial work on UHTCs was conducted under Task 4, the remainder of this information has been incorporated in the Task Order 0007 section on Ultra High Temperature Ceramic Materials.

The research conducted under this task has been varied in nature and has provided valuable insight into the behavior of ceramic materials under differing applications and conditions. The collaborations formed during this research period are extremely valuable and will continue, at least, in the near term.

6.2 Technical Results and Discussion

6.2.1 Evaluation of Oxide Composites in Combustor Rig

Oxide–oxide composites were evaluated in a novel combustor design requiring higher wall temperatures than the conventional combustors. The evaluation was based on a combination of numerical modeling and experimental rig testing. The modeling included computational fluid dynamics (CFD) calculations whose results were used in a thermo-mechanical analysis using finite element modeling (FEM). The composites tested experimentally were obtained from a commercial vendor; they were reinforced using Nextel™ 720 fibers. The rig tests showed that aluminosilicate matrix composites with higher room temperature strengths suffered cracking while the weaker alumina matrix composites performed satisfactorily. The results were consistent with numerical models that predicted residual stresses from creep during service. The models showed that in-plane gradients and their effects were more severe than those of through-thickness gradients and suggest that tailoring fiber architecture is important in transitioning these composites to applications [1].

6.2.2 Effect of Salt Water Exposure on Fiber Strengths

The relative contribution of fiber strength loss to reported degradation in the mechanical behavior of Nextel 720-aluminosilicate composites after exposure to salt fog (ASTM B117) was explored. Single filament tension tests were performed on Nextel 720 (3M, Inc., Minneapolis, MN) fibers after immersion in NaCl solutions followed by high-temperature exposure in air. The results were compared with the behavior of control specimens that received high-temperature exposure but were not immersed in NaCl solution. There was no degradation in fiber strengths for NaCl solutions below 1 wt%. However, significant degradation was observed at 5 wt% NaCl upon exposure to temperatures between 900 °C and 1150 °C, while no degradation was observed upon an exposure to 1200 °C. The relative contribution of fiber strength loss to composite degradation was estimated as nearly 50%, indicating that both fibers and matrix/interface degrade from exposure to salt water. X-ray diffraction and transmission electron microscopy of the exposed fibers and composites were conducted to help rationalize the observations. Microstructures of degraded fibers showed the presence of Na at grain boundaries near the surface, without any evidence of a crystalline phase, indicating weakening from segregation or formation of an amorphous phase. The degraded composites showed that matrix and fiber/matrix interfaces had Na rich regions/phases [2].

6.2.3 Physics of Failure

The aerospace industry is developing structural health monitoring systems to reliably detect, locate and quantify damage in components and use the identified damage feature to make a decision on whether to repair or replace the component or for prognosis of the remaining useful component life and system performance. Mission-readiness, minimization of costs due to unnecessary tear downs and Nondestructive Evaluation (NDE) inspections as well as safety are some of the major goals of systems health monitoring. Current structural health monitoring systems focus on detecting the damage at component level and focus less on the failure of the material. It is anticipated that microstructure-based methods will offer higher quality prognosis

and avoid unexpected and expensive failures. Knowledge of the physical mechanisms through which materials fail might motivate the NDE and Structural Health Monitoring (SHM) engineers to enter the next phase of health monitoring. Methods based on vibration signature of the structure, for example are useful in detecting damage at a global level and help predict damage level in a component; however such methods do not furnish information of failure processes at a microstructure level. The purpose of this paper is to help move the NDE and the SHM community in the direction of adopting failure mechanisms at a microstructure level whether it be in the area of damage diagnostics or prognosis. Hopefully, the discussion of various prominent failure mechanisms in structural materials presented in this paper will serve that purpose and in the future this paper will serve as a reference for either developing sensors based on material failure at a microstructure scale or for performing prognosis using microstructural parameters. Understanding of material degradation and failure mechanisms at a microstructure scale for a given set of operational conditions can be broadly termed as “Physics of Failure.” On the diagnostics side, it will be helpful to design new sensors based on an interpretation of a failure mode rather than simply suggesting that some sort of failure has occurred. For prognosis of remaining useful life it will be beneficial to not only quantify the damage but also to know the physics of damage initiation and progression to perform microstructure-based life prediction modeling. Similarly, knowing the physics of failure at spatial and temporal levels for a structure would be beneficial for structural repair and (or) better material substitution. The failure process in materials is a vast and complex field and to summarize it is a challenging task. The reader must note that this paper is an attempt to present a comprehensive view of the “Physics of Failure,” at the possible risk of oversimplification. This is thus a first-level guide to the failure mechanisms that dominate failure of components using state-of-the-art materials [3].

6.2.4 Analytical Evaluation of Hybrid Ceramic Design Concepts

Many high temperature structural applications demand a material which has a combination of high thermo-chemical stability, hot strength and good foreign object damage (FOD) resistance. The possibility of combining the advantages of ceramic matrix composite (CMC) and monolithic forms of ceramics in a single hybrid design to obtain a strong damage tolerant material design was explored using modeling. The desired advantage will be enhanced reliability retaining high strength and other density-dependent properties such as thermal conductivity. Two key factors, identified as crucial to the concept, were analyzed. One of them was the prevention of cracks that form from FOD at the surface within the CMC, from entering the monolithic core. Finite element models predict that the use a porous interphase to engineer the interface is a viable strategy, and that an optimal thickness of this layer exists for maximum tendency to deflect cracks. The second factor examined was the ability of these hybrid materials to withstand thermal gradients. The model predicts that the concept is feasible if the CMC layer is sufficiently thin (<0.5 mm). It is concluded that the hybrid design is a viable strategy for hot structures requiring damage tolerance [4].

6.2.5 Analysis of Ceramics Toughened By Non-Conventional Fiber Reinforcement

Many refractory materials that are not readily available in fiber form, including ultra-high temperature ceramics (UHTC), are attractive candidates for use in high temperature structural components. This work explores the possibility of using non-conventional fiber forms that can be

fabricated by “fibrous monolith” techniques to design composites with high strength and toughness along with 2D isotropy. The use of low-aspect ratio bone-shaped short fibers (BSSF) to improve fracture toughness and the use of composition tailoring to increase fiber strength were analyzed and it was found that both concepts need to be used in combination to achieve significant toughening. Computational models using UHTC as model materials indicate, for example, that significant improvements in fracture toughness can be realized with an aspect ratio of just 15, but only if the fiber strengths can be raised to 1.5 GPa. The use of a single outer layer of lower thermal expansivity composition is predicted to increase low temperature strength by a factor of 2, while multilayers of reasonable thickness (10 μ m) result in strengthening by a factor of 3. For UHTCs, processing improvements that reduce flaw sizes will be necessary to take advantage of these results, but considerable improvement in properties can result from such progress [5].

6.2.6 Thermal History Sensor Based on Glass-Ceramics

The degradation of mechanical properties of materials during service is strongly dependent on the history of thermal exposure resulting from thermally activated microstructural processes. This degradation can lead to catastrophic failure of engineering components; consequently, knowledge of the thermal history of a component is crucial to predicting the degradation of properties and anticipating/preventing failures. In this work, a thermal history sensor capable of operating wirelessly in severe environments has been developed which functions as much more than a thermal fuse, but less than a computer-monitored thermocouple. The sensor utilizes the thermally activated crystallization of glass-ceramics to record a thermal history fingerprint in an array of glass-ceramic substrates. Computer modeling as well as experimental results are presented as proof of concept for the sensor. Degradation state sensing as well as the effects of environmental moisture on the operation of the sensor will also be discussed. The end product will employ a pattern-matching algorithm to characterize instantly the thermal exposure by comparing to a database of thermal history fingerprints. The thermal history sensor is expected to be useful in a variety of high temperature, severe environment applications [6].

6.2.7 Tailorable Thermal Expansion Hybrid Structures

A design concept is presented for a macro or microstructure that combines materials with differing thermal expansion to achieve an overall effective expansion that differs substantially from either of the constituents. Near-zero-Coefficient Thermal Expansion (CTE) and isotropic negative expansion designs are achieved by creating compliant structures where overall expansion is compensated by internal bending deformation. Such structures have application where dimensional stability is required when subject to large thermal gradients, e.g. space mirrors. In this paper, we present closed form analytic expressions for prediction of the effective expansion, and consequent internal stressing, of the structure, as well as several finite element simulations that demonstrate the design performance under non-uniform thermal load. Further details can be found in [7].

6.2.8 Deformation of Oxide Systems

Slip systems in indented natural single crystal scheelite were studied using Transmission Electron Microscopy (TEM). Indentations with loads from 10 to 200 g were applied on (001), (100), (110), and (112) crystallographic planes at room temperature. Focused Ion Beam (FIB) technique was used to machine electron-transparent foils with pre-defined orientations from specific locations in and around the indented areas. Five families of slip systems with a total of 16 physically different slip systems were observed. Most plastic deformation was carried out by two major slip systems, $(001)\langle 110 \rangle$ and $\{112\}\langle 11\bar{1} \rangle$. The observations are interpreted using the crystallographic structure of scheelite [8].

Microhardness and fracture anisotropy of natural single crystal xenotime were studied using Vickers and Knoop indentations. Indentations with loads from 10 to 500 g were applied on (001) and (100) crystallographic planes with various orientations of the indenter diagonal around the plane normal. The indentations were characterized with optical microscopy and SEM for cleavage, the anisotropy of microhardness, and indentation fracture toughness. Crack geometry was studied using FIB. The observations are interpreted using the crystallographic structure of xenotime [9].

Dynamic response of natural, [001]-oriented, and synthetic, [201]-oriented, scheelite (CaWO_4) was studied in planar impact experiments with shock up to 20 GPa. The velocity of the interface between the sample and the PMMA window was continuously monitored by VISAR. Although the waveforms recorded in the planar impact experiments revealed different dynamic responses of the two materials, the plastic deformation in both cases is governed by the dislocation glide in $\{112\}$ planes with resolved shear stress of $\sim 0.6\text{--}0.7$ GPa. The waveform obtained from [001]-oriented material contains the signature of the second-order scheelite–fergusonite transformation. The absence of the transformation signature in the waveforms obtained after strong impact of [201]-oriented crystals is probably due to faster transformation kinetics under loading in this direction [10].

6.2.9 SiC-Ti₃Si₂ Composites

Composites in the SiC–TiC–Ti₃SiC₂ system were synthesized using reactive hot pressing at 1600 °C. The results indicate that addition of Ti₃SiC₂ to SiC leads to improved fracture toughness. In addition, high microhardness can be retained if TiC is added to the material. The best combination of properties obtained in this study is $K_{Ic} 58.3 \text{ MPa} \cdot \text{m}^{1/2}$ and $H_v 517.6 \text{ GPa}$. The composition can be tailored in situ using the decomposition of Ti₃SiC₂. Ti₃SiC₂ decomposed rapidly at temperatures above 1800 °C, but the decomposition could be conducted in a controlled manner at 1750 °C. This can be used for synthesis of fully dense composites with improved properties by first consolidating to full density a softer Ti₃SiC₂-rich initial composition, and then using controlled decomposition of Ti₃SiC₂ to achieve the desired combination of microhardness and fracture toughness [11].

6.2.10 3D Weave Architecture Modeling

Modeling of CMC with complex fiber architecture remains a challenge despite significant efforts extended in developing simulation methodologies in recent years. This deficiency hinders transitioning of CMCs into aerospace applications, especially because experimental studies of architectural effects are limited by the cost of CMC fabrication. Complex geometries of the fibers make application of standard finite element methodology problematic, particularly in view of small errors, like tow interpenetrations. In the “embedded boundary” method proposed in this paper, matrix and tows are discretized separately, matrix elements completely covered by tows are deleted, and kinematic constraints are used to ensure displacement continuity between the matrix and the tows. Only boundary nodes (elements) of the tows are thus constrained. The methodology is applicable to non-linear material models and appears to tolerate small interpenetrations of the yarns. Errors in the approximation of the stress-strain state at the tow/matrix boundaries are studied for simple geometries and are shown to be reasonably small. The latter is very important for the future generalization of the approach to include fracture, especially along the tow/matrix interfaces [12].

6.3 Summary of Unpublished Work

6.3.1 Modeling of Ceramic Matrix Composites with Complex 3D Fiber Architecture

The objective of this effort was to develop rigorous and robust methodologies for modeling CMCs with complex architectures in the general purpose finite elements package Abaqus, [13]. To achieve this goal, the following approaches were taken:

6.3.1.1 Direct Meshing

Development of a fully space filling continuous mesh with one-to-one nodal connectivity at the fiber-matrix interface (in particular) is a straightforward, albeit not always possible task. While previously it has been thought to be impossible for all but the most simple architectures or small unit cells, we have developed methods that work reasonably well for much more complicated structures.

6.3.1.2 Embedded Element (Domain Superposition)

Domain superposition, [14, 15], method was implemented using the ‘embedded element’ capability of Abaqus. In this methodology tows and matrix are meshed separately with the overlapping regions connected by kinematic constraints.

The methodology has the following limitations:

- (1) It is not generally applicable with non-linear material models.
- (2) The implementation of the method in standard packages may be limited – as it is in Abaqus – by the requirement that elastic properties’ matrix is positive-definite, which would include the fictitious material that we have to use for the embedded tow; this consideration is very important for ceramic composites, where matrix properties can be very close to the properties of the fibers.

- (3) The stresses and strains at the tow/matrix boundaries have artificial spikes that attenuate oscillating away from the boundary affecting several layers of elements on both sides; these spikes are not likely to significantly alter average properties of the composite due to the small – compared to the volume of the RVE – volume of the affected regions, but those are exactly the regions that have utmost importance for the development of fracture in composites.

6.3.1.3 Embedded Boundary

In this method tows and matrix are meshed separately, as in the embedded elements method, but the matrix elements fully overlapped by the tows are deleted. While additional computational time is needed for finding those elements and deleting them, this time is offset by the time needed for finding and enforcing all the additional kinematic constraints that are needed in the embedded elements method for connecting those deleted elements with the tow elements overlapping them. The kinematic constraints between the matrix and the tow elements are applied only to the surface elements of the tows. This results in a simple matrix/tow mesh with ‘rough’ overlapping boundaries at interfaces. No material properties adjustment for the tows is needed.

Thus, embedded boundary method is as easy to setup as the embedded elements method and it has the following advantages for the modeling of CMCs:

- (1) The method mitigates ‘spikes’ in stresses and strains at the tow/matrix interface; the errors in these fields at the boundaries cannot be totally eliminated since we *approximate* the geometry of these boundaries, but the embedded boundary approximation is superior in this respect to the embedded element approximation.
- (2) The method allows the use of ‘real’ material properties, including general non-linear material models

6.3.2 Ceramic Matrix Creep and Shrinkage Modeling

During processing of porous-oxide matrix ceramic composites, the matrix shrinks as a result of both drying and sintering. Because the shrinkage is constrained by the reinforcing fibers, the matrix usually cracks. Typically, the cracks are only transverse in a 2D cloth layup composite because shrinkage is not constrained through thickness; however in shaped (curved) parts, the constraint is three dimensional and the resulting cracks are more problematic, since they may be interlaminar. A “user element” continuum creep/sinter model has been developed to model the constrained shrinkage of the matrix (Figure 8). This model is readily combined with either 3D fiber architecture in a ‘binary model’ simulation or with a full fiber discretization model in a 2D planar simulation.

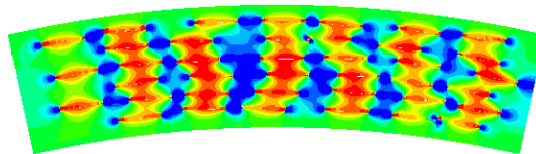


Figure 8. 2D Simulation of Fiber-Constrained Matrix Shrinkage Stress in a Cylindrical CMC Part

6.3.3 Modeling of a Ceramic Combustor Liner

A demonstrator ceramic CMC combustor liner is known to crack during testing. A full time-temperature history finite element simulation reveals that the failure is likely due to the service temperature creep strain and the consequent residual stress following cooling.

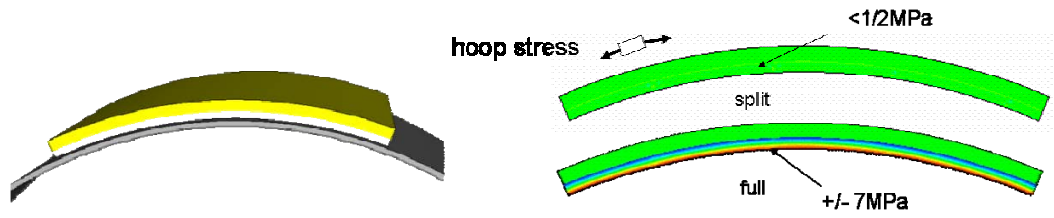


Figure 9. (a) 'Split' Ceramic Liner on Metallic Support
(b) Comparison of Stressing in Split and Continuous Liners

The existing model was modified to explore the possibility of relieving stress by splitting or segmenting the CMC liner (Figure 9). It was determined that such splitting does in fact relieve the stressing, but only in the hoop direction. Axial stresses are not improved and further the splint liner concept introduces new problems including attachment and warpage/distortion.

A renewed look at the demonstrator ceramic CMC combustor liner was undertaken in this period. Prior modeling considered a longitudinal center section. In the new model an axial-axisymmetric analysis was performed in order to examine effects of end stress concentrations and axial variations in thermal exposure. Additionally, in this model both the experimentally successful 'outer' liner as well as the problematic inner part were considered simultaneously for comparison. Accurate geometry details were incorporated, as shown in Figure 10.

As shown in Figure 11, the temperature and stress distributions in both parts are quite similar, and the initial conclusion is that both parts are predicted to fail.

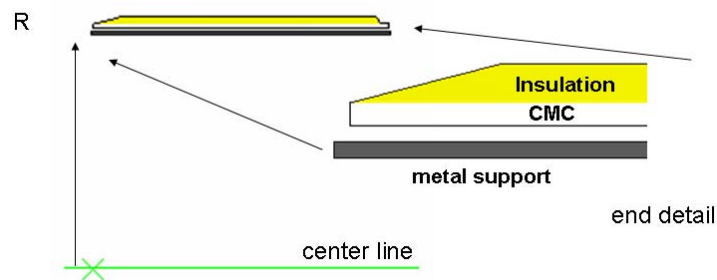


Figure 10. Axisymmetric Ceramic Liner on Metallic Support

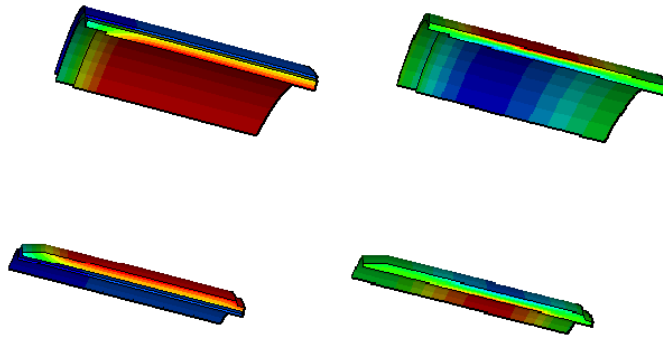


Figure 11. Axisymmetric Temperature and Stress Distributions in Both Inner and Outer Liners

After noting that severe over-stress is predicted in the known-successful outer part, a careful reexamination of the manufacturer-supplied materials data resulted in some significant improvements to our constitutive models. However, the basic conclusion remains that we are unable to explain the observed failure of the service part. A summary was prepared and passed to the part manufacturer for comment.

After observing the stress concentration resulting from the hard corners machined into the insulation layer, the manufacturer suggested that there may be some flexibility in the design permitting some stress reduction through geometry optimization. A preliminary study of a variety of end conditions (Figure 12) was prepared and sent to the manufacturer.

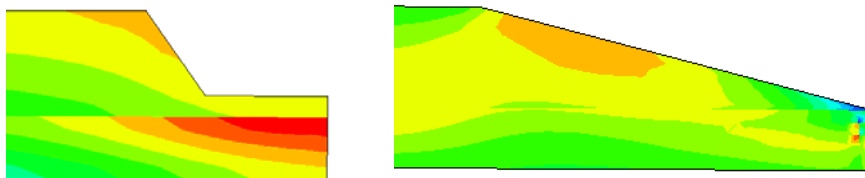


Figure 12. Examples of Different End Geometries

The manufacturer prepared for a round of sub scale testing and incorporated some of these concepts in the tests. We performed a preliminary round of analysis of the test-scale part and showed that the scale change results in a substantial change in stressing (Figure 13). However, the thermal loading in the test will certainly be an even bigger change, so this may be a minor concern.

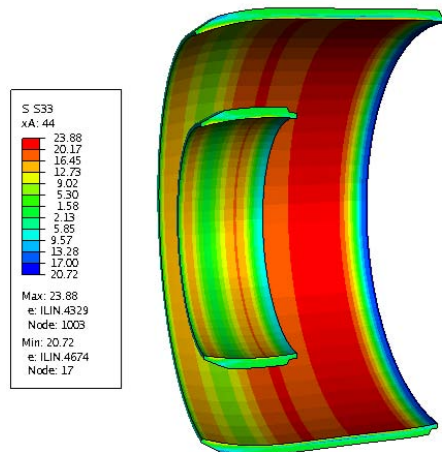


Figure 13. Axisymmetric Temperature and Stress Distributions in Both Full and Sub-scale Inner Liners

6.3.4 YAG Laser Materials

6.3.4.1 Single Crystal YAG Fiber Production

Plans began for producing YAG single crystal fiber by Edge-Defined Film-Fed (EFG) growth with the Advanced Crystal Products (ACP) fiber/furnace puller. EFG is a melt growth method for growing shaped single crystals. A seed is touched to the melt that has risen to the top of a capillary shaper whose end is in a melt reservoir. As the seed is withdrawn from the top of the shaper, a single crystal is pulled with a transverse section conforming to the perimeter of the shaper. Personnel who had previously worked at ACP and had pulled YAG fiber on their fiber/furnace puller by the EFG process were consulted about the fiber growth parameters for pulling single crystal (SXTL) YAG fiber.

For the first series of experiments at growing YAG fiber, the growth setup was a molybdenum crucible and lid. A tungsten capillary tube with a 0.010" diameter round tip was used. The charge was undoped, sintered UES YAG powder. The seed fiber initially used was 0.004-0.006" diameter SXTL sapphire fiber produced by Saphikon. The experiment began as the furnace chamber was pumped down and backfilled twice with 99.998% pure argon and then pumped down. The temperature was ramped to 1000 °C at 20 °C/min with the chamber under vacuum. At 1000 °C, the chamber was backfilled with argon and a flow of argon was established at 10 SCFH. The temperature was then ramped to 2010 °C at 20 °C/min. This is the typical procedure for ramping up to seeding temperature used in all of the subsequent experiments for the pulling of the neodymium doped YAG (Nd:YAG) sxtl fiber. In each trial before seeding is attempted, the seed fiber is fed/melted into the tip to insure there is melt in the tip of the capillary. The first attempt at seeding of the melt began as the seed fiber was lowered out of the rectangular (2" wide x 1" thick) graphite fiber guide ~0.050" above the tip. Within a short time the end of the seed fiber protruding from the fiber guide fell from the guide onto the lid of the crucible. It did not melt. More seed fiber was lowered from the fiber guide and after a short time it too fell out of the fiber guide. At this point the attempt at seeding was terminated and the experiment was

stopped. Subsequently, upon dismantling the fiber guide for cleaning, clear crystalline particles were found in the end of the fiber guide embedded in the walls of the guide channel.

In a second attempt at growing the fiber using the same growth set up, a larger diameter sapphire fiber, produced by ACP, was employed as the seed fiber. As previously, with the smaller diameter Saphikon sapphire fiber, the seed fiber extending from the fiber guide did not survive very long. The crucible was raised a small amount in the hot zone and a seed fiber of YAG produced by Saphikon was employed in an attempt at pulling the YAG. The YAG seed fiber stuck in the fiber guide and the portion protruding from the fiber guide changed its light transmission characteristics from transparent to opaque. Upon removing the seed fiber from the fiber guide, the end of the fiber in the hot zone protruding from the fiber guide had indeed changed its visual appearance from transparent to white translucent. Upon leaving it on the bench top in ambient conditions for 24 hours, it turned to a light gray powder. The kinetics of the transformation of the YAG seed fiber in the hot end of the fiber guide was slower than the sapphire single crystal fiber. The sapphire and YAG fibers may have been carbothermally reduced. With the YAG seed fiber surviving longer in the hot zone, multiple attempts at seeding were made possible by drawing the seed fiber some distance into the fiber guide from the hot end after each attempt. As the pull began, new fiber from the meniscus on the capillary tube tip was produced with a diameter the same as the seed fiber. Its diameter, however, would decrease until it dwindled to a point and pulled loose from the capillary tip. This may have been indicative of the fact that melt was not being transported by the capillary shaper out of the crucible into the capillary tip. Continuous growth of fiber was not achieved. The crucible used for the attempts at growing the YAG fiber was removed from the ACP furnace and visually inspected for possible causes that hindered growth. An effort was made to remove the lid with the capillary tube but this was unsuccessful. Therefore the lid was cut off to gain visual access to the inside of the crucible. The crucible and capillary tube were sectioned. This revealed that the melt had not reached the tip of the capillary tube. The failure to grow fiber was attributed to the lack of capillary force to cause the melt to rise to the tip of the tungsten capillary tube and also to the inability of the melt to traverse an obtuse angle of two mating machined surfaces in the tube. The angle which was not crossed is at an internal edge at the juncture of two machined surfaces where the diameter of the capillary tube transitions from 1/16" to 1/32". The angle between the two surfaces is 149°. Since this type of capillary shaper had not been used in the furnace previously, it appeared that this type of capillary tube was not designed properly to cause melt to rise from the base to the tip of the tube. However, the designer from ACP stated that ACP had used this capillary design successfully to pull fibers.

The time frame available for seeding with the YAG seed fiber was short even by employing the tactic of withdrawing into a cooler portion of the fiber guide. Therefore the feasibility of obtaining a fiber guide with a different configuration that ACP had manufactured for other fiber furnace units was undertaken by contacting both NASA Glenn and ACP's president. ACP had previously used this guide configuration to pull undoped YAG fiber. This fiber guide is 1" in diameter and has a molybdenum nosepiece, which would be in the hot zone rather than graphite. The balance of the guide outside the hot zone is graphite. This type of configuration for the fiber guide may eliminate the problem of seed fiber carbothermal reduction that had been experienced with the all graphite fiber guide. ACP indicated that our unit had a longer guide than the other units, thus the guides for the other units would not work. Therefore, upon further thought,

consideration was given to the fact that, most likely, a longer 1" diameter graphite fiber guide with a molybdenum nosepiece would not be stiff enough to keep from vibrating, which would be detrimental to pulling a good fiber. Thus, rather than investing time and effort into designing and fabricating a round graphite fiber guide with a molybdenum nosepiece, a decision was made to make a molybdenum nosepiece to fit the existing rectangular graphite fiber guide. The molybdenum nosepiece for the rectangular fiber guide and an aluminum extension for the puller stage to accommodate the added length of the fiber guide were acquired from a local vendor. In the interim, the method to prolong the use of the YAG seed fiber became more efficient with practice and the molybdenum nose piece did not have to be used.

To optimize time and effort, a vendor (VLOC, Florida) was identified that could provide dense cores from single crystal boules of 1.4% Nd:YAG charge material according to our dimensional specifications, rather than making the Nd:YAG charge from powder, which would require uniaxial pressing, isostatic pressing, and sintering to achieve a dense charge material for the crucible.

The second series of experiments began with two attempts to grow 1.4% Nd:YAG fiber from a 4-tip (0.005" dia. tips) growth setup that had been used successfully in the past to pull $\text{Al}_2\text{O}_3/\text{YAG}$ eutectic fibers. The crucible was charged with VLOC dense core material. In the first attempt, the top of the tips were positioned 3/16" below the top of the furnace heating element. In the second, the top of the tips were positioned 1/8" below the top of the heating element. The seeding and pull were attempted at temperature readings (as read from the base of the crucible) ranging from 1897 °C to 2103 °C. Starting speeds for seeding were varied, ranging from 0.025 in./min to 0.1 in./min. Ramps to the pulling speed were varied ranging from instantaneous to 30 sec. There were no indications that the seeding successfully began to grow fiber. Occasionally, a small length of material would be pulled by the seed fiber from the tip. But most likely this was material that had been melted into the tip from the YAG seed fiber.

Two more attempts were made to grow 1.4% Nd doped YAG fiber from the 4-tip growth setup. In the third attempt, the top of the tips were positioned 1/8" below the top of the furnace heating element. In the fourth, the top of the tips were positioned even with the top of the heating element. The seeding and pull were attempted at temperatures (as read from the base of the containment crucible) ranging from 1969 °C to 2015 °C. Ramps to starting speeds and starting speeds for seeding were varied. There was no indication that the seeding successfully began to grow fiber. Therefore the growth setup was removed from the furnace for visual inspection. Solidified melt was found to be occupying the space between the outer containment crucible and the growth setup crucible. The melt had seeped out of the growth setup crucible. The containment crucible cracked while trying to extract the growth crucible from it. A portion of the containment crucible fell away, exposing the bottom of the containment crucible and the base of the growth crucible. The base of the growth crucible was ~1/8" above the bottom of the containment crucible and was resting on solidified melt about its periphery. The melt was solidified around the periphery of the base of the growth setup crucible to a height of ~1/4" above the growth crucible base between the two crucible walls. There was no melt between the two crucibles in a region between their bases 3/4" in diameter centered on the centerlines of the crucibles (the centerlines of the crucibles are coincident). The growth crucible at the beginning of this series of attempts at fiber growth sat on the bottom of the containment crucible. The

elevation of the growth crucible in the containment crucible explained an anomaly in measurements of the height of the growth crucible that was noticed after the second growth attempt. Typically, the growth crucible is not removed from the containment crucible after attempts at growing fibers even when the height of the crucible tips is changed with respect to the top of the heating element. The growth crucible had an obvious crazed appearance. Upon sectioning the growth crucible, it could be seen that a few cracks penetrated through the wall of the crucible.

After these trials, a literature search was done to seek information concerning a possible reaction between YAG and molybdenum. Hay, Mah, and Cooke referenced the possibility that there could be a reaction between yttria, alumina, and molybdenum in the presence of one of the molybdenum oxides [16]. This suggests the possibility that a reaction occurred between the YAG and molybdenum, which may account for the difficulty of pulling YAG fiber from a molybdenum tip, particularly with a small I.D. where reaction products may plug the tip. The presence of the neodymium may also have contributed to the crazing.

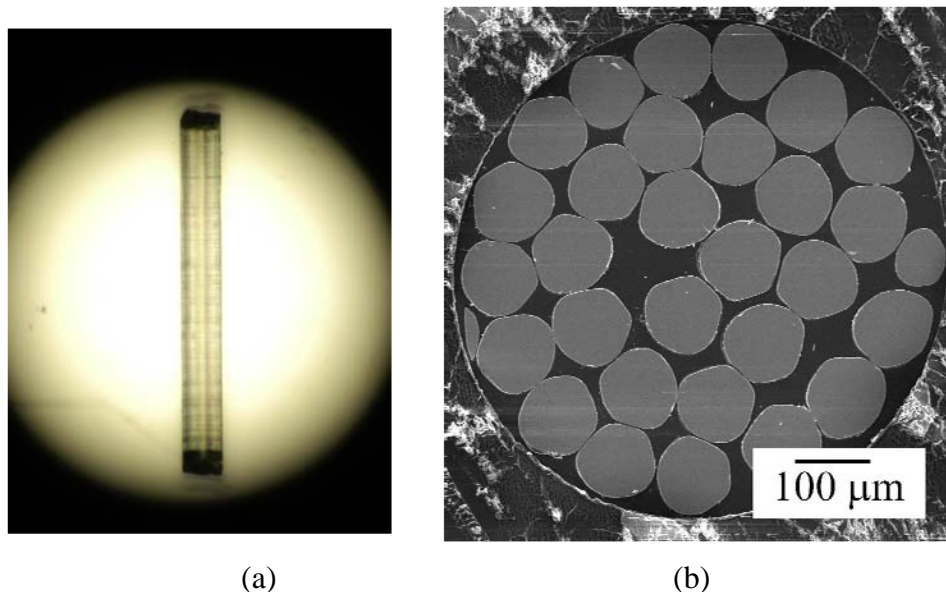
The molybdenum lid of the crucible of the second series of growth was sectioned and polished so that a slice could be made through the tips to inspect the interface between the melt and the I.D. of the tips. SEM inspection revealed that indeed there appeared to be a reaction between the melt and the tips which may have inhibited the growth of the fiber.

For the third series of experiments to grow 1.4% Nd:YAG fiber, a growth setup configuration similar to the first series of experiments was used. The crucible was a 0.75 I.D. molybdenum crucible with a molybdenum lid. A 0.125" O.D. x 0.031" I.D. tungsten capillary tube was used with a 0.003" high x 0.010" O.D tip. The base of the tungsten capillary tube was slit axially on the diameter with a 0.012 in. thick diamond blade to admit thin gage molybdenum foil. A 0.020" tungsten wire was inserted in the 0.031" I.D. of the capillary tube above the molybdenum foil. The wire extended from the transition to the 0.004" I.D. hole that passed through the tip at the top of the capillary tube and rested on the molybdenum foil. This configuration was used to enhance the rise of the melt in the capillary tube. In the first experiment of this series, the temperature to attempt seeding was set at different levels from 1970 °C to 1995 °C. The time for the ramp to seeding velocity was 10 seconds. The velocity of seeding was 0.05 in./min. The fiber would melt into the tip but no new material appeared to be pulled from the tip. Two positions of the crucible with relation to the heating element were tried. The first was with the tip of the capillary tube 0.125 in. below the top of the heating element and the second was with the tip level with the top of the heating element. In the second attempt of this series, using the same growth setup, the temperature was varied from 1977 °C to 2020 °C. A short length of fiber was pulled from the melt in the tip at 1977 °C after the crucible had seen 2020 °C. Visually, this growth was transparent with an opaque band where it began to neck down to a rounded point. Transparency may imply that it is YAG (YAP is usually opaque) and that the melt had not exceeded the conversion temperature to YAP. A third attempt was initiated but upon ramp up overnight to an intermediate temperature of 1000 °C the PLC quit controlling the furnace which subsequently shut down.

During the fourth attempt, various lengths of fiber were pulled at different temperatures and speeds with the total amount of fiber being over 15". A fifth experiment was undertaken to

explore the fastest speeds of fiber pulling that could be achieved. The fastest speed the fiber could be grown was 0.06 in./min. At this rate, growth was unstable and the fiber had hourglass-like, long range oscillations. A fiber length of 2.5" was grown. A sixth experiment was undertaken with the same growth setup and location in the hot zone as the previous experiments. Fiber was pulled overnight (23 hrs. total) at a temperature of 1970 °C and a growth velocity of 0.012 in./min; 17.5" of fiber was grown.

Examination by optical microscopy revealed fiber diameters ranging from 0.025" to 0.006". In transmitted light optical microscopy, there were periodic dark bands on the fiber indicating short range diameter oscillation (Figure 14a). XRD of the fiber, ground to a powder, identified only the presence of YAG (PDF card #08-0178). Electron probe microanalysis showed that the transverse neodymium concentration profile was relatively constant from the center to the outside of the fiber. SEM of both transverse and longitudinal sections revealed no porosity (Figure 14b).



(a) (b)
Figure 14. Micrographs of Single Crystal YAG fiber
(a) *Optical Micrograph in Transmitted Light showing Transparency*
(b) *Polished Cross-section of Single Crystal YAG fibers*

6.3.4.2 Polycrystalline YAG Fiber/Thin Disk/Slab Production

Ultra-high purity YAG powder was produced at UES, Inc. for use in fabricating polycrystalline YAG thin disk/fiber lasers. The purity of the YAG powder was demonstrated through glow discharge mass spectrometry (GDMS), which provides impurity levels for a large range of elements. Transparent YAG disks and pellets have been prepared; however, there is a lingering problem with discoloration of Si-containing samples. Chemistry tuning of the YAG precursor is in process to determine the minimal amount of silica needed for desirable consolidation. TEM samples of consolidated YAG have been prepared for analysis of discoloration in these Si-

containing YAG materials. Initial observations have confirmed the suitability of the samples produced for High Resolution Analytical TEM using the Titan microscope, and more detailed analysis will commence depending on the microscope availability.

A small amount of YAG powder and ultra-high purity YAG precursors were delivered to Dr. Fair for experimentation with the polycrystalline fiber production. Larger quantities of YAG powder will be delivered to AFRL/RXLN in FY10.

A billet of transparent undoped YAG (no silica, 13 mm thick) was delivered to Dr. R. Hay for use in the high temperature creep study of high purity YAG in a steam environment (LDF-funded). This program is being carried out in collaboration with AFIT (POC: Dr. Ruggles-Wrenn). A slightly thicker billet is needed to allow for proper evaluation of the material strain during testing; however, initial samples will be made from this billet. Additional billets will be produced from the ultra-high purity YAG powder, including both silica-doped and undoped YAG.

Currently, the polycrystalline YAG work relies heavily upon the hot isostatic press (HIP) unit at AFRL/RXL. This system is limited to a maximum rated temperature of 1550 °C; however, the unit itself should be capable of higher temperatures. An upgrade to the system was initiated; the system was switched to Type B thermocouples and the maximum temperature capability of the unit was rated at 1650 °C. The gain of 100 °C will significantly improve the processing window of the polycrystalline YAG materials, both disks and fibers.

6.3.4.3 Polycrystalline YAG Laser Host Material Modeling

The model by Dawson [17] for laser host fibers was analyzed and coded using Matlab and Excel. The model was used to generate operation maps that show the locus of power and what parameters limit the maximum power of operation. The model was verified for silica using the figure shown in Dawson's paper. The model was then used for YAG to show that YAG is significantly superior to silica in fiber form for use as laser host. The results are shown in Figure 15.

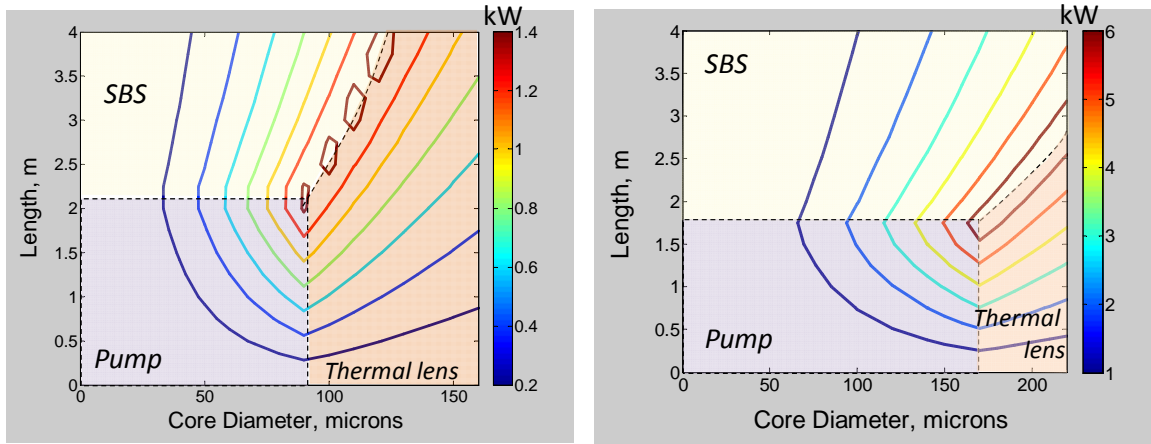


Figure 15: Charts Showing Locus of Maximum Power Output from Fiber Lasers, along with Factors that Limit the Maximum Power in Fiber Lasers

- (a) For Silica, which matches the figure in Dawson's paper
 (b) For YAG, which was calculated for this study

The contributions of various factors to the limitation on maximum power out put are shown compared in Figure 16. It is seen that pump power, thermal lens and SBS are the 3 major factors, and the other factors make negligible contributions.

The possibility of forming Nd-free YAG as cladding on a Nd-doped fiber was examined using thermodynamic and kinetic calculations. The vapor pressures were calculated using HSC Thermochemistry and are shown plotted in Figure 17.

Calculations of the diffusion distances using the data of Cherniak showed that the Nd diffusion distance in YAG is about 18 microns in 100 h at 1800 °C. Experimental results (X-ray microprobe maps, Figure 18) showed that the loss of Al dominated over Nd or Y and thus an external layer of Nd-Yttria was formed. There were no intermediate phases of YAM or YAP phases.

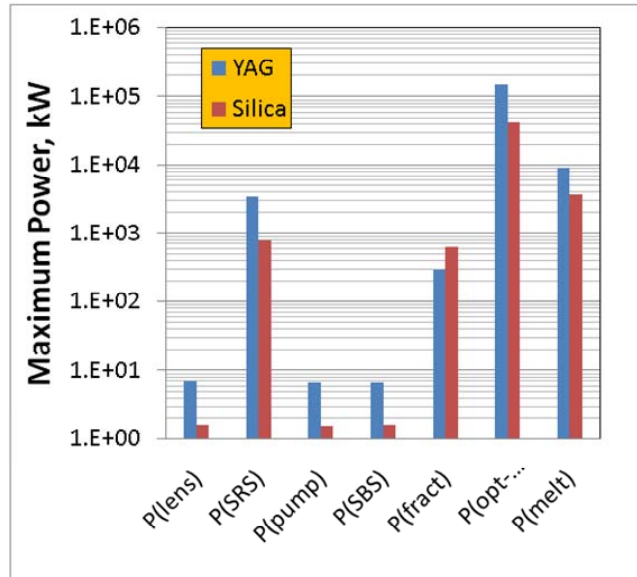


Figure 16. Contributions of Various Factors that Influence the Maximum Power in a Fiber Laser

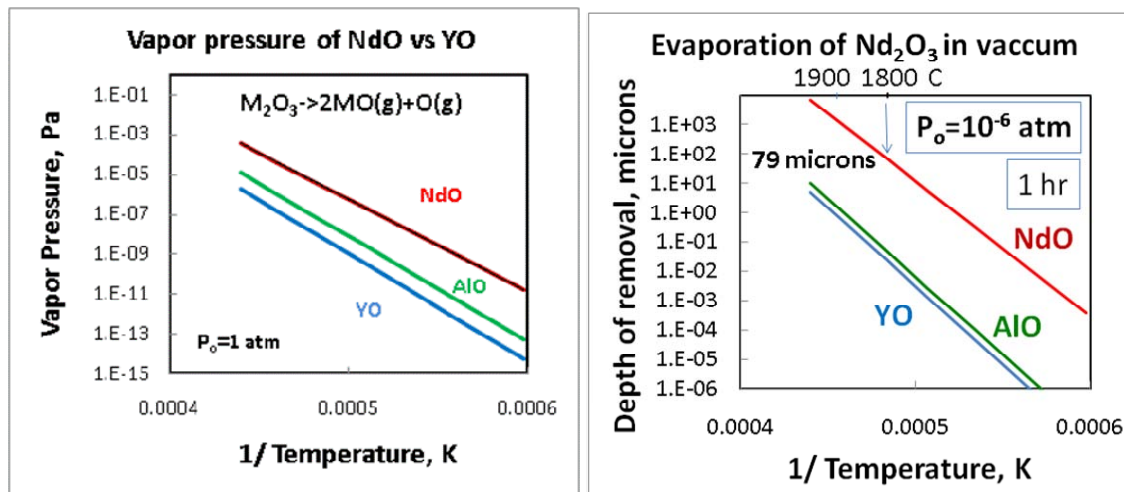


Figure 17: Vapor Pressures of Monoxides of Y, Al and Nd and the Calculated Evaporation Rates of the Elements in a Vacuum of 10^{-6} atm
Nd will preferably be lost from the surface of YAG

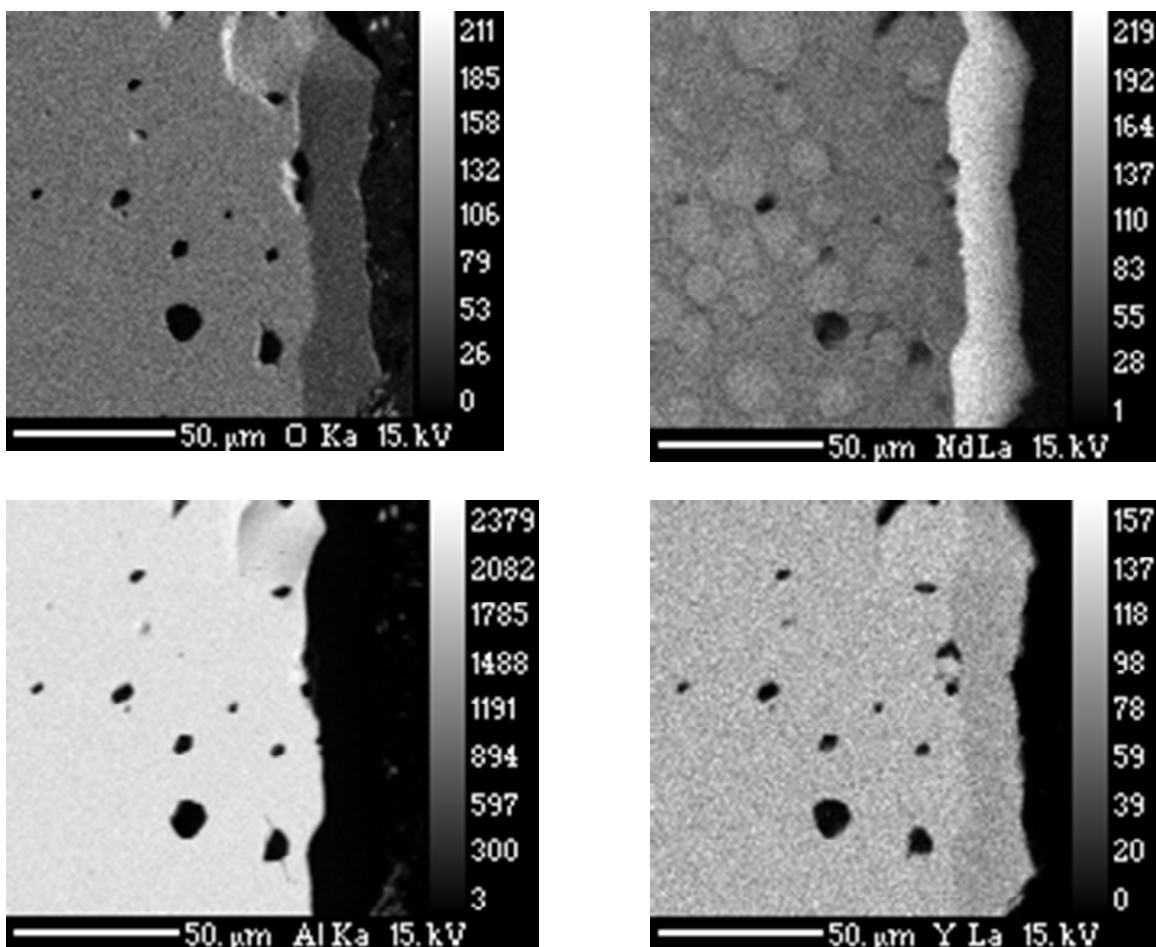


Figure 18: Experimental Results after an Anneal for 100 h at 1800 °C of a Nd-doped YAG

6.3.5 Catalyst/Bedplate

6.3.5.1 Catalyst Materials Evaluation/Production

Comparative analysis of two PSZ-based Ir catalyst support materials has been conducted to evaluate the phase compositions, catalyst distribution, and grinding properties. It was found that CeO₂ doped material consisted of monoclinic and tetragonal phases, in agreement with the earlier phase analysis, while Y₂O₃ doped material was single phase tetragonal. Grinding did not seem to affect the phase composition for either material. In the Y₂O₃ doped material, Ir was apparently deposited predominantly on the particles' external surface, while in the CeO₂ doped material, the particles were likely porous and Ir was deposited on both the external and internal surfaces of the particles.

This task was focused on the development of Ir catalyst on YAG substrates. Initial work on the nanosized Ir catalyst on YAG was done and characterized by XRD and SEM studies. Iridium trichloride (IrCl₃) solution consisting of 5 g of IrCl₃ was dissolved in 30 mls of deionized water. One half g of 12M HCl was added to make an acidic IrCl₃ solution. The concentration of Ir was

54.6 g/L. Subsequently, the solution was diluted to 5.46 g/L for catalyst coating. Five g of YAG carrier was soaked for 5 mins in 5 mls of; a) 54.6 g/L and b) 5.46 g/L Ir solution. The solution was drained and the particles were dried in an oven at 120 °C for 15 min and finally heat treated in a molybdenum disilicate furnace at 380 °C for 1 h in air. The procedure described above was repeated up to 6 times for both 54.6 and 5.46 g/L Ir solutions. Finally, the coatings were reduced in H₂ gas at 550 °C/1 h. Coatings reduced in hydrogen and x-rayed were consistent with diffraction pattern of Ir and YAG (Figure 19).

Figures 26 and 27 present IrCl₃ coatings on YAG. The 54.6 g/L solution made a continuous thick coating that showed shrinkage cracks (Figure 20). Such a coating will have a low catalytic performance since fusing of Ir catalyst particles decreases its performance. The preferred coating morphology is Ir particles that are separated from each other so that the particles do not sinter and fuse together when heated at the fuel decomposition temperature. For the polycrystalline YAG substrate coatings with the 5.46 g/L Ir solution gave the required distribution of particles on the support (Figure 21). Ir particle density on YAG substrate increased with the number of coats. For the number of coats less than 5, a high particle density was attained and Ir particles were separated from each other (Figure 21).

Currently, 10 g each of the 5-, 6-, 7- and 8-coats of Ir on polycrystalline YAG and 6- and 7-coats of IrCl₃ on single crystalline YAG was completed and shipped to RZ/Edwards Air Force base for BET surface area evaluation and PINO testing during FY10.

Lutetium aluminum garnet (LuAG, Lu₃Al₅O₁₂) was also identified as an alternative to YAG, due to its similar structure and properties, along with its slightly higher melting point (~100 °C). LuAG is a line compound and is therefore more difficult to form as a single phase. Initial trials produced a two phase mixture. DTA/TGA analysis was used to obtain more accurate results concerning the amount of absorbed water on the starting nitrate materials, which in turn led to the production of near phase-pure LuAG powders.

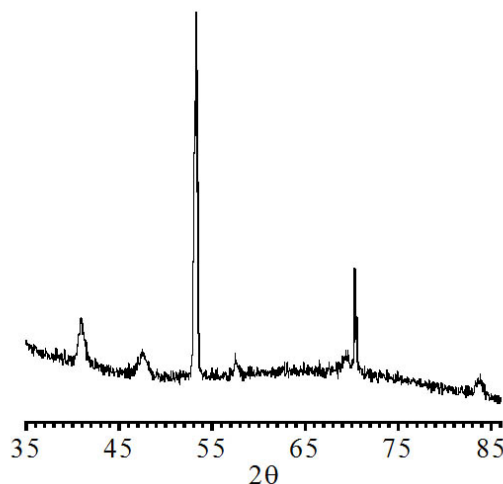


Figure 19. X-ray Diffraction of IrCl₃ Coated Single Crystal YAG-Reduced in H₂ -5.5g/L 6 Coats

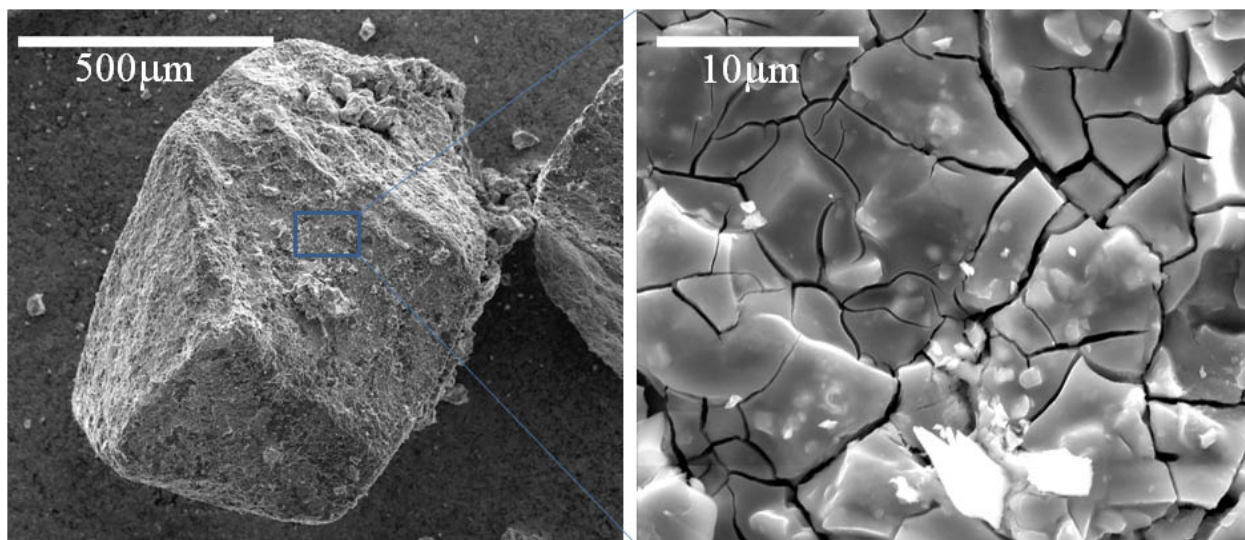


Figure 20. IrCl_3 Coating on YAG, 6 coats, 54.6 g/L Ir Solution

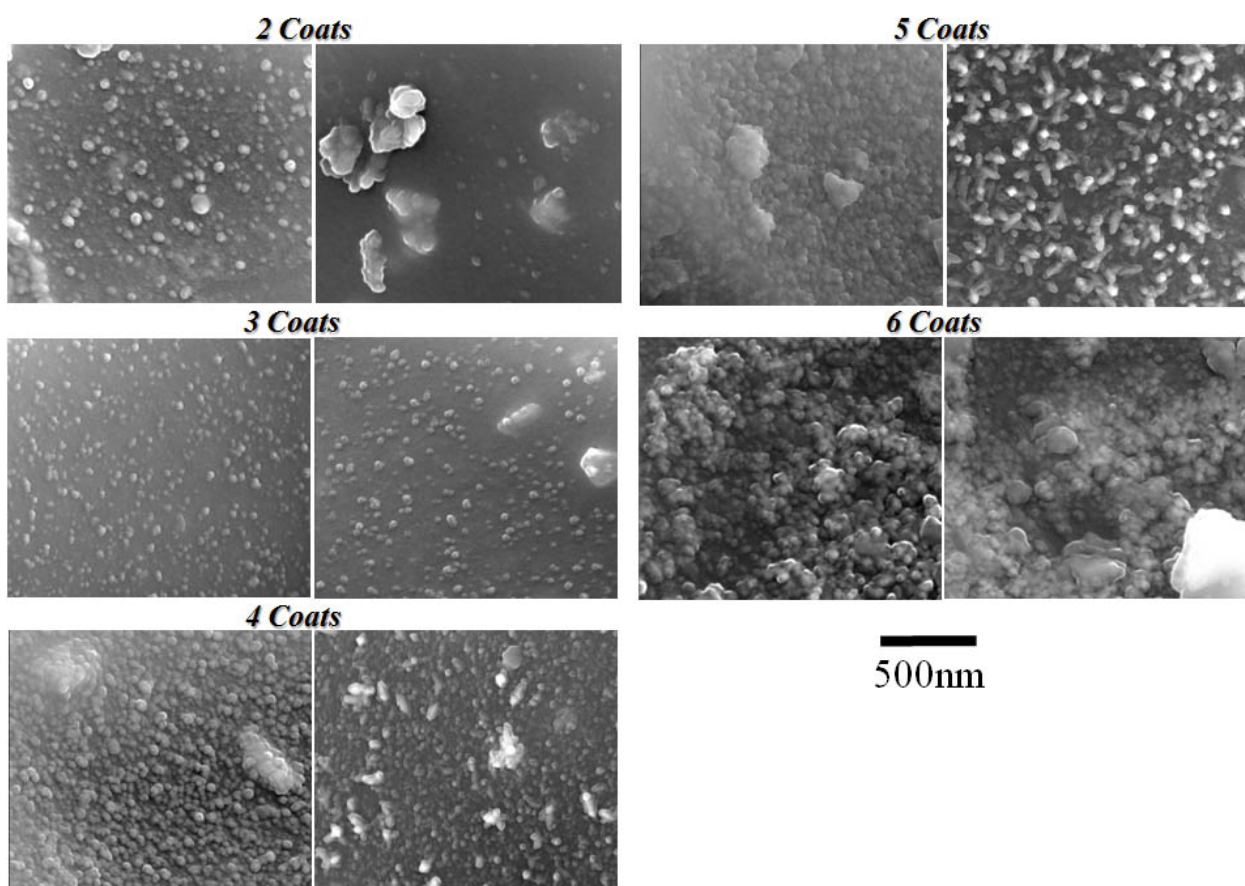


Figure 21. IrCl_3 Coating on YAG, 2-6 coats, 5.46g/L Ir Solution

6.3.5.2 Thruster Bedplate Fabrication

Two main materials, HfB_2 -20 % SiC UHTC and YAG were identified as candidates for alternative thruster bedplate materials. Both materials offer high melting points with reasonable thermal shock resistance, while YAG offers the added benefit of oxidation resistance. Lutetium aluminum garnet (LuAG) was also identified as a back-up to YAG. It is similar in structure and properties, but with a slightly higher ($\sim 100^\circ\text{C}$) melting point. An invention disclosure identifying these materials as potential bedplate materials has been submitted to the Air Force JAG office [18].

A thruster bedplate machining drawing was completed using the geometry and dimensions supplied from AFRL/RZ. Several UHTC pellets were fabricated using SPS for machining trials in-house using both plunge EDM and wire EDM. The initial design of the bedplate allowed for relatively straightforward machining of the UHTC material using plunge EDM. However, a modified design was obtained from AFRL/RZ; this new design required unsupported tines of the material, aside from a center connection point. This presented problems during both plunge EDM and wire EDM machining. These problems are solvable and will be addressed in follow-on work.

Concurrently, Bullen Ultrasonics, (Eaton, OH) was chosen to ultrasonically machine (UM) a single crystal YAG thruster bedplate. Meetings with Tom Fraga, a sales engineer at Bullen, were undertaken to discuss details of the ultrasonic machining (UM) of the bedplate and to deliver a single crystal YAG core procured from VLOC (Florida). Due to the thickness of the bedplate and the narrow width of the grooves in it, the grooves were UM'd halfway through the thickness and then the workpiece was flipped to finish the grooves from the other side. In the first attempt at machining, after the grooves were machined to the half depth, it was noticed that a fracture occurred between the periphery of the work piece and the first groove. Visual inspection under low magnification indicated that the fracture may have originated at a flaw on the sharp edge on the perimeter of the work piece. A second work piece was cut to size and the perimeter edges were radiused with a 0.010" radius. The second attempt at UM of the bedplate was successful. The bedplate was heated at 1600°C in air for one hour to relieve any residual stress in the material. The bedplate was then delivered to AFRL/RZ (POC: Paul Zuttarelli) for testing.

6.3.5.3 HAN thruster modeling

A finite element model was initiated for the HAN monopropellant bedplate. The state of the art UHTC bedplate design is fabricated with open ended slots (Figure 22a). The 'tines' tend to fail due to thermo-mechanical load, and a revised design was fabricated with closed-end slots (Figure 22b) with the aim of improving the mechanical integrity.

A transient thermal model of the two designs shows that the tines (or webs) heat up much faster than the bulkier regions of the part, due to both the thermal inertia and shielding of the edge from the hot gas flow (Figure 23). Although a stress analysis has not yet been performed, it seems likely there the closed slot design may suffer significantly higher stressing due to the webs being constrained by the cooler edge.

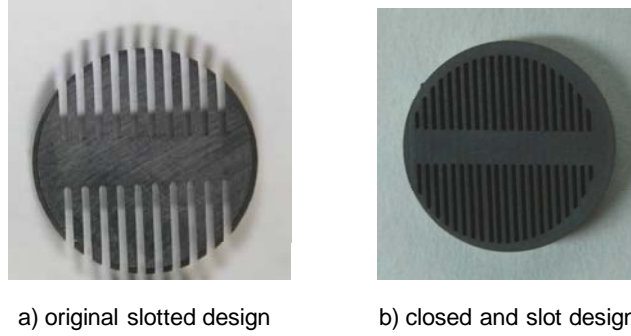


Figure 22. HAN Thruster Powder Containment UHTC Bedplate

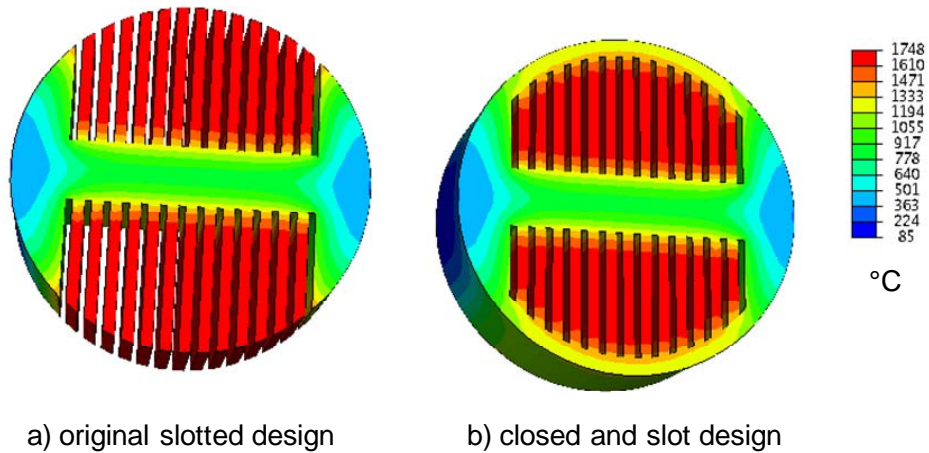


Figure 23. Transient Thermal Analysis of the Two Baseplate Designs

6.3.6 Ternary Eutectic in the B_4C -SiC- TiB_2 System

An introductory study was conducted on a calculated eutectic composition in the B_4C -SiC- TiB_2 ternary system (Figure 24) for potential use in ceramic armor development. Powders of the above ternary end members were received and characterized by X-ray diffraction. Two compositions were explored. A calculated eutectic composition from Udalov, et. al. [19] and a eutectic composition derived from experimental studies by Li, Tu, and Goto [20]. Udalov's composition (compositions given in mole percent) is 43% B_4C – 27% SiC – 30% TiB_2 . Li's composition is 51.2% B_4C – 40.7% SiC – 8.1% TiB_2 . Li et. al. determined the eutectic composition experimentally by varying the composition and comparing the microstructures.

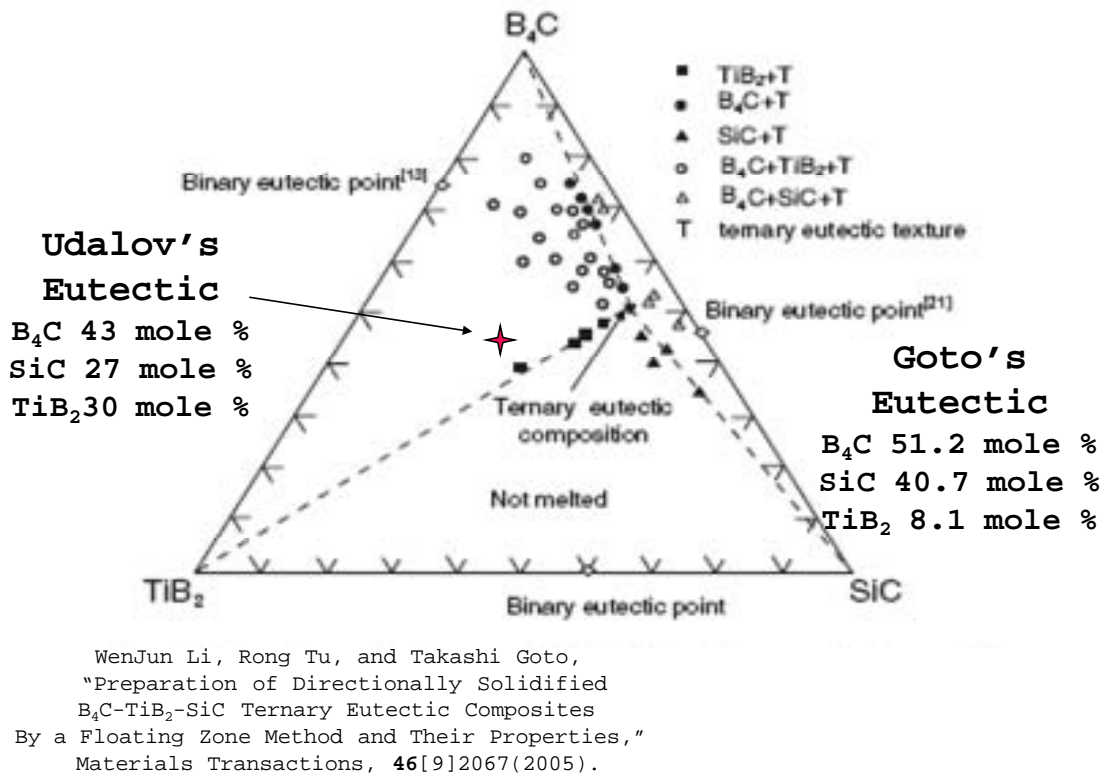


Figure 24. Ternary Phase Diagram of B_4C - SiC - TiB_2 System

Pellets of both eutectic compositions were prepared by mixing the starting powders in acetone, uniaxial pressing in a 1.5" diameter stainless steel die, and cold isostatic pressing at 50 ksi. The pellets were subsequently arc melted under an inert atmosphere on a copper hearth. The flat arc melted ingot was flipped several times during processing to ensure homogenization of the composition. The arc melts of Udalov's composition had large lathes and smaller needles of TiB_2 and smaller portions of SiC dispersed in a B_4C matrix. There was no ternary eutectic structure. The arc melts of Li's composition showed regions of ternary eutectic microstructure and regions of SiC needles in a B_4C matrix. Based on these results, Li's composition of 51.2% B_4C – 40.7% SiC – 8.1% TiB_2 was utilized for further study. Arc melted buttons of Li's composition were crushed in a shatterbox using a tungsten carbide container. The arc melted pellets were easy to pulverize into fine powders, which were estimated to be less than 325 mesh.

The powders were placed in a 1" I.D. graphite die lined with grafoil and hot pressed. Four hot pressings were conducted to determine the parameters that would yield a specimen with the density closest to theoretical: HP #1: 1990 °C/30 min/5000 psi; HP #2: 2100 °C/30 min/5000 psi; HP #3: 2075 °C/30 min/5000 psi; HP #4: 2020 °C/30 min/4000 psi. The samples melted and flashed for hot-press experiments #2 and #3, while the geometrical density measurement of HP #1 was only 85% of theoretical. HP #4 was theoretically dense (Archimedes method) and the micrographs of the polished surface showed that the arc-melted structure was maintained. The hot-pressing processing window of the ternary eutectic appears to be very narrow.

More hot-pressing experiments were carried out to first verify the reproducibility of the hot pressings and second to establish the scale-up capability. The parameters of HP #5 (2020 °C/30 min/4000 psi), were based on the conditions of HP #4 for the reproducibility study. The conditions for HP #6 were 2090 °C/30 min/4000 psi. HP #5 was theoretically dense and HP #6 showed signs of melting at the outer periphery of the disc. The hot-pressing experiments designed to study the scale-up capability used a 2 inch diameter graphite die. The hot pressing conditions for the experiments were HP #7: 1980 °C/30 min/2000 psi and HP #8: 1970 °C/30 min/2500 psi. HP #7 seemed theoretically dense, but it showed a slight sign of melting at the outer periphery of the disc. The purpose of the large billet hot-pressing was to machine a 1" diameter by ¾" long piece for ballistic testing. A CAT scan of HP #7 billet was carried out at the ARDEC, Picatinny Arsenal, NJ, in consultation with Dr. Sheldon Cytron. The CAT scan results revealed sub-surface worm-hole like continuous pores. The appearance of these continuous pores resembles the evolution of gaseous phase(s) during hot-pressing either as constituent vaporization or from the evolution of reaction products. All three constituents (B₄C, TiB₂, and SiC) and possible reaction gaseous products were evaluated using HSC Chemistry software. All of the possible reactions with the vapor phase products are positive in ΔG at the hot-pressing temperature. The oxygen partial pressure in the hot-pressing die is assumed very low. It is possible that the vaporization of SiC could occur during hot-pressing.

SEM examination was conducted on specimens HP #4 and HP #6. Polished sections of HP #6 and HP #7 were indented with a Vickers indenter on a Buehler microindenter at 100 gf and 1 kgf force. Diagonals of the indent were measured with both the indenter's optical microscope and from SEM photomicrographs. Crack propagation was investigated through SEM analysis. The average hardness value (average of 20 indents) of the hot-pressed ternary eutectic was 2661 Kgf/mm². For reference, the hardness value reported by Li et. al., ranged between 2850 – 3260 Kgf/mm². HP #7 was sectioned to make bend bars for strength and fracture toughness measurements. The strength of the ternary eutectic was measured using a 4-pt bending configuration and the average strength (6 tests) value was 200.7 MPa. The fracture surface of a strength test bend bar (228 MPa strength sample) was examined and the fracture initiating flaw size was measured to be about 280 μ m, which is in good agreement with the calculated value (~240 μ m). The fracture toughness was also measured using SENB and the average value (4 tests) was 3.95 MPa \sqrt{m} . HP #8 was given to Dr. Sheldon Cytron for analysis and testing.

6.3.7 High Temperature Resistive Heating Element

A feasibility assessment study was initiated in collaboration with David Hart of AFRL/RBSV. The research involves the simulation of spacecraft performance under very high heat flux range (100 – 1000 Btu/ft²-sec). The ground thermo-structural test mimics the thermal loads and atmosphere encountered in reentry from space. A recent literature review (by RBSV) suggests that the use of advanced materials might permit the development of a heating element that would enable such a facility. The current effort comprises experimental studies to determine the feasibility and estimate performance characteristics of advanced heating elements. Based on the discussion jointly undertaken by AFRL/RBSV and RXLN scientists, candidate materials were identified. The materials chosen are: TaC, HfC, 4TaC-5HfC, HfB₂ and HfB₂-20%SiC. These materials were densified through hot-pressing to almost theoretical density, except for HfB₂-20%SiC, which was produced using SPS. The hot-pressed sample size was such that a

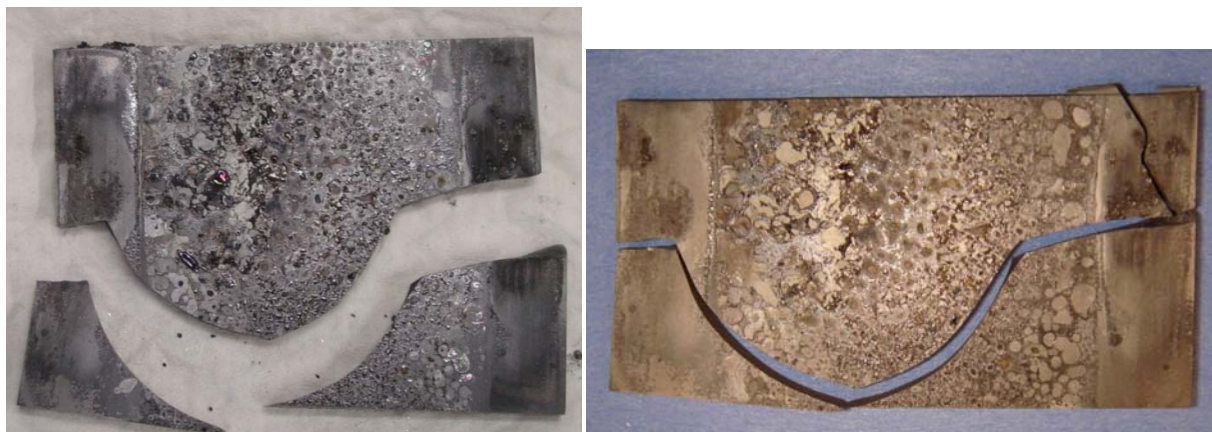
rectangular piece, 2.1" x 1.3" x 0.125", could be machined. This dimension was given as a final heating element trial specimen size. The hot-pressed specimens were analyzed by optical, SEM, and XRD for phase and microstructure analyses. Specimens were also subjected to static oxidation condition at the elevated temperature ($>1600\text{ }^{\circ}\text{C}$) for baseline data. Limited mechanical tests (microhardness and bend strength) will be also performed. After machining the billet into a heating element, the dimensions, volume and weight will be precisely measured and recorded. These heating elements will be delivered to AFRL/RBSV for testing in the black body furnace. After the black body furnace exposure, the tested material will be returned to us for the post test analysis. The analysis involves recession, weight loss, spallation and thermal shock damage. The results will be jointly analyzed and assessed by RBSV and RXLN scientists.

A number of hot-pressing experiments were carried out to establish the processing parameters (densification) of HfC, TaC, and 4TaC – 5HfC materials. For this optimization study, 1" diameter billets were produced. The processing parameters for the full densification of the above listed materials were established. Microstructural analyses of the listed materials were carried out using SEM. The XRD, hardness and strength measurements were performed on all the above listed materials and the data were documented.

In the mean time, the large hot-press was upgraded (new computer, labview software, and hydraulic system) and readied to produce large size billets (~80 mm diameter) of TaC, HfC, and 4TaC - 5HfC. After successful completion of the large billet hot-pressing, heating elements (rectangular pieces of 2.1" x 1.3" x 0.125") were EDM machined and delivered to VA. The HfB₂-20%SiC specimen was densified using SPS, and was also machined for the heating element trial using EDM. Two pieces of each type (except the HfB₂ – 20% SiC) were delivered to AFRL/RBSV at the end of FY07, along with supporting data (hardness, XRD, bend strength, fracture toughness, SEM microstructural analysis, fractography, dimensional measurements, etc.) for the materials. This concluded the delivery of the agreed upon 4 compositions (TaC, HfC, 4TaC - 5HfC, and HfB₂ – 20%SiC). After the blackbody resistive heating test by RB, the elements will be delivered to us for post characterization.

One panel of each material was exposed in the VASV test rig and the tested pieces, along with the untested pieces, were returned to AFRL/RXLN. The HfC, TaC, and 4TaC – 5HfC samples showed cracking at approximately 260 °C, presumably due to thermal and/or clamping stresses. The HfB₂ – 20% SiC sample was heated to ~1760 °C for approximately 15 minutes. Oxidation of the material occurred, as expected from work completed under Task 007; however, the material showed definite promise for use as a heating element. The HfB₂ – 20% SiC sample did crack upon cooling, which was likely due to the clamping of the sample. Further analysis was completed on only the HfB₂ – 20% SiC sample, as it showed the most promise.

The exposed piece fractured into three separate pieces, as shown in Figure 25. A slice of the material was cut for microstructural analysis. During this cutting process, an additional piece cracked, as shown in Figure 25b. The mottled surface of the material reflects the glass formation that occurred during testing.



(a)

(b)

Figure 25: HfB_2 – 20% SiC Piece Exposed in the RBSV Test Rig

(a) Image Taken by VASV Personnel

(b) Image Taken After Sectioning for SEM Analysis (Section Taken Away from Fracture Surface)

The results from the strip heater were analyzed using a model developed at AFRL/RXLN. A reasonable fit was obtained between the model and the experimentally measured data, as shown in Figure 26. The analysis shows that the cracking of the samples quite likely occurred from in-plane thermal gradients. A plan of action for future trials has been set. Samples with a smaller width (0.25”) were machined and delivered to AFRL/RB for testing using the strip heater.

David Hart of AFRL/RBSV presented details about the project to the RXLN Ceramics group, and the AFRL/RXLN Ceramics Group visited the AFRL/RBSV facilities to view the test apparatus in person. Further collaboration between the groups continued and is being handled by Lt. Aaron Kelly (AFRL/RXLN).

There was a delay in testing the materials at this point, due to the fear of hazardous volatile species being released during exposure at high temperature. After a number of discussions between AFRL/RX and RB safety personnel, the testing is scheduled to resume in FY10.

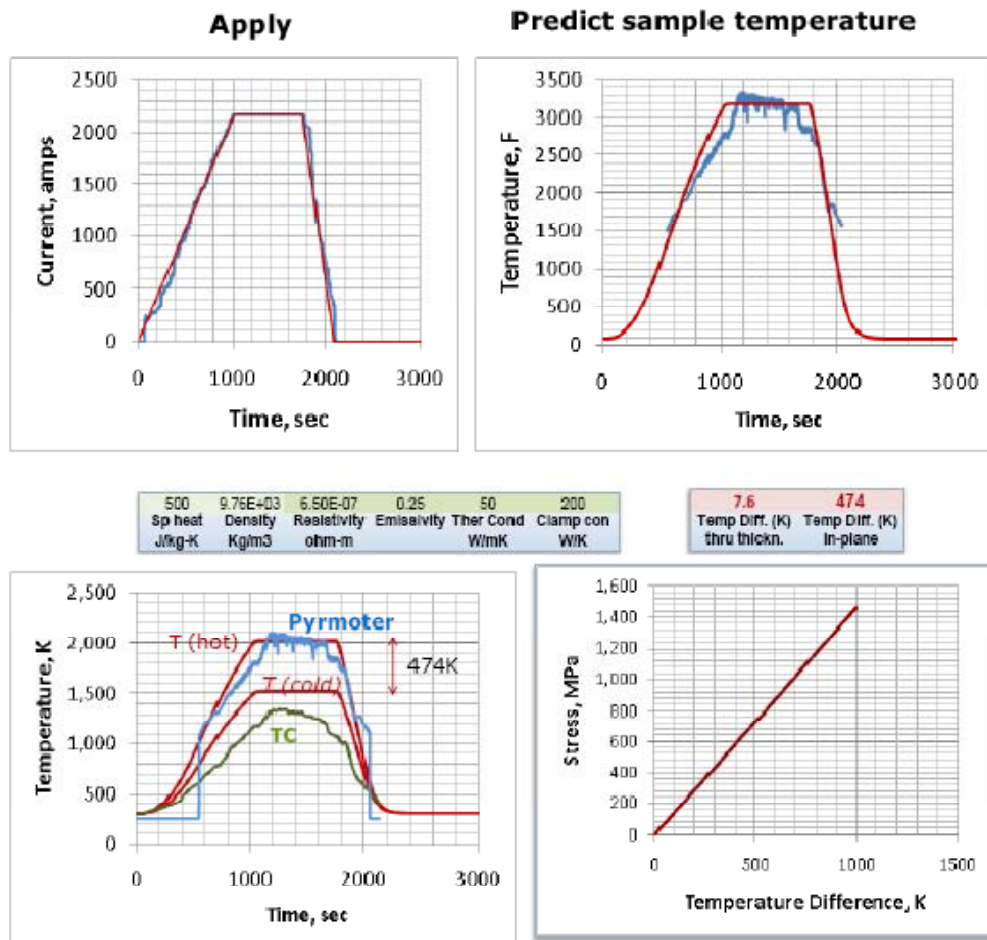


Figure 26: Model Predictions of Sample Temperatures Compared with Data Obtained During a Run of the Strip Heater using 20SiC-HfB₂ Sample

6.3.8 Deformation of Oxide Systems

Plastic deformation in indented natural single crystal YPO₄ and syntetic single crystal YVO₄ with xenotime structure was studied using TEM. Indentations with loads from 10 to 200 g were applied on (001) and (100) surfaces at room temperature. Focused Ion Beam (FIB) technique was used to machine electron-transparent foils with pre-defined orientations from specific locations in and around the indented areas. Three families of slip systems were observed. Most plastic deformation was carried out by two major slip systems, {100}<010> and {110}<1 $\bar{1}$ 0>. In addition, {101}<11 $\bar{1}$ > slip system and {112}<11 $\bar{1}$ > twinning system have also been observed.

6.3.9 Al₂O₃ – GdAlO₃ Eutectic Characterization

This work focused on evaluating the eutectic microstructures' resistance to coarsening with heat treatment. Microstructural comparisons were made between systems that form perovskites and systems that form garnet. The following systems were considered: Gd₂O₃- Al₂O₃, Sm₂O₃- Al₂O₃, Y₂O₃- Al₂O₃, and Yb₂O₃- Al₂O₃, although the primary focus was on the Al₂O₃ – GdAlO₃ system. The materials were melted and rapidly quenched by injecting the liquid between metal rollers to produce amorphous flakes. Each flake was heat treated for 30 minutes at one of the following temperatures: 900 °C, 1000 °C, 1100 °C, 1200 °C and 1300 °C. The resulting material was characterized using XRD, SEM/EDS, and TEM/EDS.

For the Gd₂O₃-Al₂O₃ system, the as-quenched material contained eutectic colonies with a pronounced crystallographic orientation. No changes were observed after the 900 °C heat treatment. Crystalline GdAlO₃ precipitates were observed after exposure at 1000 °C; clusters of GdAlO₃ precipitates exhibited preferred orientation even though they were dispersed in a still amorphous matrix. After heat treatment at 1100 °C, a eutectic-like microstructure, similar to that reported in the literature, was produced; nevertheless, the alumina phase still appears to be amorphous at this stage. After exposure at 1200 °C, a considerable portion of the material had an ordinary two-phase microstructure, though other regions contained microstructures that still resembled the eutectics with remaining crystallographic alignment of neighboring grains of GdAlO₃. Crystalline alumina appeared after heat treatment at 1200 °C and above. Items marked with an asterisk require further analysis and study.

The microstructure coarsens rapidly with the heat treatment temperature; however, eutectic colonies in the as-quenched material are coarser than the microstructure after 1000 °C and 1100 °C. This agrees with the hypothesis that eutectic colonies in the as-quenched material form from the liquid at higher temperature during solidification.

Preliminary investigations into the other listed systems revealed that at lower heat treatment temperatures (900 °C and 1000 °C), the materials are mostly amorphous. Systems with Sm, Y, and Yb have similar size eutectic microstructures after 1200 °C and 1300 °C exposures, while the Gd system had a much coarser eutectic microstructure. Alumina precipitates and some garnet precipitates were observed in most of the systems (and presumably formed in the melts), as aluminate or garnet phases are first to form. Further study is needed to confirm the described results.

6.3.10 AlON

MgO-doped AlON powders were prepared using alumina powder (Taimei) and aluminum nitride powder (Tokuyama F). Pure AlON was produced by the solid state reaction of alumina and AlN at 1500 °C for 2 ~ 5 hours. Under such reaction conditions, no significant sintering was observed so that it was possible to readily de-agglomerate the powder by conventional ball milling. MgO (0.5 wt. %)-doped AlON was prepared by adding Mg-nitrate using ethyl alcohol as a mixing solvent, followed by drying and calcination at 700 °C for 30 min in air atmosphere. The as-calcined MgO-doped AlON was granulated using a nylon sieve (-200 mesh) and hot pressed at temperatures between 1850-1870 °C for 2 hours with a BN sleeve and puncher. The hot-pressed

AlON appeared highly transparent but somewhat discolored (Figure 27). Further work on AlON was not pursued; however, experience gained in processing this transparent material was used in developing the YAG laser material discussed in this report.



Figure 27. Hot-Pressed MgO Doped AlON

6.4 Facilities

6.4.1 UCI

During this contract period, a significant amount of time was devoted to the implementation of the Unit Compliance Inspection (UCI) requirements in the RXL laboratories, as directed by the Air Force. Meetings and work were conducted on the Logistics Compliance inspection for the labs to prepare for the Unit Compliance Inspection in October 2006. Lab modules supporting RXLM (047, 047A, 048C, 049, 088, 091, 124, 128, 130, 133, 138, 140, 188, and 191) and RXLN (048C, 183, 185, 188, 191, 193, 195, 197, and 199) were brought into logistics compliance in the areas of tool control, equipment management, and support stock management for the UCI. The labs were cleaned and equipment, supplies, and tools were turned in that were no longer needed for the mission. Cabinets and drawers were cleaned and contents were organized in bins or separate containers to insure neat and orderly storage. Extensive labeling of all cabinets and drawers was accomplished. Locations for equipment on the floor and countertops were notated and labeled. Self inspection forms concerning fabrication, hydraulics, industrial safety, maintenance program tests, respiratory protection, general logistics responsibilities, equipment, tool control, and FOD programs from RXOF were completed and submitted to RXOF (some twice at their request).

An inventory of equipment with descriptors for each piece of equipment was prepared in an Excel spreadsheet. The inventory included the due dates for the Preventive Maintenance Inspection (PMI) for equipment tagged with 244's and the calibration of Test, Measurement, and Diagnostic Equipment (TMDE). This was used to populate the New Equipment and Turn-ins (NEAT) database maintained by RXOF. TMDE with calibration stickers from the Precision Measurement Equipment Lab (PMEL) were examined to insure that the equipment was within calibration or not in need of calibration. All TMDE must be in the PMEL inventory. Therefore if the TMDE had no PMEL stickers, they were tagged with an Air Force technical order (AFTO) form 350 with the designation in block 15 of "Do Not Use" or "Do Not Use Without Director Approval" in bold red letters plus the Point of Contact (POC) and other explanatory notes. This

TMDE was inventoried and listed on a New Item Calibration Determination form for each lab and submitted to PMEL. Each system that included several pieces of TMDE that needs to be calibrated was designated on another form and was submitted per lab to PMEL. A spreadsheet of commercially calibrated equipment in RXLM and RXLN was developed for RXO and copies of calibration certificates were submitted to RXO. Equipment calibration was initiated by submission of items to PMEL and by contracting manufacturers to calibrate test systems on site.

All equipment requiring periodic maintenance was tagged with an appropriately filled out AFTO form 244. Most equipment not in the category of TMDE was tagged with forms DD1574 (Serviceable), 1577-2 (Unserviceable/Repairable), or 1577 (Unserviceable/Condemned) designating the serviceability of the equipment and whether it is useable. Equipment manuals were identified, marked with "For Reference Only," and were submitted to MLOF for copying. These were then put into the Technical Data System (TDS) located on the Enterprise Business System (EBS) web site.

Another logistics area for the Unit Compliance Inspection includes tool control. Eighteen Composite Tool Kits (CTK; RXLM – 13, RXLN – 5) were established, populated with tools, inventoried, and the tools were etched by RXOF with the CTK identifier. The CTK's keys were marked, organized, and placed in a central location. The CTK's are the responsibility of the branch chief. Therefore, signatures from the branch chiefs for the CTK Master Inventory Lists were procured. The CTK's are inspected semiannually. Stock management was accomplished by determining whether the stock in each lab was component or exempt (general consumable) stock. A stock plan noting the number of containers and item category was developed for each lab having exempt stock and will be under the jurisdiction of Logistics Material Control Activity (LMCA). All spare circuit boards in 655/128 were put in Anti-Electrostatic Discharge bags and placed in storage.

Self Inspection Programs were instituted in preparation for the SAV (Staff Assisted Visit) inspections to insure that RXLN had maintained logistics compliance.

6.4.2 Safety

Monthly safety inspections were conducted with Larry Dukate and steps were taken to correct safety violations. Monthly quality assurance inspections were performed and corrective actions for violations were implemented. Monthly fire extinguisher inspections were accomplished. Annual grounds safety inspections were conducted. Various people were trained on major equipment to insure that each piece of equipment has several personnel knowledgeable in its operation. The laser inventory was brought up to date and all lasers were given permits by the base radiation safety office.

Health Risk Assessment surveys were conducted with inspections by the Environmental Safety and Occupational Health Manager, a representative of the Bioenvironmental Engineering office and the Unit Safety Representative/Chemical Hygiene Officer (currently Larry Dukate). Michael Martin (Bioenvironmental Engineering/General Dynamics contractor) and the CHO were escorted for a biennial safety assessment of ceramic labs and 188/191.

Numerous safety issues were addressed in each lab module including Personal Protective Equipment (PPE), labeling of fluid lines and the pressure they carry, and various hazards. A Lockout / Tagout (LOTO) program was initiated for each lab with inventories of equipment considered to be LOTO. Procedures for implementing LOTO for individual pieces of equipment were developed and posted on the lab doors. They were also submitted to RXOF and Larry Dukate (Unit Safety Representative). Personnel were trained in the LOTO procedures, training which is required annually.

Thoriated tungsten components were collected from the labs under the supervision of the Radiation Safety Office (Ben Wilmoth, ABW/SEVO) and Jeff Wenning (ML Safety Officer) and either turned over to the Radiation Safety Office or placed in a central location with signs posted at the location noting a radiation hazard. The Micromeritics mercury porosimeter was turned in, which required numerous meetings including a meeting with Rod Steele (CHO/RXO), Jeff Harris (AFRL Ground Safety Manager), and Phil Rich concerning the proper means of containing the mercury for instrument turn in.

6.4.3 Equipment

Equipment that was acquired during this contract period includes the TMA/SDTA (Thermo Mechanical Analysis/Single Differential Thermal Analysis) 840 (room temperature to 1100 °C) and TMA/SDTA 841e (-150 °C to 600 °C), a FCT Pulsed Electric Current Sintering unit (191), a Makino wire EDM (130), a miniature sand blast cabinet (048C) to mechanically remove residual grafoil from hot pressed specimens, a Shinagawa high temperature furnace and a Cary 500 spectrophotometer. Equipment that has been turned in or transferred this contract period includes the salt fog/humidity chamber (to AFIT), the CVD apparatus and accessories that were in and near the walk-in hood, the Brew vacuum furnace (model 426B), the K.O. Lee surface grinder and the Harrop TGA.

An upgrade to the control system of the large hot press was implemented. An emergency cooling system for both hot presses (655/048C) that can be used in case of water pump shut down due to building power failure was designed and installed. All Government Furnished Equipment on the contract were inventoried and properly marked with GFP stickers. Emergency Stop Switches and anti-automatic restart protection switches were installed on the required equipment. Coordination with computer support was implemented to set up computers for control and data collection for new equipment.

Renovations for the labs in Rm. 197 and 199 were completed. The island in room 197 was enlarged by adding new base cabinets to the existing cluster of cabinets. Utilities were provided at a corner of the island, a canopy hood was installed over the island, and a stone surface plate counter top was mounted on the cabinets. Room 199 was renovated and analytical equipment was moved into it to optimize the ability for the scientists and engineers to conduct their experiments more efficiently in a clean environment and without interference.

6.5 Publications

1. T. A. Parthasarathy, L. P. Zawada, R. John, M. Cinibulk, R. J. Kerans, and J. Zelina, "Evaluation of Oxide-Oxide Composites in a Novel Combustor Wall Application," *Int. J. Appl. Ceram. Tech.*, **2** [2] 122-132 (2005).
2. T. A. Parthasarathy, M. K. Cinibulk, and L. P. Zawada, "Combined Effect of Salt Water and High-Temperature Exposure on the Strength Retention of Nextel™ 720 Fibers and Nextel™ 720-Aluminosilicate Composites," *J. Am. Ceram. Soc.*, **89** [4] 1373-1379 (2006).
3. T. A. Parthasarathy, G. J. Jefferson, and R. J. Kerans, "Analytical evaluation of hybrid ceramic design concepts for optimized structural performance," *Mater. Sci. & Eng.*, **A459** 60-68 (2007).
4. T. A. Parthasarathy, R. J. Kerans, S. Chellapilla, and A. Roy, "Analysis of ceramics toughened by non-conventional fiber reinforcement," *Mater. Sci. & Eng.*, **A443** 120-131 (2007).
5. G. Fair, R. J. Kerans, and T. A. Parthasarathy, "Thermal history sensor based on glass-ceramics," *Sensors and Actuators*, **A141** 245-255 (2008).
6. G. Jefferson, T. A. Parthasarathy, and R. J. Kerans, "Tailorable thermal expansion hybrid structures," *Int. J. of Solids and Struct.*, **46** 2372-2387 (2009).
7. P. Mogilevsky, "Identification of slip systems in CaWO₄ scheelite," *Phil. Mag.*, **85** [30] 3511-3539 (2005).
8. P. Mogilevsky and T.A. Parthasarathy, "Anisotropy in room temperature microhardness and indentation fracture of xenotime," *Mater. Sci. and Eng.*, **A454-A455** 227-238 (2007).
9. E. Zaretsky and P. Mogilevsky, "Mechanisms of plastic deformation and shock-induced phase transformation in natural and synthetic single crystal scheelite," *High Pressure Research*, **26** [4] 555-558 (2006).
10. P. Mogilevsky, T. Mah, T. A. Parthasarathy, and C. M. Cooke, "Toughening of SiC with Ti₃SiC₂ Particles," *J. Am. Ceram. Soc.*, **89** [2] 633-637 (2006).
11. T. A. Parthasarathy, M. D. Petry, G. Jefferson, M. K. Cinibulk, T. Mathur and M. R. Gruber, "Development of a Test to Evaluate Aerothermal Response of Materials to Hypersonic Flow Using a Scramjet Wind Tunnel," *Int. J. Appl. Ceram. Technol.*, published on-line, 1-16 (2010).
12. M. Braginsky and G. Jefferson, "Modeling of ceramic matrix composites with complex fiber architecture," to be submitted to *Comp. Sci. and Tech.*, 2010.

6.6 Presentations

1. R. J. Kerans, T. A. Parthasarathy, P. Mogilevsky, "Measurement and Interpretation of Interface Properties in Ceramic Composites", presented at HTCMC-6, New Delhi, India, September 2007.
2. M. Braginsky and G. Jefferson, "Modeling of Ceramic Matrix Composites with Complex Fiber Architectures," presented at the 34th Annual Conference on Composites, Materials and Structures (US. Only/ITAR-Restricted Sessions), Cape Canaveral/Cocoa Beach, FL, January 25-28, 2010.

6.7 Book Chapters

1. K. Jata, T. Kundu, and T. A. Parthasarathy, "An introduction to failure mechanisms and ultrasonic inspection" in Advanced Ultrasonic Methods for Material and Structure. Edited by T. Kundu, Hermes Science Publishing, UK, 2006.

6.8 Patents/Invention Disclosures

1. G. Fair, T. A. Parthasarathy, and R. J. Kerans, Thermal history sensor, U.S. Patent No. 6,974,249 B1 (December 13, 2005).
2. G. Fair, T. A. Parthasarathy, and R. J. Kerans, Polymeric thermal history sensor, U.S. Patent No. 7,080,939 (July 25, 2006).
3. R. J. Kerans and T. A. Parthasarathy, Hybrid composite materials, U.S. Patent No. 7,279,230 (Oct 9, 2007).
4. G. Fair, E. E. Boakye, and T. A. Parthasarathy, Coating ceramic fiber tows and woven articles, U.S. Patent No. 7,494,691 (Feb 24, 2009).
5. G. Jefferson, R. J. Kerans, and T.A.Parthasarathy, Air Force Invention Disclosure (2005).
6. R. S. Hay, A. Craven, E. E. Boakye and K.A. Keller, "Lutetium Aluminum Garnet (LuAG) & Yttrium Aluminum Garnet (YAG), Catalyst Substrates for HAN Monopropellants," submitted for Air Force Invention Disclosure (2009).

6.9 References

1. T. A. Parthasarathy, L. P. Zawada, R. John, M. Cinibulk, R. J. Kerans, and J. Zelina, "Evaluation of Oxide-Oxide Composites in a Novel Combustor Wall Application," *Int. J. Appl. Ceram. Tech.*, **2** [2] 122-132 (2005).
2. T. A. Parthasarathy, M. K. Cinibulk, and L. P. Zawada, "Combined Effect of Salt Water and High-Temperature Exposure on the Strength Retention of Nextel™720 Fibers and Nextel™ 720-Aluminosilicate Composites," *J. Am. Ceram. Soc.*, **89** [4] 1373-1379 (2006).
3. K. Jata, T. Kundu, and T. A. Parthasarathy, "An introduction to failure mechanisms and ultrasonic inspection" in Advanced Ultrasonic Methods for Material and Structure. Edited by T. Kundu, Hermes Science Publishing, UK, 2006.
4. T. A. Parthasarathy, G. J. Jefferson, and R. J. Kerans, "Analytical evaluation of hybrid ceramic design concepts for optimized structural performance," *Mater. Sci. & Eng.*, **A459** 60-68 (2007).
5. T. A. Parthasarathy, R. J. Kerans, S. Chellapilla, and A. Roy, "Analysis of ceramics toughened by non-conventional fiber reinforcement," *Mater. Sci. & Eng.*, **A443** 120-131 (2007).
6. G. Fair, R. J. Kerans, and T. A. Parthasarathy, "Thermal history sensor based on glass-ceramics," *Sensors and Actuators*, **A141** 245-255 (2008).
7. G. Jefferson, T. A. Parthasarathy, and R. J. Kerans, "Tailorable thermal expansion hybrid structures," *Int. J. of Solids and Struct.*, **46** 2372-2387 (2009).

8. P. Mogilevsky, "Identification of slip systems in CaWO_4 scheelite," *Phil. Mag.*, **85** [30] 3511–3539 (2005).
9. P. Mogilevsky and T.A. Parthasarathy, "Anisotropy in room temperature microhardness and indentation fracture of xenotime," *Mater. Sci. & Eng.*, **A454–455** 227–238 (2007).
10. E. Zaretsky and P. Mogilevsky, "Mechanisms of plastic deformation and shock-induced phase transformation in natural and synthetic single crystal scheelite," *High Pressure Research*, **26** [4] 555–558 (2006).
11. P. Mogilevsky, T. Mah, T. A. Parthasarathy, and C. M. Cooke, "Toughening of SiC with Ti_3SiC_2 Particles," *J. Am. Ceram. Soc.*, **89** [2] 633–637 (2006).
12. M. Braginsky and G. Jefferson, "Modeling of ceramic matrix composites with complex fiber architecture," to be submitted to *Comp. Sci. and Tech.*, 2010.
13. ABAQUS Analysis User's Manual.
14. W-G Jiang, S. R. Hallett and M R. Wisnom, "Development of Domain Superposition Technique for the Modelling of Woven Fabric Composites," Proceedings of ECCOMAS Thematic Conference Mechanical Response of Composites, September 12-14, 2007.
15. W-G Jiang, S. R. Hallett, and M. R. Wisnom, "Development of Domain Superposition Technique for the Modelling of Woven Fabric Composites," in Mechanical Response of Composites, volume 10 of the book series Computational Methods in Applied Sciences, Springer Netherlands, 2008.
16. R. S. Hay, T. Mah and C. Cooke, "Molybdenum-Palladium Fiber-Matrix Interlayers for Ceramic Composites," *Ceram. Eng. & Sci. Proc.*, **15** [5] 760-768 (1994).
17. J. Dawson, et. al., "Analysis of the scalability of diffraction-limited fiber lasers and amplifiers to high average power," *Opt. Expr.*, **16** [17] 13240-13266 (2008).
18. R. S. Hay, A. Craven, E. E. Boakye and K.A. Keller, "Lutetium Aluminum Garnet (LuAG) & Yttrium Aluminum Garnet (YAG), Catalyst Substrates for HAN Monopropellants," submitted for Air Force Invention Disclosure (2009).
19. Y. P. Udalov, E. E. Valova, S. S. Ordan'yan, "Preparation and Abrasive Properties of Eutectic Compositions in the System B_4C -SiC- TiB_2 ," *Refractories*, **36** [7-8] 233-234 (1995).
20. W. Li, R. Tu, and T. Goto, "Preparation of Directionally Solidified B_4C - TiB_2 -SiC Ternary Eutectic Composites By a Floating Zone Method and Their Properties," *Mater. Trans.*, **46** [9] 2067 (2005).

6.0 TASK ORDER 0005 – SPACE MIRROR PROGRAM

6.1 Introduction

The ultimate goal of the space mirror program is to seek new functional materials systems that can be incorporated into the state-of-the-art hybrid mirror design, enabling the economic fabrication of space mirrors and tackling several critical technical barriers currently encountered in using space organic polymers. In order to achieve each of the goals, the following proposed subtasks were explored and accomplished:

1. Production of negative CTE nano-powder (zirconium tungstate: ZrW_2O_8).
2. Production of surface functionalized zirconium tungstate powders for space organic resins.
3. Fundamental studies for producing the geopolymers with tailored properties, such as coefficient of thermal expansion (CTE) and curing shrinkage.

The work has shown considerable advances in Subtasks 1 and 2. To date, the scale-up to 100 grams of nano-sized zirconium tungstate powder was very successful, with each run using a 2 L hydrothermal reactor. The production capacity can be increased by increasing the reactor size. Subtask 3 was aimed at developing inorganic geopolymer adhesives/substructures that can be applied for the replicated laminate mirrors. A successful application requires both zero-curing shrinkage and an appropriate CTE match. The results were very successful in tailoring the CTE of the geopolymer adhesives, as well as the geopolymer substructures. The CTE of the geopolymer was successfully custom tailored by incorporating nano-sized zirconium tungstate powder, which shows a negative CTE.

The organic resins currently being used for space applications have shown several critical problems, including a large curing shrinkage as well as a large CTE mismatch. One of the potential solutions may be to include inorganic filler materials with negative or low CTEs such as micron-sized glass balloons, carbon nanofibers (CNFs), or acicular zirconium tungstate powder. In order to obtain desirable results, it is of utmost importance to engineer the interfaces, where the resin matrix and the filler materials are strongly bonded together, and the CTE tailoring of the EPON828 epoxy resin was successfully demonstrated by dispersing the negative CTE acicular powder, along with a high thermal stability.

Our studies in the space mirror program have shown considerable progress in the area of geopolymers. We have learned which technical issues immediately need to be understood and improved. For example, the properties of the geopolymers strongly depend on the chemistries but the curing condition also appears to be a critical factor in the shrinkage. A single composition appeared to show many different behaviors that seemed to be linked with different curing variables and post heat treatments. The results strongly suggest that neither a single composition nor a single processing variable can determine the final properties for all applications; geopolymers themselves will need to be engineered to meet each specific application. To address this problem, further systematic studies will be required to examine the curing variables (temperature, atmosphere, time) in order to control the curing shrinkage. Various filler materials were also tried for the same purpose, and the results clearly indicated some benefits. Chemically

compatible filler materials, with a suitable morphology such as a high aspect ratio (fiber, whisker, balloon, etc.), were considered as an effective means to suppress the shrinkage through physical constraints when the filler was uniformly dispersed in the geopolymer matrix.

However, to solve all of the raised technical issues and problems, we learned that the curing process of the baseline materials system must be thoroughly understood. Information concerning the CTE and shrinkage of the baseline materials is essential and needs to be evaluated in terms of the various curing conditions and compositions. An equally important question is which materials system shows good casting capability and workability. In the beginning of the program, two baseline materials systems were explored: (1) kaolin (MK)-based geopolymer and (2) non-kaolin (commercial)-based geopolymer. Towards the end of the program, blast furnace slag and coal fly ash were utilized to improve the needed properties.

The MK-based geopolymer is historical, but little information is available in respect to its casting capability or workability. Workability is a term describing a measure of the lead time before casting. These two aspects are very important. Neither poor workability (too fast curing) nor low casting quality (due to poor rheology) are acceptable for actual use. Recent work showed that the MK-based geopolymer exhibited a very narrow processing window pertaining to these two aspects. Alternately, the non-MK system (commercial geopolymer) was outstandingly workable and castable. This difference could be primarily related to the use of different raw minerals. This seems likely, based on the differences in dissolution and speciation with different curing behavior. Because of its poor slurry rheology, MK-based specimens were not high quality and therefore, reliable measurements of CTE, as well as curing shrinkage, have not been achieved. On the contrary, the non-MK system did not show such problems; however, the measured properties (e.g. CTE, shrinkage) were shown to have a strong dependency on both the curing conditions and the post heat treatments. This was also observed to a moderate extent in MK-based geopolymers. However, the slag-based geopolymer with an addition of MK resulted in near-zero curing shrinkage and high thermal stability. Currently, various curing conditions are being explored for the better results by using a humidity-controlled chamber.

Based on our experimental observations and knowledge of the technical barriers, it suffices to say that the geopolymerization and the final material properties could largely depend on the choices of starting materials, curing conditions (temperature, time, and atmosphere), and post heat treatments, although the overall chemistry is the same. As the results, the further systematic exploration will be needed to obtain a thorough understanding, as well as to practice for use in potential applications.

6.2 Overview

Space based mirrors that operate under ambient thermal conditions are currently made from glass. These glass mirrors have a high areal density on the order of 30 kg/m^2 because glass is not a good structural material. Therefore, facesheets, webs, and backplates have to be fabricated as thick sections. New materials such as SiC are being investigated both as the mirror or just its structural substrate to reduce weight and areal density. New design methodologies such as a hybrid mirror design are being considered to reduce cost and schedule. Here the structural substrate and a replicated faceplate are fabricated separately and bonded together eliminating the need to polish each mirror. In order to make this design work the coefficient of thermal expansion (CTE) of all the materials have to be matched and there can be no shrinkage of the bonding agent. Much work is needed to make this technology possible.

The primary objective of this work was the development and characterization of non-shrinking, CTE tailorable geo-polymer adhesives. To achieve this goal, several subtasks were identified.

Subtask 1: Production of negative CTE nano-powders for CTE tailorability of inorganic geo-polymer adhesives.

Subtask 2: Modification of CTE tailored adhesives to achieve zero shrinkage upon curing.

Subtask 3: Conduct bonding trials with the candidate adhesive(s).

6.2.1. Subtask 1 - Production of Negative CTE Nano-Powders for CTE Tailorability of Inorganic Geo-Polymer Adhesives

Much work has been conducted to establish the foundation of the negative coefficient of thermal expansion behavior [1-5]. The isotropic thermal contraction and unusually large value of coefficient of negative thermal expansion ($-9 \sim -5 \times 10^{-6}/\text{K}$) are the most attractive features, and one can speculate that, by incorporating the negative CTE compound into the given materials system, the thermal expansion behavior can be tailored.

However, the cubic zirconium tungstate exhibits a narrow temperature stability range ($1100 \sim 1200^\circ\text{C}$). In general, the powder can be synthesized through solid state reactions at high temperatures. This precludes the powder production with a single phase, due to the high volatility of WO_3 , and it has been difficult to obtain submicron-sized powder [6-11] with this method. Consequently, the lower temperature routes are favorable, and this has remained a challenge. We have recently been developing a low temperature process to produce single phase, nano-sized cubic zirconium tungstate powder using a novel solution chemistry, along with a hydrothermal process. The goal of the research program was to develop an economic process that can produce highly pure nano-sized powder with an easy scale-up and high processing fidelity.

Recent technical advancements showed that nano-sized, cubic ZrW_2O_8 powder with acicular or spherical particle morphologies can be successfully produced by a combination process of the hydrothermal process and a novel precursor chemistry at temperatures below 600°C .

6.2.1.1 Experimental Procedures and Results

Zirconium oxychloride hydrate (Alfa), $\text{ZrOCl}_2 \cdot 8\text{H}_2\text{O}$, and ammonium metatungstate hydrate (Alfa), $(\text{NH}_3)_4\text{W}_{12}\text{O}_{39} \cdot x\text{H}_2\text{O}$, were used to prepare the precursors. First, 0.1 mole of zirconium oxychloride hydrate was dissolved in 1000 cc of de-ionized (DI) water, and titrated with 1:1 NH_4OH (conc. NH_4OH diluted with DI water with a 1:1 v/o). The white gel (zirconium oxy-hydroxide) was precipitated. Subsequently, the precipitate was filtrated, washed, rinsed until the pH reached ~ 7.5 , and finally re-dispersed with 500 cc of DI water. The re-dispersed white zirconium oxy-hydroxide precipitate was then completely dissolved by adding a diluted 1:1 HNO_3 (1:1 v/o) solution under vigorous stirring with a magnetic Teflon bar. Subsequently, the Zr concentration was estimated using thermogravimetric analysis (TGA) at 1000°C for 1 hour in air. Also, 0.2 mole of the as-received ammonium metatungstate hydrate was dissolved in 1000 cc of DI water, and the thermogravimetric assay was then conducted by calcination at 550°C for 5 hours in air using a platinum container with a lid. The calcined product appeared yellow and was identified as WO_3 by X-ray powder diffraction. To increase the accuracy, the TGA assay was repeated more than three times, and the average value was used to prepare the precursor mixtures.

The solid precursor for ZrW_2O_8 was prepared with the precursor mixtures, after mixing the equivalent amounts of the stock solutions containing Zr and W, followed by the addition of more than twice the number of moles of ammonium nitrate with respect to the metal cations. This was designed to avoid the precipitate, and to control the reaction kinetics between zirconium oxynitrate and ammonium metatungstate. Without the addition of ammonium nitrate, the whitish gel-like precipitates formed immediately upon mixing, resulting in hard aggregates after washing and drying.

Two hundred and fifty cc of the precursor mixture was transferred to a 500 cc glass flask with a tight seal, and subsequently aged for 24 hours in an ambient atmosphere. The white precipitate slowly formed during the 24 hour aging. Then, the precursor mixture was finally transferred in an oven (70°C), and further aged for 24 hours to complete the precipitation. The precipitates were then vacuum filtrated, washed thoroughly, and finally rinsed with ethanol prior to drying at ambient temperature. The dried, amorphous precipitates appeared very weakly agglomerated, to flow well, and to be easily dispersed.

The dried precipitates (~ 4 g) were mixed with 200 cc of 6 M HCl , and refluxed for 3 \sim 10 hours at $50 \sim 60^\circ\text{C}$ under vigorous stirring. The refluxed precipitates were then hydrothermal processed at $170 \sim 175^\circ\text{C}$ for 5 \sim 15 hours using a Teflon-lined Parr pressure vessel. The as-hydrothermal processed precipitates were filtrated, washed, rinsed with Ethanol, and dried in an ambient atmosphere. Differential thermal analysis (DTA) and XRD were performed to study the phase transitions as well as to identify the phases. The morphologies and sizes of the particles were examined using scanning electron microscopy SEM analysis.

The results associated with refluxing are summarized in Figure 28. The dried precipitates without refluxing were also hydrothermally processed at various conditions. The morphologies and sizes of the particles can be seen in Figure 29.

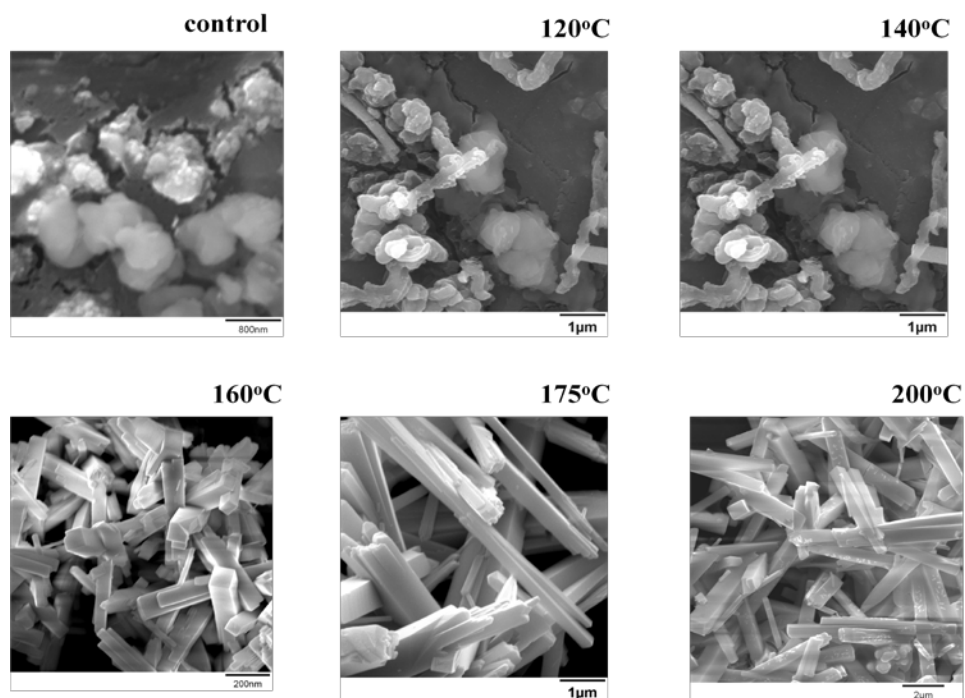


Figure 28. Refluxed Particle Morphologies after Hydrothermal Processing for 7 hours at Different Temperatures

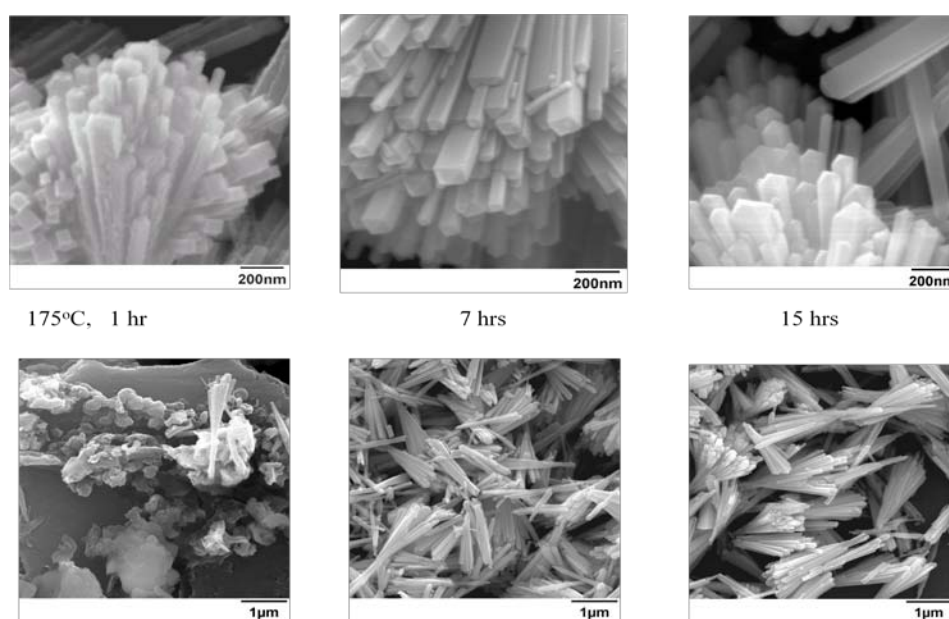


Figure 29. Particle Morphologies without Refluxing after Hydrothermal Processing at 175 °C for Different Time periods

As seen in Figures 28 and 29, the dried precipitates after hydrothermal processing appeared as acicular particles, regardless of refluxing at temperatures above 170 °C. The particle size can be increased with refluxing. Also, the re-precipitation may be completed at least at temperatures above 160 °C. Particularly, the nano-sized, acicular hydrates with crystalline phase (tetragonal), as well as with an aspect ratio of 4~5, was predominant at 160 °C. These crystalline hydrates can be converted to crystalline cubic ZrW_2O_8 after calcining at 600 °C. The particle morphology (Figure 30) was retained after calcination.

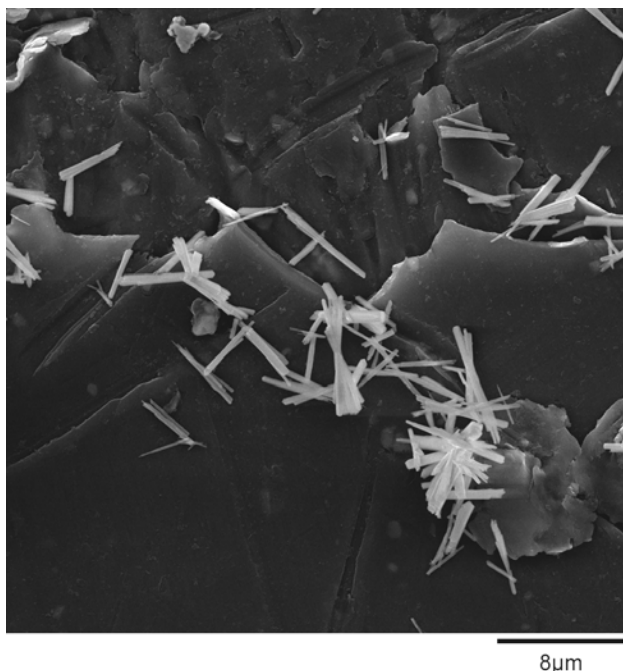


Figure 30. Acicular Crystalline Cubic ZrW_2O_8 After Calcination at 600 °C

The crystalline hydrates appeared very fragile, and thus readily ball milled to nano-sized powder with a spherical shaped morphology. Subsequent calcination at 600 °C produced the crystalline cubic ZrW_2O_8 powder with the spherical particle morphology, as shown in Figure 31.

The X-ray powder diffraction patterns of the dried precipitates, as well as the crystalline hydrates after hydrothermal processing, are compared in Figure 32, along with crystalline cubic zirconium tungstate, which was calcined at 600 °C for 30 minutes in an ambient atmosphere. All of the peaks for the hydrates and zirconium tungstate were identified as those peaks of the crystalline phases of tetragonal $\text{ZrWO}_7(\text{OH})_2 \cdot 2\text{H}_2\text{O}$ and cubic ZrW_2O_8 , respectively. No extra peaks were observed.

The zirconium tungstate powder, produced by the hydrothermal process is compared in Figures 33 and 34 with a commercially available zirconium tungstate powder (Wah Chang). In Figure 33, a few extra peaks, which have not yet been identified, are observed for the commercial powder. SEM analysis (Figure 34) revealed that the commercial powder was coarse, with sizes ranging from a few microns to tens of microns in size, while the AFRL/UES powder was nano-sized.

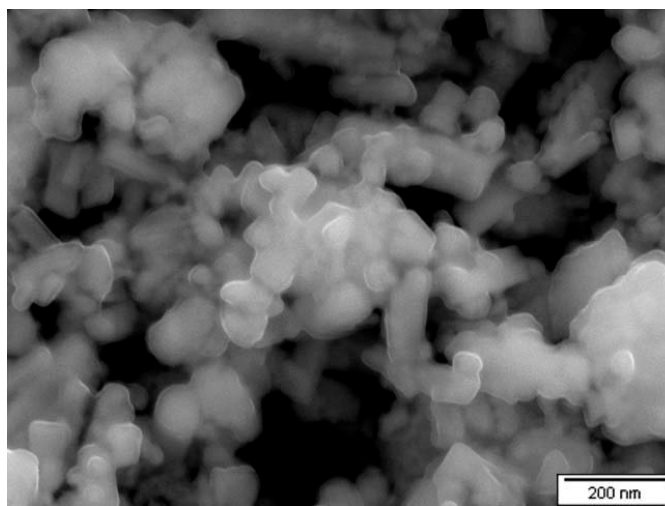


Figure 31. Crystalline Cubic ZrW_2O_8 After Calcination Followed by Ball Milling the Crystalline Hydrates

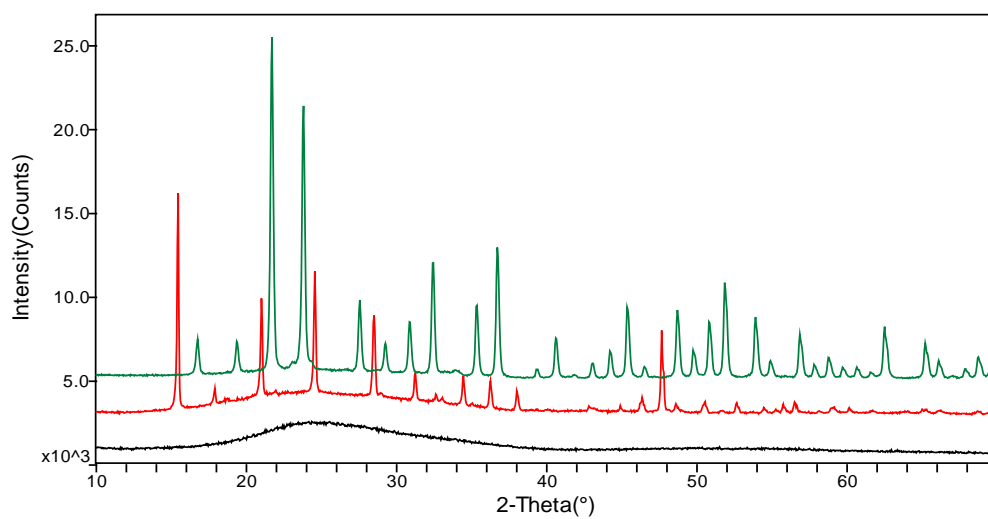


Figure 32. X-ray Powder Diffraction Patterns
 (a) *Precipitates,*
 (b) *Hydrates after Hydrothermal Processing, and*
 (c) *Cubic Zirconium Tungstate After Calcination at 600 $^\circ\text{C}$*

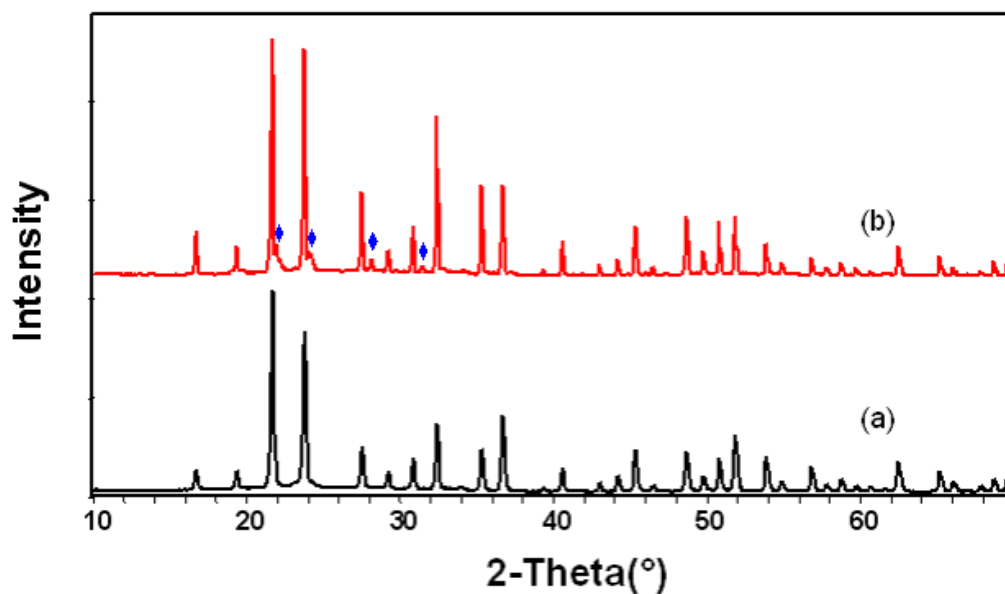


Figure 33. X-ray Diffraction Patterns of Cubic Zirconium Tungstate
 (a) AFRL/UES
 (b) Commercial Powder (Wah Chang)

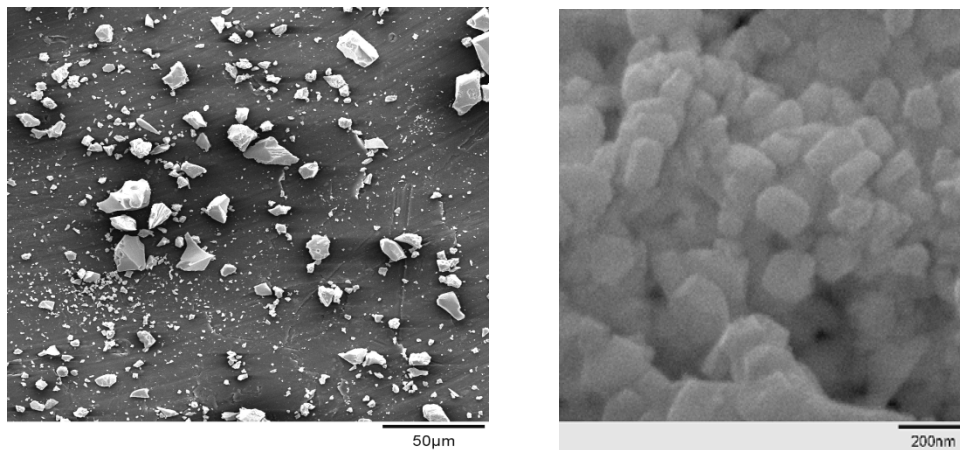


Figure 34. SEM micrographs of Zirconium Tungstate Powder
 (a) Commercial Powder (Wah Chang) Showing very Coarse Particles with a Wide Size Distribution (a Few Microns to Tens of Microns in Size)
 (b) Nano-sized Powder Produced using a Novel Chemistry Followed by Hydrothermal Processing (AFRL/UES)

6.2.1.2 Scale-Ups for Powder Production

Based on the preliminary results, a scale-up study was conducted to produce a large volume of crystalline hydrate ($\text{ZrWO}_7(\text{OH})_2 \cdot 2\text{H}_2\text{O}$) powder. Because of a potential reaction between the hydrothermal reactor and the precursor mixture solution, a preliminary study was carried out to determine a suitable material for the high pressure reactor; this was conducted in collaboration with the vendor (Parr Instrument Company, IL). A series of alloy coupons were obtained from the vendor; SUS 304 and 316, Ti64 alloy, alloy 600 and 400, alloy B-2 and C-276, Hastelloy C-2000, alloy 20CB3, and Zr alloy. All of the alloy coupons were put into a Teflon-lined small reactor and hydrothermally processed with the precursor mixture solution. The results showed that the Zr alloy was the best, with a minimal sign of reaction. A 2000 cc reaction vessel was made of Zr-alloy material, along with a stirrer and a thermocouple envelope. The pressure was monitored by 0-1000 psi pressure gage with a buffer junction. The 2-L reactor can be heated up to a maximum temperature of 300 °C, with a pressure up to 720 psi.

Based on a series of studies, 100 grams of crystalline hydrate powder were successfully produced per each run at temperatures between 160 °C and 170 °C for a 2 hour reaction period. The as-hydrothermally processed slurry was filtrated and rinsed for the final calcination. The as-filtered solvent (HCl aqueous solution) was preserved and reusable; so far, more than 15 runs were made with an original solvent, and the solvent condition appeared to be continuously reusable.

6.2.1.3 Subtask 1 Summary

A highly crystalline, phase pure cubic zirconium tungstate (ZrW_2O_8) powder with two different particle morphologies (acicular and spherical particle shapes) have been successfully produced via a two-step powder synthesis process. First, the solid precursor was prepared by co-precipitating the liquid precursor mixtures with a controlled precipitation process. The effects of the refluxing process were examined in terms of the particle morphologies, and the results suggested a slight effect on the particle size; the refluxed precursor resulted in large particles compared to un-fluxed precursor after hydrothermal processing at the same conditions. The as-precipitated amorphous precursor (dried precipitates) was then hydrothermally processed in an acidic atmosphere (6 M HCl) at temperatures below 175 °C to produce tetragonal crystalline hydrates ($\text{ZrWO}_7(\text{OH})_2 \cdot 2\text{H}_2\text{O}$). Subsequently, the crystalline cubic ZrW_2O_8 was produced by calcining crystalline hydrates at 600 °C. The particle morphologies remained identical before and after calcination. The particle morphologies can also be tailored to acicular or spherical, depending on the initial morphologies of the crystalline hydrates; the crystalline hydrates appeared initially acicular in shape but they can be readily ground to a spherical shape by a high energy ball milling process.

The cubic crystalline ZrW_2O_8 powders produced by a hydrothermally-assisted lower temperature calcination process (a two-step powder synthesis) showed high quality powder characteristics, including high phase purity, softly agglomerated, and custom-tailored particle morphologies.

6.2.2 Subtask 2: Modify the CTE Tailored Adhesives to Achieve the Objective of Zero Shrinkage Upon Curing.

6.2.2.1 Tailoring Thermal Expansion of Geopolymer with Negative CTE Oxide Powders

Geopolymers and their composites are a relatively new class of ceramic materials whose intrinsic properties and potential applications are relatively under-explored. Pure geopolymers (Figure 35) are rigid, inorganic, aluminosilicate hydrated gels, charge balanced by the presence of Group I cations such as Na^{+1} , K^{+1} , or Cs^{+1} . Geopolymers have a range of compositions, and are totally inorganic, acid resistant, thermal shock resistant and refractory. Upon heating, these refractory adhesives become even stronger as the gel converts to a ceramic of corresponding starting composition. The intrinsic microstructure is nano-porous (~ 3.4 nm radius) and nano-particulate (≤ 5 nm in size), and the typical porosity constitutes $\sim 40\%$ by volume of the material. The porosity can be modified and enhanced by the choice of Na^{+} or K^{+} charge balancing cations, the addition of aluminum (Al) submicron nano-particles, curing with hydrogen peroxide (H_2O_2), or the addition of micron-sized hollow spheres of graphite (C), alumina (Al_2O_3), silica (SiO_2), or organics (eg. polyethylene).

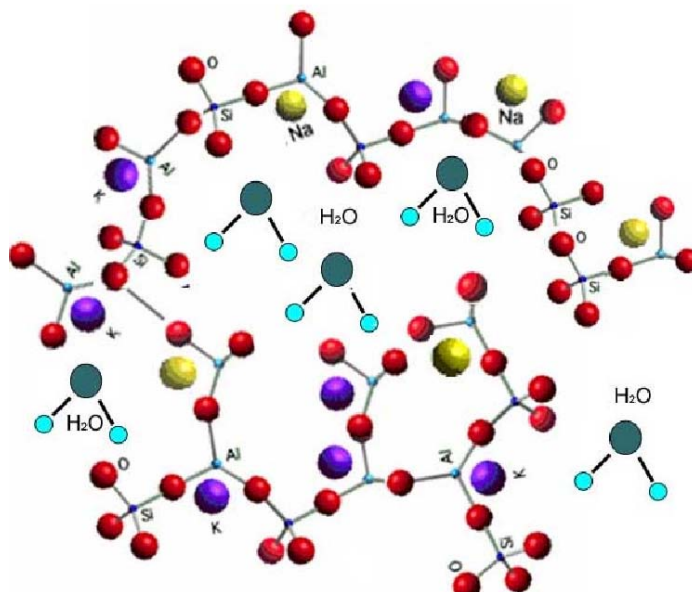


Figure 35. Molecular Diagram of Aluminosilicate Geopolymer

Recently, the geopolymer can be considered as a potential substructure or inorganic adhesive to bond a SiC-based backing structure (CTE ~ 4 ppm) with a highly stiff silicon carbide/silicon nitride laminate (CTE ~ 4 ppm), which is deposited on the optical mirror thin metal films. The thermal expansion behavior of the geopolymers can vary depending on its chemistry and

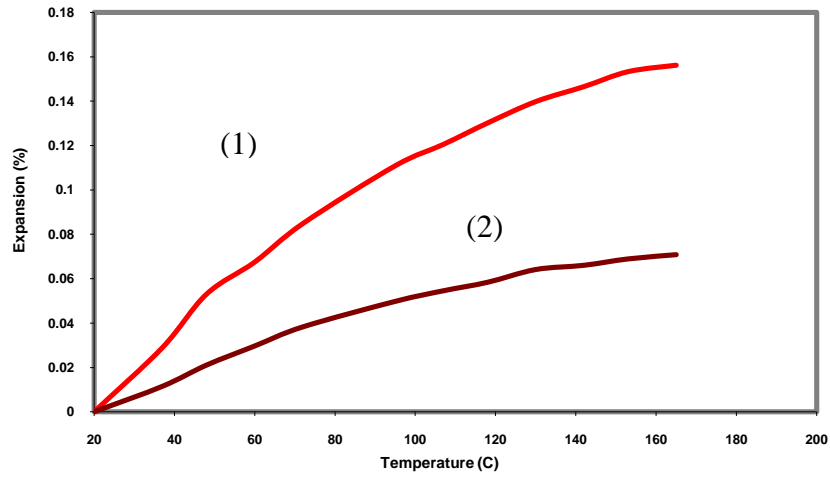
processing condition, so it is necessary to measure the CTE of the geopolymer, which was produced in AFRL.

6.2.2.2 Experimental Procedure and Results

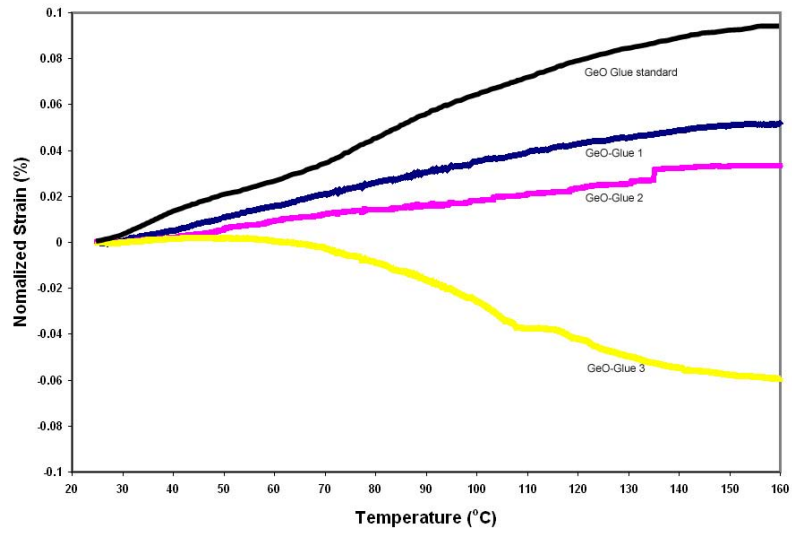
The geopolymers, as well as the geo-glues, were prepared by mixing aqueous potassium silicate ($0.20 \text{ K}_2\text{O} \cdot 0.90 \text{ SiO}_2$) and fine sized de-hydrated kaolin (meta-kaolin: $\text{Al}_2\text{O}_3 \cdot 2\text{SiO}_2$) powder. The mixture was cast in the mold (10 mm x 10 mm x 40 mm), and cured at ambient atmosphere or 60 °C in an oven for 24 h. During this period, the geopolymer hardened through what is referred to as the “geo-polymerization process”, and gained sufficient strength for handling. The as-cured geopolymers were then transferred to the oven at 100 °C for an additional 24 h. During the curing process, volume shrinkage occurred, as much as ~7 %. It seems that the shrinkage depends on the chemistry, water concentration, and the degree of geo-polymerization. However, it was reported that the shrinkage can be greatly minimized by incorporating filler materials (e.g., silica fume), as well as chemistry tuning and curing conditions. A similar effect was observed when the geopolymer was mixed with negative CTE oxide (ZrW_2O_8) powders, which results in negligible lateral shrinkage.

The CTE of the as-cured geopolymers, as well as the as-cured geo-glues, were measured using Thermal Mechanical Analysis (TMA) from room temperature to 200 °C, and was estimated to be ~ 9.5 ppm. This is clearly a larger value than that of the laminate (~ 4 ppm), so the CTE of the geopolymer was adjusted. The addition of 30.2 vol % of negative CTE oxide powder (ZrW_2O_8) was estimated to adjust the CTE to ~ 4 ppm. The added ZrW_2O_8 was incorporated in the geopolymerization process, and cured following the same conditions. The CTE of the geopolymer- ZrW_2O_8 composites was measured at the same temperature range. The results are plotted in Figure 36, and compared with the as-cured geopolymer and the as-cured geo-glue.

The potential reaction between geopolymer and ZrW_2O_8 was monitored by x-ray powder diffractometry after CTE measurements. The results are shown in Figure 37 indicating no sign of reaction. All of the peaks are indexed to original ZrW_2O_8 . Please also note that a few peaks overlapping with the geopolymer.



(a)



(b)

Figure 36. Thermal Expansion Behavior of Geopolymer-Based Materials
 (a) geopolymer ($\text{Al}_2\text{O}_3 \cdot 2\text{SiO}_2 \cdot \text{K}_2\text{O}$): (1) as-cured and (2) geopolymer- ZrW_2O_8 composite
 ($\alpha \sim 4.29 \times 10^{-6}/\text{C}$)
 (b) geo-glue ($\text{Al}_2\text{O}_3 \sim 6\text{SiO}_2 \cdot \text{K}_2\text{O}$): 0 v/o ZrW_2O_8 , GeO-Glue 1: 30 v/o ZrW_2O_8 , GeO-Glue 2: 45
 v/o ZrW_2O_8 , and GeO-Glue 3: 70 v/o ZrW_2O_8 powder.

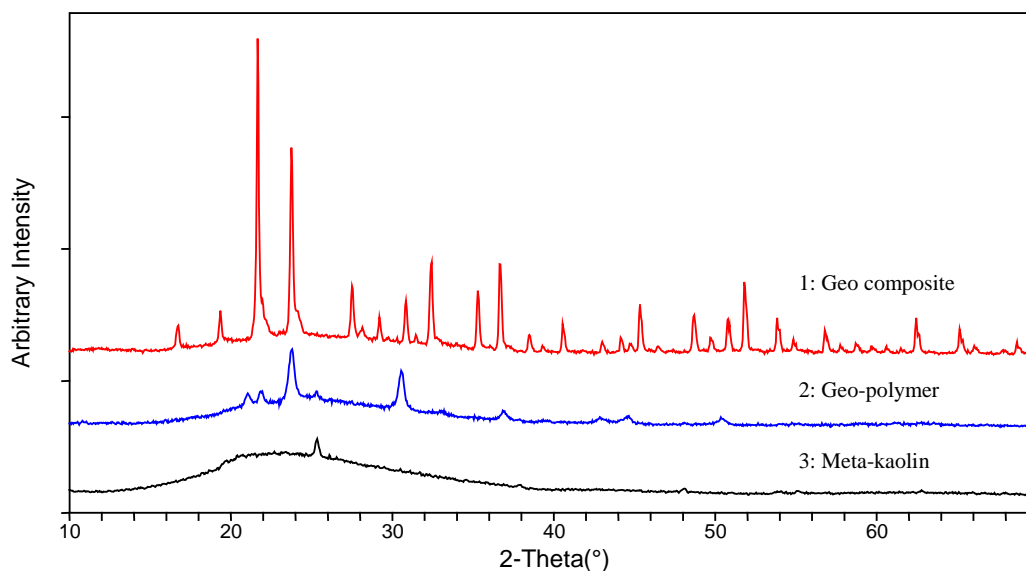


Figure 37. XRD Results of (1) Geo-Composite, (2) Pure Geopolymer, and (3) Meta-Kaolin

6.2.2.3 CTE Tailored Cr_2O_3 - ZrW_2O_8 Composite

A reactive Cr_2O_3 infiltration was utilized with the ZrW_2O_8 matrix, anticipating a near zero CTE dense body that can be produced at temperatures below 600 °C. First, the ZrW_2O_8 powder was dispersed in iso-propanol and tape cast onto the Teflon substrate. After solvent removal in ambient atmosphere, the as-dried ZrW_2O_8 was calcined at 600 °C in air for 1 hr. The as-calcined ZrW_2O_8 was infiltrated with an aqueous Cr-precursor, dried, and subsequently heat treated in air at 600 °C within a half hour and immediately cooled down to room temperature within a half hour. The total time for the heat cycle was therefore one hour. We repeated the same process until the rate of weight gain was saturated. The phase compatibility of the dense composite was examined by X-ray powder diffractometry, which confirmed that there was no reaction between Cr_2O_3 and ZrW_2O_8 . Finally, the CTE was measured from room temperature to 600 °C in air with a 2 °C/min ramping rate. The results are shown in Figure 38, where the thermal expansion (%) is plotted as a function of temperature. As seen in Figure 38, the composite expands up to around 80°C and begins to contract continuously to 600 °C. The dimensional change in this temperature range was estimated to be below ~ 0.01%.

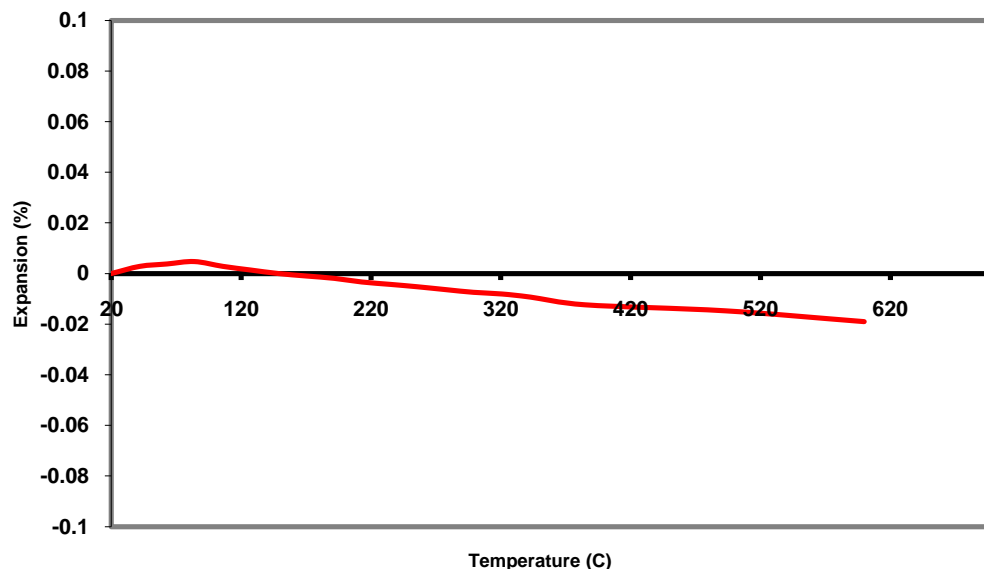


Figure 38. Thermal Expansion Properties of the $\text{Cr}_2\text{O}_3\text{-ZrW}_2\text{O}_8$ Composite

6.2.2.4 CTE Characterization of Organic Resin (EPON 828) Composites with Silane-Coated ZrW_2O_8 Powder

One of the potential applications of a negative CTE oxide can be as a useful additive in tailoring the CTE of organic resins [12-15]. It is possible to lower the CTE of the resins by dispersing fine particles of negative CTE oxide into the resin matrix. For this application, a strong interface between the resin and the particles is essential. We modified the surface of nano-sized ZrW_2O_8 (ZWO) powder with a silane coupling agent. The organo-functional silanes are known as very useful surface modifiers that change the particle surface chemistry, offering strong heterogeneous interfaces. Epoxy silane (Z-6040: Dow Chemical) was applied to modify the surface chemistry because the resin matrix, EPON 828, is an epoxy resin.

IR spectroscopy was used to study the surface chemistry of the silane-modified ZrW_2O_8 powder, but the results were not able to confirm the presence of $-\text{O-Si-R}-$, where R is epoxy, probably due to the resolution limit of the instrument. However, TEM studies were conducted to confirm whether the surfaces were coated with silanes.

The epoxy silane (Z-6040, Dow Chemical)-modified ZrW_2O_8 (ZWO) powders were prepared through two different routes: aqueous and non-aqueous. For a non-aqueous base, ZrW_2O_8 powder was dispersed in a mixture of silane:water:EtOH (5:5:90 v/o) while keeping the pH at ~ 4.5 by the addition of acetic acid. Subsequently, the mixture was reacted at ambient temperature for 24 hours and filtrated, rinsed and finally dried in an oven (100°C). Alternately, ZrW_2O_8 powder was dispersed in a silane:water (5:95 v/o) mixture at a pH of ~ 4.5 , with the addition of acetic acid.

The surface modified powders were filtrated and subsequently rinsed with de-ionized water and ethanol. The rinsed powders were dried first at 60°C overnight, and then further dried at 110°C

in the oven overnight. The dried powders were sieved using a -325 nylon mesh. The visual appearance of the two powders was significantly different. The powder produced through the aqueous route looked hydrophilic, whereas the powder from the non-aqueous system appeared hydrophobic.

The surface chemistry of the as-coated powders was characterized by FT-IR spectroscopy. The results are summarized in Figure 39. However, it was difficult to draw any conclusions; a few peaks did appear different, but these were insufficient to draw a conclusion. This may be due to a surface layer that is too thin, which is beyond the resolution of IR spectroscopy.

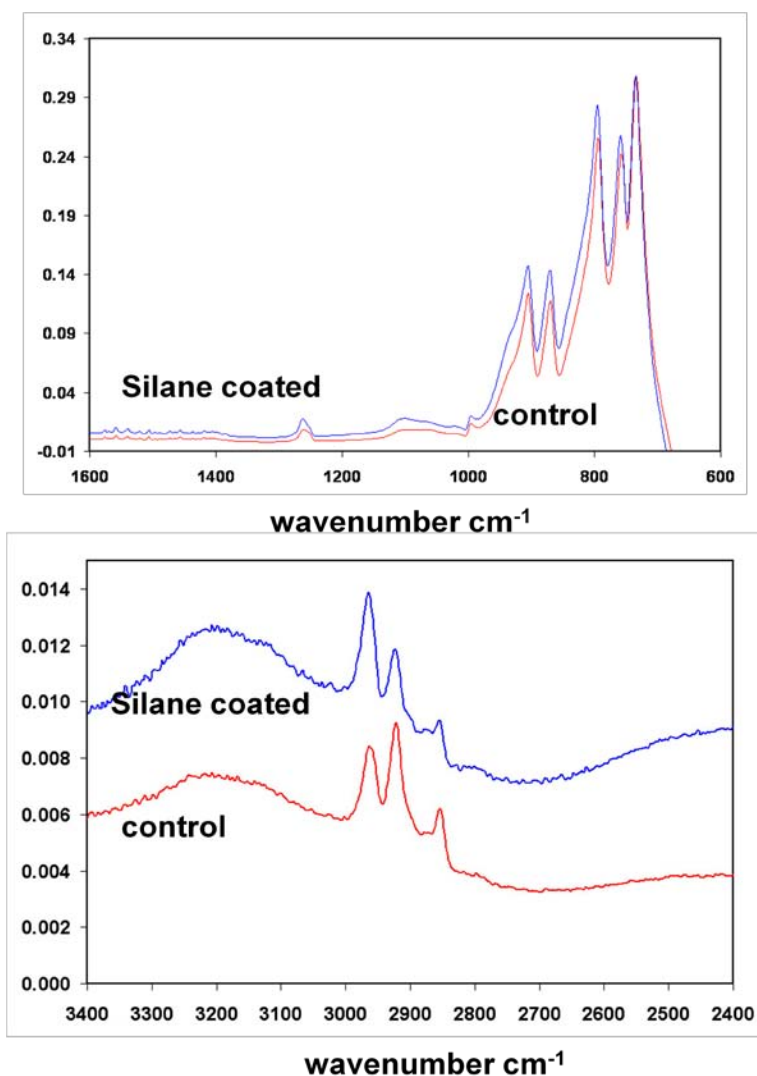


Figure 39. FT-IR Results of the As-silane Coated ZrW_2O_8

The powders were also analyzed by TEM. The results of TEM analyses are shown in Figure 40. Very thin layers are clearly seen on the particle surfaces, suggesting the presence of a silane coating. However, the EDS elemental analysis was not successful in identifying the coating chemistry due to the peak overlap of tungsten and silicon.

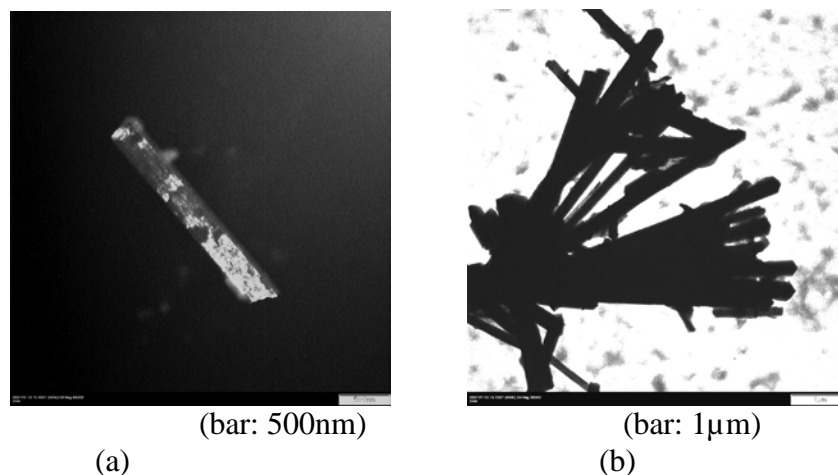


Figure 40. Dark Field Images of Silane-Modified ZrW_2O_8 Powders
 (a) *aqueous coating system*
 (b) *non-aqueous coating system*

The resin mixtures were then prepared by mixing different volume percentages (2, 5, 10 v/o) of three different powders: two silane-modified powders and a control powder. A Thinky mixer was used to obtain homogeneous mixing; one minute of mixing at 2000 rpm and one minute of de-airing at 2200 rpm was used. The mixing was repeated twice for each mixture.

The homogeneous mixtures were then cast into rectangular bars ($5 \text{ mm} \times 5 \text{ mm} \times 10 \text{ mm}$) using a silicon rubber mold, as shown in Figure 41. The left-over mixtures were also cast into disk-type plastic molds. The samples were cured for 72 hours under ambient atmosphere. The as-cured bar samples were ground to produce flat surfaces for CTE characterization through TMA, as well as for thermal fatigue testing.

The CTE measurements of three as-cured specimens are summarized in Table 3. The data indicates that the CTE of the resin is substantially decreased with additions of the ZWO powder; 2.8 vol.% and 3.0 vol.% of ZWO powder yielded a CTE difference of 15.43% and 20.51%, respectively. Theoretically, the CTE of the resin composite with 3 vol.% of ZWO powder should be 55.4 ppm.

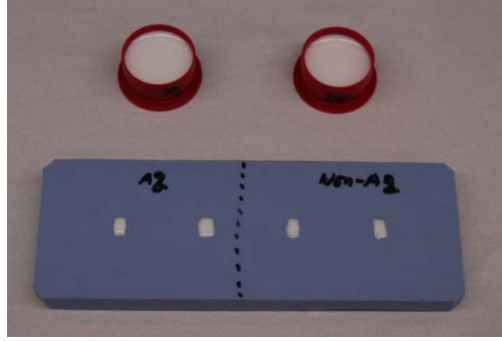


Figure 41. CTE-Tailored EPON 828 Resin Composites for CTE and Thermal Fatigue Characterization

Table 3. CTE Measurements of As-Cured Specimens

	EPON 828	EPON 828/ZWO (~2.8 v/o)	EPON 828/S**-ZWO (~3.0 v/o)
CTE* (ppm)	70.95	60.0	56.4
Δ CTE (%)		-15.43	-20.51

* average value from three measurements.

** silane-treated powder.

In order to evaluate any degradation that may occur, the three specimens were thermally fatigued for 24 hours. This was accomplished by using a thermal cycler that raised the temperature of the specimens up to 100 °C and then allowed them to cool back to room temperature; this was repeated for 24 hours. This cycle consisted of 10 minutes at 100 °C and then ten minutes at 25 °C. This was repeated for a total of 72 cycles. The thermally cycled specimens were characterized in order to study any sign of CTE change. The results are summarized in Figure 42. As seen in Figure 42, the CTE values for the silane-treated specimens gradually increased as the number of CTE measurements increased. This result suggests that the interface was weakened during the CTE measurements; this was not expected for the resin composite with the silane-treated powder.

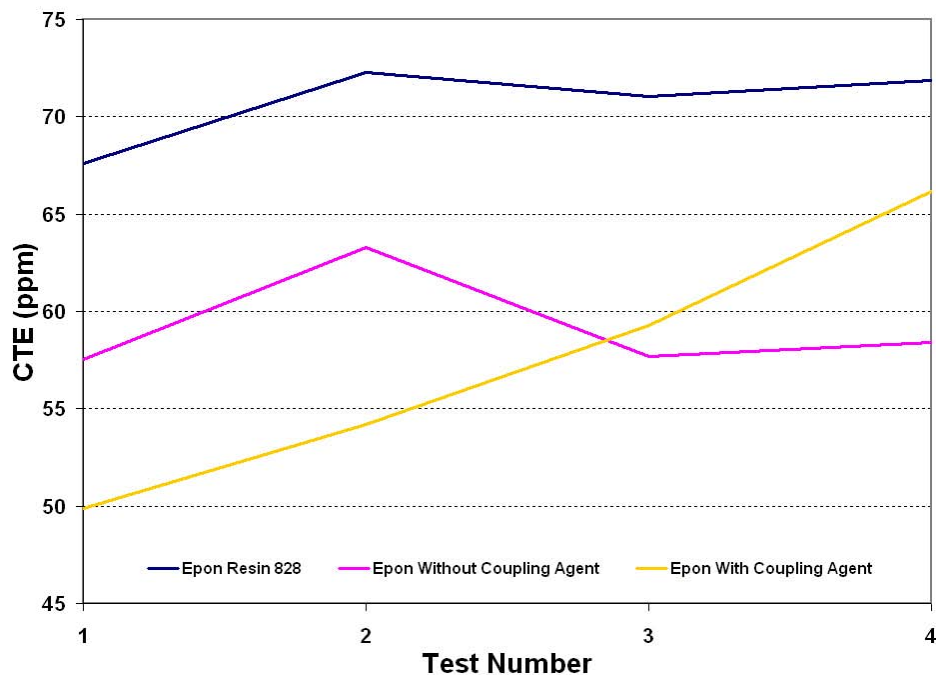


Figure 42. CTE Variations of Three Thermally Fatigued Specimens Versus the Number of CTE Measurements

In order to confirm the preliminary results of the thermal stability of EPON828 with the silane-coated powder, systematic studies were conducted with more samples followed by CTE measurements and thermal fatigue testing, along with two different coating processes. The samples were prepared in the same manner by differing the amount of the powders.

The average CTE of three measurements at each data point is plotted in terms of the volume percentage of the filler (Figure 43). For comparison, a theoretical estimation, as well as a control sample, is also included. As seen in Figure 43, a significant deviation from the estimation is observed. This may be attributed to the inhomogeneous mixing state of the ZrW_2O_8 filler; thus, proper mixing order as well as filler dispersion can be important.

However, it is worthy to note that the control sample mixed with 2 v/o of the powder showed a nearly theoretical value. This may indicate that there is a distinct difference in dispersion state between the silane-modified ZrW_2O_8 fillers and the unmodified ZrW_2O_8 powder; the surface chemistry also plays an important role.

The primary purpose of the surface modification of the filler materials was to provide strong bonding between the matrix and the fillers. Thus, an increase of thermal stability can be anticipated. However, it was observed that the surface modification also influences the dispersion, and that needs to be further optimized.

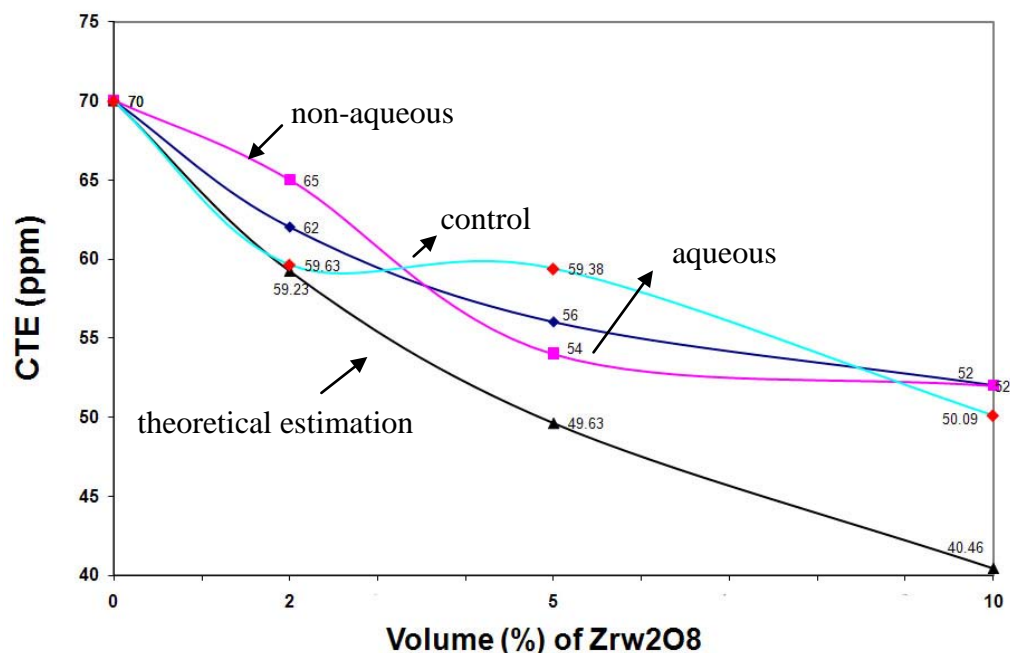


Figure 43. CTE Variations of the EPON 828 Resin Composites with ZWO Filler

The thermal stability was examined by monitoring the variation of the CTE values before and after thermal cycle testing. The samples were thermally cycled between room temperature and 100 °C; the samples were rapidly transferred to a furnace chamber at 100 °C, followed by a 20 minute hold, and then rapidly cooled down to ambient temperature with a 20 minute holding period. This one thermal cycle was repeated 72 times. After 72 thermal cycles, the CTEs of the samples were characterized using TMA. The raw CTE values obtained from the TMA after the fourth heat treatment are summarized in Table 4. The average CTE values along with the variances for each sample set were also estimated, and the results are reviewed in Table 5.

Table 4. CTE Measurements After Thermal Cycling

Sample:	1 st run	2 nd run	3 rd run	4 th run	5 th run	6 th run	7 th run	8 th run	9 th run
Aq 2%	61.35	63.68	64.59	62.07	63.91				
Non-Aq 2%	65.47	67.32	67.17	65.05					
Control 2%	62.98	64.68	63.51	58.73					
Aq 5%	55.99	61.01	53.97	60.79					
Non-Aq 5%	52.23	60.50	62.44	58.89	62.00				
Control 5%	56.09	58.81	50.43	60.76	61.25	64.63	58.69		
Aq 10%	46.35	53.66	52.15	51.63	51.98	48.66	51.73	52.07	51.42
Non-Aq 10%	51.79	55.29	53.77	56.77	57.89	52.82	54.28	53.13	
Control 10%	49.14	53.02	53.32	52.00					

Table 5. Averaged CTE with the Degree of Variance

Sample:	Aqueous:	Non-Aqueous:	Control:
2%:	Average: 63.12 Variance: 1.83	Average: 66.25 Variance: 1.35	Average: 62.48 Variance: 6.74
5%	Average: 59.30 Variance: 5.43	Average: 59.21 Variance: 17.18	Average: 58.67 Variance: 20.19
10%	Average: 51.07 Variance: 4.30	Average: 54.47 Variance: 3.74	Average: 51.62 Variance: 2.19

As noticed in Table 5, there is a clear trend of stability in the 2% and the 5% samples. The variance between the CTE values, within each data set, seems to be the least in the aqueous system, and highest in the control samples. However, the same trend is not observed with the 10% samples; in fact, it is the opposite. This is usually not the case because the stability generally was highest with the aqueous samples in the previous results. In terms of average CTE values, the 10% systems consistently showed the lowest average CTE values, as expected.

All data collected with the nine samples up to the fourth heat treatment are summarized in Table 6, with averaged CTE values, along with its variance. All of the data, along with the fourth heat treatment, are plotted in Figure 44. As seen in Figure 44, the 4th data sets follow similar trends as previously observed.

Table 6. Averaged CTE Values and Variances of Nine Samples

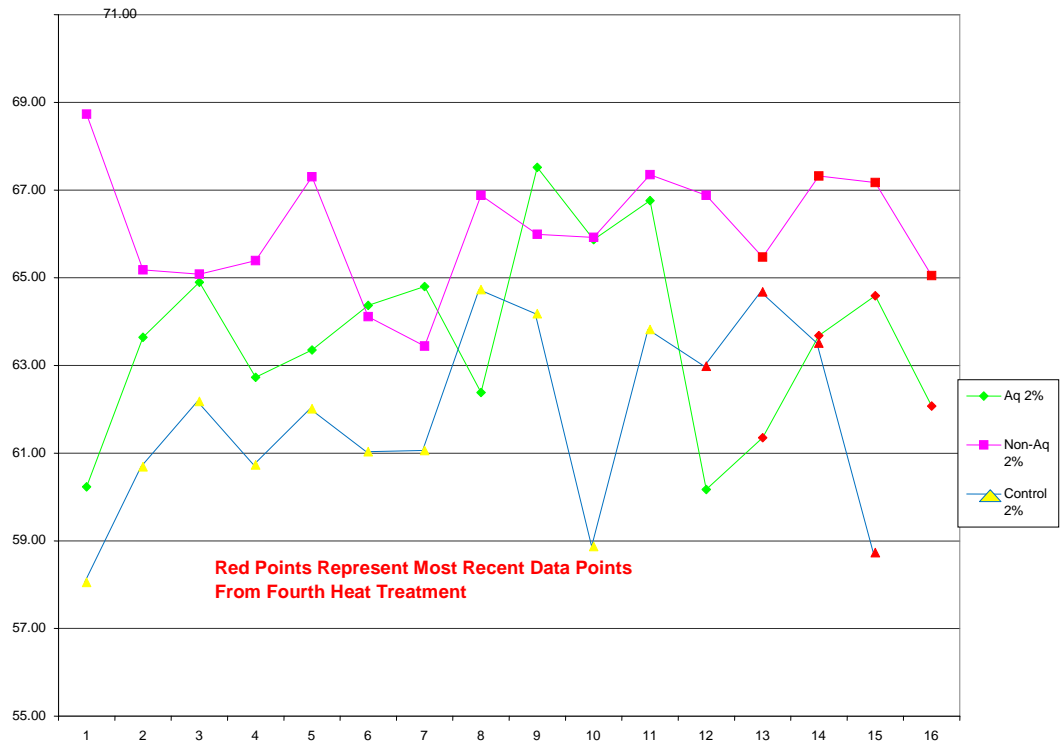
	VAR:			Average: (CTE)		
0 T/C	Aq	Non-Aq	Control	Aq	Non-Aq	Control
2%	5.84	4.32	2.09	62.92	66.33	60.31
5%	1.73	1.59	1.76	56.90	54.79	60.03
10%	1.19	3.25	3.42	52.96	52.02	49.36
1st T/C						
2%	na	na	na	na	na	na
5%	na	na	na	na	na	na
10%	na	na	na	na	na	na
2nd T/C						
2%	0.55	3.77	0.31	64.17	65.43	61.37
5%	0.01	5.35	2.41	56.69	58.35	59.61
10%	1.72	2.70	8.45	53.06	53.81	50.86
3rd T/C						
2%	9.84	0.49	7.36	64.54	66.54	62.90
5%	2.88	8.88	14.4	58.91	59.14	60.21
10%	2.55	12.99	4.91	51.70	52.60	50.81
4th T/C						
2%	1.83	1.35	6.74	63.12	66.25	62.48
5%	5.43	17.18	20.19	59.30	59.21	58.67
10%	4.30	3.74	2.19	51.07	54.47	51.62

* T/C: thermal cycled

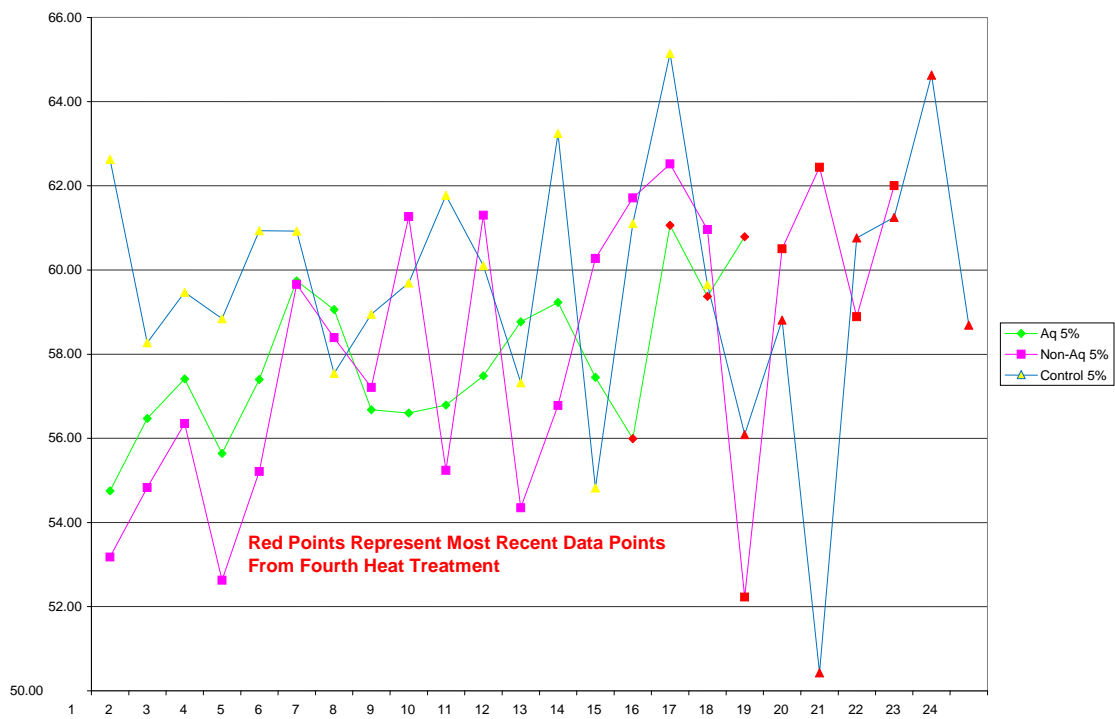
In Figure 44, the most distinguished feature is the control sample. The CTE values of the control sample seem to become more and more fluctuated as the number of runs increases, and clearly show the least stability. The non-aqueous sample also shows significant variance, but not quite as much as the control sample. The aqueous sample does show a high stability compared to other two. Another trend here is the slow increase in CTE value as the number of runs increases; this is most clearly seen with the aqueous system.

Compared to the 5% samples, much higher stability in terms of the variance and the CTE values are observed for 10% samples. It seems that the aqueous sample is the most stable, and the control and non-aqueous samples are similar in terms of the stability.

In summary, through all of the heat treatments, the average CTE values for the aqueous system showed the lowest values, along with the most consistent trends. Also, the data shows that the aqueous system is the most stable, while the control and non-aqueous samples are more scattered in terms of their CTE values.



(a)



(b)

Figure 44. Variation of the Average CTE Measurements
(a) 2%, (b) 5%, and
(c) 10% samples in terms of thermal cycles

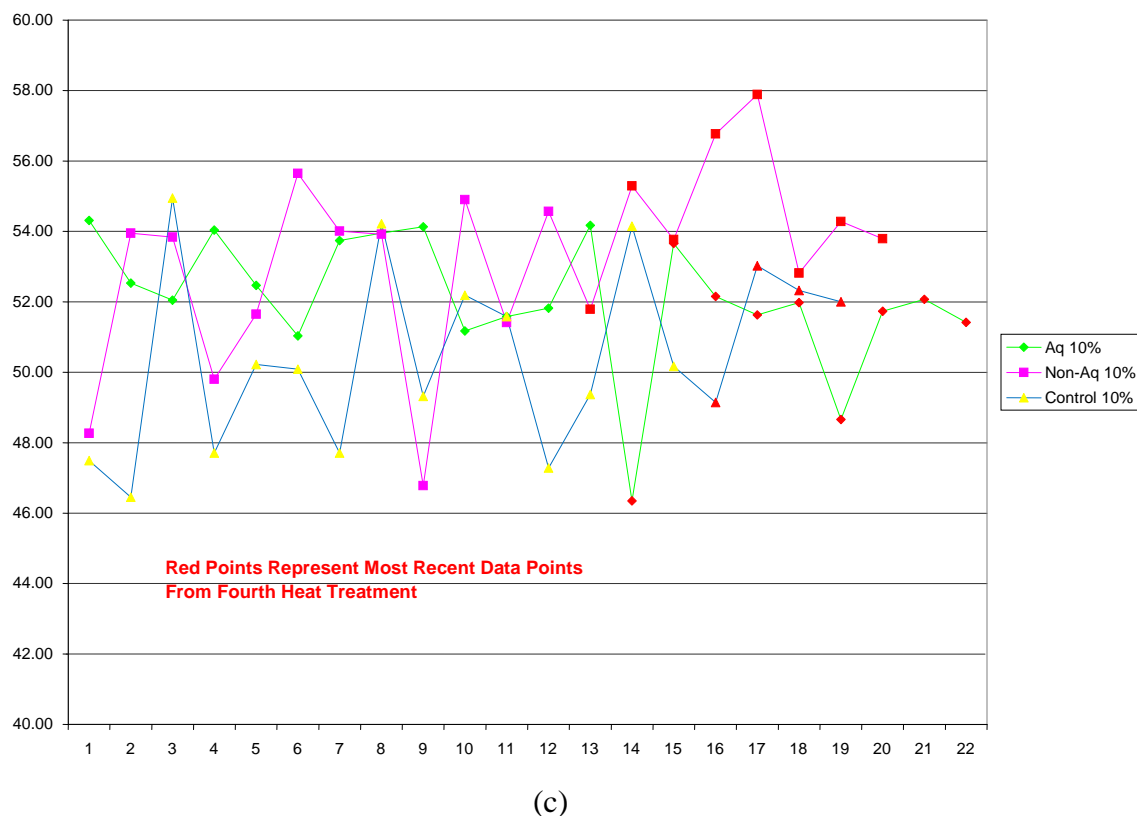


Figure 44 (continued). Variation of the Average CTE Measurements
(a) 2%, (b) 5%, and
(c) 10% samples in terms of thermal cycles

6.2.2.5 ZWO (ZrW_2O_3) Coating on Glass Balloons

It is a very intriguing question whether ZWO-coated glass balloons can be effective in controlling the curing shrinkage as well as the CTE of the organic resins. It has been demonstrated that glass balloons are a very useful means to control the curing shrinkage as well as the CTE. This has encouraged us to seek more effective means of tailoring the CTE and curing shrinkage. Thus, the primary idea of ZWO-coated glass balloons was to achieve a synergetic result by utilizing the negative CTE behavior of ZWO. However, its synergetic effect and the thermal response at the interface between ZWO and the glass balloons remains in question at elevated temperatures. Moreover, the coating technology is not yet developed.

The first attempt at depositing a ZWO coating on the glass balloons was made by using homogenous precipitation. Two precursor solutions for Zr and W were prepared: zirconium oxynitrate and meta-tungstate aqueous solutions. A direct mixing of the two precursors caused immediate precipitation. A few complexing agents (citric acid, EDTA, etc.) were utilized to suppress the precipitation, but the results were too successful; little precipitation was observed

even at elevated temperatures. To solve the precipitation problem, ammonium nitrate was added to temporarily suppress the precipitation. The mixture containing ammonium nitrate appeared clear at room temperature, but it began to precipitate at temperatures around 50 °C. The precipitates were very sticky and well deposited on the inside of the glassware. This indicates that the precipitates may adhere well to the glass balloons.

The mixture precursor (100 cc) was prepared by first mixing ammonium nitrate and the tungstate solution, and then the zirconium precursor was added. This mixing order is important to avoid precipitation. One gram of glass balloons (3M ScotchLite S32) was dispersed in the mixture by mild stirring. Subsequently, the mixture was slowly warmed up to 70 °C, held for an hour, and then cooled down to room temperature under stirring. The mixture was filtrated, rinsed a few times with de-ionized water and ethanol, and dried at 60 °C. The glass balloons were examined by SEM shown in Figure 45.

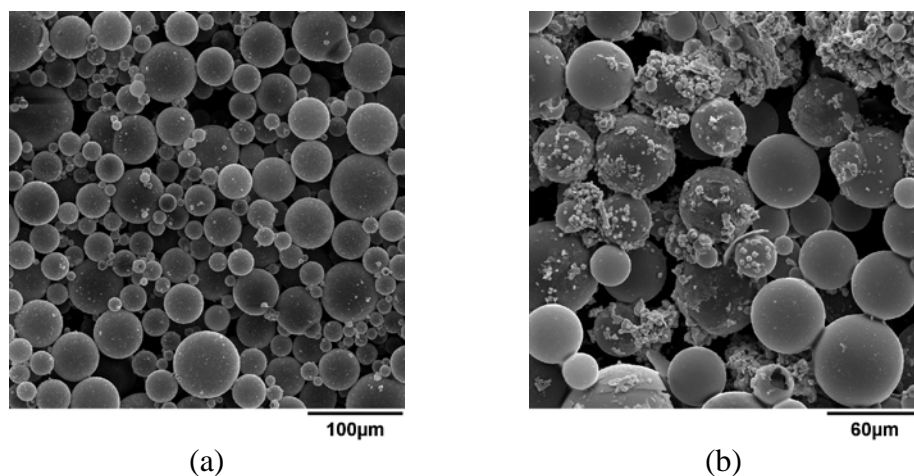


Figure 45. SEM Micrographs Showing (a) Control and (b) As-Coated Glass Balloons

At first glance, the coating seemed unsuccessful, as seen in Figure 45. Many small particles, likely precipitates, are present. Some glass balloons were likely coated but the coating coverage looked scarce. A few localized regions were examined at higher magnification and these showed the existence of the ZWO layer; this can be seen by the bright contrast in Figure 46 (b). It is likely that the coating was initially present at the surface of glass balloons but readily washed away during rinsing. This suggests that the coating was weakly adhered to the glass balloons.

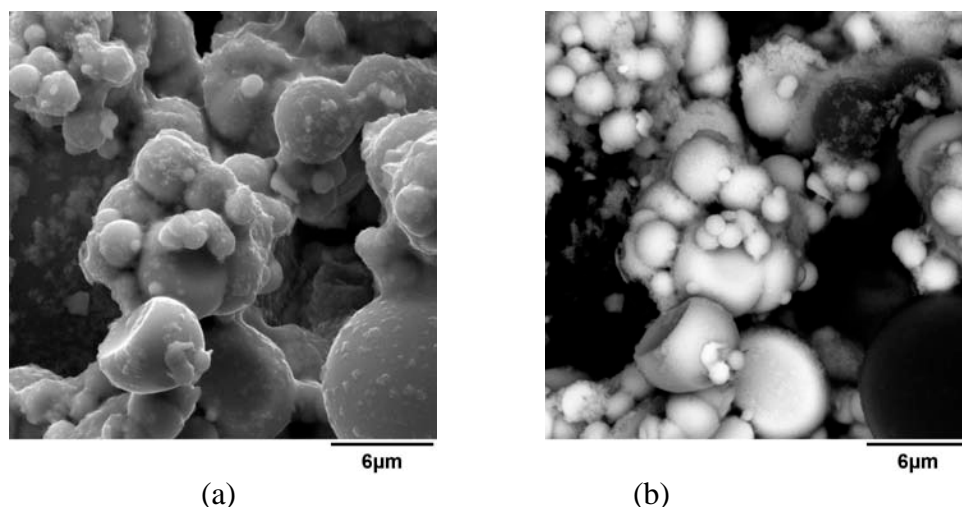


Figure 46. The as-coated balloons: (a) SEI mode and (b) BSI mode

6.2.3 Geopolymers with a Zero Curing Shrinkage

6.2.3.1 Geopolymers

Typically, geopolymers are synthesized by mixing aluminosilicate minerals and alkali metal hydroxides or alkali silicates in the presence of water. Common constituents are kaolinite ($\text{Al}_2\text{O}_3 \cdot 2\text{SiO}_2 \cdot 2\text{H}_2\text{O}$) or coal ash, NaOH or KOH, and water soluble Na- or K-silicate. The process follows a simple path after mixing all constituents in the appropriate combinations. The viscous paste or slurry, after a certain time at low temperature ($25^\circ \sim 100^\circ \text{C}$), undergoes polycondensation (hereafter referred to as geopolymerization) and becomes mechanically rigid and strong. The term geopolymerization is similar to terms such as curing, hardening or setting often used in the organic polymer community. During geopolymer processing, both aluminate and silicate ions are dissolved from the kaolinite and subsequently polymerized to form a three-dimensional network consisting of various ratios of oxygen tetrahedra of aluminum and silicon, as illustrated in Figure 47. The alkali metals act as charge compensating ions, which locate in the vicinity of aluminum tetrahedra. The by-products after geopolymerization are water molecules, which are structurally located in cavities formed at points of unusual tetrahedra connections. No discernible peaks appear in the X-ray powder diffraction patterns after geopolymerization; only broad humps are present, making it appear amorphous. NMR spectroscopy can confirm the presence of aluminum and silicon oxygen tetrahedra network after geopolymerization. The most remarkable feature arising during geopolymerization is the three-dimensional network formation that is similar to glass. Numerous fundamental studies are being carried out to determine the exact mechanism of geopolymerization and how it may be controlled/tailored.

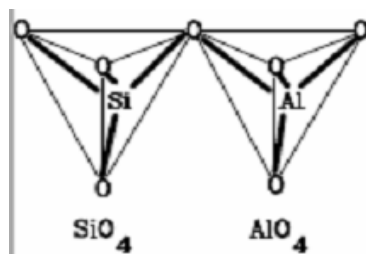


Figure 47. 3-D Structure of a Geopolymer

A brief description of the general processing steps is presented as follows. The geopolymer was produced by mixing potassium silicate ($\text{K}_2\text{O} \cdot 3.81 \text{ SiO}_2$, Kasil) and kaolin ($\text{Al}_2\text{O}_3 \cdot 2\text{SiO}_2 \cdot 2\text{H}_2\text{O}$, Aldrich Chemical). The raw kaolin was first calcined at 700°C for 30 min in air with a $1^\circ\text{C}/\text{min}$ heating rate to produce meta-kaolin ($\text{Al}_2\text{O}_3 \cdot 2\text{SiO}_2$). The mixture (10 g Kasil and 1.9973 g of meta kaolin) results in a 1:1 ratio of K_2O to Al_2O_3 . The mixture was mixed by using a Thinky mixer until the mixture turned to the viscous slurry, which is a sign of reaction (geopolymerization). Then, it was cured for approximately one day (mostly overnight) in ambient conditions, followed by a further curing in the oven ($70^\circ\text{C} \sim 100^\circ\text{C}$). After complete curing, the product showed a high water resistance even after 30 days immersion in water.

6.2.3.2 In-house Research for Geopolymers

The overall objective of this task was to produce ultra-lightweight inorganic substructures for space mirror applications with the use of tailored geopolymers, which serve as the backing structures for the mirror facesheets in developing a replicated hybrid mirror. This hybrid mirror can be created by casting the geopolymer slurries directly on the laminated mirror facesheets, allowing the geo-polymer to cure, and then replicating along with the attached metal laminate, thus producing the hybrid mirrors.

The first objective of the in-house geopolymer work was to solve the problems of shrinkage by tuning the chemistry as well as the curing conditions during the curing process, while ensuring no cracking of the geo-polymer during or after curing, adequate strength, and acceptable adhesive strength to the metal laminate, which allows for successful replication of the mirror surface. The geopolymer also needed to be thermally stable within a necessary temperature range, which includes a low CTE and resistance to degradation due to thermal shock. To achieve or meet all these specifications, the composition of the geo-polymer had to be adjusted and a proper curing process needed to be developed. The first experiments were to explore the trends that were observed during the preliminary studies, and that was to study the shrinkage and strength as SiO_2 content was increased; it was also applied to the commercial powder. The chemistries studied in the present program were $\text{Al}_2\text{O}_3 \cdot x\text{SiO}_2 \cdot \text{K}_2\text{O} \cdot y\text{H}_2\text{O}$, where x can vary from 2 to 6, and y was experimentally determined by a direct observation of the flowability of the geopolymer slurries.

The second objective was to understand the effects of the variables during the curing processes and also the effect of chemical composition on the geopolymer properties. Understanding the effects of curing variables began with a commercially developed geo-polymer “kit”. Although the exact chemical composition was not known for the powder or the trigger, different curing conditions were used to help understand the effect of different curing processes. These included curing in ambient conditions, higher temperatures, elevated pressures (CIP and autoclave), and different curing times. In addition to these conditions, the geopolymer slurries were also either left open to the desired environment, sealed within vacuum bags or Zip-Lock bags, or many different combinations of the mentioned methods. The results from these experiments did not provide a definitive curing process, but showed that sealing the geopolymer slurry within a vacuum bag or Zip-Lock bag during curing significantly reduced the curing shrinkage and the amount of cracking in the sample. The results also showed that when sealed, higher temperatures helped reduce the curing time from a number of days to less than 24 hours. These trends helped create a foundation for other curing procedures attempted.

The meta-kaolin based 1:4 geopolymer corresponds to $\text{Al}_2\text{O}_3 \cdot 4\text{SiO}_2 \cdot \text{K}_2\text{O} \cdot x\text{H}_2\text{O}$, where $x \sim 13$. This was the baseline composition for the in-house geopolymer study. The meta-kaolin was prepared by calcining Kaolin (Aldrich) at 600~700 °C for 2 hours in an ambient atmosphere. The trigger solution was prepared by dissolving the fumed silica (Degussa) with a KOH (or NaOH) aqueous solution (Table 7). A series of trigger solutions were prepared with keeping the amounts of water and silica constant while varying the alkali content. These triggers were then used in different mixing ratios with meta-kaolin powder and cured with the various curing processes previously mentioned.

Table 7. Trigger Compositions

Trigger:	Water: (g)	Silica: (g)	Alkali: (g)
KOH 3	326.70	39.10	69.45
KOH 4	326.70	39.10	81.03
KOH 5	326.70	39.10	92.60
KOH 6	326.70	39.10	115.75
NaOH 3	326.70	39.10	49.50
NaOH 4	326.70	39.10	57.75
NaOH 5	326.70	39.10	66.00
NaOH 6	326.70	39.10	82.50

When using the potassium triggers, it was found that higher alkali concentrations in the slurries led to a reduction in cracking during curing. In addition, based on observations of the slurry viscosity, it was realized that higher alkali content and the use of sodium rather than potassium led to a higher extent of reaction. This was determined from the assumption that higher alkali content led to breakdown of the meta-kaolin more rapidly, and sodium has a higher reactivity than potassium due to its smaller ion size. Use of sodium triggers at first showed promise of yielding a geopolymer that met the needed properties, but when tested for adhesive strength potassium-based samples showed better adhesion to the metal laminates (silver, gold) than sodium-based samples, depending on the powder used. Also, sodium-based slurries reacted with

the silver metal, leading to discoloration, as well as formed amorphous whitish carbonate phases on the surface of the geopolymer when it was exposed in an ambient atmosphere. These observations led to potassium-based geo-polymers becoming the main focus of attention.

Further variations in the chemical composition were also made to study their effects; the changes were to the concentration of water and later silica in the geopolymer. The first experiment involved the reduction of the amount of water in the slurry by creating triggers with successively lower amounts of water, although the amount of silica and potassium hydroxide were kept constant. Water content in the two original trigger solutions that had been used, was cut by about 33% and 66%. A series of samples were cast and cured in ambient conditions, the compositions of which are shown in Table 8.

Once the samples were fully cured, it could be seen that a majority of samples developed noticeable cracks. However, one particular trend could be seen; the samples that developed cracks were those chemistries with a ratio further from 1:1 between alumina and potassium in the slurry. The samples fabricated until this point in time always contained potassium at concentrations lower than the theoretical, which should be equal to the moles of aluminum in the slurry to balance out the negative charge it carries in the geopolymer; however, too much potassium also led to cracks. Another result observed from this experiment was that every sample underwent thermal shock when raised to 120 °C and then brought to room temperature.

Table 8. Sample Compositions with Reduced Water Triggers

Series:	Samples based on KOH #5 Solution		Samples based on KOH #6 Solution	
A (66% Reduced)	1 Al ₂ O ₃ : 2.815 SiO ₂ : 1.037 K ₂ O	1 Al ₂ O ₃ : 3.0 SiO ₂ : 1.274 K ₂ O	1 Al ₂ O ₃ : 2.822 SiO ₂ : 1.304 K ₂ O	1 Al ₂ O ₃ : 2.956 SiO ₂ : 1.519 K ₂ O
B (33% Reduced)	1 Al ₂ O ₃ : 2.576 SiO ₂ : 0.733 K ₂ O		1 Al ₂ O ₃ : 2.585 SiO ₂ : 0.918 K ₂ O	
C (Original)	1 Al ₂ O ₃ : 2.437 SiO ₂ : 0.563 K ₂ O		1 Al ₂ O ₃ : 2.452 SiO ₂ : 0.711 K ₂ O	

It was clear that another parameter needed to be changed to help strengthen the geopolymer as well as increase the adhesive strength. The first change made was to increase the silica content in the trigger solution. This was based on the preliminary studies, as well as what was found in the previous reports, which described optimum Al₂O₃: SiO₂ ratios of around 1:4. The samples were then prepared with the Al₂O₃: SiO₂ and Al₂O₃: K₂O ratios fixed at 1:4 and 1:1 respectively. Initially these slurries showed large amounts of curing shrinkage when cured at ambient conditions, but they did show good adhesive properties when the slurry was cast on gold film. On the contrary, the slurry cured inside a vacuum bag at 60 °C for about 18-24 hours showed very good results without any curing shrinkage, no cracking, and complete curing within 24 hours consistently depending on the amount of slurry. In addition to these results, the geopolymer showed good adhesive strength to the gold film, successfully creating a mirror surface on multiple occasions. However, these geopolymers again suffered thermal shock when thermally cycled between room temperature and 120 °C.

It was known that using a commercial trigger solution produced strong geopolymers, but this trigger solution contained a high concentration of silica and water and had a low alkali content. This trigger was used in combination with the previous trigger solution (1:4), where the incrementally higher percentage of the (1:4) trigger was replaced with KASIL solution (Table 9).

Table 9. Trigger Compositions.

Trigger:	Silica: (g)	Water: (g)	Alkali: (g)
(1: 4) Trigger	25.76	50.18	24.06
KASIL	20.47	69.79	9.73
(1: 4.15) Trigger	26.16	49.92	23.92
(1: 4.25) Trigger	27.38	49.89	22.73
(1: 4.5) Trigger	29.21	47.88	22.91
(1: 5) Trigger	34.24	44.45	21.31
(1: 6) Trigger	48.65	49.92	39.35

Although all the samples from this experiment eventually shattered or broke apart due to thermal shock, it led to the decision to experiment with increasing silica concentration. This was based on the knowledge and observation that higher silica content would lead to stronger adhesive strengths and possibly better thermal shock resistance. Therefore new trigger solutions were made, which created slurries with Al_2O_3 : SiO_2 molar ratios of 1:4, 1:4.15, 1:4.25, 1:5, and 1:6 and the Al_2O_3 : K_2O ratio was kept at a constant 1:1. However, the water content needed to increase to accommodate the increase in silica in solution. When the samples were made using these trigger solutions and meta-kaolin, a few things became apparent. The adhesive strength of the samples did in fact increase as the silica content increased, but at the same time the amount of curing shrinkage and curing time increased significantly. The curing shrinkage was the biggest problem, leading to distortion and contorting of the geopolymers as they cured. These results led to the use of KASIL-based slurries, not as a backing structure, but rather as highly adhesive “geo-glue”. The adhesive slurry was composed of a small amount of meta-kaolin (0.25 g) to 4 g KASIL. It was applied at the interface between a metal laminate surface and a pre-cured meta-kaolin or commercial geo-polymer. This process was successful in creating a mirror, but a direct cast method was still an issue.

Based on the results seen from altering the chemical composition of the geopolymer, it was determined that the (1:4) composition would be made with various fillers to try and strengthen it. The first filler used was aluminum nitride (AlN). The geopolymers were prepared in the same manner, cured at 60 °C and sealed within vacuum bags. Aluminum nitride was added in increasing concentrations in a series of fabricated samples. However, the addition of aluminum nitride did not alleviate the problem and this filler material was discarded. Zirconium tungstate was also considered and used with the same base geopolymer, but once again this filler material did not seem to help at all. The micro-balloons had previously been used to reduce the density of certain samples and at the same time it was able to strengthen the meta-kaolin-based geopolymers, but at a different chemical composition. When applied to the (1:4) composition, the slurry became too viscous to work with and there was no significant advantage to using the micro-balloons. As a result, a new material, coal fly-ash, was examined.

Pure coal fly ash samples were made with a various number of triggers and curing processes that had been used previously. The one that showed the best result was made using the same (1:4) trigger, although the exact chemical composition was not known, and cured at 60 °C within a vacuum bag. This fly ash-based geopolymer showed excellent adhesive strength, low curing shrinkage, and did not undergo thermal shock. However, it was later found that fly ash geopolymers are very unstable in water, due to the nature of how it cures. Fly ash powders are highly stable and therefore do not react with the trigger solution (Table 10). The hardening process was simply the trigger drying and acting as a “glue” to keep the fly ash particles together for the most part, suggesting that this is not an actual geopolymerization process. Based on this result, fly ash powder was incorporated as filler with meta-kaolin geopolymers, and was shown to help strengthen the samples against thermal shock, but multiple thermal cycles up to 120 °C would eventually break apart the sample, even with fly ash concentrations of 40% of the total slurry weight in meta-kaolin geopolymers.

Table 10. Chemical Composition of Fly Ash and Slag

Species (% mass):	SiO ₂ :	Al ₂ O ₃ :	CaO:	MgO:	K ₂ O:	Fe ₂ O ₃ :
Fly Ash	43.41%	21.11%	4.82%	1.20%	2.14%	23.17%
Blast Furnace Slag	39.25%	9.85%	39.13%	10.71%	1.31%	0%

In order to improve thermal shock resistance, the compositional matrix was set up to observe the effect of adding blast furnace slag and fly ash to a meta-kaolin system, which was not (1:4), but a composition that could be cured in ambient conditions and originally underwent thermal shock, as shown in Figure 48. Fly ash and blast furnace slag was added to the base meta-kaolin slurry in 10% increments of the base slurry’s mass, up to 40%. A total of 16 samples were made and cured with either blast furnace slag, fly ash, or a combination of both along with meta-kaolin. It was found that at high enough additions of blast furnace slag and fly ash, the sample would not go through thermal shock. These samples were tested for adhesive strength and shown to be ineffective at replicating a mirror surface. The addition of fly ash and blast furnace slag was applied to meta-kaolin samples with a (1:4) composition, but again thermal shock was a problem and would require even more than the 40% addition of fly ash and blast furnace slag.

Based on the previous result, it was decided to focus on the blast furnace slag-based geopolymers due to their stability, low curing shrinkage, thermal shock resistance, and indications of good adhesive strength to titanium film. Again, different triggers and curing conditions were used initially with this material. Once again the (1:4) trigger with 60 °C and vacuum sealed curing led to the best result in terms of free standing samples. However, a slight curing shrinkage was shown. In order to minimize the curing shrinkage, meta-kaolin was considered to be added; previously, 1:4 meta-kaolin based geopolymers had not shown any shrinkage when it was cured inside the vacuum bag.

To remedy shrinkage problem, meta-kaolin was added to the blast furnace slag in an attempt to increase the extent of reaction (geopolymerization) and create a more rigid geopolymer framework, due to meta-kaolin’s higher reactivity. It was successful, with the addition of 5% of the total slurry’s weight of meta-kaolin; curing shrinkage was brought down to an amount not

noticeable by visual inspection. The next step was to create a curing regimen for these samples to maximize or create the best condition for bonding to the metal laminate or mirror surface. It was found that a two step process was the optimum. The slurry would be cast in ambient conditions and left out for 50 min to cure, then immediately sealed within a vacuum bag and placed into the 60 °C oven, where it would cure for 24 hours. This slurry was then used with a mirror surface composed of layers of titanium, gold, and carbon all on the glass mandrel.

The slurry would be in contact with the titanium layer and would cure and bond to that layer and therefore pull off the gold, leaving the carbon behind on the glass, creating the mirror surface on the bottom of the geopolymer. This procedure was repeated for 1 in. to 4 in. samples and in each case, successful replication of the mirror surface occurred, when the curing and casting process was carried out properly. The best results have been obtained using this type of geopolymer and curing process. However, there is still a small amount of curing shrinkage that does occur, although not noticeable to the eye; when viewed through an optical microscope, wrinkles can be seen on the mirror surface indicating some amount of shrinkage.

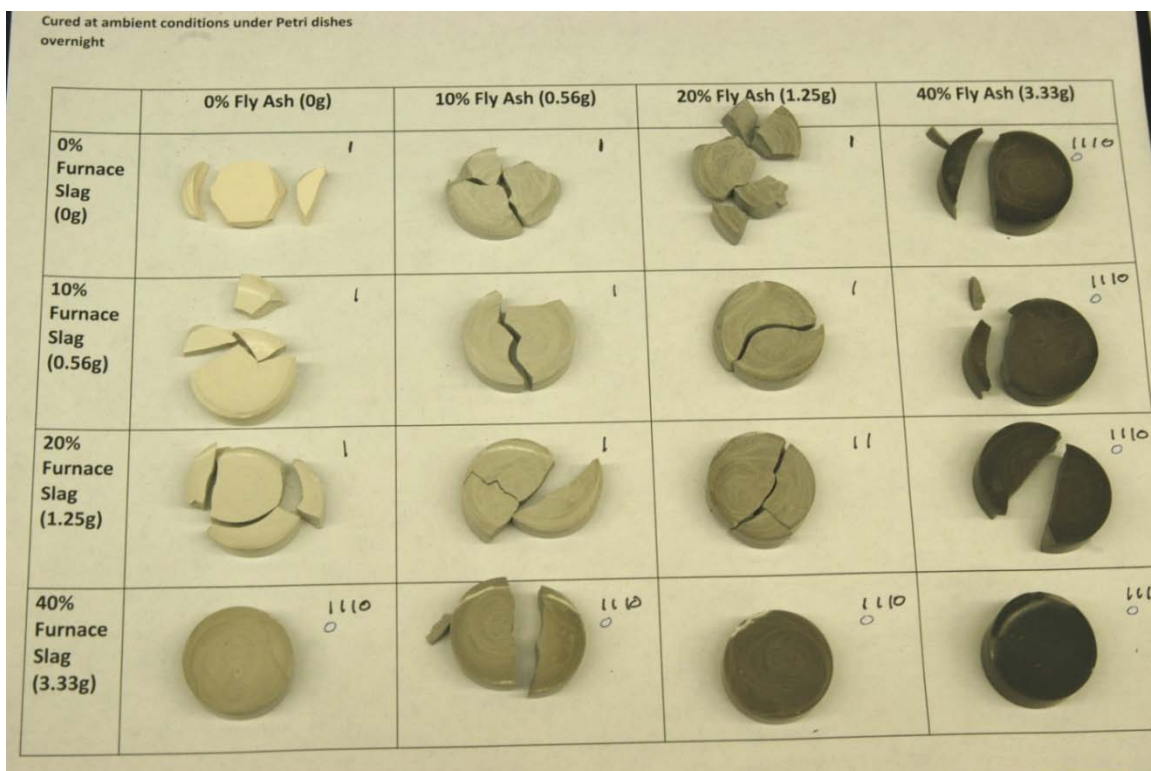


Figure 48. Thermal Shock Experiment Matrix

A number of different approaches have been explored to address a few critical issues related to the geopolymers prior to full deployment. A precise control of curing shrinkage was the most challenging task, along with retaining strength, thermal stability, and adhesive strength, which are key factors to determine their use in practical applications. The most important result is the chemistry of the geopolymer that can determine the curing shrinkage regardless of different

material sources. However, the other properties strongly depend on the chemistry. Consequently, it is desirable to leverage the variables based on the needed properties; no single composition that can satisfy all the required properties. Various geopolymers were produced during the present research period, examples of which are shown in Figure 49.

Nevertheless, the geopolymer based on blast furnace slag appeared very feasible for tuning the curing shrinkage while maintaining acceptable other properties. The slag-based geopolymer followed by curing inside the vacuum bag produced the best outcome. However, the vacuum bagging process may not be appropriate for use in an actual production, and an alternative curing process that can provide identical curing conditions as the vacuum bagging needs to be developed. The humidity oven is currently being utilized to remove the small amount of shrinkage that takes place in the slag based geopolymers. The exact conditions at which curing shrinkage does not occur should be studied. Also, curing within a humidity oven is more feasible when working with larger scale samples. Current work is involved in creating a suitable curing process, where curing shrinkage is minimized by adjusting the curing temperature, time, and humidity.

The geopolymers are functional material systems for use in the space mirror applications. The properties can be readily tailored in many different ways. Ultra-light substructures ($\rho \sim 1 - 2$ g/cc) with acceptable strengths are highly feasible by incorporating micro-glass balloons or carbon nano-fibers. The results have clearly demonstrated the technical feasibility with many advantages plus new functionalities (thermal stability, low CTE, and chemical inertness) when organic resin-based components are replaced with the geopolymers.

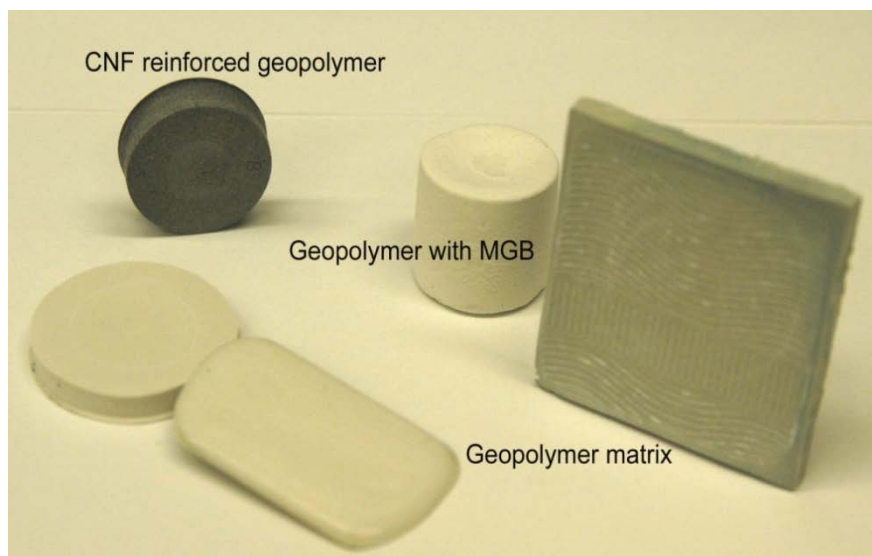


Figure 49. Various Geopolymers and Geopolymer Composites Developed in AFRL

6.2.3.3 Exploration of Commercial Geopolymers

Three commercial geopolymers (Davy 20, 65, 60) were purchased from Geopolymer Institute, France. According to the vendor's information, Davy 20 and 60 are K-based geopolymers, whereas Davy 65 is Na-based. The exact chemistry of all is proprietary and is not available. X-ray powder diffraction analyses were carried out for the three geopolymers. The results suggested that the raw material for the aluminosilicate (AS) sources of all three were identical, and the peaks could consistently be indexed as a mineral (Illite-2M1), whose chemistry can be assigned as $(K, H_3O)Al_2Si_3AlO_{10}(OH)_2$. Davy 20 was chosen for the CTE measurement. Recently, the composition as well as the curing process has been studied. The composition was fixed at 63 AS – 37 AAS (wt.%), where AS and AAS stand for aluminosilicate powder and aqueous alkali silicate solution, respectively. The following steps were used to prepare the specimen.

Mixing (2 min with Thinky mixer) → De-airing (1 min Thinky mixer) → casting (plastic mold) → vacuum bagging & curing at ambient atmosphere (3 days) → curing at 60 °C with vacuum bagging (5 days) → curing at 110 °C (1 day)

XRD analyses were carried out to obtain insights into any phase change during the curing process. As seen in Figure 50, the cured specimen seems predominantly amorphous, which is a sign of geopolymerization. This phase evolution is much different from what was previously observed in the MK-based geopolymer.

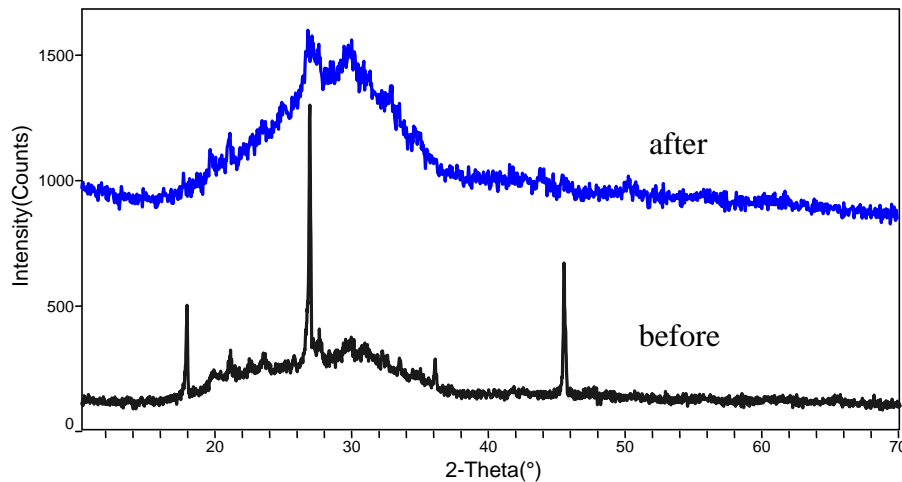


Figure 50. X-ray Diffraction Analysis of Davy 20 Commercial Geopolymer Before and After Curing Process

The cured specimen was then cut into approximately 7 mm × 6 mm × 3.5 mm (t) pieces for CTE measurement. The CTE measurement was conducted in the temperature range between 25 °C and 170 °C with a ramping rate of 1 °C/min. The CTE was measured three times using the same specimen. The results are summarized in Table 11.

Table 11. CTE of Davy 20 Commercial Geopolymer

*Davy 20 (25 - 80°C)	20.24 ppm (1 st)	12.15 ppm (2 nd)	-11.29 ppm (3 rd)
-------------------------	------------------------------	------------------------------	-------------------------------

* CTE was estimated between RT and 80 °C due to nonlinear behavior (see Figure 24)

It is noted that the measured CTEs of Davy 20 showed entirely different values at each measurement. Also, as seen in Figure 51, the three curves are all nonlinear, showing that the specimen underwent expansion and contraction. Such results were not expected. This suggests that the specimen may incompletely be cured (or geopolymerized) or mass loss might happen due to de-hydration that can closely be linked to the current curing conditions. The weight change was checked before and after CTE measurement, but it was negligible. Strikingly, the result of the third measurement showed a negative CTE (-11.29 ppm) value that cannot be currently rationalized. A systematic study is necessary to sort out the cause of this unusual CTE.

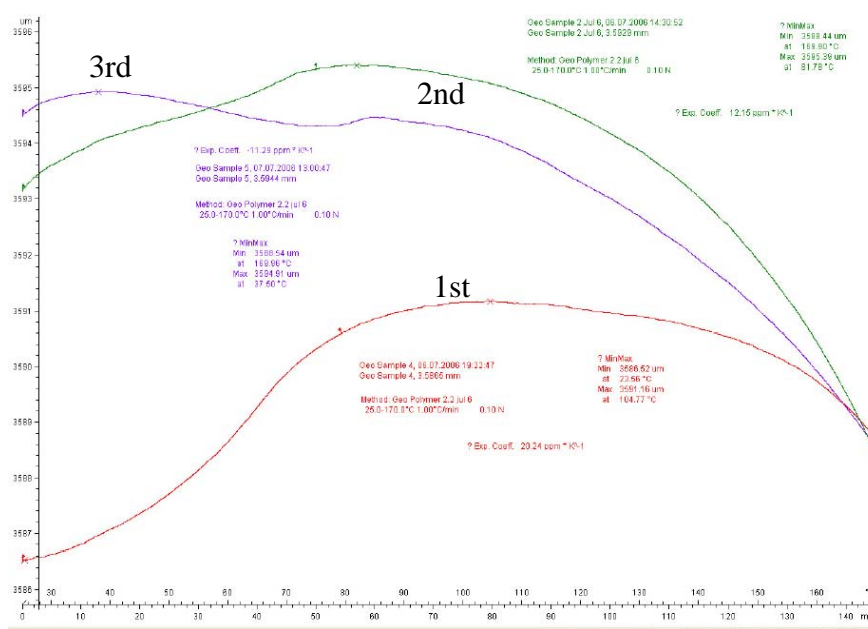


Figure 51. CTE Measurements of Commercial Geopolymer (Davy 20) by TMA

The three commercial geopolymers were used to study the curing process. The primary objectives were to examine whether the commercial geopolymers show a reasonable casting capability, and also whether the vacuum bagging is an effective way to suppress the curing

shrinkage as well as crack formation. All of the as-mixed commercial geopolymers exhibited good casting capability. The best castability was seen with Davy 20. The shrinkage was estimated by measuring the dimensional change. For Davy 20, the curing shrinkage of 5 to 10 % was observed without vacuum bagging, whereas 0.5 to 1.0 % shrinkage was found with vacuum bagging. Also, many cracks were seen in the cured specimen without vacuum bagging. The large curing shrinkage can be attributed to fast drying, where the water (from AAS) could be rapidly dried without bagging.

The technical feasibility of making mirror-quality surfaces by directly casting the geopolymer on the mandrel was also examined. The mixed geopolymers were cast on the glass mandrels and then cured. After curing, the geopolymers were released from the mandrels. Davy 65 showed significant interfacial reaction with the glass substrate, while less reaction was observed with Davy 60 and the least reaction occurred with Davy 20. Close examination of the glass surface under optical microscopy revealed some reaction. Nevertheless, the surface of the as-released geopolymer that was made of Davy 20 appeared very smooth and shiny. A high light reflectance can be visible in Figure 52. This preliminary result reflects that the direct cast and cure on the substrates is feasible for producing a single body Geo-Mirror. However, the question arises as to whether it is possible to produce an optical grade surface replica. An inert buffer layer (e.g. thin carbon layer) may be beneficial to minimize the interfacial reaction between the geopolymer and the substrates so that better surface quality may be expected. This potential advantage will be investigated during future work.

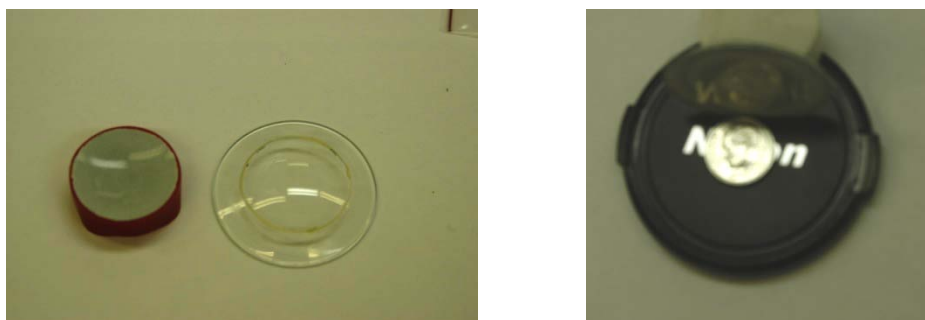


Figure 52. Surface of the As-Released Davy 20 Commercial Geopolymer with (1) Curved Surface and (2) Flat Surface

In the process of geopolymerization, water is an essential ingredient. The primary role of water is as a solvent, but water seems to fill many roles in the course of the curing process (geopolymerization). Typically, the water content can vary from 25 % to 35 % depending on the starting composition as well as the type of raw materials. This suggests that a large quantity of water may possibly remain at the end of the curing process. Also, it is conducive to leave the pores inside the geopolymer when water is removed under certain circumstances. The amount of the retained water could vary on the curing conditions. It is likely that some portion of water (bound-water) serves to build a network structure and the rest may remain as excess water molecules in some places in the geopolymer structure. This, named as free water, could be eliminated during curing process by increasing the temperature (up to 110 °C) and for a

sufficient period of curing. However, the bound-water may not completely be removed and thus, can be account for some of the physical changes. For this, it is worth studying the weight change of the cured geopolymer at elevated temperature.

For this purpose, the commercial geopolymer (Davy 20) was chosen, and subsequently cured following the same curing process as earlier applied, and finally heat treated up to 170 °C for 30 min with 0.5 °C/min heating and cooling rates. A TGA was employed to measure the weight change. The heating and cooling segments were assigned as follows; 1: ramp 1.0 °C/min to 100 °C, 2: isothermal for 60 min, 3: ramp 1.0 °C/min to 25 °C, 4: isothermal for 20 min, 5: ramp 1.0 °C/min to 200 °C, 6: isothermal for 60 min, 7: ramp 1.0 °C/min to 25 °C, 8: isothermal for 60 min, 9: ramp 1.0 °C/min to 300 °C, 10: isothermal for 60 min, 11: ramp 1.0 °C/min to 25 °C. The result is plotted in Figure 53 and it suggests many important issues. First, the weight change was observed up to 100 °C from room temperature, reflecting that significant moisture capture from the ambient atmosphere occurred in the geopolymer. Also, this indicates that open spaces (or pores) exist inside the cured geopolymer. Second, continuous weight loss happens as the temperature increases up to 300 °C. The weight loss above 100 °C cannot be contributed by solely moisture absorption and this may be accounted for through de-hydration of the bound-water. This de-hydration could intimately be linked to the curing atmosphere. Third, the weight change appears reversible and it is likely that the geopolymer looks as if it is breathing on heating and cooling.

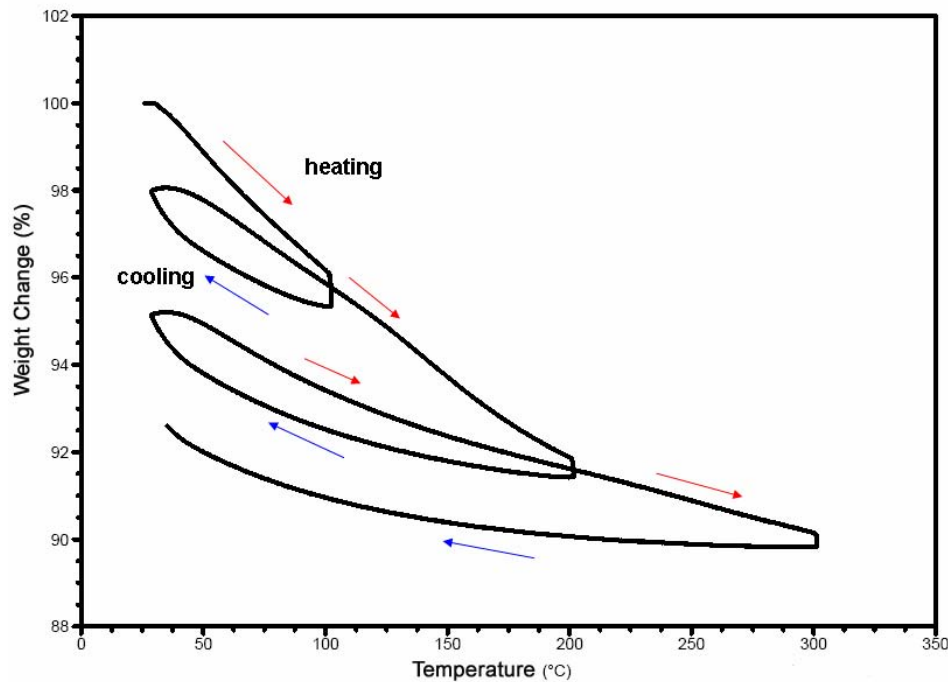


Figure 53. Weight Change of Davy 20 on Heating and Cooling

From the TGA result, it is suffice to say that the cured geopolymer contains many open spaces as well as bound-water (or hydrated water), which is likely related to the curing conditions. However, quick examination of the surface of the geopolymer under an optical microscope up to

1000 X revealed a dense and fine microstructure. The surface was also highly shiny, and such a highly porous body with a shiny surface raises many interesting questions. One plausible answer may be nano-sized open pores (as seen in zeolite-like structures) that can form a gradient across the body. The details of microstructure will be explored in future work using a high resolution SEM.

6.2.4 Subtask 3: Hybrid Mirror Replication

The fabrication of lightweight mirror assemblages via a replication technique offers great potential for eliminating the high cost and schedule associated with the grinding and polishing steps needed for conventional glass or SiC mirrors. A replication mandrel is polished to an inverse figure shape and to the desired finish quality. It is then, coated with a release layer, the appropriate reflective layer, and followed by a laminate for coefficient of thermal expansion (CTE) tailorability and strength. This optical membrane is adhered to a mirror structural substrate with a low shrinkage, CTE tailored adhesive. Afterwards, the whole assembly is separated from the mandrel. The mandrel is then cleaned and reused for the next replication run. The ultimate goal of replication is to preserve the surface finish and figure of the optical membrane upon its release from the mandrel. Successful replication requires a minimization of the residual stresses within the optical coating stack, the curing stresses from the adhesive and the thermal stress resulting from CTE mismatch between the structural substrate, the adhesive, and the optical membrane. In this paper, the results on replicated trials using both metal/metal and ceramic/ceramic laminates adhered to light weighted structural substrates made from syntactic foams (both inorganic and organic) are discussed [16].

6.3 Publications

1. B. T. Cesul, S. Mall, L. Matson and H. D. Lee, "Suitability of Geopolymers for Spacecraft Applications," Proc. Of 22nd Annual AIAA/USU Conference on Small Satellites, September 2008.
2. M. Y. Chen, L. E. Matson, H. D. Lee and C. Chen, "Replication of Lightweight Mirrors," *Proc. of SPIE, Optical Materials and Structures Technologies IV*, **7425** 74250S (2009).

6.4 References

1. T. A. Mary et. al., "Negative Thermal Expansion from 0.3 to 1050 K in ZrW_2O_8 ," *Science*, 272 (1996).
2. J. S. O. Evans, et. al., "Negative Thermal Expansion in ZrW_2O_8 and HfW_2O_8 ," *Chem. of Mater.*, **8** [12] 2809 – 2823 (1996).
3. M. S. Dadachova and R. M. Lambrechtb, "Synthesis and crystal structure of zirconium tungstate $\text{ZrW}_2\text{O}_7(\text{OH},\text{Cl})_2 \cdot 2\text{H}_2\text{O}$," *J. Mater. Chem.*, **7** [9] 1867–1870 (1997).
4. A. W. Sleight, M. A. Thundathil, and J. S.O. Evans, "Materials with low or negative thermal expansion," U.S. Patent 5,919,720 (1999).
5. J. S. O. Evans, "Negative thermal expansion materials," *J. Chem. Soc. Dalton Trans.*, 3317–3326 (1999).
6. A. P. Wilkinson, C. Lind, and S. Pattanaik, "A New Polymorph of ZrW_2O_8 Prepared Using Nonhydrolytic Sol–Gel Chemistry," *Chem. Mater.*, **11** [1], 101–108 (1999).

7. Q. Xing, et. al., "Single crystal growth of ZrW_2O_8 by hydrothermal route," *J. Cryst. Growth*, **283** 208–214 (2005).
8. J. A. Colin, D. V. Camper, S. D. Gates, M. D. Simon, K. L. Witker, and C. Lind, "Zirconium tungstate hydroxide hydrate revisited: Crystallization dependence on halide and hydronium ions," *J. Solid State Chem.*, **180** 3504–3509 (2007).
9. K. De Buysser, et. al., "Aqueous sol–gel processing of precursor oxides for ZrW_2O_8 synthesis," *J. Sol-Gel Sci. and Tech.*, **43** [3] 347–353 (2007).
10. N. Keishi, et. al., "Preparation and Properties of Zirconium Tungstate with Isotropic Negative Thermal Expansion," *J. Soc. Inorg. Mater. Jpn.*, **14** [327] 69–74 (2007).
11. J. Tani and H. Kido, "Precursor effects on ZrW_2O_8 formation kinetics," *Ceram. Int.*, **34** [6] 1533–1537 (2008).
12. M. Kofteros, S. Rodriguez, V. Tandon, and L. E. Murr, "A preliminary study of thermal expansion compensation in cement by ZrW_2O_8 additions," *Scripta Mater.*, **45** [4] 369–374 (2001).
13. L. M. Sullivan and C. M. Lukehart, "Zirconium Tungstate (ZrW_2O_8)/Polyimide Nanocomposites Exhibiting Reduced Coefficient of Thermal Expansion," *Chem. Mater.*, **17** [8] 2136–2141 (2005).
14. A. Kelly, R. J. Stearn, and L. N. McCartney, "Composite materials of controlled thermal expansion," *Comp. Sci. and Tech.*, **66** 154–159 (2006).
15. L. Sun, A. Sneller, and P. Kwon, " ZrW_2O_8 -containing composites with near-zero coefficient of thermal expansion fabricated by various methods: Comparison and optimization," *Comp. Sci. and Tech.*, **68** 3425–3430 (2008).
16. M. Y. Chen, L. E. Matson, H. D. Lee and C. Chen, "Replication of Lightweight Mirrors," *Proc. of SPIE, Optical Materials and Structures Technologies IV*, **7425** 74250S (2009).

7.1 TASK ORDER 0006 – METALLIC TPS

7.1 Beta Gamma Alloy Development

7.1.1 Conventional Gamma Alloys

Gamma (TiAl) alloys possess attractive attributes such as low density, high high-temperature strength and modulus retention, and excellent burn resistance [1-4]. Furthermore, over the years, remarkable improvements have been achieved in high temperature creep and oxidation resistance, making them technically viable for use at temperatures up to as high as 1650 °F depending upon applied stress and time [2, 3]. However, because of their inadequate ductility, poor impact-resistance and high production cost, gamma alloys have found only limited applications. High production cost is due in part to processing difficulties related to low ductility at temperatures up to and even significantly above their high brittle to ductile transition temperature's (BDTT) that increase rapidly with strain rate. Ingot castings have large, anisotropic columnar structures that further complicate the processing path to a viable product. These degrade the already difficult processability, often resulting in wrought-processing induced defects.

7.1.2 Alloy Design Concept and Experiments

Having recognized the potential benefits of beta solidification and subsequent transformation pathways that will minimize or remove the limitations as well as deficiencies in the current, peritectically-solidified gamma alloys, exploration work was initiated to explore a new class of multi-component TiAl-based alloys where such benefits could be realized. A comprehensive alloy design concept was formulated such that the new alloys are to: 1) be beta solidified (Al~45at% or lower), 2) contain reasonable amounts (3-6 at%) of Nb for enhanced oxidation resistance, 3) be alloyed with one or two beta formers (Mo, Cr, Mn, V) having relatively low solubility and moderate density, 4) have reasonably high beta volumes at temperatures greater than 1000°C and low volumes to none at lower temperatures, 5) have the phase distribution within $(0.75-0.96)\gamma-(0.20-0.04)\alpha_2-(0-0.20)\beta/B2$ at $T < 1000\text{ }^{\circ}\text{C}$, 6) have significantly finer grain sizes in both cast & wrought conditions than conventional gamma alloys, 7) be resistant to creep at temperatures at least up to 700 °C and as high as 900 °C.

Based on the alloy design concept described above and available ternary Ti-Al-M (M=Mo, Cr, Mn or V) phase diagrams, various compositions were selected within the range of Ti-(40-45)Al-(0-6)Nb-(0-3)Mo-(0-3)Cr-(0-6)Mn-(0-6)V-(0, 0.2)B and alloy buttons were produced by arc-melting. Coupon samples from each button were equilibrium heat treated at selected temperatures and quenched in water. The Nb equivalency (Nb_{eq}) of each beta-forming element was calculated from the ternary Ti-Al-M phase diagrams [5]. Using the phase and micro-composition data and information attained from the samples treated at 900 °C, an isothermal section at 900 °C of a generalized ternary phase diagram was constructed around the three phase field. Selected beta gamma alloys were produced in ingot forms, having a (6.3-7.0) cm diameter, using the induction skull melting (ISM) technique, followed by hot isostatic pressing (HIPing) under 1185 °C/173 MPa/4 h. Compositions were analyzed by the atomic absorption method and

often validated by the electron probe micro-analysis (EPMA) and compensated by estimation using the phase distribution obtained by the electron backscattered diffraction (EBSD) analysis. Canned hot extrusion was carried out at the AF Processing Lab, and forging of ingot billets was conducted isothermally at Wyman-Gordon or canned quasi-isothermally at AF Processing Lab. Tensile testing of round-bar specimens from the extrusion were conducted at Metcut Research.

7.1.3 Results and Discussion

7.1.3.1 Determination of Composition Range and Transformation Pathways

The phase relations centered around the ternary (g, α_2 , beta) field in the number of compositions within Ti-(40-45)Al-(2-7)Nb-(1-10)(Cr,Mn,V,Mo)-0.2B [6, 7] in the equilibrium conditions was determined. An isothermal section at 900°C of a generalized ternary phase diagram, Ti-(20-60)Al-(0-30)Nb_{eq}, was constructed and converted for multi-component systems, Ti-(20-60)Al-(0-8)Nb-(0-20)M (M=CR, Mn, V, Mo), based on the collected data and information and the Nb equivalency (Nb_{eq} values) listed in Table 12 of alloying elements. The equivalency values were derived from the ternary phase diagrams compiled by Kainuma [6]. Beta gamma alloys, rich with gamma phase, are classified into three, A, B. and C, depending on the phase relations, which are compared with the two-phase conventional gamma alloy G. The isopleth containing PQ in Figure 54a was estimated based on the phase relations as a function of temperature shown in Figure 54b. This isopleth shows that all three types of beta gamma alloy compositions are first solidified by beta solidification process and go through unidentified transformation pathways in the shaded area to end up different phase relations at low temperatures. The complex phase relations in the shaded area need to be quantified through additional experiments and thermodynamics calculation.

Table 12. Beta Forming Chemical Effectiveness (CE) and Their Normalized Values to Nb, Nb_{eq}, in Ti Alloys and Beta Gamma Alloys

Beta Forming	Ti Alloys [10]		Beta Gamma Alloys* [9]	
Element	CE	Nb _{eq} ,	CE	Nb _{eq} ,
Cr	1.0	4.5	1.0	3.3
Nb	0.22	1.0	0.3	1.0
V	0.53	2.4	0.6	2.0
Mn	1.3	5.9	0.7	2.3
Mo	0.8	3.6	2.1	6.3

Nb_{eq} = CE normalized to that of Nb

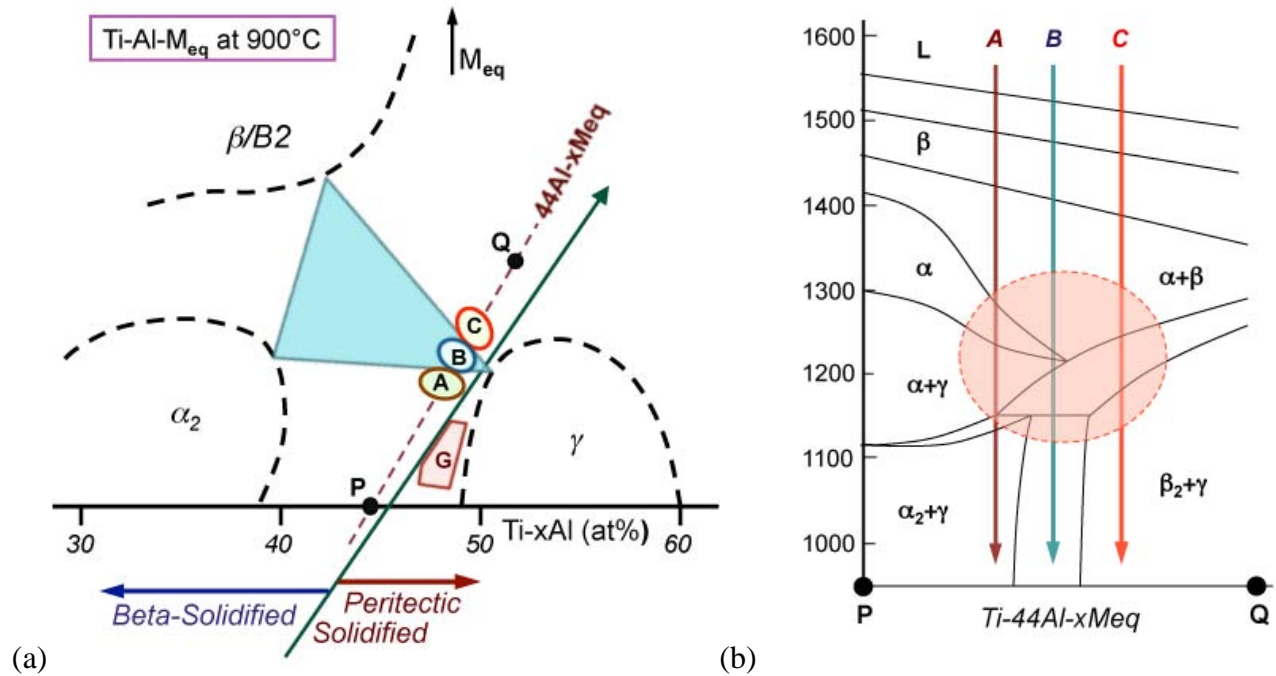


Figure 54. (a) Isothermal Section (900°C) Around the Three-Phase ($\gamma+\alpha_2+\beta$) Field of a Ti-Al-M_{eq} (M_{eq} = Nb_{eq} of All Alloying Elements) Phase Diagram Showing the Areas of Conventional Gamma Alloys (G) and Three Types of Beta Gamma Alloys (A, B, C) [6, 7] (b) Schematic of a Predicted Isopleth, Ti-44Al-xM_{eq}, that Cuts Through Beta Gamma Alloy Regions along PQ and Shows Their Three Estimated Transformation Pathways

These three groups of beta gamma alloys (A, B, C) have the compositions that lie within the broad range of Ti-(43-45)Al-(2-7)Nb-(1-6)M-0.2B-(0.1-0.3)C (at%), where M is one or two of beta-stabilizing elements (Mn, Cr, V, Mo). The desired phase distributions of these gamma rich beta gamma alloys are estimated and listed in Table 13.

Table 13. Desired Phase Distributions in Beta Gamma Alloys at T<1000 °C

Alloy Group	γ (vol. %)	α_2 (vol. %)	β/B (vol. %)	Phase Relation
A	80-96	20-4	<1	Conv. Gamma Alloys
B	80-96	15-2	2-13	Three-Phase Beta Gamma
C	85-98	<1	15-2	Two-Phase Beta Gamma

Preliminary experiments clearly showed that these alloys exhibited forging and rolling properties that are significantly superior to conventional gamma TiAl alloys. Group A alloys are essentially the conventional gamma alloys in terms of phase-relation, however they are beta solidified which produces a fine cast lamellar grain microstructure, with significantly reduced segregation. Figure 55 compares the as cast microstructure of an A alloy having a composition of T-43.2Al-4Nb-1.2Mn-0.7Mo (b) with that of conventional gamma alloy, K5 (a).

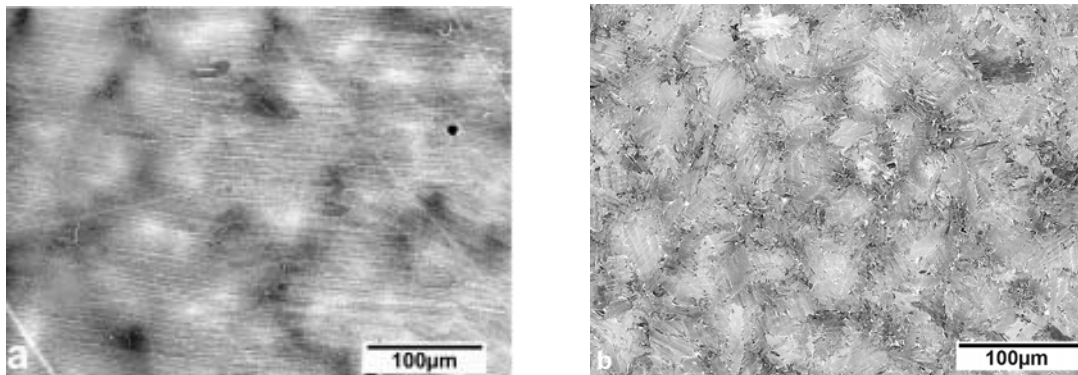


Figure 55. BEI of Cast Microstructures of (a) a Conventional Gamma Alloy K5 and (b) a Typical Group B Beta Gamma Alloy

7.1.3.2 Select Beta Gamma Alloys

Table 14 lists the beta gamma alloys that were designed for evaluation. The phase distribution and microstructure evolution in ISM ingot material was evaluated as a function of temperature. Based on the evaluation, ingot billets were extruded followed by phase and microstructure evolution investigation and then appropriate microstructure control. Tensile property testing and evaluation was conducted on the controlled microstructures.

Table 14. Aim and Analyzed Compositions of Beta Gamma Alloys

ID	Aim Composition (at%)	Actual Composition (at%)
7A	Ti-44Al-4Nb-3Mn-1Cr-0.2B-0.2C	T-44.24Al-4.20Nb-2.0Mn-1.09Cr-0.19B-0.14C
7B	Ti-44Al-4Nb-2Mn-1.5Cr-0.2B-0.2C	T-44.35Al-4.23Nb-1.77Mn-1.56Cr-0.19B-0.20C
7C	Ti-43Al-4Nb-2Mn-2Cr-1V-0.2B	Ti-43.50Al-4.07Nb-1.92Mn-2.03Cr-0.96V-0.19B
7D	Ti-44Al-4Nb-2Mn-1Cr-1V-0.2B	T-43.52Al-3.98Nb-4.05Nb-1.85Mn-1.04Cr-0.18B
8F	Ti-44Al-4Nb-1Cr-1V-0.5Mo-0.2B	Ti-43.34Al-4.08Nb-1.11Cr-0.94V-0.52Mo-0.19B
8G	Ti-44Al-4Nb-2Cr-1Mn-1V-0.2B	Ti-43.22Al-4.02Nb-1.05Cr-0.91Mn-0.92V-0.18B
9CN*	Ti-44Al-4Nb-2Cr-0.2B	Ti-43.6Al (estimated based on EBSD data)
9EN*	Ti-44Al-4Nb-1.5Cr-0.5Mo-0.2B	Ti-43.9Al (estimated based on EBSD data)

7.1.3.3 Evaluation of Alloys 7A, 7B, 7C, 7D

Phase Distribution: Figure 56 plots the phase distributions in the ingot materials as a function of temperature. All alloys show a three phase field below 1300 °C with a beta phase volume peak centered about 1200 °C. They also show a local maximum in the alpha phase volume centered around 1300-1350 °C, with a relatively narrow single alpha phase field for alloys 7A, 7C and 7D but no single alpha field for alloy 7B. 7A and 7B ingot billets were extruded canned at temperatures around 1200 °C. All alloys were smoothly extruded with no cracking, and as extruded microstructures are relatively non-uniform and banded with areas of finely mixed phases and coarse grains.

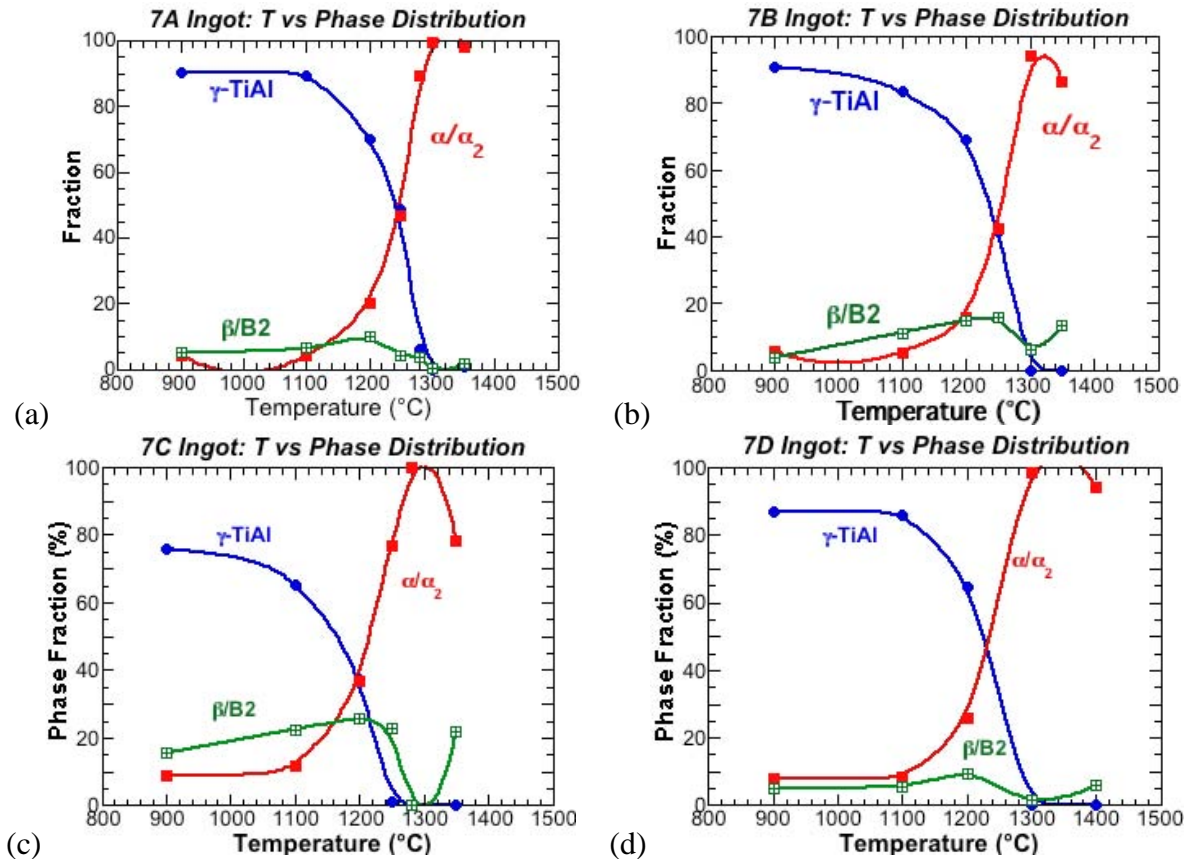


Figure 56. Equilibrium Distributions of Constituent Phases Against Temperature Shown for Alloy Ingot Material (a) 7A, (b) 7B, (c) 7C and (d) 7D the beta-phase distribution contains a local maximum peak centered around ~1200 °C

Extrusion and Tensile Properties: The heat treatment conditions for leading to desired microstructure forms were determined for all extrusions. Smooth dog bone tensile specimens were tested at RT under a strain rate, 4×10^{-4} sec, and at either 700 °C or 800 °C under the same strain rate. Alloy 7A material showed the best strength-ductility combinations in fine-grained material forms. The structures were found to need further optimization for more uniform distribution of microstructure and improved phase distribution. Nevertheless, the yield strength and fracture strain combination (802 MPa and 2.8%) is remarkable in spite of relatively non-uniform grain size distribution and relatively low (<90%) gamma grain volume (Figure 57a). The elevated tensile data plotted against temperature (Figure 57b) shows that selected duplex materials exhibit excellent high temperature strength retention. Nearly fully lamellar (NFL) material (alloy 7D) has higher strength levels throughout the tested temperature range, however, with much reduced fracture strain. The BDTT's, ranging from 520-660 °C, are significantly lower than those (650-800 °C) of conventional gamma alloys. The low BDTT range may have important implications for fabricating thin sheets and foils.

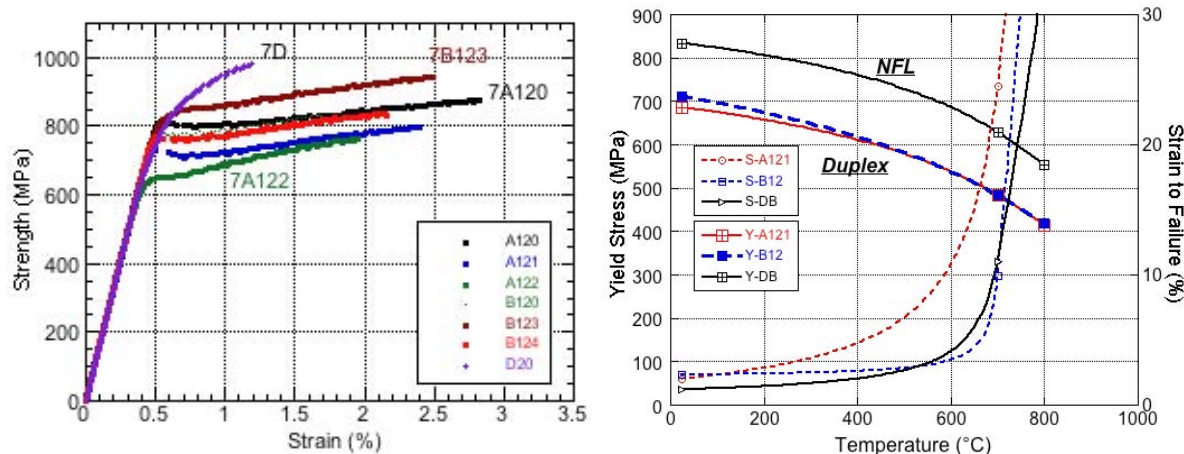


Figure 57. (a) Stress-Strain Curves of Tensile Specimens Tested at RT and (b) Tensile Yield Strength and Strain-to-Failure Variation against Temperature in Alloy 7A (triplex), 7B (triplex) and 7D (NFL or Nearly Fully Lamellar) Materials

Microstructure-Property Relationships: All tested microstructures are equiaxed triplex except for 7D-20 specimens whose structures are lamellar. The relationships between alloy composition, extrusion condition, post extrusion heat treatment, microstructure evolution and RT tensile properties are complex, Figure 58a. Nevertheless, several significant observations can be drawn. The strength levels are high, but they are not related to grain size or phase distribution within the range of equiaxed microstructure features. The fracture strain and ductility of alloy 7A are related to the gamma phase distribution (Figure 58b) and both alloys the yield strength (YS) and fracture strain (FS) decrease with increasing heat treatment temperature.

The usual inverse relationship between strength and total or FS at RT is not apparent. The material having the lowest YS (7A1-22) shows the smallest fracture strain among alloy 7A materials conditions. Lowering the alpha 2 or increasing the gamma volume increases the fracture strain and elongation in alloy 7A extrusion. The specimen with the greatest gamma volume (~88%) shows a very high YS as well as the greatest FS among those tested. This suggests that a composition generating a higher gamma volume can produce greater ductility (>2.5%) and YS level (>850 MPa). The proportional relationship between strain and strength shown in alloy 7A is unusual and worth further investigation. In alloy 7B extrusion, the situation is unclear, which may be because the differences in constituent phases are relatively small among the alloy samples. Nevertheless, it can be said that the gamma volume greater than 82% and the alpha volume less than 10%, may be required for the material to exhibit reasonably high fracture strain with sufficient strength levels.

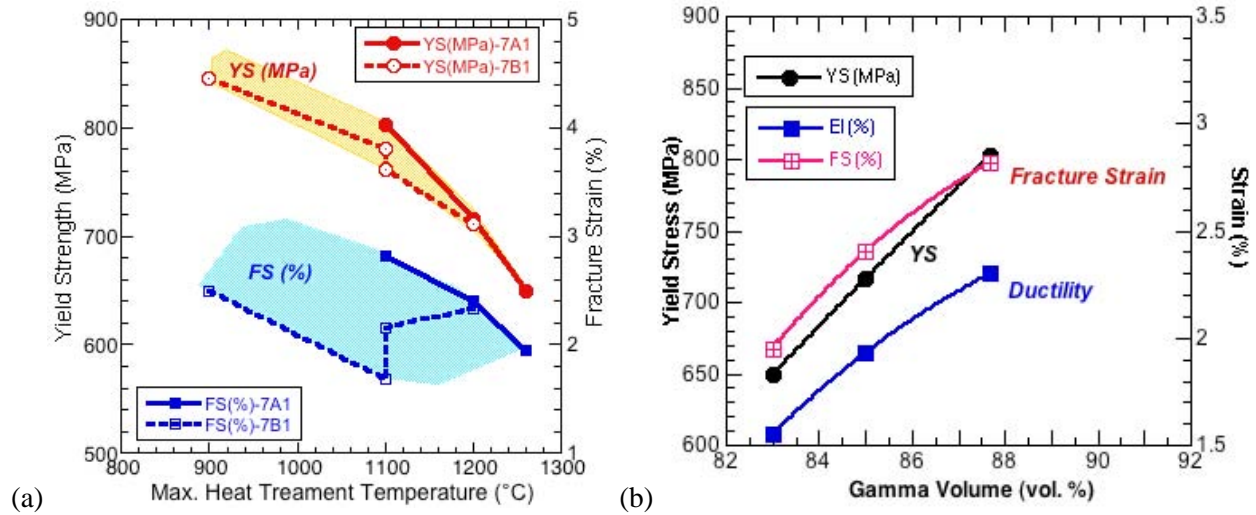


Figure 58. (a) Tensile YS and FS Values Plotted Against the Maximum (or Starting) Heat Treatment Temperature for both 7A and 7B Specimens and (b) Yield Strength and Fracture Strain in Alloy 7A Extrusion against Gamma Volume Fraction in Heat-Treated Conditions

7.1.4 High Beta Containing Beta Gamma Alloys

Two alloys used for this study, 8F and 8G, listed in Table 15 were formulated for their Nb_{eq} values to be 12 and 14, which are compared to $Nb_{eq}=13$ for alloy 7A. Additional beta-forming elements, V and Mo, were introduced in these ISM alloys. If the aim compositions are achieved in the ingots, these alloys would contain the gamma volume at 900 °C which is the same as that (~91v/o) in alloy 7A. The actual Al contents were appreciably lower than the target compositions, which resulted in relatively low gamma contents at 900 °C. However, both alloys contained the gamma volumes at 900 °C that are still within the desired range (Table 15), and exhibit remarkably refined cast + HIP microstructures, as shown in Figure 59a for alloy 8G. This, along with their ample beta phase volumes (Figure 59b), was expected to ease hot working significantly. In fact, the 8F ingot billet was isothermally (1150 °C) side-forged to a large plate very smoothly to convert the lamellar microstructures to fine equiaxed microstructures. The 8G cast plates having a prominent local maximum of beta phase centered around 1200 °C (Figure 6b) were pack-rolled to thin sheet readily through 90% reduction, which was the first direct rolling ever reported.

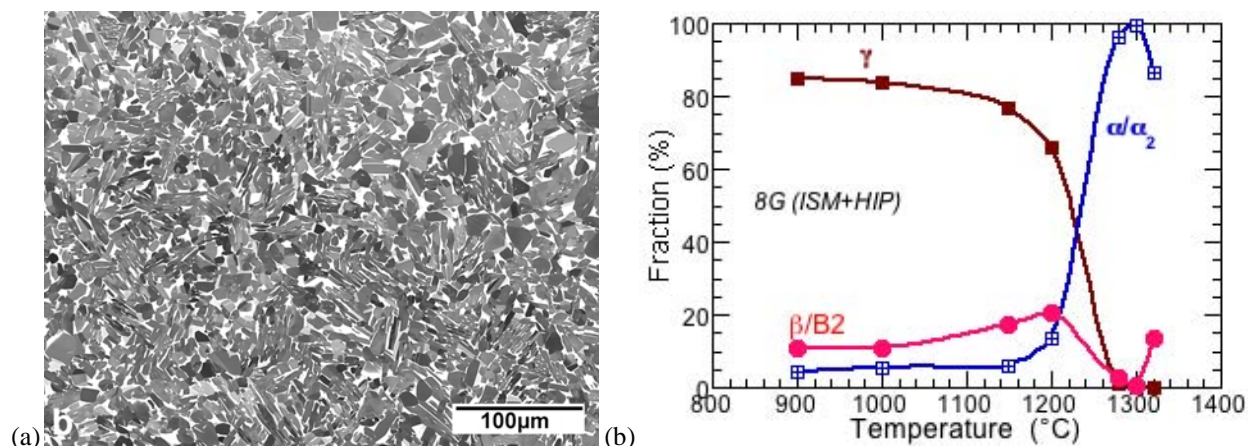


Figure 59. (a) BEI of Alloy 8G ISM Ingot Microstructure After HIP (1150 °C under 173 MPa for 3 h) and (b) Phase Distribution as a Function of Temperature

7.2 Summary

A new class of TiAl-based alloys, beta gamma alloys, have been developed utilizing the beta solidification and the benefits of subsequent solid-state transformation pathways. The ranges of beta gamma alloy compositions within Ti-(43-44)Al-4Nb-(1-4)(Cr, Mo, V, Mo) microstructure features, and processing conditions/parameters for improved ductility are better understood in extruded material forms. The best, achieved plastic ductility was 2.3% with a total strain of 2.8%, along with significant strength levels. Control of phase distribution and microstructure features could increase the tensile ductility to 3%. Significant advances made in the understanding of beta gamma alloys and the relationships between alloy-processing-microstructure-properties. The melting practice to achieve target compositions of beta gamma alloys has not been optimized. This needs to be further investigated. Demonstration was made in the possibility of direct processing circumventing the conversion process required for conventional gamma alloys.

7.3 Publications

1. M. Karadge, Y-W. Kim, and P. I. Gouma, "Synergistic Precipitation Strengthening in TiAl Alloys," *Appl. Phys. Lett.*, **89** 181921 (2007).
2. J.S. Kim, Y.H. Lee, Y-W. Kim, C.S. Lee, "High temperature deformation behavior of beta gamma TiAl alloy," *Mater. Sci. Forum*, **539-543** 1531-1536, (2007).
3. Y-W. Kim, Paper 3-1 in "3rd International Workshop on γ-TiAl Technologies", eds. F. Appel, V. Guether, and Y-W. Kim, 29-31 May 2006, Bamberg, Germany.
4. D.S. Shi and Y.W. Kim, Ti-2007, vol II (2008), JIM, pp. 1021-1024.
5. S. Russ, C. Woodward, Y-W. Kim, and F. Yoltan, "Effect of Al Content on Microstructure/Phase Distribution and Strength/Ductility in a PM Gamma Alloy," pp. 51-60 in *Structural Aluminides for Elevated Temperatures*. Edited by Y-W. Kim, D. Morris, R. Yang and C. Leyens, TMS, 2008.

8.4 References

1. Y-W. Kim, *JOM*, 46 (1994) 30-39.
2. Gamma Titanium Aluminides 1999, eds. Y-W. Kim, D.M. Dimiduk and M.H. Loretto, TMS, Warrendale, PA (1999).
3. Structural Intermetallics 2001, eds. K.J. Hemker and D. M. Dimiduk, et al., TMS, Warrendale, PA (2001).
4. 2006 International Symposium on Gamma TiAl Technologies, eds, V. Guether, F. Appel and Y-W. Kim, May 29-31, 2006, Bamberg, Germany.
5. R. Kainuma, Y. Fujita, H. Mitsui, I. Ohnuma, and K. Ishida, *Intermetallics* **8** 855-867 (2000).
6. Y-W. Kim, pp. 29-31 in 3rd International Workshop on γ -TiAl Technologies. Edited by F. Appel, V. Guether, and Y-W. Kim, Bamberg, Germany, May 2006.
7. Y-W. Kim, S-L. Kim, D.M. Dimiduk, and C. Woodward, unpublished work, manuscript to be submitted to *Intermetallics* (2010).
8. *Advanced Materials & Processes*, p. 67 (June, 2005).
9. T. Carneiro and Y-W. Kim, "Evaluation of ingots and alpha-extrusions of gamma alloys based on Ti-45Al-6Nb," *Intermetallics*, **13** 1000-1007 (2005).
10. M. Yoshihara and Y-W. Kim, "Oxidation behavior of gamma alloys designed for high temperature applications," *Intermetallics*, **13** 952-958 (2005).

8.0 TASK ORDER 0007 – UHTC TPS

8.1 Introduction

The increasing demand for higher responsiveness and operability of aircrafts has resulted in a demand for materials that can withstand extreme thermal environments. UHTCs, such as $\text{HfB}_2\text{-20SiC}$, show the most promise in terms of surviving the demanding conditions of hypersonic vehicles. The leading edge and fuel injection struts require materials to withstand high temperature gradients and high fluid velocity environments. This task addressed the processing, characterization, and understanding of the process-structure-property correlations in these materials, with an emphasis on oxidation and erosion.

Fundamental research on UHTCs was conducted, including varying the composition and processing variables of these materials and studying their effects on properties with an emphasis on oxidation and erosion. The oxidation/erosion behavior of UHTCs was modeled in order to predict the lifetimes of these materials under use. Preliminary work in the process development and characterization of UHTC composite materials was initiated through work with SRI International and in-house.

The key concern in evaluating UHTCs for hypersonic applications is our ability to test the materials under conditions that are close to the real application. The conditions experienced by the leading edge under hypersonic flight are complex and difficult to simulate in a laboratory. The rig at the Propulsions Directorate is one of the unique facilities that simulate the combustion chamber of hypersonic flight. This facility was used to study UHTC materials under conditions that are arguably the most realistic conditions available in a laboratory.

8.2 Oxidation Resistance of UHTC Materials

Dense samples of ZrB_2 20 vol% SiC were successfully fabricated by spark plasma sintering without the use of sintering aids. Oxidation behavior of these samples was characterized by exposing them to 1400 °, 1500 °, and 1600 °C in an ambient atmosphere for 150 min, and by measuring the weight gains of the sample and crucible, as well as the thickness of the oxide scale and the glassy outer layer. The effects of gravity on the viscous outer layer are shown to result in significant heterogeneity within a sample. The oxidation scales were characterized by scanning electron microscopy and transmission electron microscopy with energy dispersive spectroscopy analysis. The oxide scale was found to be composed of three layers: (1) a SiO_2 -rich glassy outer layer, (2) an intermediate layer of a ZrO_2 matrix with interpenetrating SiO_2 , and (3) a layer containing a ZrO_2 matrix enclosing partially oxidized ZrB_2 with Si-C-B-O glass inclusions [1].

Oxidation resistance tests were carried out on $\text{HfB}_2\text{-20 vol.}\%$ SiC prepared by spark plasma sintering. The dense samples were exposed from 1400 to 2000 °C in an ambient atmosphere for 1 h. For comparison, the same material was tested using an arc jet to simulate an atmospheric reentry environment. The oxidation properties of the samples were determined by measuring the weight gain per unit surface area and the thicknesses of the oxide scale. The oxide scale consists of a SiO_2 outer layer, porous HfO_2 layers, and an HfB_2 layer depleted in SiC. A transition in

HfO₂ morphology from equiaxed to columnar and a decrease in SiO₂ viscosity between 1800 and 1900 °C accompanied a rapid increase in weight gain and scale thickness [2].

8.3 A Model for the Oxidation of ZrB₂, HfB₂ and TiB₂

A mechanistic model that interprets the oxidation behavior of the diborides of Zr, Hf and Ti in the temperature range of 1000–1800 °C was formulated. Available thermodynamic data and literature data for vapor pressures and diffusivities were used to evaluate the model. Good correspondence was obtained between theory and experiments for weight gain, recession and scale thickness as functions of temperature and oxygen partial pressure. At temperatures below about 1400 °C, the rate-limiting step is the diffusion of dissolved oxygen through a film of liquid boria in capillaries at the base of the oxidation product. At higher temperatures, the boria is lost by evaporation, and the oxidation rate is limited by Knudsen diffusion of molecular oxygen through the capillaries between nearly columnar blocks of the oxide, MO₂ [3].

8.4 A Model for Transitions in Oxidation Regimes of ZrB₂

A mechanistic model that interprets the transition in oxidation behavior of zirconium diboride as the temperature is varied from 600 °C to 2500 °C is presented. Available thermodynamic data and literature data for vapor pressures, oxygen permeability in boria, and viscosity of boria were used to evaluate the model. Three regimes and the temperatures of transition between them were identified. In the intermediate temperature regime, viz., 1000 °C to 1800 °C, good correspondence was obtained between theory and experiments for weight gain, recession, and scale thickness as functions of temperature and oxygen partial pressure. In this regime, the rate-limiting step is the diffusion of dissolved oxygen through a film of liquid boria in capillaries at the base of the oxidation product. At lower temperatures, an external boria scale forms, but it was not found to contribute significantly to oxidation resistance. Comparison with literature data on recession is very good, but weight gain is predicted to be higher than experimentally observed unless flow of viscous boria is included. At higher temperatures, the boria is lost by evaporation, and the oxidation rate is limited by diffusion of molecular oxygen through the capillaries between nearly columnar blocks of the oxide MO₂; this regime is soon followed by a rapid acceleration of recession due to vaporization of the oxide MO₂ itself.[4]

8.5 Evaluation of SPS Phenomena

A systematic study of current path in spark plasma sintering was conducted to determine its effect on the sintering of an insulating material. The current, voltage, temperature, and densification characteristics of Al₂O₃ held under constant pressure in a graphite die were determined. A comparison was made between samples in a graphite die with and without a BN coating. The BN coating prevented the current from flowing through the graphite punches and into the die body so that no indirect heating could occur. When no BN coating was used, the sample densified as expected; however, when a BN coating was used, no heating of the sample was observed. A brief comparison between the use of a BN coating with insulating and conductive samples is made using powders of HfB₂–24 vol% SiC as an example [5].

8.6 UHTC Exposure in the Direct-Connect Scramjet Combustor Test Facility

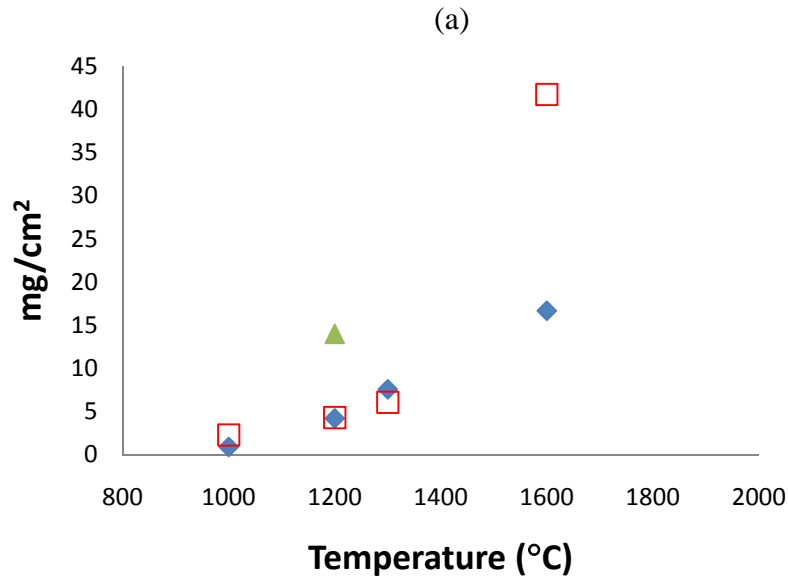
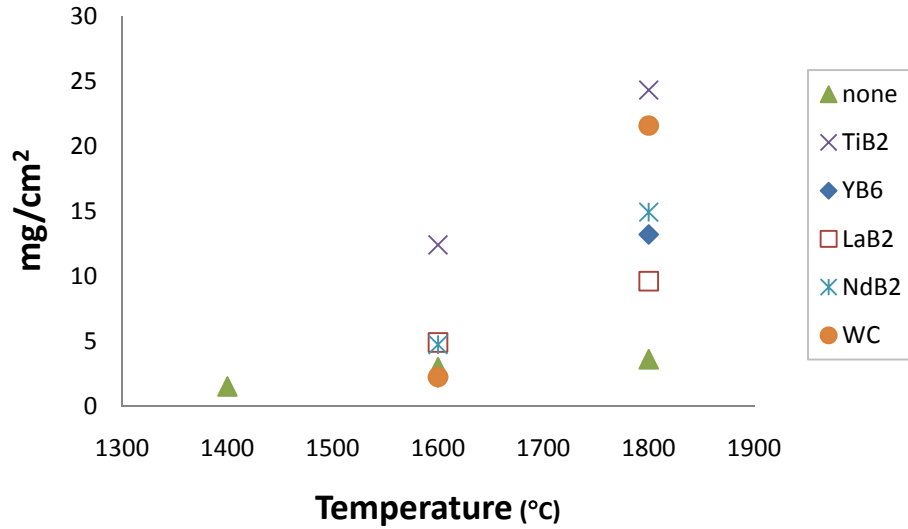
A methodology to evaluate the aerothermal response of sharp leading edge materials by exposing them directly to hypersonic flow up to Mach 7 was developed and evaluated. The exposure was conducted using a prototype scramjet engine as a wind tunnel. A sample holder was designed using combustion fluid dynamics results as inputs into structural models. The rig conditions were evaluated and found to be close to those during free flight, with respect to aerothermal parameters of importance for material survivability. Samples of ultra high-temperature ceramics and SiC were found to withstand the short-term exposure that simulated Mach 6.5 at 25 km altitude [6].

8.7 Summary of Unpublished work

8.7.1 Effect of Additives on Oxidation Resistance of UHTC Materials

During the course of research on the oxidation of $\text{HfB}_2\text{-SiC}$ and $\text{ZrB}_2\text{-SiC}$ it was found that the oxidation resistance became poor for $\text{HfB}_2\text{-SiC}$ materials at 1800 °C and for $\text{ZrB}_2\text{-SiC}$ materials at 1600 °C. These are also the same temperatures at which the SiO_2 -rich outer glassy layer begins to flow from the respective sample and are near the transformation temperature from monoclinic to tetragonal for the diborides. The transformation results in a volume loss of around 3% and has been shown to affect the oxidation resistance of pure diboride samples. Oxidation of these materials produces a layered structure that, in general, consists of a protective SiO_2 -rich outer layer and a porous metal oxide inner layer. In our samples we see a morphology change at these temperatures and an infiltration of the SiO_2 glass into the HfO_2 layer. In order to improve oxidation resistance of these materials three paths can be explored: (1) increase the viscosity of the SiO_2 layer by adding rare earth ions to promote phase separation; (2) add transitional metals that will stabilize one form or another of the hafnia or zirconia or; (3) densify the porous metal oxide scale to slow oxygen ingress. Towards this goal the following additives were mixed with SiC containing HfB_2 and ZrB_2 -based UHTCs: NdB_6 , TiB_2 , LaB_6 , YB_6 , CeB_6 , and WC. The majority of the additives were introduced as borides to limit the number of species present in the samples. The volume percent of each species was chosen based on analysis of the phase diagrams minimizing the concentration of additive to achieve the desired result such as phase stabilization.

Of the studied additives, the TiB_2 and YB_6 were the only ones to stabilize the tetragonal phase of MeO_2 at a lower temperature than for the pure oxide. The plots in Figure 60 show that the addition of any of these additives did not improve oxidation resistance over the entire tested temperature range. In particular, the regime above 1600 °C is negatively impacted by the addition of any of the studied additives. Extensive XRD and SEM analysis with EDS revealed that the boride additives all interacted with the SiO_2 scale that is formed during oxidation. The lengths of the oxide scale were longer for the samples with additives compared to the $\text{MeB}_2\text{-SiC}$ sample which is consistent with the observed higher weight gain.



(a)

(b)

Figure 60. Weight Gain per Surface Area for UHTCs
 (a) $\text{HfB}_2\text{-SiC}$ and (b) $\text{ZrB}_2\text{-SiC}$ with Various additives

8.7.2 Mechanical Testing of UHTC Materials

There is limited data in the literature on the mechanical properties of UHTC materials and strength measurement data only exists for temperatures up to 1500 °C. Four-point flexural strength was tested at room temperature and at 1600 °C in an inert environment. Two sets of mechanical testing data were obtained. For the first $\text{HfB}_2\text{-20vol\% SiC}$ sample, the room temperature strength was only 487 MPa which is well below the expected values. Investigation of these samples revealed large agglomerates of SiC that were decreasing the sample strength. Processing refinement including longer milling times and smaller screened sieving led to a more

homogenously distributed SiC phase. The mechanical strength of these HfB_2 -20vol%SiC samples was 727 MPa at room temperature and 218 MPa at 1600 °C. Similar samples in the literature are reported to possess a room temperature strength of 770 ± 35 MPa and fall to 310 ± 15 MPa at 1500 °C.

8.7.3 Fiber-Reinforced UHTC Materials

8.7.3.1 Subcontract with SRI International

Through a small subcontract with UES, SRI International fabricated minicomposites and small fabric composites containing SiC fiber (IBN Sylramic, uncoated and coated with BN/SiC) in a UHTC matrix ($\text{ZrB}_2 + \text{SiC}$). SRI developed a process to produce UHTC coatings under previous AF funding and this process was extended to the composite formation. Their process utilizes a slurry/polymer mixture for the matrix formation, followed by multiple PIP cycles with a preceramic polymer (SMP-10).

Minicomposite samples were initially produced under this program and the fabricated samples were sent to AFRL/RXLN for mechanical testing and characterization. Samples were heat treated at either 1000 °C or 1500 °C during processing. Tensile testing of the minicomposites showed that the samples heat treated at the higher temperature showed lower maximum loads. There was also a visible difference between the samples, with the 1500 °C samples showing a lighter color. Due to the small number of samples (1 per condition), definitive minicomposite strength values were not attained. However, information about the composite processing was obtained.

The minicomposites were fabricated using either uncoated fiber or BN/SiC coated Sylramic fibers. In the latter case, the coatings were sufficiently thick to prevent optimal infiltration of the matrix between the fibers. Figure 61 shows low magnification images of samples with a) uncoated and b) BN/SiC coated fibers. The dispersion of the uncoated fibers appears very good, with excellent matrix infiltration between the fibers. Alternately, the sample with the coated fibers shows areas of fiber “clumping” and more porosity. Figure 62 shows a higher magnification image of sample 61b, which shows bridging between the coated fibers, along with several areas of poor infiltration.

Overall, SEM analysis indicated that there was no obvious reaction between the fiber, matrix and/or the fiber coating. The samples that underwent multiple infiltrations with SMP-10 appeared denser than the uninfiltrated samples; further, the samples annealed at 1000 °C appeared denser than the samples heated to 1500 °C. This difference can be attributed to the generation of porosity from the SMP-10 precursor during heating from 1000 °C to 1500 °C. Oxygen is also present in the sample, as is commonly seen with the SMP-10 precursor. This can lead to the formation of oxides, followed by carbothermal or boro-thermal reductions at the higher temperatures (1500 °C).

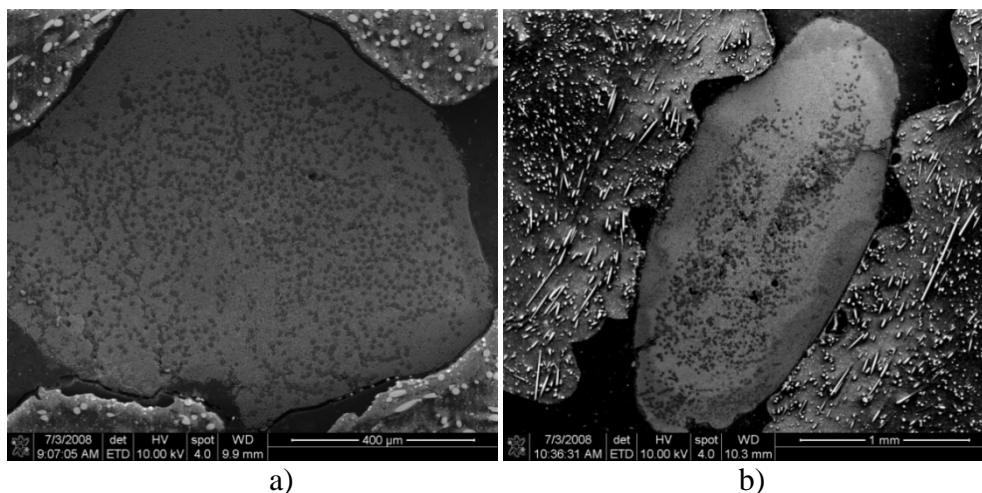


Figure 61. SRI-produced SiC/UHTC Minicomposites

- a) UF35 – uncoated Sylramic IBN fiber infiltrated with UF27 (48.8g ZrB₂, 4.43g SMP-10, and 7g cyclohexane), infiltrated twice with SMP-10 and heat treated at 1500°C for 1 hour*
- b) UF43 – BN/SiC coated Sylramic IBN fibers infiltrated with UF27 (48.8g ZrB₂, 4.43g SMP-10, and 7g cyclohexane), infiltrated twice with SMP-10 and heat treated at 1500°C for 1 hour*

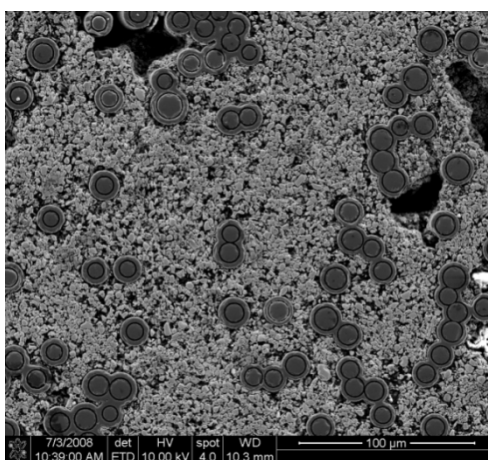


Figure 62. Higher Magnification SEM Image of UF43 Sample (Figure 61b)

Small fabric samples (~1" x 1", three layers thick) were produced under this effort using both coated and uncoated Sylramic fabrics. Initial trials utilized the coated fabric; however, the matrix infiltration was more difficult due to the thickness and bridging of the coatings. A second set of trials were conducted using the uncoated fabric. Final conclusions from SEM analysis of the ZrB₂-SiC composites (SiC fiber + ZrB₂-SiC matrix) revealed that the best infiltration of the matrix occurred with uncoated SiC fibers, due to bridging of the BN coatings applied to the fibers. Good infiltration and densification of the matrix was found with one infiltration of the ZrB₂-SMP-10 slurry followed by two infiltrations of SMP-10. After three infiltrations of SMP-10, agglomerates of SiC formed in the composite.

8.7.3.2 In-House UHTC CMC Fabrication Trials

In order to develop SiC fiber composites with a UHTC matrix in-house, research was conducted to prepare a suitable slurry. The SiC preceramic polymer, SMP-10, was used as the binder while HfB₂ powders were used as the solid phase. As-received HfB₂ powder was ball milled to reduce the particle size from a bimodal distribution with peaks at 4 and 10 microns to a distribution with peaks at 2 and 6 microns. The liquid carrier was toluene. With this slurry, it was possible to infiltrate both tows and fabrics of SiC fibers (Nicalon). A processing method was devised to infiltrate and cure composite samples under vacuum at 120 °C. Four to five layers of SiC fabric were infiltrated individually and then stacked under pressure while heating. The samples were then annealed under Ar to achieve either an amorphous or crystalline SiC phase. SEM investigation of the samples showed uniform distribution of the HfB₂ throughout the sample. Future work will include processing improvements to increase the matrix density, additional infiltration cycles and testing for properties such as oxidation resistance and mechanical strength.

8.7.4 Stability of Monazite-coated SiC Fiber with SMP10

Past work in the group showed that there was a window of oxygen partial pressures where LaPO₄ (monazite) coatings on SiC fibers were stable. This work concluded that monazite did not remain stable in reducing atmospheres at certain temperatures. Since one of the more common methods of creating SiC-SiC composites is through the infiltration of the SiC fibers with a preceramic polymer that is then annealed in an oxygen deficient atmosphere, it is necessary to determine if the LaPO₄ coatings can withstand the composite processing. LaPO₄ coated Hi Nicalon S fibers were dipped in SMP-10 and cured to 1000 °C in an atmosphere containing 497 ppm oxygen balance argon. The same fibers were also heated to 1000 °C in a 497 ppm oxygen balance argon atmosphere without SMP-10. TEM analysis of both samples showed that the LaPO₄ coating remained intact with the same microstructure as the original coating. Future work includes studying a temperature range up to 1400 °C to determine the ultimate stability regime of LaPO₄ with SMP-10.

8.7.5 Resistance Heater

A setup was constructed to pass 100 s of amps through a small cross-section of UHTC samples to rapidly heat the specimens in a localized manner. A series of HfB₂ – 20 vol% SiC were tested using the resistance heater. The samples were heated to 1600, 1700, 1800, and 1900 °C for 10 minutes. The rapid heating rate (>70 °C) of the resistance test allowed us to reduce the effect of oxidation on heating and compare these samples with those heated in the furnaces. SEM micrographs of some of these samples show oxide scale microstructures that are similar compared to those heated in the furnaces.

8.7.6 UHTC Samples for MISSE

Six samples were prepared for the Materials International Space Station Experiment (MISSE) test program: 3 HfB₂-20 vol% SiC and 3 ZrB₂-20 vol% SiC. Samples with the same matrix were prepared from the same powder batch. The samples were sintered as 20 mm pucks in the SPS and were cut to 19 mm pucks by EDM. The sample faces were ground to remove the residual

carbon from sintering and the oxidation layer from EDM cutting. One face was polished to a 1 micron finish. One of each sample type was imaged by SEM and then stored. The remaining 4 samples were delivered to be sent to the international space station, where they will receive approximately 18 months of exposure on the outside of the station.

8.7 Publications

1. C. M. Carney, P. Mogilvesky, and T. A. Parthasarathy, "Oxidation Behavior of Zirconium Diboride Silicon Carbide Produced by the Spark Plasma Sintering Method," *J. Am. Ceram. Soc.*, **92** [9] 2046–2052 (2009).
2. C. Carney, "Oxidation resistance of hafnium diboride—silicon carbide from 1400 to 2000 °C," *J. Mater. Sci.*, **44** 5673–5681 (2009).
3. T. A. Parthasarathy, R. A. Rapp, M. Opeka, and R. J. Kerans, "A model for the oxidation of ZrB_2 , HfB_2 and TiB_2 ," *Acta Mater.*, **55** 5999–6010 (2007).
4. T. A. Parthasarathy, R. A. Rapp, M. Opeka, and R. J. Kerans, "A Model for transitions in oxidation regimes of ZrB_2 ," *Mater. Sci. Forum*, **595-598** 823–832 (2008).
5. C. M. Carney and T. Mah, "Current Isolation in Spark Plasma Sintering of Conductive and Nonconductive Ceramics," *J. Am. Ceram. Soc.*, **91** [10] 3448–3450 (2008).
6. T. A. Parthasarathy, M. D. Petry, G. Jefferson, M. K. Cinibulk, T. Mathur, and M. R. Gruber, "Development of a Test to Evaluate Aerothermal Response of Materials to Hypersonic Flow Using a Scramjet Wind Tunnel," submitted to *Intl. J. Appl. Ceram. Tech.*, 2010.

8.8 Presentations

1. C. Carney, P. Mogilevsky, E. E. Boakye, T. A. Parthasarathy, and K. Keller, "Processing and Oxidation Behavior of $MeB_2 - 20 \text{ vol\% SiC}$," presented at Ultra High Temperature Ceramics: Materials for Extreme Environments ECI Conference, Lake Tahoe, CA, August 3-8, 2008.
2. T. A. Parthasarathy, M. D. Petry, M. Cinibulk, T. Mathur, and M. Groeber, "Development of a test to evaluate aerothermal response of materials to hypersonic flow using a scramjet wind tunnel," presented at the 34th Annual Conference on Composites, Materials and Structures (US. Only/ITAR-Restricted Sessions), Cape Canaveral/Cocoa Beach, Florida, January 2010.

LIST OF ACRONYMS, ABBREVIATIONS, AND SYMBOLS

ACP	Advanced Crystal Products
BC	Boundary Conditions
BDTT	Brittle to Ductile Transition Temperature
BMG	Bulk Metallic Glasses
CFD	Computational Fluid Dynamics
CMC	Ceramic Matrix Composites
CMSX-4	Single-Crystal Superalloy
CPR	Corrosion Penetration Rate
CTK	Composite Tool Kit
DC	Direct Chill
DDS	Discrete Dislocation Simulation
DSC	Differential Scanning Calorimetry
DTA	Differential Thermal Analysis
EBS	Enterprise Business System
EBSB	Electron Back Scattered Diffraction
EBSD	Electron Backscattered Diffraction
ECAP	Equal Channel Angular Pressing
EDS	Energy Dispersive Spectroscopy
EDX	X-ray Spectroscopy
EMPM	Electron Probe Micro-Analysis
FCC	Face Centered Cubic
FEM	Finite Element Modeling
FIB	Focused Ion Beam
FOD	Foreign Object Damage
FS	Fracture Stain
GDMS	Glow Discharge Mass Spectrometry
GFA	Glass Forming Ability
GND	Geometrically Necessary Dislocations
HIP	Isostatic Pressing
ILT	Interlaminar Tension
ISM	Induction Skull Melting
LMCA	Logistics Material Control Activity
LOTO	Lockout/Tagout
LSHR	Low Solvus High Refractory
MK	Macro-kinks
NDE	Nondestructive Evaluation
NEAT	New Equipment and Turn-ins
NFL	Nearly Fully Lamellar
OIM	Orientation Imaging Microscopy
PMEL	Precision Measurement Equipment Laboratory
PMI	Preventive Maintenance Inspection
POC	Point of Contact
PPE	Personal Protective Equipment (PPE)
RT	Room Temperature

LIST OF ACRONYMS, ABBREVIATIONS, AND SYMBOLS (Continued)

SAV	Staff Assisted Visit
SEM	Scanning Electron Microscopy (SEM)
SHM	Structural Health Monitoring
SHR	Strain-Hardening Rate
SNDS	Saturate and Dunk
SOC	Self-Organized Criticality
SPF	Super Plastic Forming
SXTL	Single Crystal
TDS	Technical Data System
TEM	Transmission Electron Microscopy
TGA	Thermogravimetric Analysis
TMDE	Test, Measurement, and Diagnostic Equipment
TMP	Thermal-Mechanical Processing
UCI	Unit Compliance Inspection
UHCT	Ultra-High Temperature Ceramics
VFT	Vogel-Fulcher-Tammann
VLS	Vaper-Liquid-Solid
VRG	Vacancy-rich Cluster
XRD	X-ray Diffraction
XRF	X-ray Fluorescence (XRF)
YAG	Yttrium Alumina Garnet
YS	Yield Strength